Polaritons unidimensionnels dans les microfils de Zno : vers la dégénérescence quantique dans les gaz de polaritons unidimensionnels

Aurélien Trichet

UNIVERSITÉ DE GRENOBLE

THÈSE

Pour obtenir le grade de

DOCTEUR DE L'UNIVERSITÉ DE GRENOBLE

Spécialité : **Physique**

Arrêté ministériel : 7 août 2006

Présentée par

Aurélien Trichet

Thèse dirigée par **M. Richard**
et codirigée par **Le Si Dang**

préparée au sein **de l'Institut Néel**
et de **l'Université de Grenoble**

One-dimensional polaritons in ZnO microwires

Towards one-dimensional quantum degenerate gas of bosons

Thèse soutenue publiquement le **9 février 2012**,
devant le jury composé de :

Dr. Andre Régis
Directeur de Recherche au CNRS à l'Institut Néel, Président
Dr. Bloch Jacqueline
Directrice de Recherche CNRS au Laboratoire de Physique des Nanostructures, Rapporteur
Pr. Wouters Michiel
Chercheur au département de Phyisique de l'univeristé of Antwerp, Rapporteur
Pr. Grandjean Nicolas
Professeur à l'Ecole Polytechnique Fédérale de Lausanne, Examinateur
Dr. Richard Maxime
Chargé de Recherche CNRS à l'Institut Néel, Directeur de thèse
Dr. Le Si Dang
Directeur de Recherche CNRS à l'Institut Néel, Co-Directeur de thèse

b

UNIVERSITÉ DE GRENOBLE

THÈSE

Pour obtenir le grade de

DOCTEUR DE L'UNIVERSITÉ DE GRENOBLE

Spécialité : **Physique**

Arrêté ministériel : 7 août 2006

Présentée par

Aurélien Trichet

Thèse dirigée par **M. Richard**
et codirigée par **Le Si Dang**

préparée au sein **de l'Institut Néel**
et de **l'Université de Grenoble**

One-dimensional polaritons in ZnO microwires

Towards one-dimensional quantum degenerate gas of bosons

Thèse soutenue publiquement le **9 février 2012**,
devant le jury composé de :

Dr. Andre Régis
Directeur de Recherche au CNRS à l'Institut Néel, Président
Dr. Bloch Jacqueline
Directrice de Recherche CNRS au Laboratoire de Physique des Nanostructures, Rapporteur
Pr. Wouters Michiel
Chercheur au département de Phyisique de l'univeristé of Antwerp, Rapporteur
Pr. Grandjean Nicolas
Professeur à l'Ecole Polytechnique Fédérale de Lausanne, Examinateur
Dr. Richard Maxime
Chargé de Recherche CNRS à l'Institut Néel, Directeur de thèse
Dr. Le Si Dang
Directeur de Recherche CNRS à l'Institut Néel, Co-Directeur de thèse

d

Remerciements

Tout d'abord, je souhaite remercier mes deux guides durant cette thèse: Maxime Richard et Le Si Dang. Maxime, tu as toujours pris le temps de répondre à mes questions et de m'aider quand tu le pouvais. Tes qualités scientifiques et ta façon de présenter la Science m'ont clairement aider à me forger à la recherche. Pour ces trois années, TF(merci)! Dang, tu auras été le vieux mentor qui avait toujours une vision d'ensemble sur mes problèmes. Max' avait souvent les meilleures réponses, et toi, les meilleures questions. Ta pédagogie, ton esprit de synthèse ainsi que la pertinence de tes questions ont marqué mon apprentissage dans ce milieu. A vous deux, merci de m'avoir former au monde de la recherche scientifique: promis j'irai prêcher la bonne parole!

Quel goût aurait eu cette thèse sans Claire et Samir, mes deux compagnons de galère - joie - débauche - désespoir - discussions politico-polémistes? Mine de rien, on a beaucoup partagé pendant ces trois années. Bon courage pour la suite à vous deux! Je vous souhaite plein de papiers... de toute façon, le reste, c'est surfait :-) Je remercie aussi l'ensemble des non-permanents du groupe NPSC avec qui j'ai pu intéragir et partager de bons moments: Sensei Munsch, Petr, Roman, Daniel et Igor. Au passage, un grand merci à Arnaud pour toutes les discussions autour de la machine à café qui font de l'institut un endroit agréable. Stephano, merci pour les nombreuses discussions scientifiques, bon courage pour ta permanentisation. François, cela a été un réel plaisir de travailler avec toi et j'espère que cela se reproduira. Bonne route à Clermont! Emilien, tu as maintenant les clés de la menuiserie pour envoyer du polari-pâté: bon courage! A vous deux, je vous souhaite un condensat cohérent sur un mètre à température ambiante et vous remercie pour le précieux temps passé ensemble. Je tiens aussi à remercier les membres permanents du groupe NPSC avec qui j'ai pu intéragir: Jacek, Jean-philippe, Lucien, David, Gilles, Henri, Régis, Joël, Alexia, Hervé. Enfin, merci à Françoise Hippert et Frank Hekking pour m'avoir guider vers cette thèse.

Cette thèse aurait été impossible sans ces fameux microfils. Je tenais ici à lister ici les meilleurs d'entre eux qui ont donné leur vie pour faire avancer la Science: de R1 à R33 avec une reconnaissance toute particulière pour les deux meilleurs R5 (brulé au combat), R33 (fugue sans laisser de mot) mais aussi, Gros Pillier (5 μm de diamètre quand même!), Bobby six killer et Albert. Bien entendu, je tiens surtout à remercier les orfèvres qui fabriquent ces microfils: l'équipe du Pr. Zhanghai Chen pour les microfils de ZnO et Jesus Zuniga Perez et Blandine Alloing pour les microfils de GaN. Pour ce qui est des microcavités ZnSe, merci à Kathrin Sebald et Carsten Kruse pour le travail effectué ensemble et pour cette collaboration qui va pouvoir maintenant prendre toute son ampleur.

Merci à mes potes de Grenoble avec qui j'ai partagé trois ans de maxi bonheur (par ordre croissant de [critère à choisir par le lecteur]): Pierrot (un petit Desert strike, mec?), Lolo (aka den hore), Clox (Courage!), Rami (je kiffe ton canap' mec), Prèz (tiens c'est marrant, il est bien aussi le tien de canap'), Djou (geek masta, qu'on le veuille ou non), Grand (rédiger une thèse: négligeable...), Rem's (Ooooooooohhh!) et mes deux collocs: Zouav (un morceau de lapin peut-être? Courage en Suisse!) et Bou (surtout quand il est en robe de chambre). Spécial merci à Jenna, pour tout ce qu'elle m'a fait vivre et tout ce qu'elle représente. Dans un tout autre registre, Rem's, Cyr' et Alex, mes compagnons de Zététique ainsi qu'à Richard Monvoisin: je vous descerne les remerciements les plus creux qui se trouvent dans ma poche ;-). Je me dois aussi de te remercier, Carole, pour notre histoire et tout ce qu'elle m'a apporté. Je te souhaite, plus que jamais, d'être heureuse dans ce nouveau chapitre.

Enfin, il me reste à remercier les personnes les plus importantes dans ma vie: ma famille. Pierre et Martine, vous avez toujours été là pour moi quelquesoit le problème, toujours prêts à

m'aider ou à me remettre sur le droit chemin. En bref: merci pour tous les moments (et il y en a...) où vous avez été présents. Stéphane, toi aussi, je te suis reconnaissant au plus au point. Tu as toujours été de bons conseils dans les moments difficiles. A toi et Aurélie: un grand merci pour tous les bons moments passés ensemble.

Enfin, je te remercie, toi, le lecteur inconnu (enfin si tu existes un jour). En guise de cadeau de bienvenue, je te propose de retrouver Charlie, Félicie, Ouaf, Blanchebarbe, Pouah ainsi que les fautes (volontaires bien sur) d'orthographe, de grammaire, voire même de science qui se sont dissimulées entre deux polaritons: bon courage!

A ma famille,

Contents

Introduction

In our classical world, there are two practical ways to distinguish two objects. First, we can measure their intrinsic properties such as their mass or their electrical charges. If these quantities are all identical, the only possibility is to track their positions versus time. In the quantum world, because of the wave particle duality, the second method is not relevant anymore. Indeed, the resolution of the position measurement at different times is limited by one inherent principle of quantum physics, namely the Heisenberg uncertainty principle. As a consequence, original situations emerge in quantum physics in which there are, at least, two fully indistinguishable particles. However, in quantum physics, the particles can be separated into two classes depending on one internal degree of freedom, namely the spin. On one side, we have the fermions (half-integer spin) and on the other, the bosons (integer spin).

Bosons are allowed to occupy the same quantum state (which is forbidden for fermions), described by its energy, momentum and spin. The particles are indiscernible as soon as their wavefunctions overlap, ie. when the coherence length is of the order of the mean interparticle distance. In this regime, bosons tend to cooperate because of quantum interferences and they agglomerate in a single quantum state creating a macroscopic quantum wavefunction of matter. This new state of matter, which is in the quantum degeneracy regime, has an original equation of state compared to the classical case. In the peculiar case of weakly interacting particules at thermal equilibrium, this transition is called Bose-Einstein condensation and can be crossed varying one of its thermodynamics parameters such as the temperature. This phase transition has been predicted by S.N. Bose and A. Einstein [11, 12, 13] in 1924-1925. The superfluidity of liquid Helium [14, 15] has been the first experimental observation of such a quantum degenerate state of matter, ie. in the limit of indistinguishability. It took some times to interpret this effect in terms of Bose-Einstein condensation. A more direct experimental observation of a Bose-Einstein condensation has been realized using ultracold atom gas in 1995 [16], opening the way to the experimental study of Bose gas in the quantum degenerate regime. However, Bose-Einstein condensation of atoms is intrinsically limited to the ultralow temperatures (sub-microKelvin temperatures) because of their heavy mass ($\sim 10^5 m_e$). More recently, two major experimental realizations of a Bose-Einstein condensate at room temperature have been obtained: in 2006 a condensate of magnons [17], quanta of magnetic excitations in a magnetically ordered ensemble of magnetic moments, and the Einstein's dream in 2010: a condensate of photons [18]. In the following part of this introduction, we will discuss the originalities of the polariton gas compared to all of these systems and their potential as a quantum degenerate Bose gas to go beyond the Bose-Einstein condensation.

A candidate for degenerate Bose gas physics: The exciton-polariton is an interesting candidate to undergo the quantum degeneracy regime. It is a composite particle in solid state physics made up of an electromagnetic field and an electronic matter field (called exciton) in the strong coupling regime. As both of these fields are bosons, the polariton is a boson as well. The first Bose-Einstein condensate of polaritons [19] has been observed in CdTe based microcavities

for a temperature of the polariton gas of 20K in 2006. It has pioneered the emerging field of quantum degenerate polariton gas in the solid state environment which has now shown major results such as polariton superfluidity [1, 2, 3, 4, 5, 6], Josephson oscillations [7] or optical manipulation of extended polariton condensates [8].

A driven dissipative system linking Bose-Einstein condensates and lasers: Because of the low lifetime of the photonic component of the polariton ($\sim ps$), a polariton gas is, by definition, an open and out of equilibrium system with a fixed average number of particles driven by an external energy input. Quasi-equilibrium is achievable in this condition thanks to the excitonic fraction of the polariton. Interestingly, depending on the thermalization time τ_T of this gas with respect to the polariton lifetime τ_p, it is possible to link two different classes of quantum degeneracy regime [20]. If $\tau_T << \tau_p$, the system can reach a quasi-equilibrium and transit into a Bose-Einstein condensate. On the other hand, if $\tau_T >> \tau_p$, the system is definitely out of equilibrium and the polariton gas presents a laser-like transition. The polariton gas is, therefore, the missing link between the Bose-Einstein condensates and the lasers. Moreover, the dissipative character of the polariton gas brings to light another unusual property of non-equilibrium superfluids: the possibility to create a superfluid state with a ground state (ie. a lowest energy state) with a non-null momentum thanks to the constant energy input [5, 21].

Control and manipulation of the condensate: The solid state environment, despite its effect on the coherence properties of the polariton gas, provides a powerful tool to control and manipulate the condensate. For example, it allows electrical injection of polaritons [22], trapping in original geometries [8, 9, 23, 24] or transport of the degenerate gas of polaritons through a circuit [8].

Potentiality for room temperature operation: Thanks to its photonic component, the polariton has a low effective mass $\sim 10^{-5} m_e$. Since, at thermal equilibrium, the coherence length scales like the inverse of the square root of the mass, polaritons have a larger coherence length than atoms and quantum degeneracy regime can be reached at temperatures as high as 300K. Consequently, polaritons are a very interesting candidate to bring the quantum degeneracy from ultralow temperature to room temperature. A large effort has been done in this direction using new materials with robust excitons at room temperature.

During this thesis, we have studied two different strategies to study robust polaritons in the quantum degenerate limit up to room temperature and in original geometries. In both strategies, we used II-VI wide band gap materials, namely ZnO and ZnSe, because they provide a robust exciton with a high binding energy, respectively 60 meV and 17 meV, compared to the thermal energy at 300K, ie. $\sim 26 meV$. In both cases, the growth method are much less developed than GaAs growth and, therefore, is a challenging task requiring a careful characterization. The first strategy was a top-down approach. In collaboration with Pr. Hommel, C. Kruse and K. Sebald from the Bremen university, we have designed and characterized three generations of ZnSe based microcavities, a heterostructure with two Bragg mirrors and quantum wells in between. We succeeded in obtaining promising structures such as the observation of the quantum degeneracy regime at low temperature and stable polaritons at room temperature. However, the poor quality of the structures at that time, affected by a strong disorder on both the photonic and excitonic components, prevented us to go beyond these first results. As a consequence, this strategy is not discussed in this thesis. Very recently, ZnSe-based microcavities of high quality has been grown. The following step consists in etching these structures in order to trap, control and manipulate the polariton gas in the quantum degenerate limit and at room temperature. The second strategy is a bottom-up approach. The structure is a monolithic wire made of bulk ZnO with a diameter around micrometer scale (called ZnO microwires). It is much less demanding from the growth point of view compared to ZnSe-based microcavities since it does not involve any heterointerface.

The microwire geometry is an original semiconductor structure and have been poorly studied before from the strong coupling regime point of view. From a more fundamental point of view, the polaritons in this microwire geometry are one-dimensional (1D). The study of quantum degeneracy in a system where only one degree of freedom is free is of high interest. Indeed, a rich phase diagram from 10K to 300K is expected [25] simply because, in 1D system, traffic jam-like effects result in the Tonks-Girardeau regime where the boson gas tends to "fermionize", ie. to behave like a fermion gas.

Because of the unusual structure of the ZnO microwires compared to the most common polariton devices, this thesis starts from the very basic electronic and photonic properties in such ZnO microwires (see part I). Indeed, most of their properties are directly connected to their bulk character, which has been studied decades ago [26, 27, 28] while, one of our goals, will be to demonstrate that they exhibit a robust strong coupling regime compared to the currently most used polariton structure, the microcavities.

The first chapter describes the elementary electronic properties of a bulk ZnO crystal. The exciton concept, which is a bound state resulting from the Coulomb interaction between an electron and a hole, will be presented. Then, we will focus on the three main excitons involved in the light-matter interaction. As described first by J. Hoppfield [26, 27, 28], the true eigenstate of this structure is a polariton mode, ie. a mixed state between an exciton and a photon, resulting from the coupling between the three excitons states and one photon mode. This strong coupling regime will be discussed in terms of the current knowledge on polariton devices.

The second chapter aims, firstly, to describe the photonic mode in a microwire with a hexagonal cross-section. For a sake of clarity, the photonic mode in a microwire with a circular cross-section will be discussed as a first step in order to understand the main characteristics of such 1D confinement. Secondly, our aim will be to demonstrate that the polaritons in a microwire are similar to the bulk case, ie. they have the same main properties, except for the dimensionality. In other words, the microwire geometry is simply confining the bulk polariton modes.

Once the concept of 1D polaritons in ZnO microwires is introduced, we will be able to situate these structures with respect to the up-to-date state of art in the third chapter. We will see that it is a promising system for room temperature operation because it provides robust polaritons at room temperature and it is much easier to grow than a microcavity. Moreover, its 1D character opens the way for the study of 1D out of equilibrium phase diagram from 4K to 300K.

The experimental tools used during this thesis are described in the fourth chapter. The three main goals of our experimental set-up are to inject optically a large amount of carriers in the semiconductor in order to reach the quantum degeneray regime and to address the 1D polaritons in a proper way using 1D Fourier spectroscopy.

The second part of this thesis deals with the experimental linear properties of the ZnO microwires. In the fifth chapter, we will extract the main charateristics of the strong coupling regime between the photonic modes and the three main excitons such as the light-matter strenght, called the Rabi splitting, the one-dimensional character and the polarization properties. GaN microwires have been as well investigated during this thesis because of their potential for electrical injection and allows a nice parallel with the ZnO microwires.

In the sixth chapter, the unusual situation of ZnO microwires, ie. polaritons featuring linewidths at room temperature similar to the low temperature ones, is presented. It will be explained in terms of the quenching of the LO phonon interaction allowed by the fact that the polariton splitting exceeds the LO phonon energy. This effect is particularly useful in our case since it isolates the polaritons from the main source of decoherence in our system, the phonon bath, even at room temperature.

In the third part, we will investigate the non-linear properties of ZnO microwires at low

temperature where an unusual situation is observed, ie. a quantum degenerate state of polaritons with an exceedingly high excitonic fraction of 97%. The seventh chapter aims to demonstrate that polariton gas can reach the quantum degeneracy regime at low temperature. We will focus in demonstrating the main features of a quantum degenerate polariton gas emphasizing on the fact that the strong coupling regime is preserved in this regime.

Finally, in the eighth chapter, thanks to the unusual microwire geometry, we will be able to address the dynamics of the excitonic reservoir and the relaxation mechanisms from the reservoir towards the polariton state through the polariton lasing regime. This study is of particular interest since it allows an insight in the dynamics and the thermodynamics of the polariton gas and its environment.

Part I

Introduction to polaritons in ZnO microwires

Chapter 1

Bulk exciton polaritons in ZnO crystal

Contents

ZnO microwires exhibit a peculiar situation of strong coupling regime between excitons and photons in an original structure. Firstly, they are made of pure ZnO: there is no heterostructure. Secondly, they have a wire-like shape with a diameter of the order of one micrometer. Therefore, before entering into the detailed description of the strong coupling regime in these structures, it is thus convenient to describe the electronic properties of a bulk crystal of ZnO. Indeed, the complex ZnO band structure has important consequences on the strong coupling regime in microwires.

In this part, we will start from the crystal structure and the band structure of ZnO, in order to explain the exciton levels in ZnO. In particular, we will focus on the "bright" excitons which interact with light. Then, we will recall that excitons are not the proper eigenstates in a bulk semiconductor. Their strong coupling regime with light results in a new quasi-particle: the bulk polariton. We will discuss how this coupling modifies ZnO exciton levels using linear response theory. Since a ZnO microwire is a bulk structure from the electronic point of view, this review will provide the required background to introduce microwire polaritons. Indeed, most of the properties of microwire polaritons derive from those of bulk polaritons.

1.1 Excitons in ZnO

1.1.1 Crystal structure

ZnO is a semiconductor which belongs to the II-VI group. The electronic configuration of Zinc (equation 1.1) and Oxygen (equation 1.2) allow sp^3 hybridization.

$$^{64}_{30}Zn : (1s)^2(2s)^2(2p)^6(3s)^2(3p)^6(3d)^{10}(4s)^2 \tag{1.1}$$

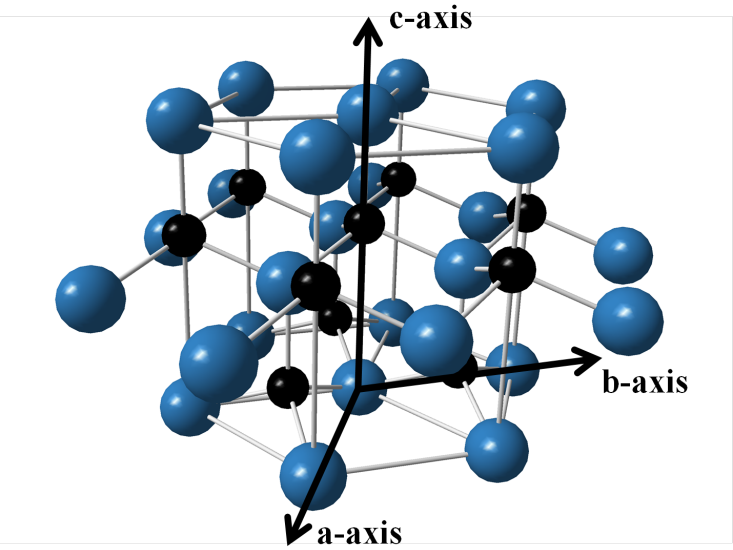

Figure 1.1: Wurtzite type lattice. Blue and black sites correspond to the two different species. a, b and c axis of the wurtzite structure are represented with the black arrows

$$^{16}_{8}O : (1s)^2(2s)^2(2p)^4 \tag{1.2}$$

As a consequence, there are four equivalent orbitals organized in a tetrahedron geometry for each atom site of the crystal. In this kind of arrangement, most common crystal structure, at ambient conditions, are zinc blend or wurtzite structures. In the case of ZnO, wurtzite is the most stable phase and is easier to grow [29]. Our microwires have this structure, therefore this is the one we will consider in this chapter.

The lattice of a Wurtzite structure is hexagonal (see figure 1.1) with two ZnO units per unit cell. This crystal is anisotropic with two equivalent axis called A and B (lattice constant a=b=0.325 nm at ambient condition) and a third one called C (lattice constant c=0.52 nm at ambient condition). This characteristic results in anisotropic electronic and excitonic properties.

1.1.2 ZnO band structure

Historically, a semiconductor is defined as a material which requires energy input (such as photoexcitation, electric field, thermal exitation, etc..) to switch from insulator behavior (electrons cannot be accelerates) to conductor behavior (electrons are free). In the case of an inorganic semiconductors, an energetic splitting arises from the periodicity of the unit cell resulting in an energy band gap where no electronic states are present. Below (respectively above) band gap, energy bands are called valence (respectively conduction) bands. Without any energy input, valence band is entirely filled by electrons. They cannot move through the crystal because of the Pauli exclusion principle. On the other hand, without any energy input, conduction band is empty.

Band structure in ZnO

ZnO belongs to direct semiconductor group and is interesting for optoelectronics in the near UV wavelength range. Indeed, its band gap energy at room temperature is 3.3 eV (375 nm). The fine structure of the valence bands of ZnO results from the wurtzite crystal structure, the spin-orbit interaction and the crystal field. It is represented on the figure 1.2. Spin-orbit interaction couples the spin of an electron with its orbital momentum. The crystal field corresponds to the electrostatic field induced by the different electronegativity of the compounds (1.65 for Zn and 3.44 for O) and the crystal anisotropy. It can split spatially degenerate states in which more than one spatial configuration of the wavefunction is possible.

We will now focus on a qualitative description of the band structure of wurtzite ZnO (details discussed in [29]).

In ZnO, the lowest conduction band is a s-like state. It is associated to one wavefunction with a zero orbital momentum $L = 0$ twice degenerated because of 1/2 spins. As the orbital momentum is zero for this band, spin-orbit does not affect it. Its energy is modified by the crystal field but it is not split because s-like wavefunction is isotropic. On the contrary, the highest valence band is a p-like state. It corresponds to three wavefunctions with a non-zero orbital momentum $L = 1$ two-fold degenerated because of spins. The crystal field removes the degeneracy of the p-like state. As it is an uniaxial anisotropy, the three p-like states are split into two degenerate states in the plane ($L_z = \pm 1$) at higher energy and one state along the c-axis ($L_z = 0$) at lower energy. In ZnO, contrary to other II-VI materials, spin orbit interaction can be seen as a weak perturbation compared to the crystal field because of its very ionic character. Therefore, the spin-orbit term involved in the Hamiltonian of the system (usually proportional to $\vec{S}.\vec{L}$ with $\vec{S}$ the spin of the electron) can be approximated to be proportional to $\vec{S_z}.\vec{L_z}$. Spin orbit interaction is relevant only along the z axis and the momentum quantum number of interest is $\vec{J_z} = \vec{L_z} + \vec{S_z}$. In this case, only the degenerate states $L_z = \pm 1$ of the valence band is split into $\vec{J_z} = \pm 3/2$ and $\vec{J_z} = \pm 1/2$.

Finally, as shown on figure 1.2, there are three different valence bands called, from low to high energy, A, B and C bands. In the very peculiar case of ZnO, because of the strong p-d coupling in the valence band leading to a negative spin-orbit interaction, the two upper valence bands are inverted compared to usual wurtzite semiconductor (see page 78 of [29] and [30]).

Electronic wavefunction in semiconductor materials

We will now discuss the electronic excitations in a semiconductor to derive, later, the electron hole bound states. In this case, an electron from the valence bands is promoted to the conduction band. In the Born-Oppenheimer approximation [31], nuclei are assumed to form a static lattice creating a periodic potential landscape. Conduction (valence) electrons interact with the potential and their wavefunctions $\psi_{c,\vec{k}}(\vec{r})$ ($\psi_{v,\vec{k}}(\vec{r})$) with a momentum $\vec{k}$ and a position $\vec{r}$ satisfy Schrödinger equation. Since these particles are indistinguishable and using the Hartree-Fock approximation, the ground state of the crystal $\phi(\vec{r_1}, ..., \vec{r_N})$ for N electrons is given by the following Slater determinant:

$$\phi(\vec{r_1}, ..., \vec{r_N}) = \frac{1}{\sqrt{N!}} Det(\psi_{v,\vec{k_1}}(\vec{r_1}) ... \psi_{v,\vec{k_N}}(\vec{r_N})) \tag{1.3}$$

with a zero total momentum. In this equation, all the electrons are in the valence band.

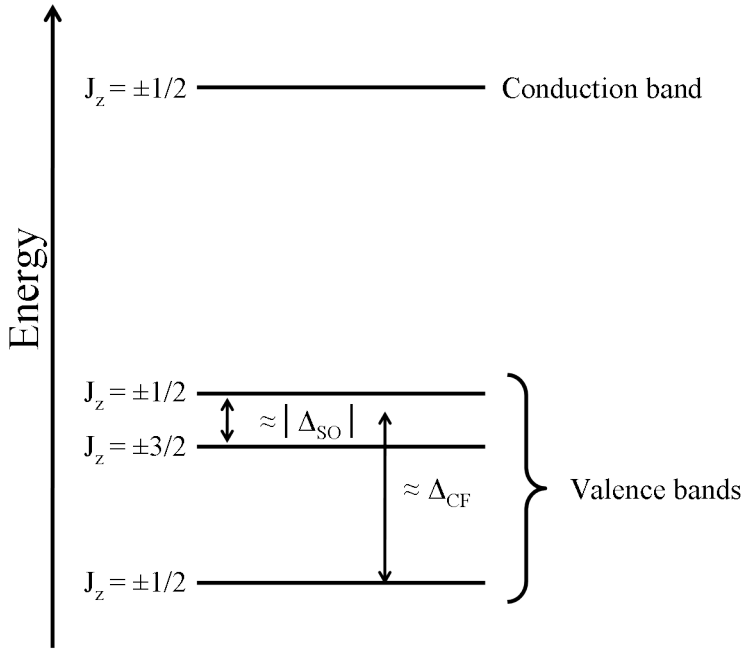

Figure 1.2: Level structure of ZnO presenting the conduction band and the three valence bands. Δ_{SO} (Δ_{CF}) corresponds to the spin-orbit (crystal field) energy and J_z to the total momentum of the electronic band in the weak perturbation limit.

Neglecting electron-electron interactions via Coulomb force, the first excited state reads:

$$\phi_{\vec{k}}(\vec{r_1},...,\vec{r_N}) = \frac{1}{\sqrt{N!}} Det(\psi_{v,\vec{k_1}}(\vec{r_1})...\psi_{c,\vec{k_n'}}(\vec{r_N})...\psi_{v,\vec{k_N}}(\vec{r_N})) \tag{1.4}$$

where one electron is promoted to the conduction band. Its momentum is given by $\vec{k} = \vec{k_n'} - \vec{k_n}$ where $\vec{k_n}$ ($\vec{k_n'}$) is the momentum of the electron in the ground state (in the excited state). In this state, one electron is in the conduction band and can participate to conduction through the semiconductor.

1.1.3 Excitons in ZnO

In usual semiconductors, an electron and a hole attract each other via electrostatic interaction and form a new quasi-particle: an exciton that has a lower energy than the band gap. Switching on Coulomb interaction in state 1.3 and 1.4 results in this bound electron hole states.

Generality on exciton: electron hole pair bound by Coulomb interaction

Exciton wavefunction, Hydrogen-like model and binding energy An example of a complete derivation of the exciton concept can be found in reference [31]. The crucial point of this development is that the exciton is an elementary excitation in a many body system with Coulomb interaction. In this case, the first excited state of the crystal is not described by equation 1.4 but by the exciton wavefunction. In a first order perturbation theory, exciton

wavefunction is a linear combination of the electronic wavefunctions 1.4 given by:

$$\phi_{exc,\vec{k}} = \sum_{\vec{k'}} A_{\vec{k}}(\vec{k'})\phi_{\vec{k'}} \tag{1.5}$$

where $A_{\vec{k}}(\vec{k'})$ is the Fourier transform of the wave function of the excited state in real space. As a result, many electron states participate to the exciton wavefunction (ie. $A_{\vec{k}}(\vec{k'})$ is small compared to 1). Therefore, at low density, the electron states involved in an exciton state fully satisfy the Pauli exclusion principle.

It can be shown that the envelope function of the exciton (ie. the Fourier transform of $A_{\vec{k}}(\vec{k'})$ in equation 1.5) satisfies hydrogen-like Schrödinger equation, with an effective binding energy E_b and Bohr radius a_B^* given by:

$$E_b^n = \frac{R_y^*}{n^2} = \frac{\mu e^4}{2\epsilon^2\hbar^2 n^2} \qquad where\, n = 1, 2, ...$$

$$a_B^* = \frac{\hbar^2\epsilon}{\mu e^2}$$

where $\mu^{-1} = m_e^{-1} + m_h^{-1}$ is the reduced mass of the electron-hole system, R_y^* is the effective Rydberg radius. n refers to the principal quantum number of the hydrogen model and, consequently, to the shape of the electron-hole envelop wavefunction (s-state, p-state, etc...) and ϵ is the absolute permittivity. Around zero momentum, exciton has an effective mass $M = m_e + m_h$ and its energy dispersion reads:

$$E_X = E_g - E_b^n + \frac{\hbar^2|\vec{K}|^2}{2M}$$

with E_g the band gap energy and $\vec{K}$ the total momentum of the exciton.

In the case of ZnO, for $n = 1$ state, the exciton reduced mass is $\mu = 0.19\ m_0$ [29] where m_0 is the free electron mass, the Bohr radius is 1.8 nm [29] and the binding energy is approximately 60 meV [29]. This last value is higher than in other materials used for polaritonic devices based on inorganic materials: GaAs (4.8 meV), CdTe (10 meV), GaN (25 meV) or ZnSe (17 meV) [32]. As this binding energy greatly exceeds room temperature thermal energy (26meV), this exciton is stable at high density and high temperature. It has been shown experimentally that ZnO excitons are not ionized at room temperature [33].

Radiative recombination Exciton features a non-zero dipole momentum. Therefore, it is coupled with light and recombines into photons. However, radiative recombination of excitons is possible only under certain conditions and, therefore, some excitons are "bright" and other "dark". In this paragraph, we will discuss these selection rules.

The first requirement concerns the dipolar nature of excitons. Let us consider a bare exciton, one can apply the first order perturbation theory to the light-matter interaction hamiltonian. Assuming that the dipolar matrix element between electrons and holes is independent of their momentum, the dipole-transition probability reads [34]:

$$|\ H_X^D\ |^2 = |\ <X\ |\ H_X^D\ |\ 0>\ |^2 = \frac{1}{N_{eh}}\ |\ \varphi_{nlm}(0)\ |^2 |<\psi_c^e\ |\ H_e^D\ |\ \psi_v^e>|^2 \tag{1.6}$$

where $|\ X>$ corresponds to the exciton wavefunction, $|\ 0>$ corresponds to the ground state, N_{eh} is defined in 1.1.3, $\varphi_{nlm}(0)$ is the envelop function at a zero radial coordinate with usual

hydrogen quantum numbers n, l and m, $H^D_{X/e}$ is the dipole interaction hamiltonian for exciton (X) or electron-hole (e) and $\mid \psi^e_{c/v} >$ is the wavefunction of an electron in a conduction (c) or valence (v) band.

As a result of equation 1.6, since $\mid \varphi_{nlm}(0) \mid^2$ is non zero only for $l = 0$, only s-like exciton can recombine via dipole interaction. Exciton with $l \neq 0$ would be dipole forbidden (ie. $\mid H^D_X \mid^2 = 0$) and would decay via quadrupole interaction with a much smaller probability. Fortunately, exciton ground state has a s-like wavefunction with $l = 0$.

The second requirement concerns the spin of the heavy-hole exciton. Indeed, exciton recombination involves the recombination of an electron (spin projection $\pm 1/2$) and a heavy hole (spin projection $\pm 3/2$) resulting in four exciton states with total momentum $J = \pm 2$ and $J = \pm 1$. Since photons have a spin ± 1, excitons with a total orbital momentum $J = \pm 2$ cannot recombine radiatively unless the recombination process involves a spin-flip process. As a consequence, they are not directly coupled to light and are called "dark excitons". On the opposite, excitons with a total orbital momentum $J = \pm 1$ can directly recombine radiatively.

ZnO exciton states: Three "Bright" excitons

The previous concepts (wavefunction, binding energy, effective mass and recombination) are applicable in more realistic structures such as ZnO crystal. However, they get more complex due to the anisotropy and the multiple valence bands, for example. In ZnO, exciton states result from the possible transitions between the conduction band and the three different valence bands. Wavefunction of the exciton is a combination of the one of the electron, the hole and the envelop function. According to the group theory (exact formulation in [29, 35]), in ZnO, for the $n = 1$ state, one can write the exciton group symmetry as a direct product of the symmetry groups of its components:

$$\begin{array}{c}\text{Exciton group}\\ \text{symmetry}\end{array} = \begin{array}{c}\text{Electron group}\\ \text{symmetry}\end{array} \otimes \begin{array}{c}\text{Hole group}\\ \text{symmetry}\end{array} \otimes \begin{array}{c}\text{Envelop function}\\ \text{group symmetry}\end{array}$$

Using group notation [29, 35], it corresponds to:

$$\Gamma_X = \Gamma_7 \otimes (A\Gamma_7 + B\Gamma_9 + C\Gamma_7) \otimes \Gamma_1$$

$$\Gamma_X = A\Gamma_1 + A\Gamma_2 + A\Gamma_5(\times 2) + B\Gamma_6(\times 2) + B\Gamma_5(\times 2) + C\Gamma_1 + C\Gamma_2 + C\Gamma_5(\times 2)$$

where $(\times 2)$ means twice degenerated state and Γ refers to the symmetry of the wavefunction.

As a result, there exist twelve excitons in ZnO among which only five are bright. Indeed, depending whether the recombination involves a spin-flip or is dipole-allowed, the radiative transition probability is drastically modified. Table 1.1 summarizes these properties. Finally, five excitons have a large oscillator strength resulting, because of degeneracy, in three resonances with different energies. $A\Gamma_5$ and $B\Gamma_5$ excitons interact both with light linearly polarized perpendicularly to c-axis of the wurtzite structure whereas $C\Gamma_1$ exciton, at higher energy, mainly interacts with light linearly polarized parallel to c-axis. Because they have a large oscillator strength (ie. a high transition probability), these three excitons will be the largest contributors in the near band-edge light-matter interactions in ZnO bulk crystal.

Table 1.2 summarizes some properties of the three "bright" excitons A, B and C in ZnO. Most of these physical quantities have been already discussed and new ones, such as LT splitting, will be discussed later.

Exciton state	Spin-flip involved	Dipole allowed	Transition probability
$A\Gamma_1$	Yes	Yes for $E \parallel c$	**Small**
$A\Gamma_2$	Yes	No	**Very small**
$A\Gamma_5(\times 2)$	No	Yes for $E \perp c$	**Large**
$B\Gamma_6$	Yes	No	**Very small**
$B\Gamma_5(\times 2)$	No	Yes for $E \perp c$	**Large**
$C\Gamma_1$	No	Yes for $E \parallel c$	**Large**
$C\Gamma_2$	Yes	No	**Very small**
$C\Gamma_5$	Yes	Yes for $E \perp c$	**Small**

Table 1.1: Selection rules of the A, B and C excitons. ($\times 2$) means twice degenerated state. [29]

1.2 Bulk polaritons as eigenstates of a ZnO crystal

In reality, excitons are not the true eigenstates of an infinite crystal. J. Hopfield [26, 27, 28] understood back in 1958 that exciton is in the strong coupling regime with light because of the reversible exchange of energy between these two oscillators. The true propagative eigenstates in this system are bulk polaritons which are an exciton-photon mixture. As ZnO microwires studied in this thesis are made of bulk material, it is interesting to enter the detailed description of bulk polaritons in an infinite crystal of ZnO.

In this section, we will first describe the linear response theory which allows to understand the effect of the light-matter strong coupling regime on the optical properties of a semiconductor. This method was first developped by J. Hopfield to describe optical response of excitons in bulk semiconductors and especially ZnO [26, 27, 28]. Then, we will discuss the concept of bulk polaritons in detail and, especially, in the case of ZnO. Finally, we will obtain the expression of the Rabi Splitting in bulk material and in ZnO microwires.

1.2.1 Linear response theory for excitons

Linear response theory describes the macroscopic response of a material under electromagnetic excitation. This semi-classical theory relies on a macroscopic quantity $\epsilon(\omega)$ which characterized the amount of polarization field generated by an electromagnetic excitation. This effective dielectric function $\epsilon(\omega)$ in the vicinity of a resonance like the exciton transition can be understood by a mechanical analogy where the exciton is described by an harmonic oscillator. The Maxwell equations solved with this dielectric function $\epsilon(\omega)$ accounts for energy properties of the strong coupling regime in the limit of the linear response, ie. the first order in the polarization field.

Lorentz oscillator

Lorentz oscillator model corresponds to the motion equation of a polarization field under electromagnetic excitation. Using the fundamental principle of dynamics, the scheme 1.3 can be described by the equation:

$$m\ddot{x} = \parallel \vec{F}_s \parallel + \parallel \vec{F}_f \parallel + \parallel \vec{F}_{exc} \parallel \tag{1.7}$$

with, the Hooke's law for the spring: $\parallel \vec{F}_s \parallel = -kx$, the viscous resistance force $\parallel \vec{F}_f \parallel = -\gamma\dot{x}$ and an electromagnetic excitation $\parallel \vec{F}_{exc} \parallel = e \parallel \vec{E} \parallel = eE_0e^{-i\omega t}$

Exciton	Energy at 0K (meV)	Energy at 300K (meV)	Polarization selection rules
A	3375.5 [10, 36, 37]	3309 [38]	mainly $E \perp c$
B	3381.5 [10, 36, 37]	3315[38]	mainly $E \perp c$
C	3420 [10, 36, 37]	3355[38]	mainly $E \parallel c$

Exciton	Wavefunction group symmetry	LT splitting (meV)	Oscillator strength (meV^2)
A	Γ_5	1.5[38, 39]	10000
B	Γ_5	11.1[38, 39]	73600
C	Γ_1	13.9[38, 39]	93300

Table 1.2: Brief summary of A, B and C excitons properties

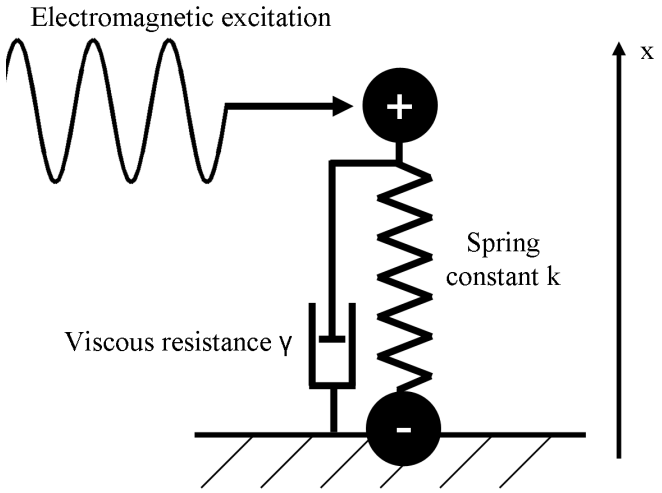

Figure 1.3: Mechanical analogy of a Lorenz oscillator under electromagnetic excitation

where k is the spring constant, γ is the friction coefficient and E_0 is the strength of the electric field at a pulsation ω.

Injecting $\gamma' = \frac{\gamma}{m}$ as well as the resonance pulsation $\omega_0^2 = \frac{k}{m}$ and Fourier transforming equation 1.7, we can write:

$$x(\omega) = \frac{\frac{eE_0}{m}}{\omega_0^2 - \omega^2 + i\gamma'\omega}$$

This oscillating motion will generate a polarization field in the medium characterized by its polarizibility $\hat{\alpha} = \frac{ex(\omega)}{E_0} = \frac{\frac{e^2}{m}}{\omega_0^2 - \omega^2 + i\gamma'\omega}$. This equation has a strong divergence at the resonance ω_0 (see figure 1.4 left panel) which is softened by the linewidth γ' (see figure 1.4 right panel). This divergence will result eventually in the strong coupling regime.

Effective dielectric function

In the following, we will see how the polarizibility can be inserted in the Maxwell equations. Around exciton resonances, a semiconductor can be described as an ensemble of identical and independant oscillators. If we define N_v, the density of oscillator per unit volume, the induced polarization reads: $\vec{P} = N_v\hat{\alpha}\vec{E}$. As a result, one can define the electric displacement $\vec{D}$ as the sum of the electromagnetic excitation and the electromagnetic emitted by the dipoles:

$$\vec{D} = \epsilon_0\vec{E} + \vec{P} = \epsilon_0(1 + \frac{N\hat{\alpha}}{\epsilon_0})\vec{E}$$

Relative permittivity is defined by $\vec{D} = \epsilon_0\epsilon\vec{E}$ and leads to an effective complex value of ϵ including exciton resonance:

$$\epsilon = 1 + \frac{\frac{N_v e^2}{\epsilon_0 m}}{\omega_0^2 - \omega^2 + i\gamma'\omega} \tag{1.8}$$

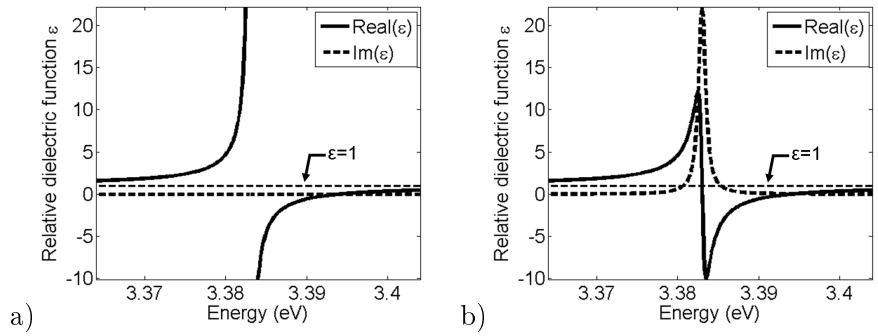

Figure 1.4: a) shows the dielectric function associated to the $B\Gamma_5$ exciton of ZnO at low temperature with $\sqrt{f} = 274meV$, $\hbar\omega_0 = 3.383eV$ and $\hbar\gamma' = 0meV$. b) shows the function with $\hbar\gamma' = 1meV$ [40]

Oscillator strength

The quantity $f = \frac{N_v e^2}{\epsilon_0 m}$ is defined as the oscillator strength and corresponds to the numerator of the fraction of equation 1.8. It characterizes the strength of the light-matter interaction for the resonance of interest. In the case of excitons in semiconductor, oscillator strength can be derived more rigorously in a quantum mechanical way using dipole-field interaction seen in 1.1.3:

$$f = \frac{2N_v\omega_0}{\epsilon_0\hbar} \mid H_X^D \mid^2$$

The factor $\hbar$ has been added to to preserve homogeneity of the equation. In this case, the oscillator strength f unit is eV^2.

Complex dielectric function: Polarization response and dissipation in a semiconductor

The relative dielectric function $\epsilon(\omega)$ is a complex number. The real part of equation 1.8 describes the polarization response (including exciton resonances) of the semiconductor material. The imaginary part of equation 1.8 describes the dissipation of the energy in the semiconductor material (via absorption). Equation 1.8 can be rewritten:

$$Re(\epsilon) = 1 + \frac{f((\hbar\omega_0)^2 - (\hbar\omega)^2)}{((\hbar\omega_0)^2 - (\hbar\omega)^2)^2 + ((\hbar\gamma')(\hbar\omega))^2} \tag{1.9}$$

$$Im(\epsilon) = \frac{-f(\hbar\gamma')(\hbar\omega)}{((\hbar\omega_0)^2 - (\hbar\omega)^2)^2 + ((\hbar\gamma')(\hbar\omega))^2} \tag{1.10}$$

The imaginary part of ϵ is vanishing for $\hbar\gamma' = 0meV$ because $\hbar\gamma'$ is characterizing the oscillation damping. $\hbar\gamma' \neq 0meV$ corresponds to the broadening of the excitonic transition via non-radiative losses or dephasing induced by exciton phonon scattering for example. Figure 1.4 a) shows the dielectric function for $\hbar\gamma' = 0meV$ with a vanishing imaginary part and a divergent real part at resonance. On the other side, figure 1.4 b) shows the same function but with $\hbar\gamma' = 1meV$.

Longitudinal Transverse (LT) splitting

For each exciton, two states are electromagnetic active and are split. In the case of ZnO "bright" excitons, this splitting is 1.5 meV for $A\Gamma_5$, 11.1 meV for $B\Gamma_5$ and 13.9 meV for $C\Gamma_1$[39].

The first active state is at resonance $\hbar\omega_0 = 3.383eV$ where the dielectric function diverges as shown on figure 1.4. Indeed, at this point, the Maxwell equation $\vec{\nabla}\vec{D} = \epsilon(\omega)\vec{\nabla}\vec{E} = \vec{0}$ with $\epsilon(\omega) \neq 0$ leads in the Fourier space to the relation $\vec{k}.\vec{E} = \vec{0}$. The total electromagnetic field (ie. the sum of the electromagnetic excitation and the polarization field) is then polarized (for both electric and magnetic fields) in a plane perpendicular to the propagation: it is a transverse field. Excitation and dipole electromagnetic fields oscillate in phase in a transverse mode and propagate through the crystal. Since it is transverse, this field can couple to the modes exterior to the crystal.

The second active state is at $\hbar\omega = 3.394eV$ exactly at 11.1 meV above the exciton resonance. In this peculiar point, $\epsilon(\omega) = 0$ and the field is not necessarily transverse. The exciton dipole and the electromagnetic field are longitudinal and oscillate out of phase (even in an isotropic medium). For longitudinal waves, the fields points in the opposite direction to the polarization induced by the oscillators. Consequently, it acts as a supplementary restoring force for the oscillators characterized by the oscillator strength (ie. the light-matter coupling). This consideration explains that the pulsation of this mode is higher than the transverse mode and physically connect these two quantities. From the equations 1.10 and $\epsilon(\omega) = 0$ with $\hbar\gamma' = 0meV$, one can compute a relation between f and ω_{LT}, assuming a small LT splitting ($\omega_{LT} \ll \omega_0$):

$$f = 2\hbar\omega_{LT}\hbar\omega_0$$

ω_{LT} is a measurable quantity (by reflectivity measurement for example) which is known for a lot of materials. It is interesting that this quantity provides in a straightforward way the Rabi splitting (ie. $\Omega = \sqrt{f}$ as we will see further) of the bulk polaritons.

Spatial dispersion: ensemble of coupled oscillators

As we have seen in 1.1.3, energy and pulsation of excitons depend on the momentum $\vec{k}$. Therefore, the dielectric function including the excitonic resonance depends on this factor as well. This means that the response of the medium to the electromagnetic field is non-local and depends on the spatial position. For symmetry consideration of the system, $\omega_0(\vec{k})$ is a symmetric function and can be developed around Γ point:

$$\hbar\omega_0(\vec{k}) = E_X = E_g - E_b^n + \frac{\hbar^2k^2}{2M} = \hbar\omega_0 + \frac{\hbar^2k^2}{2M}$$

The dielectric function, in this case, depends explicitly on the wavevector $\vec{k}$ and reads:

$$\epsilon(\omega, \vec{k}) = 1 + \frac{f}{(\hbar\omega_0(\vec{k}))^2 - (\hbar\omega)^2 + i\hbar\gamma'\hbar\omega}$$

1.2.2 Bulk polariton in ZnO crystal

As we have seen in 1.2.1, linear response theory allows to describe the response of an excitonic resonance to an electromagnetic excitation. In this subsection, we will discuss the propagating states in a bulk crystal by applying Maxwell equations with the dielectric function including excitonic resonance. Bulk polaritons will naturally appear. Then, we will focus on the experimental observation of such quasi-particles in ZnO bulk crystal and their specific properties. As

we will see, multiple bulk polaritons dispersions can be observed which are related to the three excitons A,B and C of ZnO.

Bulk polariton dispersion

To obtain the polariton dispersion, we need to take the dieclectric function $\epsilon(\omega)$ into account in the photon dispersion. Three equations have to be solved together to obtain the polariton dispersion:

1. The uncoupled photon dispersion relation:

$$E^{\gamma} = \frac{\hbar c k^{\gamma}}{\sqrt{\epsilon_0}} \tag{1.11}$$

   where E^{γ} is the energy of the uncoupled photon mode for a given momentum k^{γ}. This first equation 1.11 relation gives the vacuum photon dispersion relation without any excitonic contribution to the dielectric function.

2. The dielectric function:

$$\epsilon(E) = 1 + \sum_{i=A,B,C} \frac{f_i}{E_{X_i}^2 - E^2 + i\hbar\gamma_i' E} \tag{1.12}$$

   where E_{X_i} is the energy of the i^{th} exciton resonance.

3. The polariton dispersion:

$$E^p = \frac{E^{\gamma}}{\sqrt{\epsilon(E^p)}} \tag{1.13}$$

   where E^p is the polariton energy. This last equation 1.13 gives the polariton dispersion relation. It is similar to the uncoupled photon dispersion equation 1.11, however, the dielectric function (equation 1.12) including the excitonic resonances has been taken into account. Moreover, it is an implicit equation compared to equation 1.11: E^p is in both side of the equality.

By solving these three equations 1.11,1.12 and 1.13 in the general case and including the spatial dispersion, it is possible to numerically compute the relation between the polariton energy energy E_p and its momentum $\vec{k}$. The result in ZnO is shown on figure 1.5 by taking into account only the B exciton. Dashed lines shows the uncoupled case, ie. $f = 0$. As one can see, because of the oscillator strength of the exciton, there is a splitting in the region where the uncoupled transitions cross. This splitting is a result of the anticrossing behavior in the strong coupling regime. The modes of propagation in the crystal are mixed states between exciton and photon: the two polarization fields exchange energy. This is the strong coupling regime. The low (high) energy branch is called the lower (upper) polariton branch.

Interestingly, it is possible to solve the equations 1.11,1.12 and 1.13 in a simple case. Indeed, in the case of one excitonic resonance with $\gamma' = 0$ and without any spatial dispersion (condition satisfied in the light cone) and assuming that the polariton energy E_p is close to the uncoupled exciton and photon resonance compared to the square root of the oscillator strength $\sqrt{f}$, it is possible to obtain the simple two oscillators model equation:

$$(E^p - E_X)\,(E^p - E^{\gamma}) = \frac{f}{4} \tag{1.14}$$

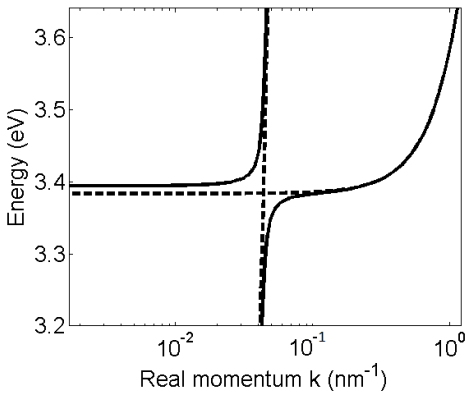

Figure 1.5: Bulk polariton dispersion for the B exciton alone in ZnO with $\hbar\gamma' = 0meV$ (log scale). Full lines corresponds to the strong coupling regime and dashed lines to the uncoupled case (pure exciton and photon).

This equation gives rather simple expressions for the lower (+ sign) and upper (- sign) polariton branches:

$$E^p_{UP/LP} = \frac{E_X + E^\gamma \pm \sqrt{(E_X - E_\gamma)^2 + f}}{2}$$

We will now link the oscillator strength of excitons in bulk crystal with the so-called Rabi splitting using the equation . Rabi splitting is defined by the minimal splitting between the two eigenstates and is achieved when the two non-coupled modes are resonant. Using these conditions and equation 1.2.2, calculation leads to a very simple relation:

$$\Omega = \sqrt{f} = \sqrt{2\omega_0\omega_{LT}}$$

which is the Rabi splitting associated to the bulk polaritons when the exciton-photon overlap is equal to unity. In semicondutors, this value is generally large as compared to Rabi splitting encountered in the literature in micro-cavities. For example, in CdTe, $\Omega^{CdTe}_{bulk} = 36meV$ while in CdTe based-microcavities, the Rabi splitting is of the order of 26 meV.

For a set of excitons separated by an energy much smaller than their respective Rabi splittings, the total oscillator strength can be obtained by adding the oscillator strength of each of them. So for bulk polaritons in ZnO, in the polarization $E \perp c$, the total Rabi splitting is $\Omega_{E\perp c} = \sqrt{\Omega_A^2 + \Omega_B^2} = \sqrt{(135meV)^2 + (268meV)^2} = 300meV$. For $E \parallel c$, we obtain $\Omega_{E\parallel c} = 288meV$. Since the overlap between photon and bulk exciton in ZnO microwires is close to unity, this value is an indication for a Rabi splitting of the same order of magnitude in these structures.

Momentum space mapping in ZnO

Experimental observation of bulk polaritons is a challenging task. Indeed, the key feature of the polariton concept is the anti-crossing behavior. However, it is not directly accessible using linear spectroscopy techniques such as reflection, transmission or luminescence without an elaborate theoretical fit. Moreover, the lower bulk polariton dispersion is situated outside the light cone and, thus, is difficult to study using resonant excitation for example. However, as described in reference [32], it is possible to access the polariton dispersion using non-linear experimental techniques such as two photon absorption or two photon Raman scattering.

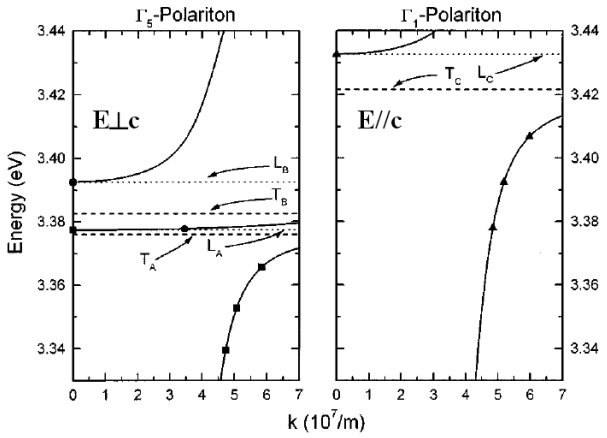

Figure 1.6: Polariton branches in bulk ZnO. Squares, circles, and triangles refer to resonances of the $A\Gamma_5$, $B\Gamma_5$, and $C\Gamma_1$ states, respectively, measured by three-photon difference frequency generation and two-photon excitation spectroscopy at 4K. T: transversal exciton, L: longitudinal exciton. Taken from reference [41]

Figure 1.6 , taken from reference [41], presents a three-photon difference frequency and a two photon absorption experiments on a bulk crystal of ZnO. One can see the anticrossing behaviour around $k = 4.10^7 m^{-1}$ for the $E \perp c$ polarization as shown in figure 1.5 as well as the LT splitting. In this polarization, $A\Gamma_5$ and $B\Gamma_5$ have to be taken into account resulting in a third branch in between the two excitons called middle polariton branch. Therefore, there are three polariton branches resulting from the coupling of the $E \perp c$ polarized light and the $A\Gamma_5$ and $B\Gamma_5$ excitons (see left panel of figure 1.6). On the other hand, there are two polaritons arising from the coupling of the $E \parallel c$ polarized light and the $C\Gamma_1$ exciton (see right part of figure 1.6). Indeed, $A\Gamma_5$ and $B\Gamma_5$ excitons, on one hand, and $C\Gamma_1$ exciton on the other results in two linearly cross-polarized independent families of polaritons. Because of polarization selection rules, in the case of bulk ZnO, these two cross-polarized set of polaritons are not coupled together. Interestingly, this situation will not be fully recovered in ZnO microwires.

Excitonic and photonic fraction of a polariton state

The excitonic fraction of the polariton depends on its spectral position with respect to the energy of the bare exciton and photon states. When both uncoupled states are at resonance, the lower and upper polariton fields are made up of half excitonic field and half electromagnetic field. The excitonic and photonic fraction of the polariton field can be computed thanks to the linear response theory. In this framework, the quantity of interest is the energy carried by each fields. In a dispersive medium characterized by its permittivity ϵ and permeability μ, the time-average energy density w, in a general formulation, reads:

$$w = \frac{1}{2} Re \left[\frac{1}{2} \frac{d(\omega\epsilon)}{d\omega} |\vec{E}|^2 + \frac{1}{2} \frac{d(\omega\mu)}{d\omega} |\vec{H}|^2 \right]$$

where $|\vec{E}|^2$ and $|\vec{H}|^2$ are the magnitude of the electric and auxiliary magnetic fields. In a semiconductor, close to the excitonic resonance, the important variation of the dielectric function ϵ has to be taken into account while the permability μ is constant. Considering a plane electromagnetic wave in the semiconductor at an energy $\hbar\omega$ propagating without any losses (ie. $\gamma' = 0$),

it leads to:

$$w = \frac{\epsilon_0 |\vec{E}|^2}{2} \left[1 + \frac{f}{2} \frac{\left(\omega^2 + \omega_0^2\right)}{\left(\omega_0^2 - \omega^2\right)^2} \right]$$

in which the constant part corresponds to the usual time-averaged energy density for a plane wave and the energy dependent part corresponds to the energy stored in the exciton field. Assuming $\frac{\omega}{\omega_0} \sim 1$, the proportion of energy stored in the exciton field $|X|^2$ reads:

$$|X|^2 = \frac{f}{f + 4(\hbar\omega - \hbar\omega_0)^2} \tag{1.15}$$

The excitonic fraction, given by equation 1.15, is coherent with the exciton-photon mixing picture : $|X|^2 = 1$ for $\omega = \omega_0$ (pure exciton case), $|X|^2 = 0.5$ for $\omega = \omega_0 - \frac{\sqrt{f}}{2}$ and $|X|^2 = 0$ for large value of ω (pure photon case). As a consequence of equation 1.15, the excitonic fraction of a polaritons changes from zero to unity depending on its spectral position.

The fact that a polariton is a mixed state provides scientifically motivating properties compared to pure exciton or pure photon. First of all, contrary to a pure photon, a polariton can interact with its environment and other polaritons through its excitonic fraction $|X|^2$. If the polariton has a non-zero ground state (like in a cavity for a photon), it can lead to a thermal equilibrium. On the other hand, its photonic component will tend to lower the polariton mass compared to the pure exciton case because of its steep dispersion compared to the exciton dispersion. Therefore, like in a laser, polariton can undergoes bosonic stimulation at high density but, contrary to the laser, polaritons are interacting, can thermalize and one can goes from pure photon stimulation to pure exciton stimulation in a solid state environment.

Limits of the polariton pictures in a semiconductor

Strong coupling regime requires a coherence condition which in certain situation can break down leaving two weakly coupled states. In this subsection, we will explore some relevant limits of this regime for exciton-polaritons in relation with some interesting features of the polaritons in ZnO microwires.

Reversible oscillations The first condition to reach strong coupling is a reversible coupling between photons and excitons. Indeed, to observe the strong coupling regime, exciton radiative decay has to be reversible. For example, this condition is realized in bulk semiconductor crystal where excitons and photons can exchange energy indefinitely. However, in a single bare quantum well structure for example, because of the broken translation symmetry, excitons in the light cone are coupled to a large continuum of photonic modes (outside the quantum well) and then, strong coupling regime is unreachable.

Do we need a "one to one coupling": dimensionality issues? "One to one coupling" rule states that an exciton state defined by its momentum $\vec{k}$ will be coupled to only one photon mode with the same momentum. It is a sufficient condition to reach the strong coupling regime. This is the case, for example, in a bulk crystal, where the exciton and the photon are both three dimensional. However, it is possible to observe strong coupling regime even if this condition is not met, as explained in appendix C_{III} of reference [42]. In this case, the coupling between single state (ie. like a photon mode $(E, \vec{k_1})$) and a continuum of states is studied. It is shown that

the parameter of interest is the spectral linewidth of the continuum to be compared to the Rabi splitting. The density of states in the continuum coupled to the single state $\Delta(E)$ reads [42]:

$$\Delta(E) = \rho(E)|H_I(E)|^2$$

where $\rho(E)$ is the density of states of the continuum coupled to the single state and $|H_I(E)|$ is the matrix element of interaction between them. $\rho(E)$ is increasing with increasing energy (in the three-dimension case) while $|H(E)|$ is generally decreasing. In the three dimension case, the density of states $\Delta(E)$ coupled to the single state is a "bell curve" with a linewidth Γ_0. As discussed in appendix C_{III} of reference [42], if Γ_0 is much smaller than the coupling strength of the system (ie. the Rabi splitting in the case of exciton-polariton), then, the system is in a strong coupling regime limit.

This argument is valid, for example, for bulk planar microcavities. In this case, the exciton is free to move in the three dimensions of space whereas the photon propagation is limited to two dimensions. Therefore, a given photon state defined by its two-dimensional momentum $\vec{k}_\gamma$ is coupled to a one-dimensional continuum of exciton states. The matrix element $|H_I(E)|$ is non-zero only in the light cone where the exciton dispersion is almost flat. Therefore, it is possible to overestimate the linewidth of the continuum Γ_0 by the relation:

$$\Gamma_0 < \frac{E_X^2}{2M_X c^2}$$

which leads to $\Gamma_0 \sim 10\mu eV$ for ZnO. This value is 10^4 times smaller than the bulk Rabi splitting and explains why the strong coupling regime is achievable in a bulk planar microcavity whereas the dimensionality of the photon and excitons states are different. As we will see in the following part, this point is as well the reason why strong coupling regime is possible in a structure like ZnO microwires where photonic modes are one dimensional whereas excitons are three dimensional.

Do polaritons require spatial coherence? This criterion has been greatly discussed in reference [43] by L. C. Andreani. Spatial coherence of the exciton was thought to be an important criterion to reach strong coupling regime [44, 45]. It states that the exciton coherence length should be larger than the wavelength of the light. Qualitatively, the coherence length can be computed directly using the coherence time and the group velocity of the exciton. However, a simple criterion is impossible to set mainly because the exciton group velocity $v_g = \frac{dE_x}{dk}$ depends explicitly on the momentum. Nevertheless, using equation 1.13 with $\hbar\gamma \neq 0meV$ and including the spatial dipersion of the exciton, one can show that the two polariton dispersions presented on figure 1.5 start crossing at a critical broadening γ'_c given by [44, 45]:

$$\hbar\gamma'_c = 2\Omega\sqrt{\frac{\epsilon_0\hbar\omega_0}{Mc^2}} \tag{1.16}$$

This critical broadening γ'_c is directly connected to the exciton coherence time corresponding to an exciton coherence length of the order of the wavelength of the photon states involved in the strong coupling regime. Exciton-polariton spatial coherence seems to require $\gamma' < \gamma'_c$. Using the parameter for a bulk crystal of ZnO, we obtain $\hbar\gamma'_c = 8.3meV$. If we compare this value to thermal broadening measured in reference [46, 47], strong coupling should be greatly suppressed in bulk ZnO above 175K. This is incompatible with experimental observations [48, 49, 50, 51, 52] and the criterion 1.16 breaks up.

Actually, the spatial coherence is guaranteed by the extension of the photonic wavefunction over many exciton wavefunctions. In other words, excitons involved in the polariton state are

selected by the photonic wavefunction to preserve spatial coherence and, then, the strong coupling regime holds. This criterion has been greatly discussed by V. Savona in reference [53] from the point of view of the disorder in microcavities. In this case, quantum well excitons can be localized by interface fluctuations leading to a small coherence length (ie. of the order of the Bohr radius). In this review, using theoretical modeling, it is shown that the polariton is not really affected by the exciton disorder thanks to spatial motional narrowing. Moreover, it is shown that polariton localization length (and then its coherence length) is of the order of the micrometer thanks of its photonic component. This fact has been checked, as well, for Frenkel excitons (localized on a molecule scale) for organic planar microcavities [54].

And temporal coherence? From the temporal point of view, both components of a polariton should not experience decoherence during, at least, one Rabi oscillation. As a consequence, the excitonic and photonic linewidths should satisfy:

$$\Gamma_{\gamma/X} < \Omega \tag{1.17}$$

If this condition breaks down, the system is in the so-called weak coupling regime. The Rabi splitting between the polariton states is impossible to resolve at resonance and the concept of strong coupling is not valid anymore.

In a bulk ZnO crystal, the Rabi splitting Ω is equal to $288meV$ which corresponds to a beating period $\frac{2\pi}{\Omega/\hbar} = 14fs$. A photon is not affected by decoherence via interaction with matter and its coherence time is then limited by its lifetime (which is finite in nanostructures due to the photonic losses). However, exciton is interacting with phonons as well as free carriers and other excitons resulting in finite homogenous linewidth. This linewidth temperature dependency [46] as well as direct measurement of decoherence time via four-wave mixing experiments [47] have been realized on bulk crystal of ZnO. It leads, at room temperature, to a homogenous broadening of 20 meV (half-width at half maximum) which corresponds to a coherence time around $60fs$. The criterion 1.17 is satisfied by one order of magnitude even at room temperature in a bulk crystal of ZnO.

However, we will see further in this dissertation that exciton homogenous broadening should be considered in a different way and the criterion 1.17 is not valid anymore. Indeed, in ZnO microwires, linewidth of polaritons cannot be directly inferred from the excitonic linewidth caused by phonon scattering. Normally, polariton linewidth is computed by taking into account the excitonic and photonic linewidth. Actually, we will see that in ZnO microwires, phonon interactions are only a perturbation to the polariton state (and not the exciton state!). Therefore, strong coupling regime preserved if the polaritons are protected from the phonon bath (for example) whereas the exciton is not.

Finally, what is the most relevant criterion to observe strong coupling regime? Finally, one criterion needs to be fulfilled in any case to reach the strong coupling regime. The polariton linewidth has to be small enough to observe an anti-crossing behavior which can be expressed by the following criterion:

$$\Gamma_p < \Omega$$

where Γ_p is the polariton linewidth.

Chapter 2

Polaritons in ZnO microwires

Contents

In the previous chapter, we have seen that bulk polaritons are the proper eigenstates of bulk semiconductor, and a fortiori in ZnO where oscillators strength is so large. The A and B excitons are coupled to the light polarized E$\perp$ c whereas C exciton is coupled to the light polarized E$\parallel$ c with a Rabi splitting of the order of 300 meV. In this thesis, we are interested in ZnO microwires with a diameter of the order of micrometer in order to confine the light in the cross-section. This confinement has important consequences on the photon dispersion and its dimensionality whereas it is not affecting the excitonic properties. The goal of this chapter is to understand how the polaritons properties are modified in these structures compared to bulk material.

Firstly, we will show that the photonic modes in a cylindrical microwire are the so-called whispering gallery modes. Then, we will be able to understand the photonic modes (called hexagonal whispering modes) in a more complex structure: ZnO microwires with a hexagonal cross-section. These modes are coupled to A, B and C excitons resulting in a peculiar strong coupling regime between three dimensional excitons and one dimensional photonic modes that will be discussed.

2.1 Structural description of ZnO microwires

The microwires we have been studied in this thesis are single-crystalline wurtzite ZnO structures with a hexagonal cross-section with a typical length of $50 - 300\mu m$ and a diameter around $1\mu m$ (see figure 2.1). On the c) panel of figure 2.1 is shown an scanning electron microscopy micrograph of a ZnO microwire where three facets of the hexagon are visible. Wurtzite c-axis is found to coincide with the wire main axis. The first generation of microwires were grown by a vapor-phase transport method under atmospheric pressure at 900°C by the team of our collaborator professor Zhanghai Chen [55]. The results of this method is a powder consisting mostly of ZnO tetrapods shown on figure 2.1 a). On each tetrapod, there are four ZnO microwires with a gradient of radius (see figure 2.1 b)). The tetrapods are broken and the wires are dispersed on a substrate in order to isolate single wires (see figure 2.1 c)). Surprisingly, this rather simple growth method provides excellent regularity of the hexagonal shape and very low surface roughness. Moreover, as we will see this thesis, at low temperature, sharp lines are observed with linewidths below meV thanks to the excellent ZnO quality. However, only less than one percent of the wires exhibit strong coupling regime with well-definied polaritons at room temperature because of the random character of this method. Indeed, in this method, neither the average radius of the wire nor its gradient of radius is controlled. The length without any photonic or excitonic disorder along the wires is small: between one to few microns.

The second generation of ZnO microwires (not studied in this thesis) are grown by metalorganic vapour phase epitaxy (MOCVD). These wires exhibit a regular diameter over tens of microns. Almost every MOCVD microwires exhibit well-definied polaritons at room-temperature.

2.2 Whispering gallery modes (WGM) in cylinder

With the hexagonal cross-section of the ZnO microwires, the confinement regime for the light trapped within the microwire is more complicated because of the broken rotational invariance. Before its complete description, it is interesting to understand the photonic modes in a simplified geometry: a microwire with a circular cross-section. We will see how the light is confined in this structure and why these modes are interesting.

2.2.1 Confined modes in the cross-section of the wire

Energy of WGM

In a wire shaped dielectric material, light can remain confined within the cross-section by total internal reflection on the air-dielectric interface. WGM corresponds to photonic modes confined in the circular cross-section and free to propagate along the wire axis. They are fundamentally different from guided modes because they are still confined even if they are not propagating along the wire axis (ie. zero momentum along this axis). For WGM, the confinement relies on the total internal reflections on the circular cross-section. Total internal reflections are circular cross-section wire made of a material with a refractive index n_0 larger than in air. Using Maxwell equations, electric $\vec{E}$ and magnetic $\vec{B}$ field inside the structure satisfy the equation [56]:

$$\left(\nabla^2 + \mu\epsilon\frac{\omega^2}{c^2}\right)\left\{\begin{array}{c}\vec{E}\\ \vec{B}\end{array}\right\} = \vec{0} \tag{2.1}$$

where ω is the energy of the mode, ϵ the dielectric constant, μ the permittivity, c the light speed and ∇ the Nabla operator. In a elongated cylindrical wire, the system can be considered

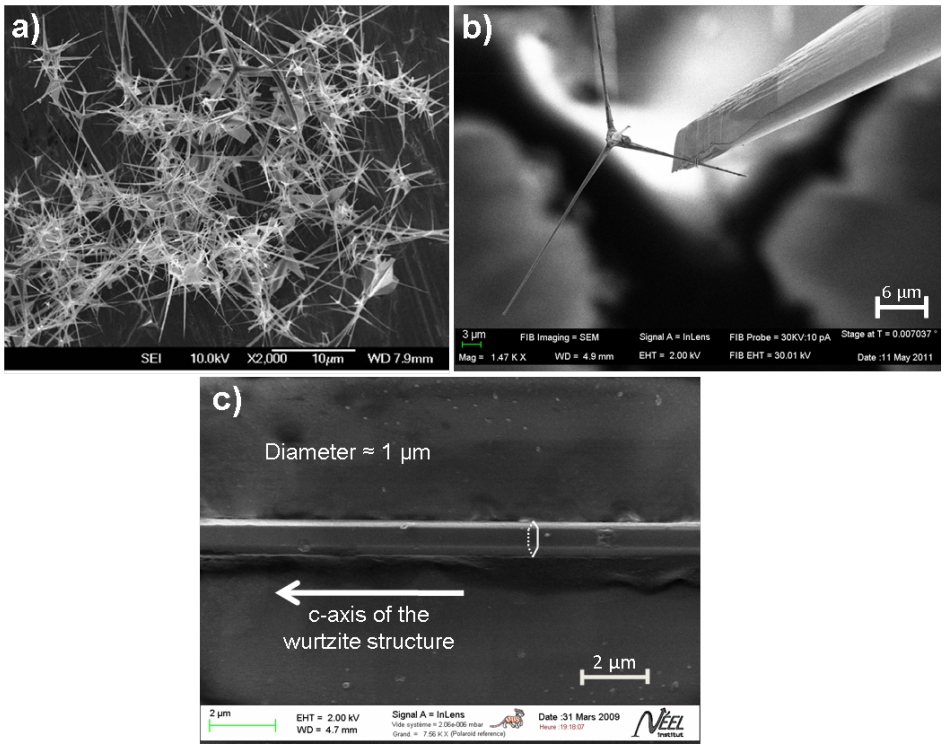

Figure 2.1: Scanning electron microscopy image of : a) powder of ZnO tetrapods b) single tetrapod with four needle-shape microwires c) single microwire lying on a glass substrate. The hexagon cross-section is materialized with the white line on the panel c). Three facets of the hexagon are visible

invariant under a translation along the wire axis (called z-axis here) and any rotation around this axis. Consequently, the solutions of equation 2.1 can be written, for both the electric and magnetic field in the form: $R(r)e^{i(m\phi+k_z z-\omega t)}$ where r, ϕ, z are the cylindrical coordinates, t the time variable, $R(r)$ a radial function, m the azimuthal number of the mode and $k_z$the momentum along the z-axis. The radial function $R(r)$ are given by Bessel's function of the first kind inside the wire and Hankel's functions of the first kind outside the wire.

From the resolution of equation 2.1, two set of modes split in energy are found for $k_z = 0$:

- Transverse Electric (TE) modes: No electric field along z-axis $E_z = 0$
- Transverse Magnetic (TM) modes: No magnetic field along z-axis $B_z = 0$

For $k_z = 0$, energy of each mode E is defined by its azimuthal number m (ie. the number of half-wavelength in one roundtrip in the cross-section), its radial number j and its polarization TE or TM. Assuming a wire radius much larger than the wavelength of light and neglecting decay, a simplified equation of eigenfrequencies is given by [57]:

$$E_{j,m,^{TE/TM}} = \frac{hc}{4n_0\rho}\left(2j + m \pm 1/2\right) \tag{2.2}$$

where ρ is the radius of the wire and the + (-) signs corresponds to the TE (TM) and n_0 is the background refractive index. In this equation, the term $2j$ (m) describes the number of wavelength along the radius (around the cross-section). The term $\pm 1/2$ corresponds to the phase shift accumulated by reflection along the circular cross-section for TE and TM modes. The free spectral range between two modes of successive azimuthal numbers is $\Delta = \frac{hc}{4n\rho}$. In cylindrical ZnO wires, this splitting would be equal to 260 meV (for $\rho = 500nm$ and $n = 2.4$). Note that TE and TM modes are degenerate in this model. Indeed, a TE mode described by the numbers j and m is degenerated with a TM mode described by the numbers j and $m+1$ as well as other TE/TM modes.

Linewidth and Q-factor

WGMs have dragged a lot of interest in microspheres [58, 59] or microdisks [60, 61] because of the long-lived electromagnetic modes existing in these geometries. Indeed, WGMs do not have the drawback of mirrors since the reflectivity for total internal reflection is equal to unity in the limit of the ray model of light. Photonic losses, in these ideal structures, are only limited by diffraction: its wavefunction spills over the cross-section. The Q factor of a confined electromagnetic modes characterizes the storage efficiency of the light: $Q = \frac{\omega_0}{\Delta\omega_0}$. It is related to the number of oscillations of a mode before leaking out of the system. For WGM in microdisks, Q factor up to 12000 has been measured[60, 61]. In microspheres, this value has reached $10^7 - 8.10^8$ [59, 58]. The main advantage of these modes is that they are supported by structures made of bulk material without any heterostructures such as Bragg or metallic mirrors.

In reference [57], theoretical linewidth of a WGM in GaAs cylindrical has been calculated versus the azimuthal mode number m and is displayed in figure 2.2. Linewidth of WGMs decreases almost exponentially for increasing azimuthal quantum number m. Indeed, WGM with high azimuthal number are closer to the ray light model where linewidth tends to zero because of total internal reflection. In other words, by increasing the azimuthal number, the wavelength of light decreases and, therefore, photonic losses due to diffraction decrease.

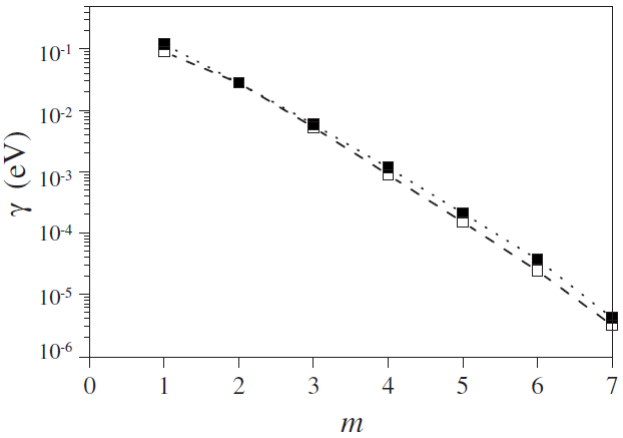

Figure 2.2: Dependence of the radiative decay rate on mode azimuthal number m of the first mode with radial quantum number j=0 at photon energy 1.515 eV (parameters taken for GaAs). Open (solid) symbols correspond to the TM (TE) polarization. Figure taken from [57].

Dispersion of confined photons

In a given WGM defined by the mode numbers (j, m), photons have only one degree of freedom left characterized by its momentum k_z along the free axis: these modes are one-dimensional. Energy of a photon in a dielectric material is given by the relation: $E = \frac{\hbar ck}{n_0}$ (see subsection 1.2.2) with n_0 the refractive index of the medium and k the magnitude of the momentum vector. In a confined system, the magnitude of the momentum k depends only on its component along the free axis and can be written: $k = \sqrt{k_z^2 + k_0^2}$ where k_0 is a constant. The degrees of freedom k_0 are quantized in the other axis. As a consequence, confined photons have a ground state (ie. a non-zero energy state at $k_z = 0$) in the light cone. The exact value of the energy of the ground state E_0 is given by the equation 2.2 and depends on the mode numbers j and m. As shown on figure 2.3 a), photonic dispersion is a hyperbola. In semiconductor optics, we will focus in the light cone region (ie. around $k_z \sim 0$) where the photon dispersion is a parabola (see figure 2.3 b)). In this region, the one-dimensional photon dispersion can be written:

$$E = \frac{\hbar ck}{n} = \sqrt{E_0^2 + \left(\frac{\hbar ck_z}{n_0}\right)^2} \overset{k_z \sim 0}{\approx} E_0 + \frac{(\hbar k_z)^2}{2M^*} \tag{2.3}$$

where the effective reads $M^* c^2 = n_0^2 E_0$. k_z is defined on figure 2.3 c). In the range of energy of interest for ZnO, this effective mass is $M^* \approx 20eV \approx 4.10^{-5} m_e$ where m_e is the electron mass. According to their dispersion relations, confined photons behave like finite mass particles. Their masses is extremely small compared to the exciton mass (ie. $m_X \sim 0.1 m_e$). As a consequence, curvature of the photon dispersion is much more pronounced than the curvature of the exciton dispersion and, generally, exciton dispersion is negligible within the light cone because its spectral shift in this region is generally much smaller than its linewidth.

Polarization versus momentum relation

Even in isotropic material, confinement into WGMs can result in complicated polarization properties which can affect in turns polarization properties in the strong coupling regime. As a consequence, it is interesting to study this relation in an isotropic and, then, in an anisotropic

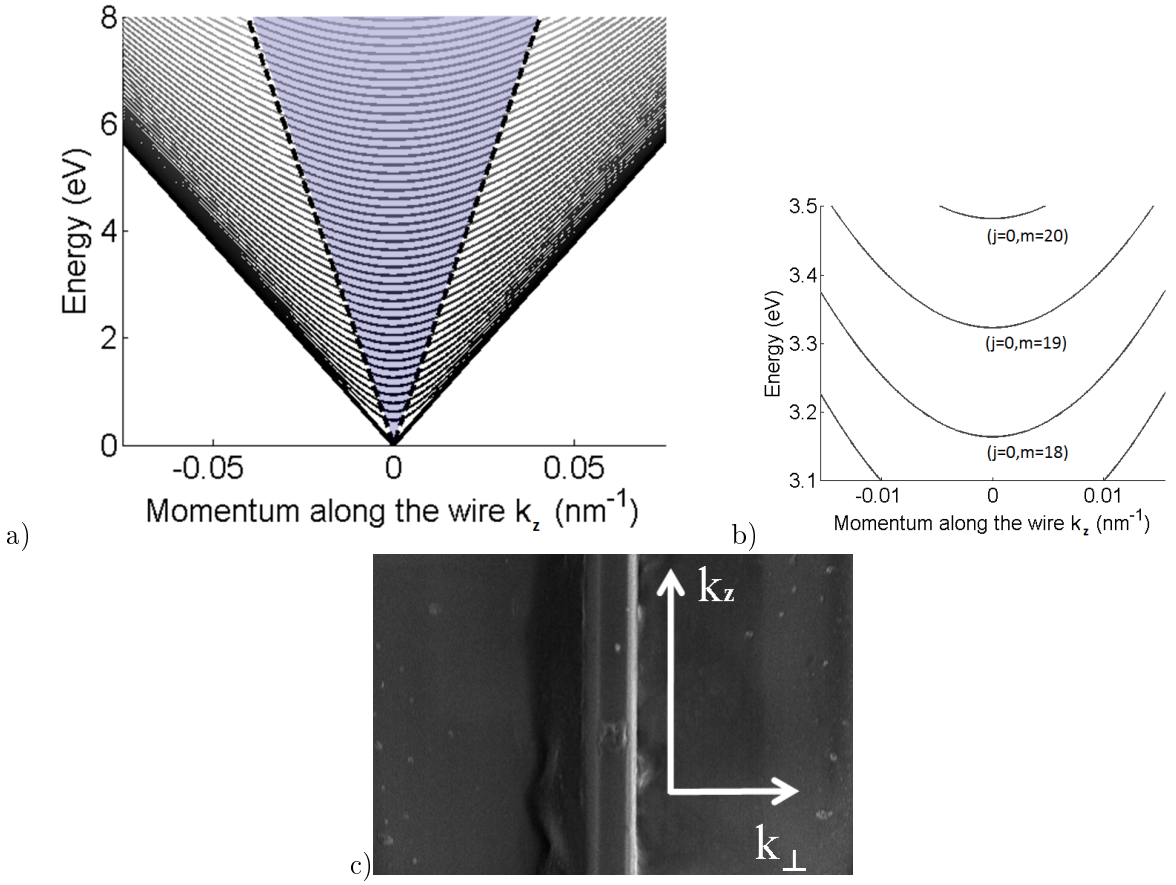

Figure 2.3: a) Dispersion of free photon in the vacuum (dashed lines and semi-transparent blue), of the free photon in ZnO (solid lines) and confined photons in ZnO microwires for j=0 and m=1 to 48 (grey scale color solid line) using ZnO microwires characteristics $\lambda \sim 375nm$, $n \sim 2.6$ and $R \sim 500nm$. Free photon dispersion in solid line (semi-transparent blue) are shown assuming zero (non-zero) momentum along the other directions of space. b) Zoom in the region of interest for ZnO (around 3.3 eV) in the light cone. Dispersions of confined photons are hyperbolas. c) Definition of the momentum parallel k_z and perpendicular $k_\perp$ to the wire

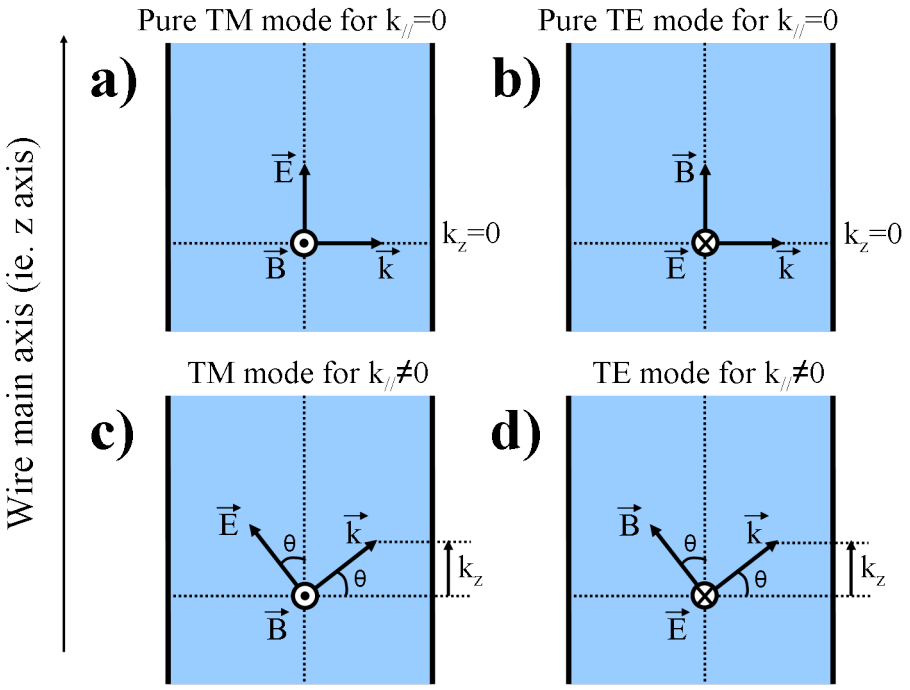

Figure 2.4: Electric and magnetic fields orientation with respect to the wire for pure TE/TM modes at $k_z = 0$ (figure a) and b)) and for mixed modes for $k_z \neq 0$ (figure c) and d)).

cylindrical microwire to understand its effect on the strong coupling regime between WGMs and excitons.

Isotropic structure In an isotropic cylinder, from the point of view of the refraction index, there is no birefringence. Refractive indexes along the wire and perpendicularly to the wire are exactly the same. The dielectric function ϵ is a scalar quantity independent of the polarization direction. In an isotropic cylinder, Maxwell equations read:

$$\vec{\nabla}.\vec{D} = \epsilon\vec{\nabla}.\vec{E} = \epsilon\left(\vec{k}.\vec{E}\right) = 0 \tag{2.4}$$

$$\vec{\nabla}.\vec{B} = \vec{k}.\vec{B} = 0$$

As a consequence, $\vec{k}$, $\vec{E}$ and $\vec{B}$ are respectively orthogonal. Figure 2.4 shows the different orientations of the electric and magnetic field inside the material for $k_z = 0$ and $k_z \neq 0$. Following the definition given in 2.2.1, pure TM modes exist only for $k_z = 0$. For $k_z \neq 0$, a component of the electric field appears perpendicularly to the wire. There is a mixture of polarization for $k_z \neq 0$.

To have a better insight on these polarization properties versus the momentum along the wire axis k_z, we can derive a rule of thumb. The degree of polarization ρ of a photonic mode as a function of k_z is defined as:

$$\rho = \frac{I_{TM} - I_{TE}}{I_{TM} + I_{TE}}$$

where I_{TM} (respectively I_{TE}) is the intensity of the electric field parallel (respectively perpendicularly) to the wire. This physical quantity can be directly measured using polarization

sensitive optical components. Notice that these components are in general sensitive only to the electric field component of the electromagnetic field. Assuming a wire diameter much larger than the wavelength of light, it is possible to infer the relation between the degree of polarization with respect to the angle θ between the total momentum $\vec{k}$ and the cross-section plane of the wire (see figure 2.4). The degree of polarization of a TM mode is expected to switch from 1 to -1 for increasing k_z whereas it has a constant value -1 for TE modes. For TM modes, it can directly be expressed, inside the material, using the angle θ, by:

$$\rho_{TM/in} = cos(2\theta)$$

Thus, WGMs purely TM at $k_z = 0$ acquire some TE components at $k_z \neq 0$. In ZnO microwires, it means that, in the strong coupling regime, pure TM WGMs at $k_z = 0$ will be coupled to both A, B and C excitons at larger momentum k_z. The simple figure 2.4 gives a rather good physical interpretation to the polarization behavior. However, for a wire diameter of the order of the wavelength of light, a complete understanding requires a wave model based on the resolution of the Maxwell equations in the geometry of the wire. In this case, the scheme given in figure 2.4 turns wrong. Such a wave model will be presented in the subsection 2.3.

Anisotropic structure The anisotropy of ZnO makes the pictures even more complicated because of the birefrengence between the c-axis and the a-b plane. The mismatch between the two refractive indexes, of the order of few percents in ZnO, has to be taken into account to reproduce the polarization dependency with the momentum along the wire. Indeed, in an anisotropic structure such as ZnO, equation 2.4 becomes:

$$\vec{\nabla}\vec{E} = \vec{k}.\vec{E} = k_{\|}E_{\|}\left(1 - \frac{\epsilon_r}{\epsilon_z}\right) \neq 0$$

where $k_{\|}$ (respectively $E_{\|}$) are the projections of the momentum $\vec{k}$ (respectively $\vec{E}$) along the z-axis. This equation is zero (ie. $\vec{k}$ and $\vec{E}$ are perpendicular) only in the isotropic case or at $k_{\|} = 0$. Therefore, a stronger polarization mixing is expected at $k_z = 0$ as compared to the isotropic case.

In this case, electric and magnetic fields can be written as a linear combination of the cylindrical harmonics (see reference [62]):

$$\Psi_{m'}^{anis\ cyl}(r, \phi, z, t) = \sum_m A_m \Psi_m^{cyl}(r, \phi, z, t)$$

where A_m is a weighting term obtained by introducing the boundary conditions, $\Psi_m^{cyl}(r, \phi, z, t) = R(r)e^{i(m\phi + k_z z - \omega t)}$ where $R(r)$ is a radial function given by Bessel's function of the first kind inside the wire and Hankel's functions of the first kind outside the wire and m' the azimuthal number of the WGM in the anisotropic case.

2.3 Hexagonal whispering gallery modes in microwires

In the previous section, ZnO cylindrical microwires has been studied to get a simple a physical interpretation of the photonic modes in these structures. Our microwires have a hexagonal cross-section. Therefore, we will now focus on the differences provided by this unusual geometry. These differences comes from the photonic modes supported by a hexagon cross-section: the so-called hexagonal whispering gallery modes (HWGMs). Firstly, we will describe them with a simple

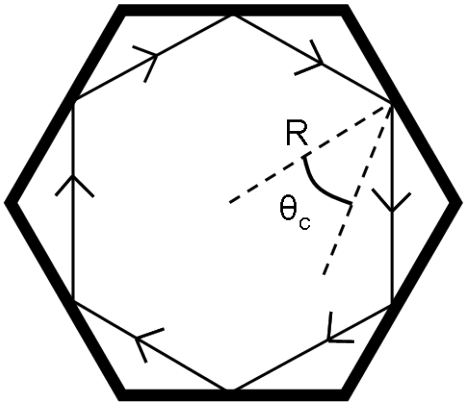

Figure 2.5: Ray light representation of HWGM. R corresponds to the minimal radius of the hexagon

ray-light model which is relevant for large diameter compared to the wavelength of light. Then, we will move on a wave model based on Maxwell equations. Finally, we will discuss the strong coupling regime in this structure.

2.3.1 Hexagonal whispering gallery modes (HWGMs)

Ray light model

Hexagonal whispering gallery modes (HWGM) are the eigenstates of the electromagnetic field in a hexagonal microwires. They are the analogs of whispering gallery modes in a resonator with circular cross-section but without full rotational invariance around the cross-section. Using Snell-Descartes law, the difference of refractive between the air and the material leads to a critical angle value given by: $\theta_c = arcsin(n_{material})$ assuming air outside (see figure 2.5). In the case of ZnO, $n_{material} = 2.6$ this critical angle is $\theta_c = 23°$. As shown on figure 2.5, it is then possible to find closed ray-lights in this cross-section involving total internal reflection. In the ray-light model, these modes cannot leaks out of the hexagon.

Using figure 2.5 and Fresnel relations, one can compute the quantization of the wavelength for this simple ray light HWGM model. Indeed, in one round, the length of the path $6R$, should be equal to an integer number of wavelength in the material plus a term of phase shift added for the reflection at the interface. This leads to:

$$6R = \frac{\lambda}{n_0}\left(m + \frac{6}{\pi} arctan(\beta_{TE/TM}\sqrt{3n^2 - 4})\right) \tag{2.5}$$

with n_0 the background refractive index of the material, m the azimuthal quantum number such as $m \geq 1$, R, the minimal radius of the hexagon defined in 2.5 and $\beta_{TM} = n^{-1}$ for TM modes ($E \parallel c$) and $\beta_{TE} = n$ for TE modes ($E \perp c$)[63].

This simple ray model of light describes correctly HWGMs energies for large values of the azimuthal mode number m where the HWGMs wave character vanishes. Using ZnO microwires parameters ($\lambda \sim 375nm$, $n \sim 2.6$ and $R \sim 500nm$), one finds that the mode number m corresponding to an energy approaching that of the band edge of ZnO is around 18 whereas in planar microcavity this number is, generally, situated between one and five. This model is then a good first approach to understand the HWGM spectrum in ZnO microwires.

However, to go one step further and to understand also the linewidth and polarization properties in such structures, a wave-model has been developed in references [64], [65] and [62] specifically for hexagonal cross-section resonators. It is based on Maxwell equations in a hexagonal cross-section including the anisotropy of the refractive index. In this subsections, we will see the main differences with the circular cross-section case.

Wave model

Eigenstates and dispersion As we have seen in the subsection 2.2.1, electric and magnetic fields in a circular cross-section are given by $\Psi_m^{cyl}(r,\phi,z,t) = R(r)e^{i(m\phi+k_z z-\omega t)}$ where $R(r)$ is a radial function given by Bessel's function of the first kind inside the wire and Hankel's functions of the first kind outside the wire. In the anisotropic case, we have seen that the electric and magnetic fields can be written as a linear combination of the cylindrical harmonics (see reference [62]).

The following step consists in taking into account the hexagonal shape. Again, electric and magnetic fields are written as a linear combination of the cylindrical harmonics, but in the anisotropic case this time [62]:

$$\Psi_M^{anis\,hex}(r,\phi,z,t) = \sum_{m'} A'_{m'} \Psi_{m'}^{anis\,cyl}(r,\phi,z,t) \tag{2.6}$$

where $A'_{m'}$ is a weighting term obtained by introducing the hexagonal boundary conditions and M the azimuthal number of the HWGM in the anisotropic case. M corresponds to the mode number of the cylindrical mode with the higher contribution. The approximations made in this model are based on Rayleigh hypothesis for expansion of fields in cylindrical waves [66]. This model is valid if the perturbation to the cylinder geometry is small (see reference [62] for more details) which is satisfied for a hexagonal cross-section. However, the sharper the corners, the more harmonics contribute. Therefore, geometries with sharp corners, this condition is not satisfied.

Using boundary equations in hexagonal geometry, our collaborators in the LASMEA laboratory [62] obtained the dispersion of HWGMs (see figure 2.6) using ZnO parameters. Interestingly, they show that HWGMs dispersion and spectral position can be easily reproduced by a WGM model with a slightly different refractive index. Therefore, is is possible to describe HWGMs dispersion with a WGMs based model which is a lot less demanding from the numerical implementation point of view.

Linewidth of HWGM Like WGMs, HWGMs feature losses caused by diffraction. However, the losses are much larger in HWGM due to the six sharp corners. Figure 2.7 presents the calculated near-field intensity pattern for a given HWGM done by Wiersig [64] where an important proportion of the field is situated in the corner region.

Therefore, as shown on figure 2.8, HWGM linewidth is at least two orders of magnitude larger than WGMs. However, HWGMs have a sufficiently small linewidth ($\sim 1-4meV$ on figure 2.8) compared to the ZnO Rabi splitting ($\Omega \sim 300meV$) to be strongly coupled to the excitonic resonance in ZnO.

Polarization dependency The qualitative behavior of the polarization dependency of HWGM with the angle of emission θ is similar to the WGMs case. The quantitative change comes from the mode mixing described by equation 2.6. This effect if presented on figure 2.9 where the polarization degree ρ of HWGMs has been compared to WGMs. TE modes remain still close to

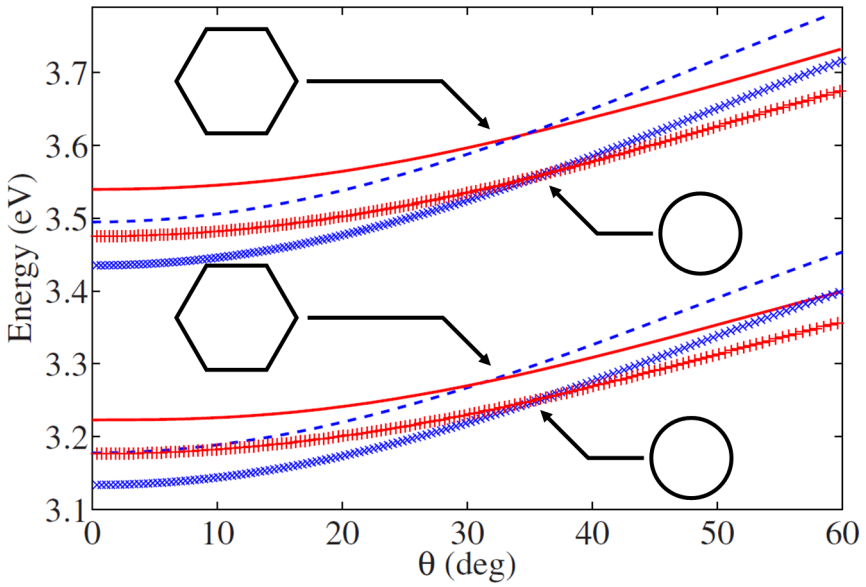

Figure 2.6: Dispersion of TE and TM modes within circular cross-section wires: TE, m=8 (× symbols, blue) and TM, m=9 (+ symbols, red) and for the corresponding hexagonal modes: TE, m=2 (dashed blue line) and TM, m=3 (full red line). The four upper branches are the same modes but replacing m by m+1. The angle θ relates to the photon angle of emission which is directly connected to the momentum along the wire axis. Taken from [62]

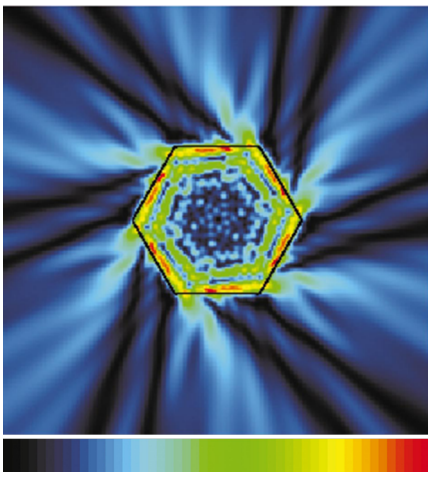

Figure 2.7: Calculated near-field intensity pattern of a HWGM with well-defined chirality which is the analogous to a ray of light circling counter-clockwise within the cross-section. Intensity is higher for redder colors, and vanishes in the dark regions. Taken from [64]

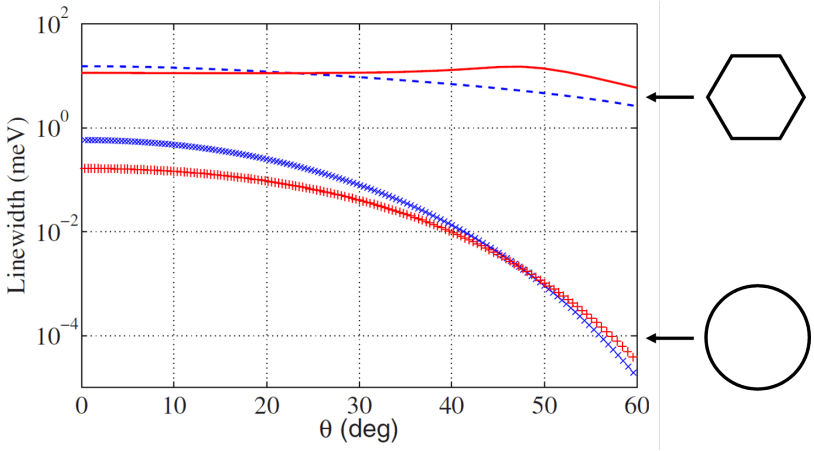

Figure 2.8: Linewidths of the lower energy modes of the figure 2.6 versus the angle of emission θ. Red solid line: TM mode in hexagon cross-section. Blue dashed line: TE mode in hexagon cross-section. Red + symbols: TM in circular cross-section. Blue × symbols: TE in circular cross-section. The index of refraction is n=2.5 and the cross-section area S=0.09 µm². Taken from [62].

-1 over 60°. On the other hand, polarization degree of TM modes is affected by the hexagonal geometry. Indeed, it almost switches to TE modes between 40° and 60°. Therefore, in the strong coupling regime, this "TE" modes will be coupled to the three A, B and C excitons. Measurement of the polarization versus the angle of emission θ in the strong coupling regime will be studied in the part II and compared to this theoretical results.

2.4 General properties of the strong coupling regime in ZnO microwire

Like we discussed in chapter I, in ZnO, A, B and C excitons are in the strong coupling regime with light. The microwire shape does not affect the excitonic properties of ZnO and the dielectric function remains unchanged with respect to the bulk material case. On the other hand, as shown in the previous subsection, photonic density of states is modified. In the dispersion relation $\left(\frac{c\vec{k}}{\omega}\right)^2 = \epsilon_0\epsilon(\omega,\vec{k})$, only the left hand-side term characterizing the photonic component is modified: photonic states are confined into the WGMs. In this subsection, we will discuss the theoretical polariton dispersions resulting from this confinement and the expected properties of such polaritons compared to the bulk case.

2.4.1 Polariton dispersion in ZnO cylindrical microwire

Assuming only one excitonic resonance, polariton dispersion in ZnO cylindrical microwire can be computed by combining the three equations 1.11,1.12 and 1.13 given in the subsection 1.2.2) of chapter 1. In these equations, only the dispersion of the photon state is modified because of the confinement and reads:

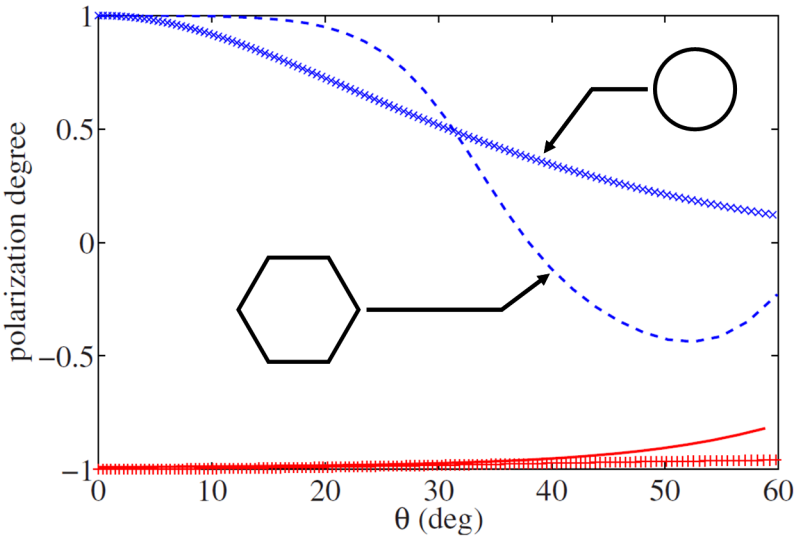

Figure 2.9: Polarization degree of the lower energy modes of the figure 2.6: hexagon modes m=2 (TE, red full line) and m=3 (TM, blue dashed line) and corresponding cylindrical modes. Taken from [62].

- Uncoupled photon dispersion relation:

$$E^{\gamma} = \frac{\hbar c k^{\gamma}}{\sqrt{\epsilon_0}} = \sqrt{(E_0^{\gamma})^2 + \frac{(\hbar c k_z)^2}{\epsilon_0}} \tag{2.7}$$

  where E_{γ} is the energy of the uncoupled photon mode for a given momentum k_z and E_0^{γ} is the energy of the WGM at zero momentum. This equation 2.7 gives the photon dispersion relation (ie. energy E^{γ} versus momentum along the wire axis k_z) without any excitonic contribution to the dielectric function.

Figure 2.10 a) presents the theoretical polariton dispersion for a WGM resonant with the exciton resonance at $k_z = 0$ obtained using these three equations 2.7,1.12 and 1.13. Close to the excitonic resonance, assuming $\hbar\gamma' = 0meV$, the dielectric function 1.12 is divergent and so does the refractive index. Consequently, for large momentum k_z, the momentum dependent term in the polariton dispersion equation 1.13 vanishes and the polariton dispersion tends to the exciton energy. This is a typical feature of the strong coupling regime resulting in the anti-crossing between the lower and upper polariton branches. This anti-crossing behavior, resulting in an inflexion point, is clearly seen on figure 2.10 a).

As shown in the polariton dispersion equation 1.13, the polariton energy E_p at $k_z = 0$ scales like $1/\sqrt{\epsilon}$. Therefore, the polariton free interval spectral range depends on the dielectric function in the strong coupling regime and is decreasing for polaritons getting closer to the exciton energy as it is observed in figure 2.10 b).

Another characteristic feature of the strong coupling regime is the modification of the curvature of the polariton dispersion around $k_z \sim 0$ observed in the figure 2.10 b). Indeed, as the dielectric function diverges close to the excitonic resonance, the curvature of the polariton (ie. its dependency on the momentum along the free axis) close to $k_z \sim 0$ is decreased. Therefore, by measuring the curvature in momentum space of a given polariton modes versus its spectral position with respect to the exciton resonance, one can compute the dielectric function of the system (see chapter 5). This is a direct measurement of the Rabi splitting in microwires.

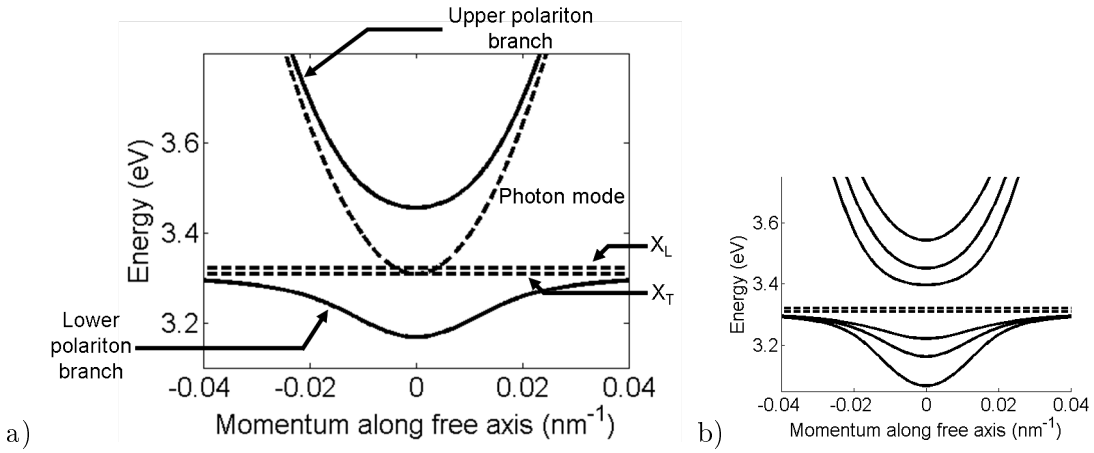

Figure 2.10: a) Dispersion of lower and upper polariton branches (solid lines) resulting from the coupling of the B exciton (flat dashed line) with a photonic mode (dispersed dashed line) calculated using linear response theory. $X_L(X_T)$ stands for longitudinale (respectively transverse) exciton. b) Dispersion of three lower and upper polariton branches involving different photonic mode energy (ie. 3.15 eV, 3.3 eV and 3.45 eV). In both case, ZnO microwires parameters at room temperature have been used.

2.4.2 Strong coupling regime, Rabi splitting

Depending on the WGMs linewidths, the strong coupling regime can be preserved in these kind of microwires [57]. Indeed, modes with a large azimuthal quantum number have a small linewidth. For example, on figure 2.2, mode with $m = 4$ have a linewidth of the order of meV. From the excitonic point of view, these kind of structures are made of bulk material without any heterostructure. Therefore, excitonic linewidth is not limited by disorder. For a ZnO crystal, at low temperature, excitonic linewidth is of the order of the meV. Finally, in a ZnO-based structure ($\Omega = 300meV$), it is possible to easily fulfill the criterion $\Gamma_{\gamma/X} < \Omega$ which is sufficient to reach the strong coupling regime. Notice that the Rabi splitting taken into account is the bulk Rabi splitting $\Omega = 300meV$ because of the strong confinement providing a close to unity exciton-photon overlap. In this case, as the free interval spectral range for WGM is around 240 meV, many WGM will be coupled to the excitons resulting in a set of polaritons and not only one polariton state. Finally, as the Rabi splitting greatly exceeds thermal energy at room temperature (˜26 meV), strong coupling regime would be preserved at this temperature.

2.4.3 Why 1D photonic modes and 3D excitons would be in the strong coupling regime? What is the dimensionality of such a polariton?

As we have seen in the chapter I, it is possible to reach the strong coupling regime between a single state and a continuum of state if the spectral linewidth of the continuum is smaller than the Rabi splitting. In the case of ZnO microwires, HWMGs have one degree of freedom while excitons have three degrees of freedom. Figure 2.11 represents the momentum space in such a structure. A given state of the electromagnetic field in a HWGM is fully determined by its energy $E_{j,m}$ and its momentum along the wire axis k_z^0, ie. two scalars. On the other hand, for a momentum k_z^0, there is a continuum of excitonic modes coupled to this HWGM state with energies given by the relation: $E_X = E_X^0 + \frac{\hbar^2}{2M_X}(k_x^2 + k_y^2 + (k_z^0)^2)$ where x and y axis corresponds to the cartesian axis in the cross-section of the wire. An excitonic state is determined by four

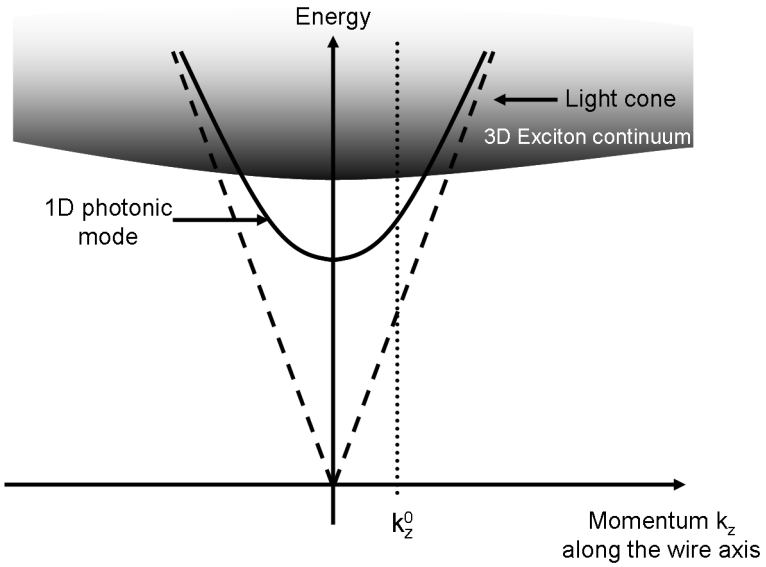

Figure 2.11: Schematic representation of an uncoupled 1D photonic mode and the 3D excitonic continuum in the momentum space.

numbers (its energy and a three-dimensional wavevector) among which only the component k_z^0 of its wavevector must match the one of the photon state. Therefore, a photonic mode defined by (E, k_z^0) is coupled to a 2D excitonic continuum.

We should now consider the extension of the photonic mode in the x-y momentum space to know to which excitons it is coupled to. By definition, the extension of the photonic mode in the x-y momentum space (which is simply the Fourier transform of the wavefunction in the wire cross-section) never exceeds the light cone. Therefore, a photonic mode (E, k_z^0) is only coupled to excitons within the light cone. Since the mass of an exciton is 10^4 times larger than the effective mass of the photonic mode, we can neglect exciton dispersion in the momentum space in the light cone and, finally, a 1D photonic mode is only coupled to 3D excitons continuum which has a linewidth much smaller than its homogeonous linewidth. Therefore, in spite of this not "one to one" coupling situation, strong coupling regime is possible in this structure.

Using this reasoning, we can understand the dimensionality of the polaritons resulting from the strong coupling regime in this structure. The photonic mode is only coupled to excitons with a momentum in the cross-section matching the momentum allowed by the photonic wavefunction in this plane. Therefore, in real and momentum space, the photonic mode and the coupled excitons have exactly the same wavefunction. Finally, the resulting polariton has the same wavefunction which is one dimensional: its degree of freedom in the cross-section of the wire is quantized.

2.4.4 Density of states of the polariton modes

In the previous subsection, we have seen that the 1D polariton modes result from the strong coupling regime between 1D photonic modes and 3D exciton states. It is now interesting to wonder what is the density of states of such polariton modes. Indeed, we expect to observe a 1D-like density of states close to $k_z = 0$ for a given polariton mode while we expect to recover the 3D-like density of states of the excitons above the exciton energy. Firstly we will discuss the density of states associated to a single polariton mode and then, to the whole set of polariton modes in a microwire. For a sake of simplicity, we choose here to study a cylindrical wire with

a large radius such as we can consider the raylight model instead of the wave model. We will see afterward that these hypothesis simplify the calculations without modifying the underlying physics.

The cylindrical geometry imposes the cylindrical coordinates in the momentum space, ie. (k_r, $k_\perp$ and k_z). Since we choose to study a cylindrical wire with a large radius, the wavevector in the cross-section of a given mode is fully determined by the momentum $k_\perp$, ie. with its component along the circle perimeter. The i^{th} mode will have a momentum in the cross-section written $k_\perp^i$. The volumic number of states in an element d^3k for the i^{th} mode reads:

$$g(k)d^3k = \delta(k_\perp - k_\perp^i)\frac{2 \times 2\pi k_\perp dk_\perp dk_z}{(2\pi)^3} \tag{2.8}$$

To obtain the density of states from the expression 2.8, we just have to integrate over the momentum which let the energy constant within δE. We obtain:

$$g(E) = \frac{1}{2\pi^2}k_\perp^i \left(\frac{dE_i}{dk_z}\right)^{-1} \tag{2.9}$$

where E_i is the energy of the i^{th} polariton mode. Knowing the energy $E_\gamma^i(k_z = 0)$ of the corresponding uncoupled photonic mode at zero momentum along the wire axis (ie. $k_z = 0$), $k_\perp^i$ is obtained thanks to the formula:

$$k_\perp^i = \frac{\sqrt{\epsilon_0}E_\gamma(k_z = 0)}{\hbar c}$$

It is then possible to compute the density of states for a given polariton mode. The result is given by the black line on figure 2.12. Two 1D-like densities of states are visible below and above the exciton energy. The lowest energy one corresponds to the density of states of the polariton branch close to the ground state of the polariton mode (ie. $k_z = 0$) while the higher energy one corresponds to the region out of the light cone, ie. where the lower polariton is almost completely excitonic. Notice that the higher energy density of states is non-physical, ie. it would correspond to the density of states of a one-dimensional pure exciton. However, in order to reconstruct the smooth transition between the 1D-like density of states below the exciton energy and the 3D-like density of states above, we have to take into account this "1D-like" density of states for the exciton. Therefore, we are going to sum the equation 2.9 over all the possible momentum in the cross-section $k_\perp^i$ for the upper and lower polariton branches. The contribution of the upper polariton to this sum is negligible since its density of states (directly linked to its dispersion) is orders of magnitude below the lower polariton one. The sum over all the polariton modes reads:

$$g(E) = \frac{1}{2\pi^2}\sum_{i=1}^{i=\infty} k_\perp^i \left(\frac{dE_i}{dk_z}\right)^{-1} \tag{2.10}$$

The result of this summation is given by the blue line on figure 2.12. For a sake of claricity, the result has been convoluted with a lorentzian with a linewidth of 0.1 meV and presented in a logscale. Interestingly, we recover the 1D-like density of states well below the exciton energy while we regain a 3D-like density of states above. In between, a smooth transition is observed. The fact that, at some point, the density of states is stepped, ie. it is 2D-like (see inset of figure 2.12), raises the question of the true dimensionality of these polaritons. The answer is that the polaritons are one-dimensional only if the momentum within the cross-section $k_\perp^i$ is frozen during the polariton lifetime. For example, there should be no decay channels between polariton modes like the emission of a LO-phonon and the thermal fluctuations should not exceed the

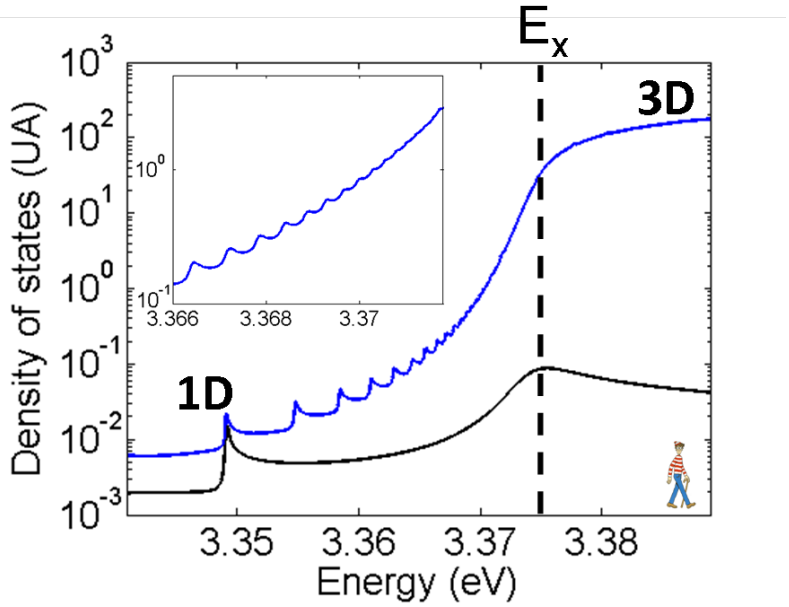

Figure 2.12: Black line: Logscale calculated density of states using the equation 2.9 for a single lower polariton mode with i = 17. Blue line: Logscale calculated complete density of states using the equation 2.10 for i ranging from 1 to 1000. Inset: same figure zoomed in the region from 3.366 eV to 3.372 eV where the density of states is 2d-like (ie. displaying steps).

spectral separation between two consecutive modes. In the case of the microwires, it is possible to find two consecutive modes with a spectral separation above the thermal energy even at room temperature, ie. 26 meV. However, it is not clear yet if there is a non-negligible channel between two polariton modes such as the emission or the absorption of the LO phonon. In any case, from the photoluminescence experiments presented in this thesis, we observe that the luminescence does not exceed few modes, around 5 to 6. Therefore, if these modes can exchange polaritons, this exchange does not exceed 5 to 6 modes and the momentum $k_{\perp}^{i}$ can take only 5 to 6 discrete values. This situation is not purely one dimensional, however, it remains extremely interesting since the wire axis degree of freedom is free while the two other are almost frozen.

2.4.5 Two set of cross-polarized polaritons

In ZnO, A and B excitons are coupled to light with a polarization $E \perp c$ whereas C exciton is coupled to cross-polarized light $E \parallel c$. For $k_z = 0$, WGMs can be separated into two families of cross-polarized modes: pure TE (ie. $E \perp c$) and pure TM ($E \parallel c$). As a consequence, for $k_z = 0$, two set of cross-polarized polaritons should result from the strong coupling regime. At larger momentum k_z, polarization dependency is more striking for two reasons: TM WGM have a mixed polarization and the strong coupling regime is mixing as well the polarization. This behaviour will be discribed theoretically and experimentally for ZnO hexagonal microwires in part II.

2.4.6 Exciton-photon overlap and strong coupling regime

In a hexagonal cross-section microwire, the strong coupling regime is close to the case of the ZnO cylindrical microwires (see 2.4). The main difference is the confinement of the photonic

mode. Indeed, for HWGMs, a non-negligible part of the electromagnetic field is situated outside the wire. Therefore, the exciton-photon overlap is decreased and, as a consequence, the Rabi splitting. This effect can be easily taken into account to compute the Rabi splitting for ZnO microwires using the formula [42]:

$$\Omega_{\mu wire}^{ZnO} = \sqrt{\alpha}\Omega_{bulk}^{ZnO}$$

where $\Omega_{\mu\text{wire}}^{ZnO}$ (Ω_{bulk}^{ZnO}) is the Rabi splitting in a ZnO microwire (bulk crystal) and α the exciton-photon overlap integral given by:

$$\alpha = \| \iiint_{x,y,z} \psi_X^*(x,y,z)\psi_\gamma(x,y,z)dxdydz \|^2$$

where $\psi_X(x,y,z)$ ($\psi_\gamma(x,y,z)$) is exciton (photon) wavefunction.

Chapter 3

Towards low dimensional Bose gas in solid state environment: a short review

Contents

Bose-Einstein condensation of polaritons has been experimentally demonstrated at 20K in 2006 [19] in a microcavity. This quasiparticle is a mixed state between two bosons (ie. with interger spin) and, therefore, is a boson as well. It has opened the way for the study of degenerate Bose gas in solid state environment. Solid state environment offers new means to manipulate and study these gases in original geometries with complex interactions with its environment leading to a very rich physics.

Polaritons in ZnO microwires are one dimensional particles stable at room temperature with a high Rabi splitting. As a consequence, these particles are potential candidates for the study of low dimensional Bose gas in solid state environment and could lead to a new class of practical

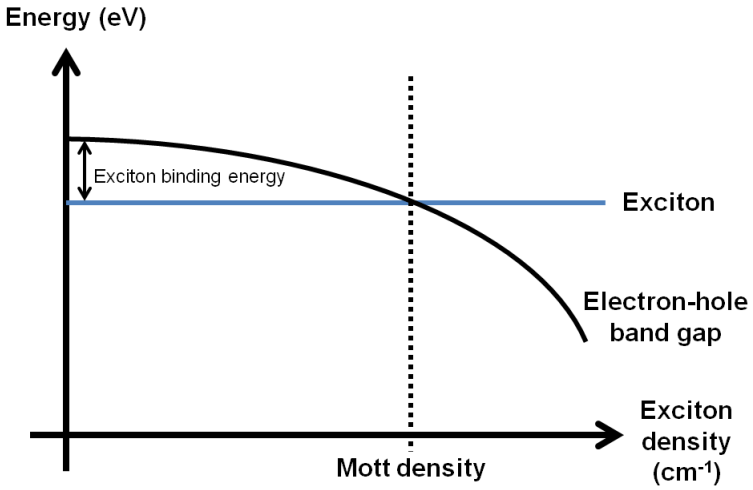

Figure 3.1: Band gap renormalization (black line) and the exciton energy (blue line) as a function of the exciton density.

devices using its macroscopic coherence properties including the low threshold polariton laser at room temperature.

In this chapter, firstly, we will describe the polariton as a candidate for degenerate Bose gas physics and look at the up-to-date Bose gas physics achievements involving this particle. Then, we will report the different works towards the goal of this thesis: 1D polariton gas Physics at high density and temperature. Finally, the motivations to study the ZnO microwires will be presented in relation to up-to-date bibliography.

3.1 Polaritons: a candidate for degenerate Bose gas physics

In this section, we will discuss the fact that a polariton is a promising candidate to study degenerate Bose gas physics. First of all, we will see that it is stable even in the quantum degenerate limit if the strong coupling does not break down. Then, we will show that it can undergo the bosonic stimulation which is characteristic of this regime. Finally, we will discuss the specificities of polaritons to study degenerate Bose gas physics compared to other bosons.

3.1.1 Polariton: a stable boson?

An exciton-polariton is a composite boson. Once strong coupling regime is reached, its stability relies on the exciton binding energy. As explained in the appendix A of reference [46], in a bulk crystal, band gap energy decreases with increasing exciton density because of exchange and correlation effects. On the other side, the exciton binding energy decreases with increasing exciton density because of ionization via exciton-exciton interaction. Finally, these two effects compensate exactly in a bulk crystal. The exciton energy is stable whereas its oscillator strength decreases with increasing exciton density as shown on figure 3.1. The Mott density is defined on this figure as the crossing point of the band gap and exciton energy. Above this density, the stable state, ie. with the lowest energy, is an electron hole plasma: exciton is unstable because it is instantly ionized.

The critical density characterizing this regime can be estimated, in a bulk crystal, thanks to the relation: $n_M \sim \frac{K}{a_{B^3}}$ where a_B is the Bohr radius and K is a model-dependent parameter,

greatly discussed in appendix A of reference [46]. In a naïve model where $K = 1$, the Mott density corresponds to one exciton in a volume delimited by the Bohr radius. However, this model is overestimating this critical density. A complete and experimentally checked model taking into account the electrostatic screening and the energy distribution of the excitons gives a value $K = 0.002$ [32, 67] which gives a mean interparticle distance of $l_m = \frac{a_B}{\sqrt[3]{K}} \sim 8\ a_B$. For ZnO, it gives $n_M = 3,4 \times 10^{17} cm^{-3}$ which corresponds to an interparticle mean distance of $l_M = 14nm$. Let us now compare this electron hole plase transition with the degenerate Bose gas regime.

For a three dimensional thermal gas, quantum degeneracy arises when the De Broglie wavelength $\Delta = \sqrt{\frac{\hbar^2}{2\pi mkT}}$ gets close to the average interparticle distance $l = \frac{1}{\sqrt[3]{n}}$. In the case of a pure exciton in ZnO at 4K, one can compute $\Delta \sim 35nm$ which leads to a critical density of $n_{deg} = 2,3 \times 10^{16} cm^{-3}$. Only one order of magnitude in terms of density separates the quantum degeneracy limit from the EHP transition for a pure gas of exciton. It partially explains the difficulty to undergo quantum degeneracy for pure excitons.

The picture is completely different for a gas of polaritons thanks to its photonic component. Indeed, the effective mass of a polariton is $10^{-4} - 10^{-5}$ times lower than an exciton. Therefore, the De Broglie wavelength associated to a polariton gas at thermal equilibrium is $\Delta \sim 5\mu m$. Quantum degeneracy is then expected well before any decrease of the binding energy of the excitonic component of the polariton. Of course, if the polariton population coexists with an excitonic reservoir, the picture is more complex.

3.1.2 Bosonic stimulation

In this subsection, we are going to briefly discuss the reason why bosons tend to occupy only one state in the quantum degeneracy limit. Firstly, we will discuss a toy model allowing to understand the role of the quantum interferences depending on the symmetry of the particle wavefunctions. Then, we will be able to understand the influence of this macroscopic occupancy on the coherence properties of such a gas.

Symmetric wavefunction for boson

The symmetrization postulate states that the multiparticle wavefunction of bosons is symmetric by any exchange of two particles. For fermions, the multiparticle wavefunction is antisymmetric. Main consequences of this postulate are the Pauli exclusion principle for fermions and the bosonic stimulation for bosons. These principles will be qualitatively explained thanks to a simple calculation.

Two particles are considered here at two positions x_a and x_b associated with two normalized and orthogonal wavefunctions ψ_a and ψ_b. If these two particles are distinguishable, one can write the two particles wavefunction $\psi_a(x_1)\psi_b(x_2)$. The mean square separation between two particles is given by:

$$< (x_b - x_a)^2 >_d = < x >_a^2 + < x >_b^2 - 2 < x >_a < x >_b$$

where $< x >_i = \int x|\psi_i(x)|^2 dx$. For two indistinguishable bosons, the wavefunction reads $\Psi_{boson}(x_1, x_2) = \frac{1}{\sqrt{2}} (\psi_a(x_1)\psi_b(x_2) + \psi_a(x_2)\psi_b(x_1))$ which is symmetric by the exchange $x_1 \leftrightarrow x_2$. On the other hand, for fermions, it is $\Psi_{fermion}(x_1, x_2) = \frac{1}{\sqrt{2}} (\psi_a(x_1)\psi_b(x_2) - \psi_a(x_2)\psi_b(x_1))$ which is antisymmetric by the exchange $x_1 \leftrightarrow x_2$. Finally, the mean square separation between two particles can be written:

$$< (x_b - x_a)^2 >_{b/f} = < (x_b - x_a)^2 >_d \mp 2| < x >_{ab} |^2$$

where $< x >_{ab} = \int x \psi_b^*(x) \psi_a(x) dx$. In the two particles case, this calculation shows that bosons tend to get closer than fermions in real space. More generally, two fermions cannot be in the same quantum state defined by its position (or its momentum), its energy and its spin whereas bosons tend to occupy one state in the quantum degeneracy regime. As shown in this calculation, this property is a consequence of quantum interferences between the particles wavefunctions. There is no interaction involved in this problem.

Bosonic stimulation

In a gas of bosons, the probability to decay from an initial state toward a final state is proportional to $N+1$ where N is the number of particles in the final quantum state. When $N \sim 1$ is reached, bosonic stimulation arises. At a certain point, a macroscopic occupation of this quantum state will be attained. This is a direct consequence of the constructive quantum interference for bosons. This behavior, true for photons in a laser as well as for polaritons, has the effect to create a non-linear increase of the population in the ground state that can be measured via the light emitted by the particles.

As a matter of comparison, for a gas of fermions, the probability to decay from an initial state to a final state is proportional to $1 - N$ where N is the number of particle in the final state. This terms is canceled when $N \sim 1$ which is a direct consequence of the Pauli exclusion principle.

Macroscopic wavefunction coherence: off-diagonal long-range order [68]

In the bosonic stimulation regime, most of the particles are in one quantum state defined, at least, by its energy and its momentum. As a consequence of the localization of the wavefunction in the momentum space, the bosons will have a coherent wavefunction over a macroscopic scale in real space.

This property is properly explained thanks to the one-body density matrix. It reads:

$$n^{(1)}(s) = < \hat{\Psi}^\dagger(r) \hat{\Psi}(r+s) >$$

and can be understood as the probability to annihilate a boson at $r+s$ and create it at r with the exact same properties. Obviously, in an incoherent system, when $s \to +\infty$, $n^{(1)}(s)$ has to vanish.

However, for a system of indistinguishable bosons, it is possible to see off-diagonal long-range coherence (ie. $n^{(1)}(s \to +\infty) \neq 0$). For a gas of bosons in the stimulated regime, the one-body density matrix in momentum has collapsed (ie. almost one quantum state is occupied) and can be approximated by a Dirac function. The one-body density matrix in real space, obtained simply by Fourier transforming the density matrix in momentum space, is then constant whatever the value of s. In this case, the gas of bosons is coherent over a macroscopic scale.

This macroscopic coherence has dragged an important interest. Indeed, a macroscopic wavefunction over µm allows to completely manipulate quantum mechanics and to bring quantum phenomena at our scale in a solid state environment. As we will see in 3.2, it has already been possible to "play" with this macroscopic wavefunction in original structures.

3.1.3 Originality of polaritons as a degenerate Bose gas

Polariton laser without inversion

We will now discuss the fact that, compared to an usual laser, polariton laser, in the ideal case, does not require population inversion to reach the amplification regime. Left panel of figure 3.2 presents the principle of a laser with two levels 1 and 2. The incident light is resonant with the two levels transition of an active medium. In this case, the absorption is equal to KN_1 whereas the stimulated emission is proportional to KN_2 where K characterized the transition probability and is similar for absorption and stimulated emission. In this simple model, we have neglected the spontaneous emission because it is only a weak contribution compared to the stimulated emission. Light amplification is possible if the stimulated emission exceeds the absorption. It leads to the criterion $N_2 - N_1 > 0$ which corresponds to the population inversion achieved using three or four levels systems.

As shown on the right panel of figure 3.2, the situation is different for a polariton laser. It has been shown in reference [69] that the population inversion condition should not be required for polaritons. Indeed, amplification of the polariton field starts as soon as there is one polariton per lifetime in the polariton state, ie. $N_p \sim 1$, since the polaritons cannot be re-absorbed by the level 2 (see figure 3.2). The polariton state is filled by N_2/τ_r particles per time unit where τ_r is the time constant characterizing the relaxation from the level 2 towards the polariton state. In this case, threshold of the amplification of the polariton field is reached when the polariton filling is of the order of the losses. It corresponds to the relation $N_2/\tau_r = N_p/\tau_p$ where τ_p is the lifetime of the polariton including radiative and non-radiative lifetime. This class of laser would be, indeed, thresholdless if $\tau_r/\tau_p \ll 1$. Therefore, polariton lasers could lead to low threshold lasers (ie. without population inversion) by taking up technological challenges using room temperature suitable materials. However, in realistic structures, it is observed that the threshold is still high because of:

- the difficulty to inject efficiently particle in the level 2 (electrically or optically) without degrading the structure
- the high value of the ratio τ_r/τ_p around 100 which is leads to the population inversion relation $N_2 \sim 100 N_p$. Indeed, the relaxation from the level 2 is generally not efficient
- the additionnal relaxation channels of the the level 2 towards other states

Specificities of a degenerate polariton gas

A polariton is a very unique boson because it is a composite quasiparticle made up of excitons and photons in a solid state environment. First of all, mainly because of its photonic component, it has a short lifetime. For example, in ZnO microwires, radiative lifetime of polaritons is of the order of one picosecond. In order to obtain a fixed average number of polaritons in the system, one needs to permanently inject polaritons to counter the photonic losses. This is possible, for example, by non-resonant optical pumping. In this case, hot carriers are injected at high energy and, then, relax towards the polariton states. Bosonic stimulation is reached, if the average number of particles of a given state attains one (ie. $N_p \sim 1$). By definition, this system is intrinsically out of equilibrium. As the average number of particles is conserved, this system is in a quasi-equilibrium and can reach thermal equilibrium.

The photonic losses have an interesting counterpart. Photons emitted by the polaritons give a direct insight on its properties. It is then possible to obtain directly the first/second order

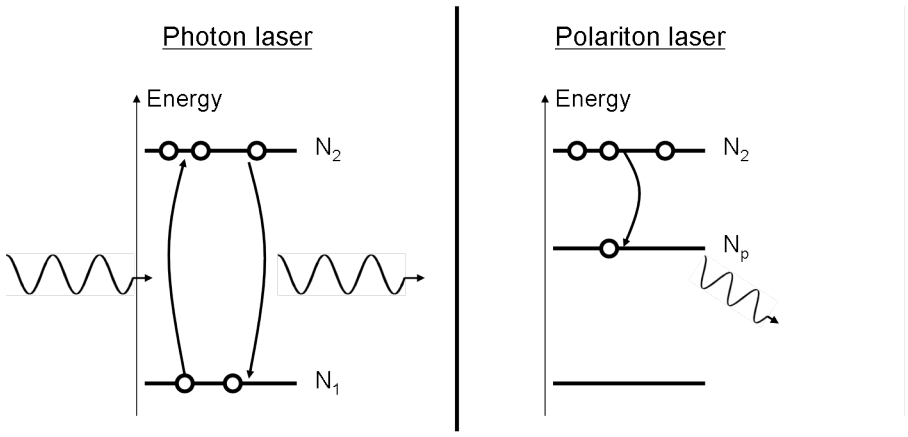

Figure 3.2: Schematic representation of the principle of the photon laser (left panel) and the polariton laser (right panel)

spatial/temporal correlation functions of the system. These quantities are directly connected to the degree of coherence of the system.

Because of its photonic component, polaritons have a low effective mass compared to a pure exciton. In the case of ZnO microwires, for example, polariton mass is $10^4 - 10^5$ smaller than the exciton mass. As a consequence, quantum degeneracy in the thermodynamic limit is possible at elevated temperatures and could lead to room temperature quantum degenerate states if the excitonic component is stable in this regime, which is the case for ZnO excitons.

Contrary to pure photons, a polariton can interact with its environment (phonons, excitons, polaritons, etc...) through its excitonic component inducing complex thermalization process. However, as we will see in chapter 6, original situations can occur in which polariton are isolated from the phonon bath at room temperature.

Finally, a polariton gas is a non-equilibrium bosonic system in a solid state environment connecting laser physics and degenerate Bose gas physics.

3.2 Polaritons: Low dimensional Bose gas physics achievements

As we have seen, polariton is a suitable particle to undergo degenerate Bose gas transition in solid state environment. In this section, we will discuss the up-to-date achievements in low dimensional polariton in the quantum degeneracy limit. We will begin by the basic work on BEC and superfluidity in CdTe 2D planar microcavity. Then, we will describe the works exhibiting interesting properties in structures with original geometries.

3.2.1 BEC/Superfluidity in CdTe microcavities

Even if true BEC is forbidden in dimension lower than three [68], it is still possible to reach quantum degeneracy in a thermal gas. The name of this kind of transition in two dimensions is the Berezinskii-Kosterlitz-Thouless transition which is the analog of BEC in 3D. As this transition presents the same properties than a true Bose-Einstein condensation (ie. macroscopic occupancy of the ground state, increase of the coherence time of the system, thermal equilibrium before threshold and coherence build-up), this phenomenon has been called, by extension, Bose-Einstein condensation of polaritons. Interesting properties of such a gas, like superfluidity or Josephson

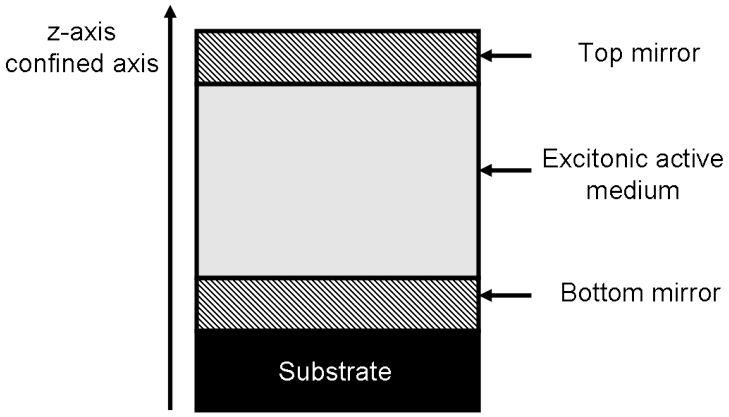

Figure 3.3: Schematic representation of a planar microcavity. Z-axis corresponds to the confined axis.

oscillations, have been demonstrated and will be discussed in this subsection. First of all, we will briefly describe a microcavity as it is the most usual structure in polariton physics.

What is a planar microcavity?

A planar microcavity has been the most widely used structure in the polariton physics. As shown on figure 3.3, it is composed of two mirrors facing each other. Photons are confined along the z-axis defined in figure 3.3 and free to propagate in the plane. An excitonic active medium is placed at the antinode of the confined photon mode. We focus here on the planar microcavities in the strong coupling regime, ie. the excitonic and photonic losses are low enough to have energy exchange between the two fields.

Mainly, two types of mirrors can be found in the literature:

- The first ones are distributed Bragg mirrors which consist of an alternation of dielectric materials with different refractive index. By adjusting the refractive index and the thickness of each layer, the reflected light by these multi-layers is constructively interfering. Exceedingly high reflection above 99.9% can be obtained. However, a large part of the electromagnetic field is located in the mirrors, which are micrometer thick, and does not interact with the excitonic active medium, reducing the light-matter coupling. From the growth point of view, these heterostructures are challenging because it requires to have lattice matching all along the structure.

- The second ones are metallic mirrors. The reflectivity of such a mirror is low in UV (65% at 380 nm for a 10 nm thick layer of Aluminum). However, if the strong coupling regime is reached with such a low reflectivity, a larger part of the electromagnetic field will interact with excitonic active medium compared to distributed Bragg mirrors resulting in a larger light matter coupling. This kind of mirrors can be deposited on any material and does not affect the quality of the excitonic active medium

Two strategies, depending on the material, exist for the active medium:

- For materials with a low exciton binding energy, well below the thermal energy at room temperature (for example, 4.8 meV for GaAs, 10 meV for CdTe), the exciton is not stable enough against high density and temperature. Therefore, in order to artificially increase its

binding energy, excitonic active medium based on these materials are composed of mutiple quantum wells. As described in [70], lowering exciton dimensionality greatly enhances its binding energy. For example, it can be doubled in quantum well system if its thickness corresponds to the exciton Bohr radius. It results in an enhanced oscillator strength, and consequently, a higher Rabi splitting. Moreover, in a microcavity, in order to preserve the strong coupling regime at high polariton density, it is possible to increase the number of quantum wells. Indeed, the polariton density per quantum well at the critical density is decreased if the number of quantum wells is increased [71]. Of course, the complete growth of these structures (Bragg mirrors and quantum wells) is a complex task.

- In large band gap materials, the exciton binding energy is much larger (60 meV for ZnO, 25 meV for GaN) and the exciton is stable even at room temperature. So, for microcavities based on these materials, the active medium consists only in a bulk crystal with a thickness of the order of hundreds of nanometers providing a larger exciton-photon overlap and coupling. Moreover, as the number of hetero-interfaces is reduced in this case, the overall structural disorder in the microcavity is reduced.

As we will see now, these structures have exhibited very interesting features such as Bose-Einstein condensation of polaritons, superfluidity and Joesephson oscillations. A part of the research effort tries to obtain a stable polariton in new material such as ZnO or GaN at room temperature in order to produce the so-called polariton laser.

Bose-Einstein condensation in CdTe planar microcavity[19]

Bose-Einstein condensation (BEC) is a thermodynamic phase transition towards a quantum degenerate Bose gas. Indeed, in this case thermal equilibrium is reached. Degenerate Bose gas regime can be obtained via increasing the number of particles or decreasing the temperature of the system in order to increase the de Broglie wavelength.

Strong evidences for BEC of polaritons have been reported at 20K in 2006 in CdTe planar microcavity [19]. Here are the proofs brought by the authors:

- Macroscopic occupancy of the ground state of the lower polariton branch
- Linewidth narrowing: indication for an increase of the coherence time in the system
- Negligible blueshift (less than 7% of the Rabi Splitting)
- Thermal equilibrium with an effective temperature of the polariton gas of 20K
- Linear polarization build-up at threshold without any correlation with the laser polarization
- The most unambiguous proof: Long-range spatial correlations over 10µm above threshold. Below threshold, spatial correlation are given by the thermal De Broglie wavelength of the polaritons (˜2-3 µm) (see figure 3.4)

This work has opened the field of polariton quantum degeneracy physics. However, CdTe microcavities suffered from photonic disorder which was localizing the condensate in fluctuating potential. A good control of the condensate wavefunction was not possible. Moreover, CdTe semicondcutor, because of the low binding energy of the free exciton ($\sim 10meV$), is not suitable for room temperature experiments.

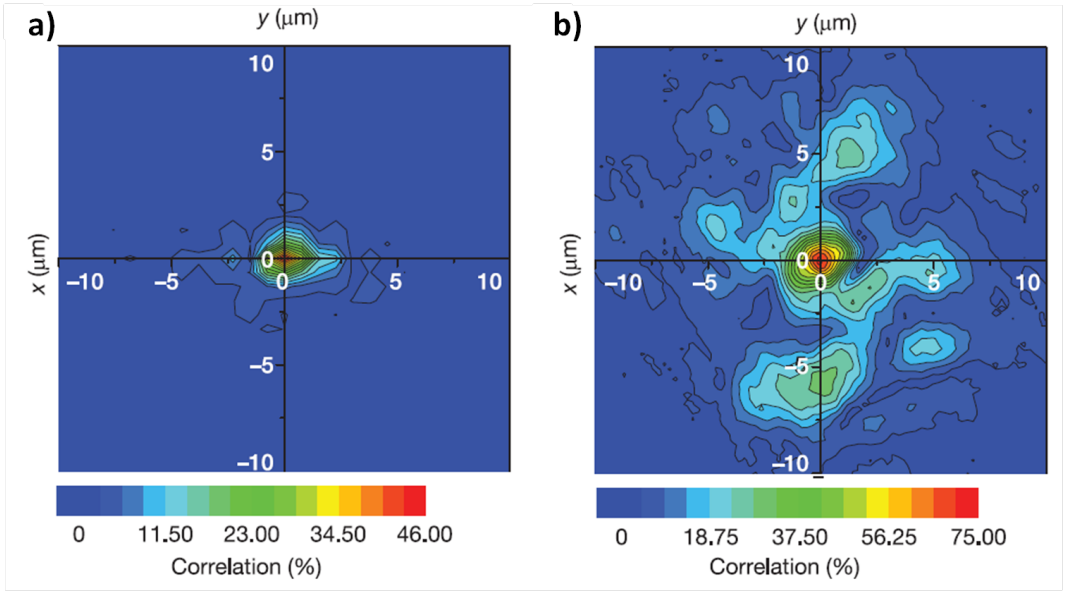

Figure 3.4: a) Correlation mapping below threshold using a linear colour scale. Each point (x, y) in the map represents the correlation between points (x, y) and (-x, -y) of the condensate. The correlation peak extends over 2.6 µm, thus providing a measurement of the de Broglie wavelength. b) Same as a) but for excitation above threshold. Some islands with a high degree of correlation (up to 30%) are formed for distances as long as 4.5 times the thermal de Broglie wavelength. These islands correspond to the bright spots caused by the in-plane spatial disorder experienced by the condensate. Figure taken from [19].

3.2.2 Superfluidity [1, 2, 3, 4, 5, 6]

As polaritons are interacting particles, BEC of microcavity polaritons exhibits superfluidity. Many superfluidity criteria have been checked:

- Landau criterion: frictionless flow below critical velocity of condensed polaritons through defects under resonant pumping[2, 1]
- Quantized vortices [3, 4, 72, 73]: A quantized vortex has a zero density of polaritons in its center and macroscopic phase shift of $n2\pi$ around its center. It is the analog of a vortex in classical hydrodynamics. In disorded system, vortices are pinned on defects. Notice that half-vortices have been studied in a polariton fluid as well (ie. phase shift of $n\pi$ in only one polarization) thanks to the spinor character of the polariton field (ie. the two polariton degenerate spin states).
- Persistent superflow [5]
- Bogoliubov dispersion using a four-wave mixing experiment [6]

3.2.3 Josephson oscillations with two coupled 0D polariton degenerate gas [7]

Josephson oscillations have been demonstrated in two polariton systems: two GaAs coupled micropillars (not published yet) and two condensates trapped in disorder traps in CdTe microcavities[7]. In both paper, two polariton traps are weakly coupled. Above condensation threshold, exchange of population and phase is observed in time-resolved experiments. This phenomenom is achievable thanks to the macroscopic wavefunction arising above condensation threshold.

3.3 Towards polaritons 1D Bose gas physics at room temperature

In this section, we will discuss the up-to-date experimental realization connected with the scope of this thesis, ie. the study of 1D polaritons at room temperature, in order to situate the ZnO microwires in this problematic. First, we will treat the planar microcavities based on large band gap semiconductor such as ZnO and GaN, designed to exhibit polariton lasing at room temperature. Then, 1D GaAs cavity wires will be described. These structures, which are the closest to the ZnO microwires, exhibit one-dimensional polaritons . However, GaAs excitons are not stable at room temperature. Finally, we will discuss ZnO nanowires where the strong coupling is realized at room temperature between the ZnO excitons and guided-modes along the wire leading to zero-dimensional polaritons.

3.3.1 Planar microcavities based on large band gap semiconductor (2D system)

ZnO is well-suited for room temperature operation thanks to its large exciton binding energy of the exciton (~60meV [74]) compared to the thermal energy (~26 meV). Therefore, it has dragged a large interest in order to reach strong coupling at room temperature [75, 76] and, therefore, the long awaited low threshold polariton laser. A microcavity based on ZnO is a technological challenge. Indeed, in order to reach polariton stimulation at a relative low pumping power, high quality factor is required. However, it is difficult to grow a high quality distributed Bragg mirrors with a small lattice mismatch with ZnO. Therefore, most of ZnO based-microcavities

suffer from excitonic and/or photonic disorder. Table 3.1 summarizes the properties of the most used materials in the ZnO-based microcavities described in this subsection and will help us to understand the issues and the technological challenge to grow such a cavity. In this subsection, we will investigate some realizations of ZnO-based microcavities which exhibit strong coupling regime and polariton lasing at room temperature.

ZnO microcavities with oxide-based distributed Bragg mirrors [77]

In reference [77], the distributed Bragg mirrors of the microcavity is based on oxide alloys (Yttria stabilized zirconia (YSZ)/Al_2O_3). The Rabi splitting was measured to be around 100 meV up to room temperature. As shown on table 3.1, YSZ/Al_2O_3 distributed Bragg mirrors have the advantage to exhibit a high index refractive mismatch 30% leading to a high quality factor of the distributed Bragg mirrors up to 700. However, the growth of a ZnO wurtzite crystal phase on amorphous layers (see table 3.1) prevents from having a good quality ZnO layer. Therefore, the exciton inhomogeonous broadening was around 15 meV because of the disorder.

Hybrid ZnO microcavities [48, 51, 49]

In hybrid ZnO microcavities, the bottom mirror is based on nitrides (AlN, GaN or their ternary alloy $(Al,Ga)N$) and the top one on oxides ($SiO_2$and Si_xN_y or HfO_2). This strategy is interesting because it allows to grow the nitride-based Bragg mirror and the ZnO layer with the same wurtzite structure and with a small lattice mismatch (less than 5%, see table 3.1). As a consequence, the quality of the ZnO layer is generally high (broadening of 5 meV measured at low temperature in reference [49]). High values of the Rabi splitting up to room temperature have been measured in such microcavities (Ω ranging from 40 meV to 58 meV). However, the low refractive index difference of $AlN/(Al,Ga)N$ and $GaN/(Al,Ga)N$ as well as cracks prevent to obtain a high quality factor (highest value $Q = 220$ in reference [48]). Generally, the top Bragg mirror is made of oxide because it has a higher reflectivity and does not induce disorder on the ZnO layer. An increase of the quality factor in these hybrid structures is crucial for the realization of a polariton laser at room temperature based on ZnO. Recently, a hybrid microcavity with a high quality factor of 500 and a Rabi splitting around 130 meV has exhibited polariton lasing at 120K [78] which is a breakthrough toward polariton lasing at room temperature in ZnO based devices.

GaN-based microcavity [79, 80]

GaN material provides a free exciton binding energy around 25 meV which is suitable for room temperature experiments. In reference [79], the bottom mirror is made of $AlInN/AlGaN$, which are almost lattice matched with GaN, and the top mirror of SiO_2/Si_3N_4 in order to obtain a good quality of the GaN layer. Notice that in order to reach a high quality factor over 2000, 35 periods of $AlInN/AlGaN$ have been grown for the bottom mirror. The active layer is a bulk GaN crystal. This sample exhibits strong coupling regime ($\Omega = 50meV$) and polariton lasing at room temperature. Over threshold, the condensate is localized because of photonic disorder. This result is very promising for obtaining electrically pumped polariton laser. Indeed, GaN is dopable and can then be electrically driven. However, the electrical injection is irreversibly destroying the heterostructure presented in reference [79] before the observation of electro-photoluminescence.

On the other hand, the microcavity presented in reference [80] is succesfully electrically driven, ie. electrophotoluminescence of the polariton modes is observed at room temperature. This structure relies on a superlattice of AlN/GaN for the bottom distributed Bragg mirror,

Material	Structure	Lattice parameter ()	Refractive index at 380 nm
HfO_2	Cubic	5	2
SiO_2	Amorphous	×	1.5
Si_3N_4	Amorphous	×	2.1
AlN	Wurtzite	3.1	2.2
GaN	Wurtzite	3.19	2.6
ZnO	Wurtzite	3.25	2.6
YSZ	Amorphous	×	2.3
Al_2O_3	Amorphous	×	1.7

Table 3.1: Summary of the crystal structure, lattice parameter (in the A-B plane for wurtzite) and refractive index around exciton resonance (~380 nm) of the material used in planar microcavities described in this chapter.

10 GaN quantum wells and a Ta_2O_5/SiO_2 top distributed Bragg mirror. The measured Rabi splitting is around 8 meV. The pillar geometry allows to efficiently evacuate the heat. The polariton lasing regime has not been yet observed in this microcavity using electrical injection: heat dissipation is not sufficient to prevent irreversible damages.

3.3.2 1D polaritonic wires [8, 9]

1D polariton in the quantum degeneracy limit has been demonstrated in well-controlled etched GaAs microcavities [8] and in a disordered potential with an elongated shape in CdTe microcavities [9]. In both cases, long-range coherence (more than tens of micrometers) is reported above threshold.

An interesting feature shown in reference [8] is the propagation and the control of the polariton condensate. It requires two phenomena: a long polariton lifetime and an initial kick-off. The first condition is fulfilled thanks to the high Q-factor of this microcavities (Q~12000 and lifetime around 30 ps). The second one is satisfied by the interaction between excitons of the reservoir and polaritons. Indeed, these wires are pumped non-resonnantly and an incoherent bath of hot carriers is created just underneath the pump spot. Exciton/polariton-polariton interaction is repulsive and kick-off the polariton condensate as soon as it is created (see figure 3.5 a)). Therefore, propagation over 50 µm is observed (see figure 3.5 b)). Moreover, as the laser induced exciton bath is creating a potential barrier for the condensate, it is possible to confine the condensate on the side of the wire. Control of the propagation of the polariton condensate opens the way toward macroscopic manipulation of a quantum wavefunction. One should notice that this behavior is a peculiar property of polaritons compared to photon lasing: polaritons can interact together via their exciton component.

However, these two structures suffer from the low free exciton binding energy in GaAs and CdTe. Therefore, polaritons are not stable against temperature. Moreover, controlled realization of such samples requires to grow lattice matched distributed Bragg mirrors and quantum wells. This heterostucture is then etched into a wire geometry. As a consequence, this sample are technologically demanding compared to ZnO microwires.

3.3.3 0D polaritons in ZnO Nanowires using Fabry-Pérot resonance [10]

Strong coupling has been observed in ZnO nanowires at room temperature. This system is really different from microcavities. The samples are ZnO nanowires with diameter around 100 to 300 nm and length around 1 to 10 µm. Photonic modes of interest are guided along the axis of the wire. The Fabry-Pérot cavity is formed by the two tips of the nanowire and gives a Q-factor around 250. This value corresponds to a radiative lifetime around $100fs$ which is relatively small to reach the quantum degeneracy regime. Finally, these polaritons are zero dimensional (contrary to the claim of the reference [81]): two axis are strongly confined and the last one is weakly confined. Thanks to momentum quantization with respect to the length of the cavity, L. K. van Vugt et al. are able to map the dispersion of these polaritons. In this kind of structure, Rabi Splitting goes up to 100 meV. The size (~100nm) and the zero dimensional confinement in this structure do not allow to create an elongated condensate and to study its properties.

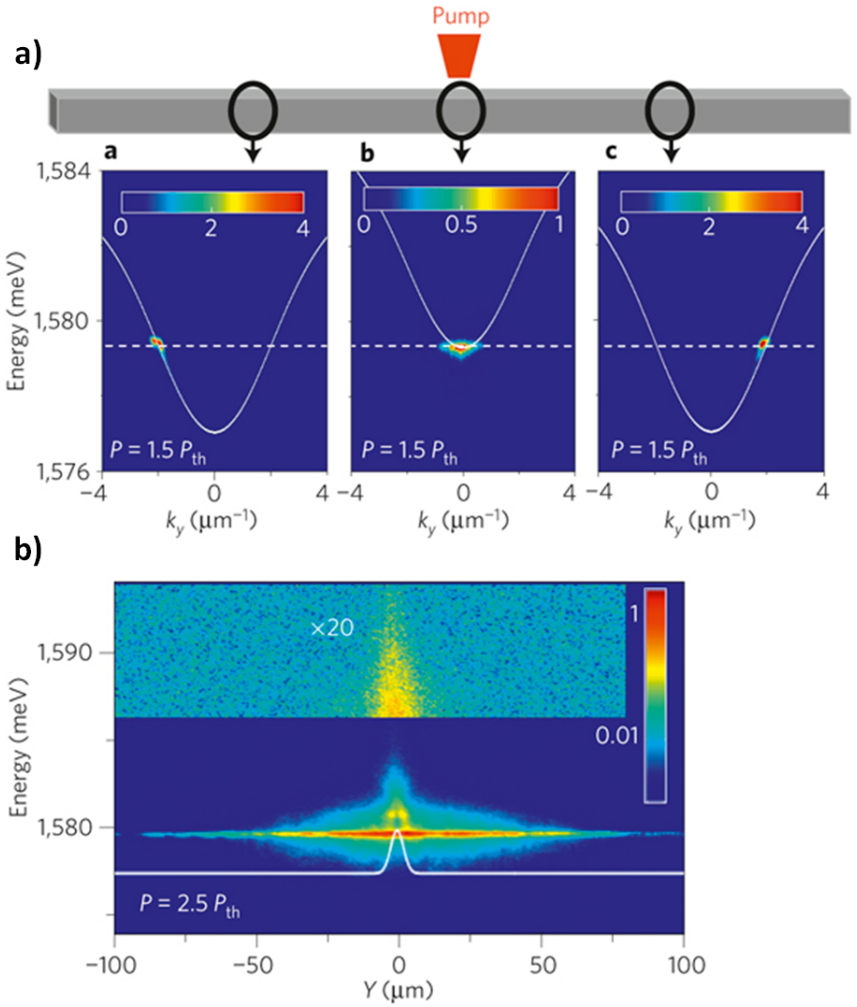

Figure 3.5: a) Far-field emission above threshold (P=1.5Pth) taken at different position along the wire. Polariton condensate is spontaneous kicked-off the laser spot. Solid line is the polariton dispersion. shows the polariton dispersion. b) Real-space intensity distribution along the wire in a coloured logarithmic scale measured above threshold (P=2.5Pth): condensed polaritons propagate over the whole wire whereas higher-energy excitons remain in the excitation area (magnified top panel); the white line shows the optically induced potential. Taken from [8]

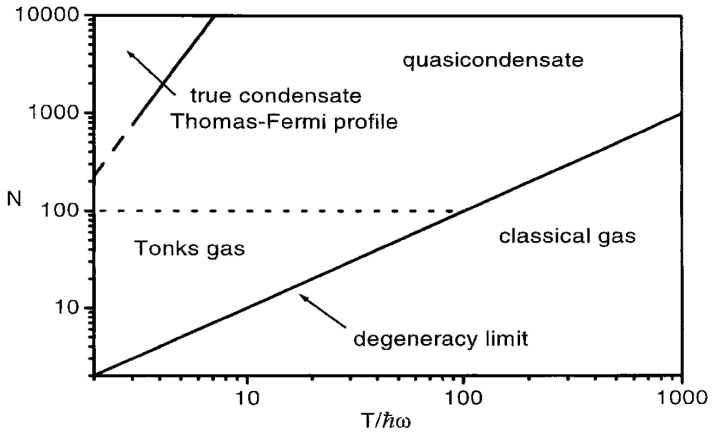

Figure 3.6: Phase diagram for a gas of 1D bosons. Ordinate axis corresponds to the number of particles in the system and abscissa axis is proportional to the temperature. Taken from [25].

3.4 Why ZnO microwires are interesting: 1D degenerate Bose gas Physics at room temperature

3.4.1 1D systems are different: Strong interaction at low density

In this subsection, we will consider a toy model demonstrating that 1D bosonic systems exhibit unusual behavior in the quantum degenerate limit. Let us imagine a gas of bosons with a mass m at zero temperature. The particles are separated by a mean interparticle distance called $\overline{r}$ satisfying $\overline{r} = \frac{1}{n^{1/d}}$ where n is the particle density and d the dimension of the system.

Kinetic energy per particle in this system can be estimated by: $E_k = \frac{\hbar^2}{2m}\frac{1}{\overline{r}^2} = \frac{\hbar^2}{2m}n^{2/d}$ whereas the interaction energy between particles read: $E_{int} = ng$ where g is the coupling constant between two particles. Strong interaction regime corresponds to a kinetic energy smaller than the interaction energy. In 3D system, we recover an usual behavior where strong interaction corresponds to high density whatever the value of the coupling constant g. In a 2D system, the interaction regime depends only on the value of the coupling constant g compared to a critical value given by $g_c = \frac{\hbar^2}{2m}$. In a 1D system, an unusual situation arises: strong interactions regime is reached at low density. This regime, specific to 1D systems, is called Tonks-Girardeau gas.

Phase diagram of 1D bosons at non-zero temperature has been studied by Petrov et al. [25]. Figure 3.6 describes this rich diagram of states. Interestingly, degenerate states are not suppressed by the temperature. In the Tonks-Girardeau regime, bosons are expected to be "fermionized" (ie. to behave like fermions) because of the strong interparticle interaction. Therefore, a spatial antibunching would be expected in such a regime.

3.4.2 ZnO microwire: stable polaritons against high temperature and density in a simple monolythic structure

As it is reported in this thesis, polaritons in ZnO microwires are stable against high temperature (up to 500K [75]) and high density thanks to the large free exciton binding energy (~60 meV). Consequently, they are well suited to study this rich phase diagram. Up to now, 1D phase diagram for polaritons has not been studied experimentally or theoretically. Deviations could be expected in taking into account the dissipative nature of polaritons as well as the exciton-exciton

interactions.

Growth of such ZnO microwires is less demanding than a microcavity as it is a monolythic structure. Recently, high quality ZnO microwires, with a constant radius over tens of microns, have been grown using MOCVD. Generally, in ZnO microwires, the excitonic disorder is of intrinsic nature (alloy fluctuations of zinc or oxygen for example) which is small in a monolythic structure. In this thesis, we will see that it is below 1 meV. From the photonic point of view, thanks to the total internal reflection involved in the HWGMs, a high confinement is reached with a quality factor up to 800 which is a key point to create an important population in the polariton state.

From the electrical injection point of view, p-doping in ZnO is still controversed. However, it has been shown recently in reference [82] that Antimony p-doping has been used to obtain a room temperature laser based on ZnO nanowires. Nevertheless, this process is not mature yet. Therefore, electrically pumped polariton laser based on ZnO is not easily realizable despite the high quality of the ZnO microwires. However, GaN microwires are studied in this thesis (see part II) and exhibit similar properties of the strong coupling regime. Structure such as PIN diode (p-doped semiconductor, insulator, n-doped semiconductor) connected with a radiator to remove heat are already available (because easier to grow than a microcavity) and will be studied soon.

As a conclusion, ZnO microwires open the possibility to study quantum degeneracy in a non-equilibrium 1D system with interacting bosons. Moreover, they are good candidates to obtain a polariton laser operating at room temperature in a simple and well controlled structure scalable towards technological applications. This very simple structure is suitable for other materials (such as GaN) and, therefore, for electrical injection.

Chapter 4

Experimental Set-Up

Contents

Polaritons are a mixed state between matter and electromagnetic fields, the latter components leak outside the system due to the finite quality factor of the optcial cavity. This light carries all the information describing the polariton field, ie. its energy, its longitudinal momentum and its coherence properties. Moreover, optical injection of hot carriers does not require any specific technological process compared to electronic transport measurements and can be performed on ZnO microwires as they stand. Furthermore, microwires have specific advantages over microcavities, mostly based on the fact that they do not feature any mirrors. As a consequence, optics provides powerful tools to address experimentally the properties of 1D polaritons in ZnO microwires.

In this chapter, firstly, we will discuss the non-resonant optical injection and relaxation in the strong coupling regime. These two processes allow to populate the lower polariton branch. In a first step, at low pumping power, it allows to study the linear properties of ZnO microwires. In a second step, by increasing the pumping power, it is possible to enter into the non-linear regime and create a degenerated gas of polaritons. Then, we will introduce the experimental and the 1D Fourier spectroscopy technique which is a key point to investigate 1D polariton dispersion in the linear as well as in the non-linear regimes.

4.1 Description of the experimental set-up

4.1.1 Non-resonant injection and relaxation towards polariton state

For photoluminescence experiments presented in this thesis, polaritons were pumped non-resonantly, ie. laser energy was higher than polariton energy and the laser energy was tuned to the A-B free excitons transition of ZnO (see figure 4.1). This configuration combines the following advantages:

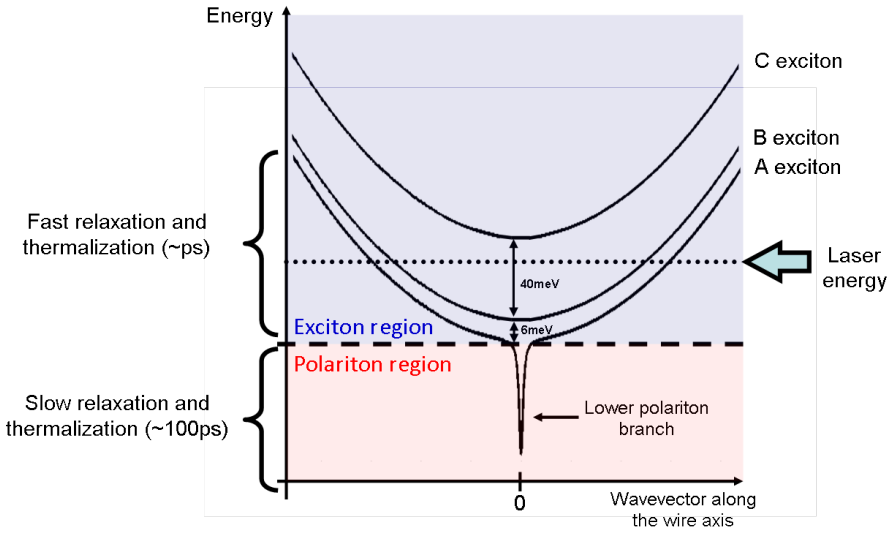

Figure 4.1: Scheme describing relaxation timescales of excitons and polaritons. In most of the experiments of this thesis, laser was resonant with A-B excitons and below band gap.

- it has an important absorption at the excitons energy (absorption coefficient: $\sim 10^5 cm^{-1}$ at the A/B exciton energy [83])
- there is a small amount of energy to relax toward the polariton states compared to an excitation above the band gap
- it prevents overheating of the excitons and the phonons bath compared to an excitation above the band gap
- it generates neutral quasi-particles and, therefore, limits the effects on the electric field close to the surface

On the other hand, this configuration has a drawback. Indeed, owing to the large absorption (absorption coefficient: $10^5 cm^{-1}$ [83]), the first 100 nanometers of the microwire only are excited.

Since ZnO is a strongly ionic material, fast relaxation and thermalization in the exciton region (see figure 4.1) is achieved by emission of LO and acoustic phonons at room temperature [84]. At low temperature, as we will see in details in part III, relaxation time constant of excitons in the exciton region is of the order of 1-10ps and exciton-exciton scattering plays an important role to reach the thermal equilibrium.

As the polariton lifetime is around picosecond and the density of states available in the strong coupling region is small, slow relaxation is observed towards the lower polariton states (see figure 4.1). This situation leads sometimes to an out of equilibrium phenomenon called bootleneck effect where the polariton population is accumulated in the anti-crossing region [85] and a small proportion only releases to the polariton ground state in $k_z = 0$. Therefore, because of the bottleneck effect and the photonic losses, a large number of pumped excitons do not relax towards the polaritons states. The quantum degeneracy regime in $k_z = 0$ is reached if the number of polaritons per state is of the order of unity (ie. $n_p \sim 1$). As a consequence, one needs high intensity lasers and an efficient injection to reach the quantum degeneracy regime.

4.1.2 Principle of the experimental set-up

The experimental set-up has been developed to provide a high efficiency of the laser injection combined with a versatile detection to measure the energy as well as the time dependency of the light emitted by the sample in either the real space or the momentum space.

Three kind of lasers, at the beginning of the injection line (see figure 4.2), have been used in this thesis:

- High peak power pulsed laser (picosecond titanium-sapphire laser): Pulsed laser has the advantage to produce high peak power compared to the same laser in a continuous intensity mode. This high peak power is a key parameter to inject a large number of carriers in small amount of time and, therefore, to reach the non-linear regime in semiconductor structures with very high threshold.

- High power continuous wave (CW) laser (titanium-sapphire laser): CW lasers provide less peak power than pulsed lasers. Therefore, they are less suitable to reach non-linear regimes. However, they have the advantage to create a steady state in the semiconductor which is much more easy to understand than the pulsed response of the system.

- Low power CW laser (Helium-Cadmium - wavelength: 325 nm): This "ready to use" laser is ideal to quickly characterize large band gap material. However, it does not provide enough power to reach the non-linear regime.

The two titanium-sapphire lasers produce light with an energy ranging from 700-900 nm and were doubled to reach the ZnO transition energy in the UV (accessible wavelength range: from 360 nm to 425 nm). They were coupled to an acousto-optic modulator which was used to chop the laser light. It allows to reduce the heating (related to the average power) without changing the peak power necessary to reach the non-linear regime. As shown in figure 4.2, the laser light was injected in a transmission configuration. It has the advantage, compared to a reflection configuration, not to used a 50/50 beam splitter on the detection range and therefore, to maximize the injected power.

The sample is located in the cryostat mounted on a three axis micrometric stage. After being collected by the objective, the photoluminescence is sent to the spectrometer to measure its energy. By removing the Fourier plane lens, it is possible to switch from Fourier to real space spectroscopy. Finally, this versatile set-up allows to quickly measure the energy of light with either spatial, time or momentum resolution.

4.2 1D Fourier spectroscopy

In order to have insight into measurements along lower polariton branch (ie. momentum k_z resolution) on a single microwire, we have designed a micro-photoluminescence set-up stable down to the micrometric scale and using 1D Fourier spectroscopy along the single translational invariant axis of the microwires. Thanks to this powerful experimental technique, it is possible to infer the dispersion of 1D polaritons inside the semiconductor and it allows to characterize light-matter interaction, momentum-space population, linewidth, etc... even during the stimulation regime. Therefore, this technique is a "must have" to study 1D polaritons.

First, we will discuss the energy and momentum conservation at an interface semiconductor-air in 1D systems. Then, using the Fourier spectroscopy on the light emitted by a polariton, we will show that it is possible to measure its 1D dispersion inside the semiconductor.

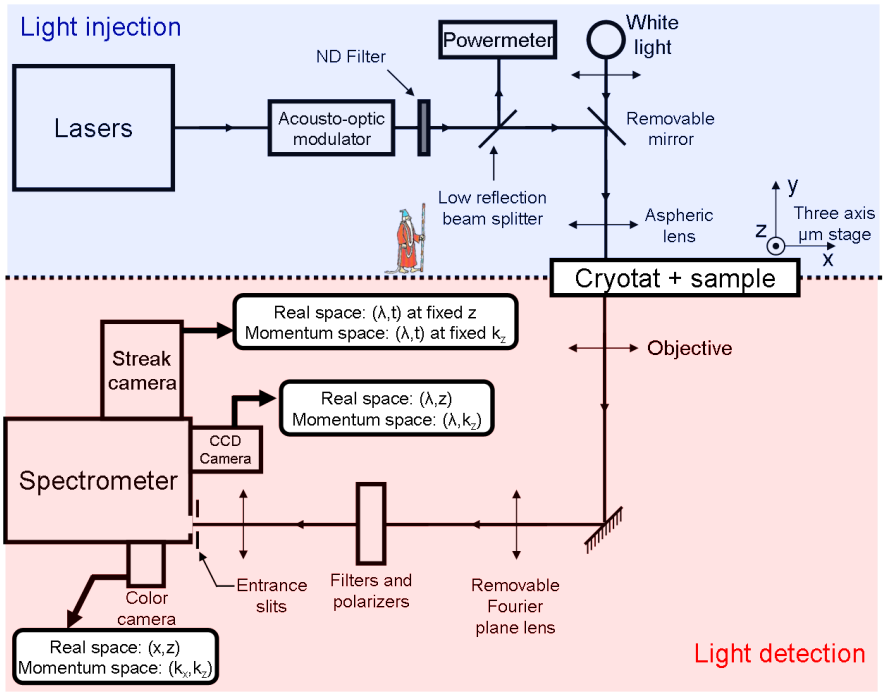

Figure 4.2: Scheme of the experimental set-up separated into the injection (blue) and the detection part (red).

4.2.1 Energy-momentum conservation and interfaces in 1D system

In the strong coupling regime, polaritons cannot emit a photon inside the semiconductor because there is no pure photon states. However, they can emit a photon outside the semiconductor through the interfaces. At the interface, two physical quantities are conserved: the energy and the momentum parallel to the interface. For a plane interface, the component of the momentum parallel to the interface, which is a two-dimensional vector, is conserved like in the refraction phenomenon for light. In a microwire, and generally in 1D systems, because of the reduced translational invariance, only the momentum parallel to the wire k_z^{in} is defined by a unique value and is conserved through the interface. The energy momentum conservation is expressed by the following formulas (see figure 4.3):

$$E_{in} = E_{out}$$

$$k_z^{in} = k_z^{out}$$

where $k_z^{out\,(in)}$ is the component of the momentum along the free axis outside (respectively inside) the semiconductor (see figure 4.3) and $E_{out\,(in)}$ is the energy of the particle outside (respectively inside) the semiconductor. As a consequence, by measuring energy and the momentum parallel to the interface k_z^{out} of the emitted photon, one measures also these quantities for the polariton that recombined.

As we will see now, a direct measurement of the light momentum parallel to the interface is possible by using an angular resolved experiment. Energy momentum relation for photons in free space reads (with the notation given on figure 4.3):

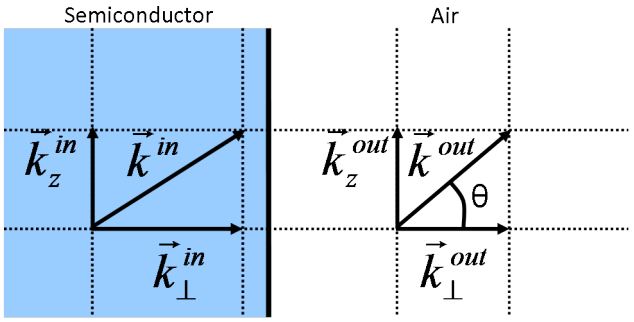

Figure 4.3: Definition of the momentum and its perpendicular and parallel projections to the interface.

$$E_{out} = \hbar k^{out} c$$

Figure 4.3 introduces the angle of emission of the photon θ. The momentum parallel to the interface inside the semiconductor can be rewritten:

$$k_z^{in} = \frac{E_{out}}{\hbar c} sin\theta \tag{4.1}$$

This equation connects outside parameters carried by the emitted photon (photon energy E_{out} and angle of emission θ, right hand-side) to the polariton momentum parallel to the interface (left hand-side). Therefore, by measuring the angle of emission and the energy of the photon, one can access to the dispersion of a polariton inside the semiconductor structure along the free axis.

4.2.2 Angular resolved experiment using Fourier imaging along the free axis

Basic principle

In our experiments, the angular resolved experiments were performed using Fourier imaging. The basic principle is described on figure 4.4. Fourier space of a given object is situated at the focal length after the lens/objective. In a configuration presented on figure 4.4 where the real space and the Fourier space are situated, respectively, at a focal length before and after the lens, the light collected in the Fourier space is the exact Fourier transform of the light emitted from the real space. This statement is limited to the paraxial approximation which is valid up to 30°. As shown on figure 4.4, Fourier space is a direct image of the directions of emission of the object. Indeed, to a given angle of emission α corresponds only one position in the Fourier space at $f\ tan\alpha$ from the optical axis. Thereafter, one can optically manipulate this Fourier plane to measure dispersion directly on a detector.

In this thesis, we have used a near-ultraviolet Mitutoyo objective with a numerical aperture of 0.5. As a consequence, the angle of emission α can be studied over a 60° range. Of course, this Fourier imaging technique can be coupled with different spectroscopy tools: photoluminescence, reflectivity, time-resolved photoluminescence, etc...

For microwires, owing to the translational invariance along the free axis, two distinct angles should be considered (see figure 4.5): the angle θ along the wire axis and the angle ϕ along the confined axis. This point is the main difference with microcavities from the experimental point of view. Indeed, for planar microcavities, there are two translational invariance and only one

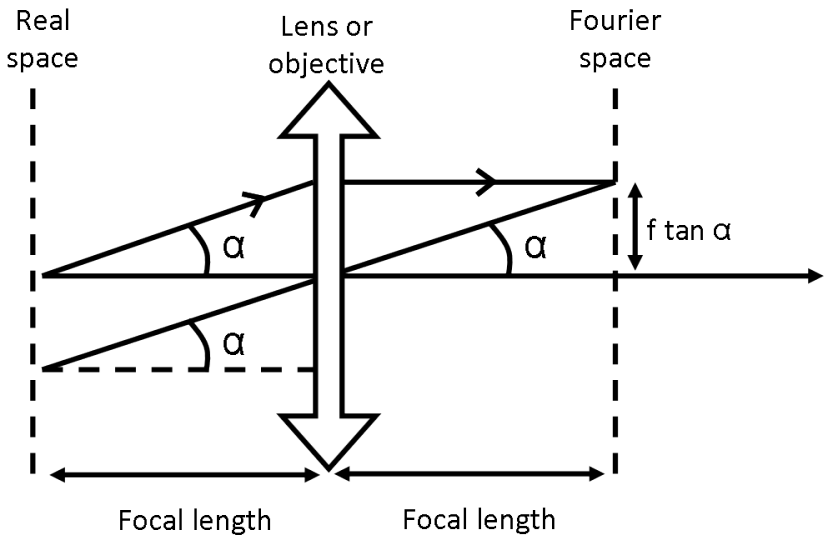

Figure 4.4: Principle of an angular resolved experiment using Fourier space imaging. θ is the angle of emission of a photon.

angle with respect to the normal of the surface of the structure has to be taken into account. Notice that angular resolved experiments along the confined axis for microcavities is much more difficult to perform than for microwires.

Angular resolved experiment along the free axis

In a microwire geometry, the polariton wavefunction $f_{pol}(x,y,z)$ has a well-defined momentum along the wire axis, and one can write: $f_{pol}(x,y,z) = f_{pol}(x,y) \times e^{ik_z z}$. By Fourier transforming this expression, we recover the fact that in the Fourier space of figure 4.4, only one position corresponds to k_z (ie. a dirac function at k_z). As already mentioned, for $\phi = 0$ (ie. angular resolved experiment along the wire axis), we have: $k_z = \frac{E_{out}}{\hbar c} sin\theta$.

Angular resolved experiment along the confined axis

Along the free axis, the polariton momentum k_z^{in} is well-defined thanks to the translational invariance. However, in the confined axis, the wavefunction of the polariton in the momentum-space spills over multiple wave-vector. For $\theta = 0$ (ie. angular resolved experiment along the confined axis), one can write: $k_\perp = \frac{E_{out}}{\hbar c} sin\phi$. Therefore, a given polariton with ($k_z = 0$,$k_\perp$) can emit photons with various angle ϕ. In this case, the Fourier space will corresponds to the far-field emission of the wire (ie. the Fourier transform of the polariton wavefunction in the cross-section).

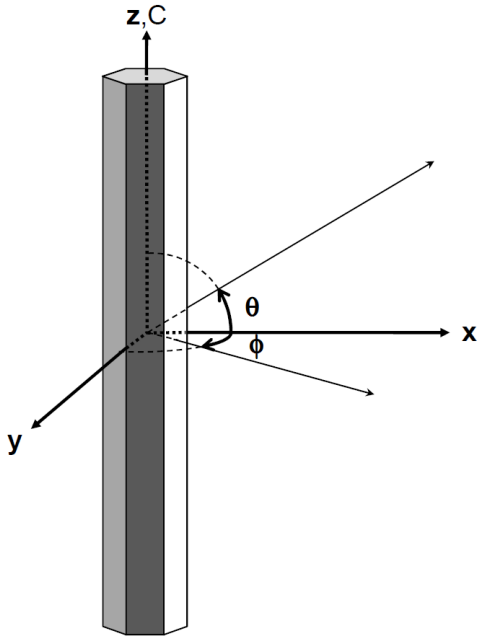

Figure 4.5: Definition of the angles θ and ϕ with respect to the wire orientation. θ (ϕ) is related to the momentum k_z ($k_\perp$) parallel (perpendicularly) to the wire.

Part II

Linear properties of polaritons in ZnO microwires

This part is dedicated to the experimental investigation of single ZnO microwires under weak optical excitation, ie. in the limit of linear optics. Indeed, it is necessary to understand the behavior of the polaritons below the quantum degeneracy limit (ie. at low excitation power) before to move on to the non-linear regime in the part III.

In the chapter 5, we will focus on demonstrating that the strong coupling regime is achieved and preserved in these structures up to room temperature. The polariton dispersions along the wire axis will be reconstructed using linear response theory especially developed for hexagonal microwires. A complex behavior appears because of the strong coupling regime between two families of three-dimensional cross-polarized excitons (ie. A, B and C ZnO excitons) and two sets of cross-polarized hexagonal whispering modes. The one-dimensional character is supported by dispersion measurements at room temperature around the wire cross-section leading to one-dimensional-like density of states. An interesting comparison between ZnO and GaN microwires will be shown in order to demonstrate that the physics developed in this thesis can be extended to other materials with the same structure. Moreover, GaN microwire, as it is a p and n dopable material, is a necessary step towards electrically injected polariton laser.

In the chapter 6, the consequence of the large Rabi splitting as compared to the phonon spectral broadening on the polariton linewidth is analyzed. Indeed, we will see that the LO phonon interaction is quenched at room temperature in the ZnO microwires. In this case, the polaritons are isolated from the LO phonon bath resulting in a lower than expected linewidth at room temperature.

Chapter 5

Strong coupling regime in a single ZnO microwire

Contents

This chapter is dedicated to the spectroscopy of a single ZnO microwire. First, we will study the spatially-resolved spectroscopy of these wire to describe the main properties resulting from the bulk character of the ZnO crystal as well as the unusual microwire geometry. Using 1D Fourier spectroscopy, we will demonstrate that the strong coupling regime is preserved from low temperature up to room temperature by modeling the polariton dispersion with the linear response theory. A direct measurement of the polariton dispersion perpendicularly to the microwire will be presented in order to prove their one dimensional character. Once the strong coupling regime will be properly established, the same physical concept will be extended to microwires made up of GaN exhibiting similar main properties than ZnO microwires. Of course, some differences will be discussed such as the effect of doping inherent in the growth of GaN microwires.

5.1 Spectroscopy of a single ZnO microwire at low temperature

5.1.1 Spatially-resolved spectroscopy

Spatially resolved photoluminescence at low temperature has been performed on a single microwire. The result at 10K is presented on figure 5.1 on a logarithmic color scale. On this figure, we can directly observe the energy of the emitted photon as a function of the position along the wire. First, it is preferable to address the different peaks on this figure separately before to describe the polaritons (lines with non-constant energy as a function of the position along the wire axis in figure 5.1). We will see that the ZnO microwires exhibit a photoluminescence corresponding to an usual bulk piece of ZnO plus the polariton states. For the sake of simplicity, we will focus on TE polarized polaritons in this section. Anyhow, TM polarized polaritons are poorly populated at low temperature because of the spectral separation between A/B excitons and C exciton $45meV$ compared to the thermal energy $\sim 1meV$ (see section 6.2 for details).

Bound exciton complex Around 3.36 eV, the several non-dispersed peaks on figure 5.1 correspond to the ZnO bound exciton complex [86]. An exciton can bond on a point defect in a semiconductor such as a substitution of a zinc or oxygen atoms by an impurity. In the case of bulk ZnO, these defects are mainly shallow donor centers with an energy just below the conduction band. Therefore, the energy of an exciton bound to a donor (called D^0X) is just below (~16 meV for ZnO) the free exciton energy. In certain cases, the exciton can bond to an ionized donor (called D^+X).

The bound exciton complex corresponds to the ensemble of peaks emitted by the bound excitons with several different kinds of impurities. In the early work of Reynolds et al. [87], they were numbered from I_0 to I_{11}. The determination of the exact nature of the impurities producing these emissions has been the topic of a large research effort (see chapter 7 of reference [29] written by B. K. Meyer for a complete review). In our case, based on the energy position given in reference [29], it is possible to retrieve the nature of this emission on figure 5.2 which is the zoom around 3.36 eV. From low energy to high energy on figure 5.2, we have two neutral donor bound excitons (I_9-I_6/I_7) and two ionized donor bound excitons ($I_4 - I_{4b}$). The shoulder at 3.376 eV corresponds to the free A exciton emission. At low temperature (ie. below 70K), bound exciton emission dominates over all the other peaks by at least one order of magnitude. Their localization energies compared to the free exciton energy is around 16 meV. Therefore, generally above 70K, thermal fluctuations prevent excitons to localize in a bound state and the bound exciton complex emission vanishes.

LO phonon replica The broad emission from 3.3 eV to 3.33 eV is the first LO phonon replica of the free exciton state. It corresponds to the emission, by a free exciton, of a LO phonon (with an energy of $E_{LO} = 72meV$ in ZnO) and a photon at an energy $E_X - E_{LO}$. The lineshape of the m^{th} LO phonon replica is given by the formula[88, 46]:

$$I_{LO}(\tilde{E}) \propto \underset{\text{matrix element}}{\text{Exciton-LO phonon}} \times \underset{\text{of states}}{\text{Exciton density}} \times \underset{\text{distribution}}{\text{Exciton energy}} \otimes \underset{\text{Linewidth}}{\text{Exciton}}$$

$$I_{LO}(\tilde{E}) \propto W_m(\tilde{E}) \times \sqrt{\tilde{E}} \times e^{-\frac{\tilde{E}}{k_B T_X}} \otimes \mathcal{L}(\tilde{E}, \Gamma_X)$$

where $\tilde{E} = E - (E_X - m \times E_{LO})$, $k_B T_X$ is the thermal energy of the exciton gas and $\mathcal{L}(\tilde{E}, \Gamma_X)$ is a lorentzian with a linewidth Γ_X. $(E_X - m \times E_{LO})$ gives the low energy side of the LO phonon replica emission. Of course, $I_{LO}(\tilde{E})$ is zero for $\tilde{E} < 0$. The matrix element $W_m(\tilde{E})$ is given by:

$$W_m(\tilde{E}) \propto \tilde{E} \text{ for m=1 and } W_m(\tilde{E}) = 1 \text{ for m>1}$$

As a consequence, the exponential decrease on the high energy side is connected to the temperature of the exciton bath. The second LO phonon replica on figure 5.1 can be fairly reproduced using this model. Firstly, it means that the exciton gas is at thermal equilibrium. Secondly, the extracted exciton temperature is $15K \pm 2K$. This value is slightly higher than the lattice temperature (10K) which means that the thermalization with the lattice is almost complete.

TE polarized polaritons A set of TE polarized polaritons can be identified on figure 5.1 because of their dispersion as a function of the position along the wire axis. These lines corresponds to the lower polariton branches. TM polarized polaritons are, generally, not populated at low temperature because of the C exciton is not thermally populated at this temperature (ie. $E_{XC} - E_{XA/B} \approx 45meV$). Bottom part of figure 5.4 is a schematic representation of the wire studied in this experiment and gives a qualitative understanding on the spectral movement of the polariton peaks along the wire. Indeed, the energy of the HWGMs is inversely proportional to the radius of the wire: $E_{HWGM} \propto 1/R$. As shown on figure 5.4, energy of the polaritons increases for decreasing radius. Interestingly, in this wire, the radius is almost constant over 10 µm length resulting in an almost constant energy of the polariton in this region. Because of the strong coupling regime, we can observe that the polariton energies on figure 5.1 does not cross the excitonic resonance: this a typical feature of the strong coupling regime. The relation between the energy of a HWGM with the radius of the wire has been used in reference [52] to demonstrate the strong coupling regime at room temperature in this structure with a Rabi splitting above $250meV$. However, as it is based on a position-radius correspondence measured by scanning electron microscopy, a very accurate measurement of the diameter of the microwire is required. In this thesis, another proof of the strong coupling regime will be given using 1D Fourier imaging by measuring the polariton dispersion at a given position on the microwire. Moreover, spatially resolved experiments do not take into account the polariton dispersion. The polariton states presented in figure 5.1 are summed over all the momentum optically accessible. To go further in the study of these structures in the linear and non-linear regime, it is necessary to measure the dispersion of these polaritons at a given position to understand properly their properties. In particular, Fourier spectroscopy is a privileged experimental tool to prove that these polaritons are one dimensional.

5.1.2 Angular resolved photoluminescence

In this subsection, we will apply 1D Fourier spectroscopy on a single ZnO microwire at 10K in order to demonstrate the strong coupling regime and to extract the Rabi splitting. These experiments are performed with a small excitation spot (diameter ~1µm) on a region of the wire where the radius is constant (for example, around 30µm on figure 5.1).

Polariton dispersion along the wire axis: experiments

Figure 5.1 displays the angular-resolved TE polarized photoluminescence experiment along the wire axis. The angle θ is connected to the polariton momentum along the wire axis by the relation: $k_{\parallel}^{in} = \frac{E}{\hbar c} sin\theta$. Several well-defined TE polarized lower polariton branches are visible from $3.3eV$ to $3eV$. These polaritons are almost fully TE polarized in the range [-30° ; 30°]. Therefore, they result from the coupling between TE polarized HWGMs and A/B excitons

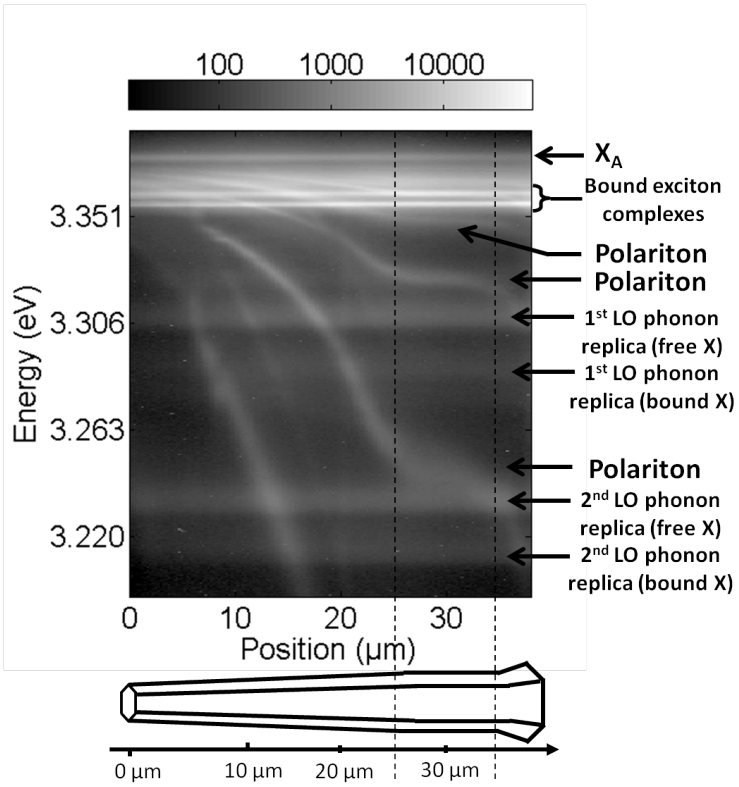

Figure 5.1: Spatially-resolved photoluminescence at 10K along the wire axis on a logaritmic color scale. X_A stands for the A exciton energy

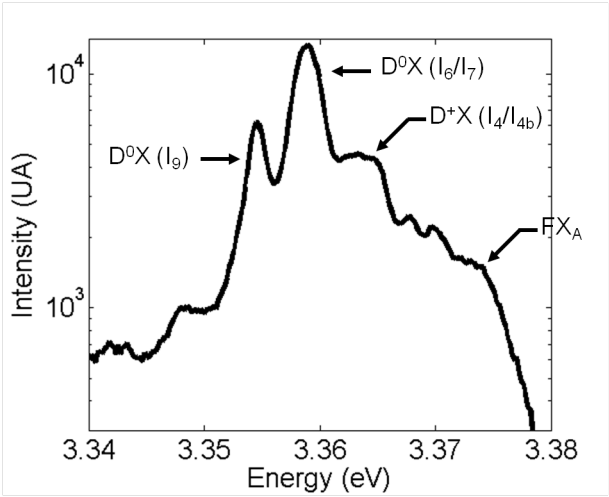

Figure 5.2: Photoluminescence spectrum of a ZnO microwire at low temperature in a logarithmic scale. Each arrow gives the nature of the emitter. D^0X (D^+X) stands for (ionized) donor bound exciton and FX_A corresponds to the free A exciton emission. The notation I_n numbered the peaks as done in reference [87].

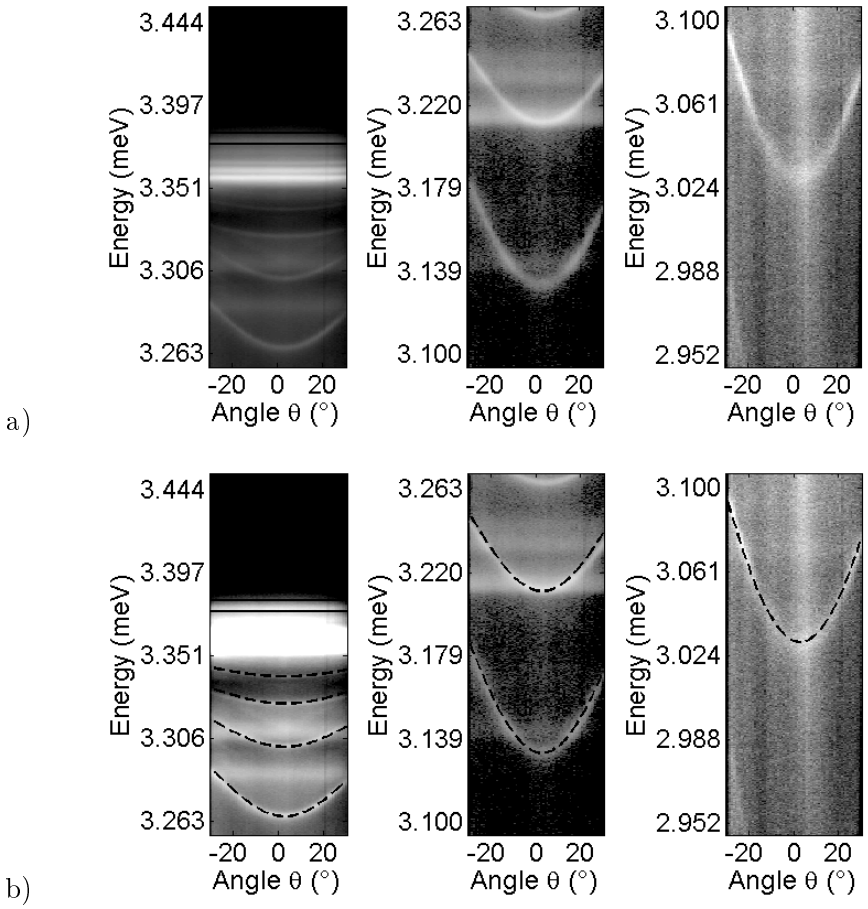

Figure 5.3: a) Angular resolved TE polarized photoluminescence at 10K along the wire axis on a logaritmic color scale for three spectral ranges. The two black lines corresponds to the A and B exciton energy. b) Same figure than a) with the theoretical modeling described in the text. Bound exciton complexes has been saturated for the claricity of the figure.

(which is coupled to TE polarized light). Their dispersion features demonstrate unambiguously the strong exciton-photon coupling regime:

- Modes of high energy (i.e., closer to the exciton resonances) have a dispersion shape that tends to flatness, while those at lower energy are markedly dispersed.
- The free spectral interval between two succesive polaritons decreases with increasing energy

A complete understanding of the polariton dispersion along the wire axis in the strong coupling regime requires a careful modeling to extract the Rabi splitting from these experiments.

Polariton dispersion along the wire axis: modeling

The goal of this model is to extract the Rabi splitting from the TE polarized emission and not to derive the eigenenergies of the modes. Therefore, we do not want to reproduce the spectral position of HWGM given by Maxwell equations as well as the TE/TM splitting. Moreover, this model will not reproduce the complex oscillator strength distribution emerging at high angle (ie.

above 30°) that is modifying the polariton dispersion (see section 5.2.4 for a discussion on the oscillator strength mixing at non-zero angle). Therefore, it will be restricted to angular resolved dispersion below 30°.

In ZnO microwires, owing to the conservation of energy and k_z, the shape of the dispersion branches measured on figure 5.3 is directly related with the spectral behavior of the dielectric function ϵ since the energy E_m of the m-th HWGM reads:

$$E_m(\theta) = E_m(0)\left(1 - \frac{sin^2\theta}{\epsilon(E_m(\theta))}\right)^{-\frac{1}{2}} \tag{5.1}$$

where θ is the detection angle of the photoluminescence with respect to the z-axis. Thus, each HWGM provides in principle a tight regular sampling of the dielectric function in the detection window. In the framework of the linear response theory, excitonic transitions can be explicitly accounted for in the dielectric function $\epsilon(E)$ under the form:

$$\epsilon_r(E) = \epsilon_\infty\left(1 + \sum_{i=A,B,C}\frac{\alpha^2\Omega_i^2}{E_i^2 - E^2}\right) \tag{5.2}$$

where ϵ_r is the dielectric function for TE-polarized light, Ω_i is the contribution to the Rabi splitting of the excitonic transition i=A, B and C of energy E_i and where the damping constant γ has been neglected. ϵ_∞ is the background dielectric constant which accounts for every other contributions to the dielectric function. α is the spatial overlap integral between the excitonic medium and the HWGMs which can be lower than 1 due to the evanescent part of the HWGMs and to an excitonic dead layer located right below the air-semiconductor interfaces.

By inserting equation 5.2 into equation 5.1, and using a set of parameters at low temperature, we can fit properly the entire set of dispersion branches of figure 5.3. The exciton energies and oscillator strengths are well documented in the literature [39, 40, 38] and, for the input parameters, we choose:

$$E_{XA} = 3.3755eV\ ,\ \Omega_A = 100meV$$

$$E_{XB} = 3.3815eV\ ,\ \Omega_B = 271meV$$

Only two parameters are left free: α and ϵ_∞. These two parameters can be fitted independently from each other since for polariton modes far below the excitons energy as compared to theΩ_i's, the right term of 5.2 vanishes and the dispersion branch is sensitive only to ϵ_∞. It is the case of the modes at the right panel of figure 5.3 a).

Note that this procedure has a significant advantage compared to a complete modeling method based on Maxwell equations (for example the model developed for ZnO microwires) since it does not require any knowledge a-priori on the energy $\tilde{E}_m$ of the uncoupled confined electromagnetic modes versus mode number m (at $\theta = 0°$) in the microwire, which depends very much on the precise shape of its cross-section. Instead, in this method the spectrum $\tilde{E}_m$ is a result of the procedure since it is connected with the measured energy of the polariton modes versus m (at $\theta = 0°$) by the relation:

$$E_m(\theta = 0) = \frac{n_\infty}{n(E_m(\theta = 0))}\tilde{E}_m$$

Polariton dispersion along the wire axis: Rabi splitting

We applied this method to the measurements shown in figures 5.3 b) (black dashed lines). For TE polarized polaritons, the contribution from C exciton can be neglected because of its small coupling to TE light compared to the A and B exciton. The extracted α, n_∞ and Rabi splitting are:

$$\alpha = 1 \pm 0.1 \ , \ n_\infty = 2.35 \pm 0.05$$

The background index $n_\infty = 2.35$ is coherent with the value found in literature for bulk ZnO [89]. The large value of α is the first main result of this since it demonstrates unambiguously the strong coupling regime at 10K.

This demonstration requires the comparison between the overall Rabi splitting Ω and the linewidth Γ_0 of the polariton mode around the resonance between the excitons and the uncoupled HWGMs (i.e. around $3.23eV$ on figure 5.3). $\Omega = \alpha\sqrt{(\Omega_A^2 + \Omega_B^2)}$ is a proper definition of the overall Rabi splitting when the latter is much larger than the energy separation between the different exciton levels. We find $\Omega = 288meV \pm 29meV$ at 10K which satisfy this condition. Indeed, the linewidth Γ_0 of the mode at $3.22eV$ is $\Gamma_0 = 3.1.meV \pm 0.2meV$. Finally, comparing Γ_0 and Ω at low and room temperatures shows unambiguously that the strong coupling regime is achieved at low temperature with a large figure of merit (defined as the ratio between Rabi splitting and polariton linewidth) of 93 at 10K.

5.2 Spectroscopy of a single ZnO microwire at room temperature

5.2.1 Near band-edge spectroscopy of a single microwire along the wire axis

Single ZnO microwire has been studied in a spatially resolved photoluminescence experiment at room temperature on the same wire than figure 5.1. Figure 5.4 is the result of this experiment in a grey scale. Four sharp peaks stand on the top of a broad emission which has a spectral width around 100 meV.

As demonstrated in reference [90] with temperature dependency expertiments, the background is dominated by the LO phonon replica of the free exciton at room temperature (generally called blue band). Since the optical LO phonon energy in ZnO is 72 meV, phonon replica of the exciton has an emission energy given by the relation: $E_X - mE_{LO} = 3309meV - m \times 72meV$ where m is a positive integer [29]. Since the emission of LO phonons is less and less likely with increasing m and it is convoluted with linewidth and the spectral distribution of excitons, it results in a broad emission at room temperature.

On the top of this background, four well-defined lines are observed with linewidths ranging from 2 meV to 6 meV and correspond to the lower polariton branches. As shown on figure 5.4, these peaks can be separated in two families: TE (ie. $E \perp c$) and TM (ie. $E \parallel c$) with respect to the wire axis (ie. c-axis of the wurtzite). Bottom part of figure 5.4 is a schematic representation of the wire studied in this experiment and gives a qualitative understanding on the spectral movement of the polariton peaks along the wire.

5.2.2 Polariton dispersion along the wire axis

In this subsection, we will apply 1D Fourier spectroscopy on a single ZnO microwire at room temperature. These experiments are performed with a small excitation spot (diameter ~1µm)

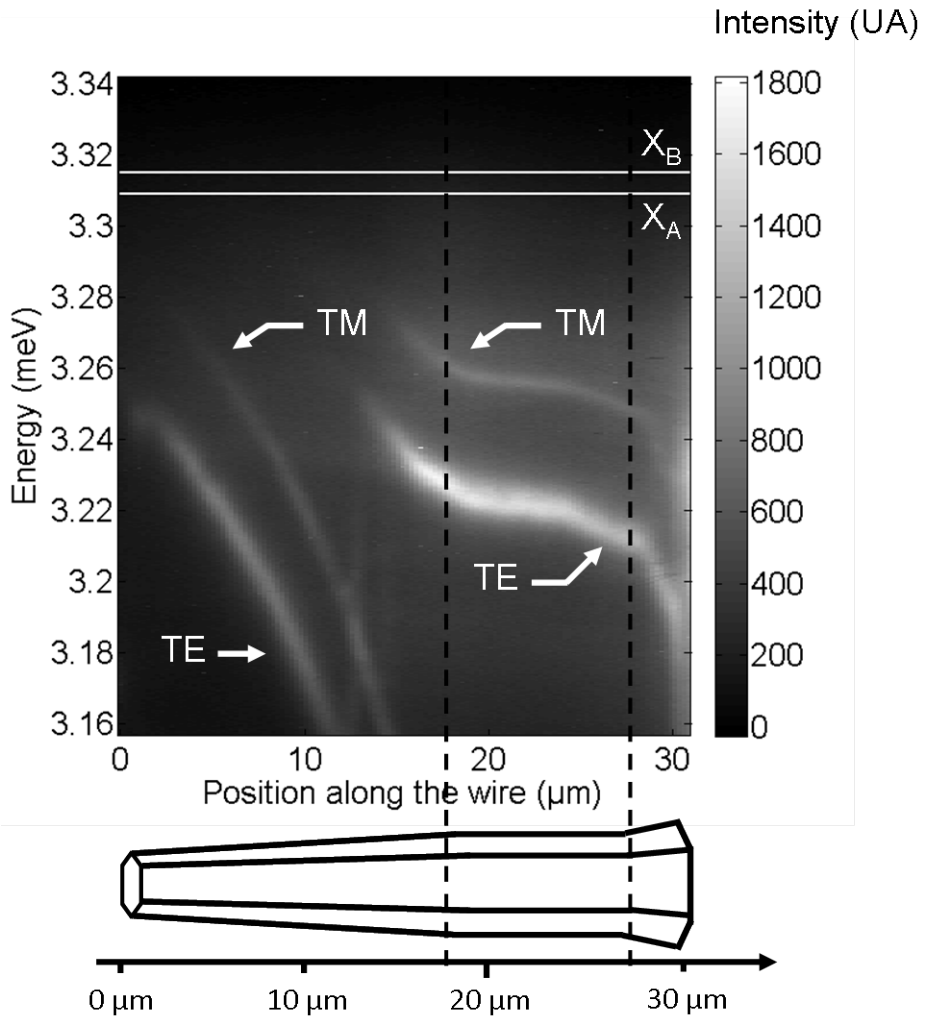

Figure 5.4: Top part: Greyscale spatially resolved photoluminescence of a single ZnO microwire at room temperature. TE/TM stands for TE/TM polarization modes. $X_{A/B}$ corresponds to the A/B exciton energy (white line). Bottom part: Schematic representation of the tapered wire with a needle-like shape studied in this experiment. There is a constant radius part between 18 µm and 28 µm.

on a region of the wire where the radius is constant (for example, between 18 µm and 28 µm on figure 5.4).

Polariton dispersion along the wire axis: experiments

Figure 5.5 a) displays the angular-resolved photoluminescence experiment along the wire axis. The angle θ is connected to the polariton momentum along the wire axis by the relation: $k_{\parallel}^{in} = \frac{E}{\hbar c} sin\theta$. Several well-defined lower polariton branches are visible, which can be separated into two families according to their linear polarization, i.e. mostly TE with respect to the main axis of the wire (electric field E perpendicular to the wire C-axis, right-hand side of the figure) or mostly TM ($E \parallel c$, left-hand side) at $k_z = 0$ ($\theta = 0$). These two polariton families result from the two linearly cross-polarized exciton families found in ZnO, i.e., A and B are TE-polarized excitons, while C are TM-polarized excitons. Within a given polarization family, several lower polariton branches are visible, stacked one over the other in energy. Each branch results from the strong coupling between free excitons and a given HWGM mode (the corresponding label of the HWGM is shown in figure 5.5b)). Their dispersion features demonstrate unambiguously the strong exciton-photon coupling regime:

- Modes of high energy (i.e., closer to the exciton resonances) have a dispersion shape that tends to flatness, while those at lower energy are markedly dispersed
- An inflexion point shows up at $\theta = 40° - 50°$, which results from the onset of anticrossing between the involved HWGM and the exciton level.

A complete understanding of the polariton dispersion along the wire axis in the strong coupling regime requires a careful modeling to extract the Rabi splitting from these experiments.

Polariton dispersion along the wire axis: modeling

The model used to fit the polariton branches in figure 5.5 is based on Maxwell equations and linear response theory and has been developed in collaboration with Guillaume Malpuech's team from the LASMEA laboratory in Clermont-Ferrand. Basically, it is based on the same model than that developed in chapter 2 for WGMs in an anisotropic cylinder. The only difference is that the anisotropy, in the strong coupling regime, is not due to the anisotropy of the background dielectric function but comes from the two dielectric functions ϵ_r in the cross-section and ϵ_z along the wire axis which are not coupled to the same set of excitons. Compared to the model developed at low temperature, this model reproduces the exact spectral position of the polariton, the TE/TM splitting and the polarization mixing at high angle of emission θ.

In ZnO microwires, the dielectric function can be written:

$$\epsilon(E) = \begin{pmatrix} \epsilon_r & 0 & 0 \\ 0 & \epsilon_r & 0 \\ 0 & 0 & \epsilon_z \end{pmatrix}$$

$$\epsilon_{r(z)}(E) = \epsilon_{r(z)}^{\infty} \left(1 + \sum_{i=A,B,C} \frac{f_i^{r(z)}}{(\hbar\omega_i)^2 - E^2 + i\hbar\gamma_i'\hbar\omega} \right) \tag{5.3}$$

where $\epsilon_{r(z)}^{\infty}$ is the background dielectric function along the radius of the wire (the wire z-axis), i runs over the A,B and C excitons, $\hbar\omega_i$ is the exciton energy of the i^{th} exciton, γ_i' is the non-radiative decay rate of the i^{th} exciton and $f_i^{r(z)}$ is the oscillator strength of the i^{th} exciton along

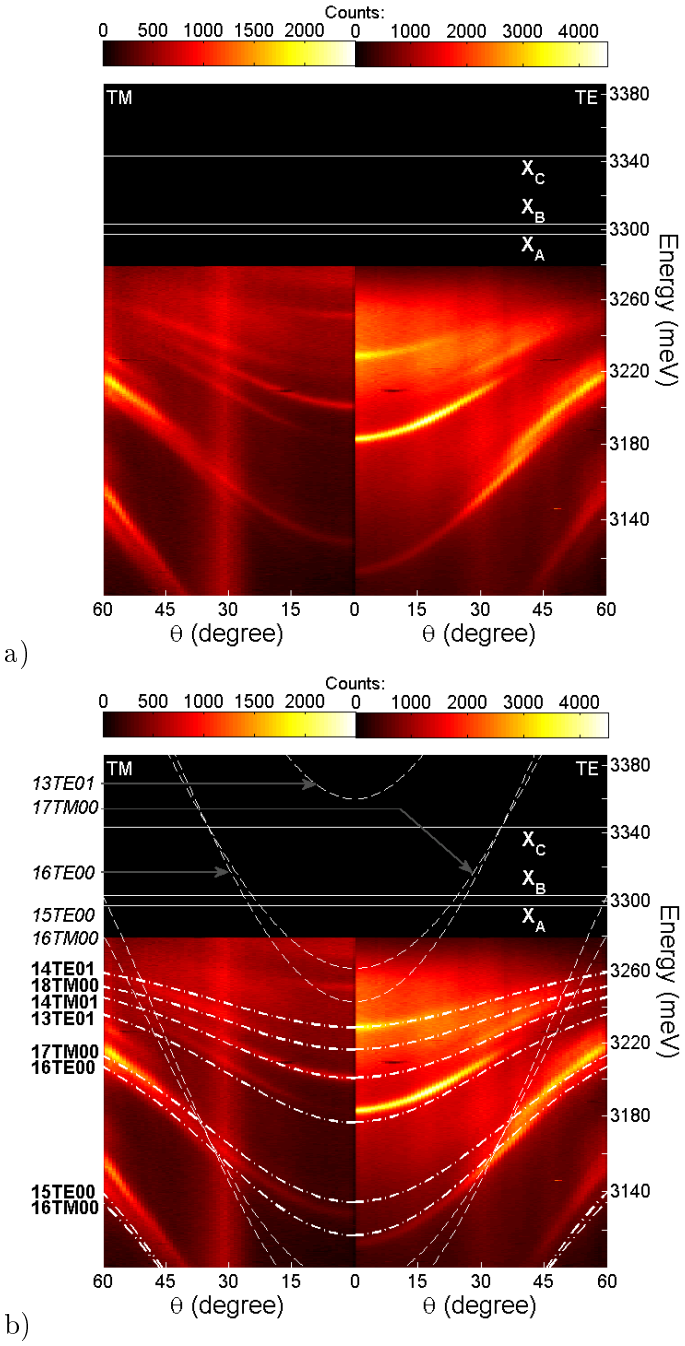

Figure 5.5: a) and b) corresponds to the dispersion measurements in ZnO microwires at room temperature as a function of the angle of emission along the wire. Both figures are split into TM (left panels) and TE (right panels) polarizations. Theoretical fitting is superimposed to experimental data on figure b). Solid, dashed and dot-dashed lines correspond, respectively, to free A, B and C excitons, uncoupled HWGM's and polaritons. The notation 17TM00 stands for the HWGM modes: the first number corresponds to m, the last one to j and TM to the polarization in $k_{\|} \sim 0$.

the radius of the wire (the wire z-axis). Notice that $f_i^{r(z)}$ satisfy the equation $f_i^{r(z)} = 2\hbar\omega_i\hbar\omega_{LT,i}^{r(z)}$ where $\omega_{LT,i}^{r(z)}$ is the longitudinal-transverse splitting of the i^{th} exciton along the radius of the wire (the wire z-axis).

In this model, HWGMs have been approximated by WGM. Indeed, it has been shown numerically (see reference [62] and chapter 2 of this thesis) that WGMs and HWGMs dispersions match by slightly tuning the background reference for WGMs. The correspondence between the radius of the hexagon R_{hex} and the cylinder R_{cyl} has been chosen to have equal surface leading to the formula: $R_{cyl} = R_{hex}\sqrt{3\sqrt{3}/2\pi}$. The electromagnetic field were computed using the Maxwell equations in an anisotropic structure. Indeed, this problem is equivalent to the case of an anisotropic cylinder except that:

- the dielectric function depends on the energy
- a supplementary anisotropy in the dielectric function is added to the problem. Indeed, A and B excitons are included in ϵ_r whereas only C exciton is included in ϵ_z. Therefore, ϵ_r will be increasing close to the A and B exciton energy while ϵ_z will not be really affected at this energy by the C exciton

As shown in reference [56], transverse electromagnetic fields can be directly obtained by knowing its components along the z-axis (ie. the wire axis) in a cylinder structure. In an anisotropic structure, the Maxwell equations for the component of the field along the wire axis are:

$$\text{For TM modes: } \frac{\partial^2 E_z}{\partial z^2}\left(\frac{\epsilon_z}{\epsilon_r} - 1\right) + \Delta E_z + \frac{E^2}{(\hbar c)^2}\epsilon_z E_z = 0$$

$$\text{For TE modes: } \Delta H_z + \frac{E^2}{(\hbar c)^2}\epsilon_r H_z = 0$$

where E_z (H_z) stands for electric (magnetic) component along the z-axis of the electromagnetic field, E is the energy of the photon mode, and $\epsilon_{r(z)}$ is the dielectric function defined by equation 5.3. The solutions of these equations have already been discussed in chapter II and are linear combinations of the cylindrical harmonics. Finally, by applying the continuity of the tangential field components at the cylinder bound to these solutions, we can determine the constants of the problem, derive the polariton dispersion relations and adjust them to the experimental data.

Polariton dispersion along the wire axis: Results

The results of the modeling process is superimposed to experimental data on figure 5.5b) and show a good agreement between theory and experiment. The notation 17TM00 stands for the uncoupled HWGM modes: the first number corresponds to the azimuthal number M, the last one to the radial number j and TM to the polarization in $k_{\|} \sim 0$. The longitudinal-transverse splitting as well as the Rabi splitting extracted from the experiment data are summarized on the table 5.1. The other fitted parameters are:

$$R_{cyl} = 500nm \ , \ \epsilon_{r(z)}^{\infty} = 6.35 \ , \ \gamma_i' = 0meV$$

$$\hbar\omega_A = 3.297eV$$

$$\hbar\omega_B = 3.303eV$$

Units: meV	$\hbar\omega_{LT,A}$	Ω_A	$\hbar\omega_{LT,B}$	Ω_B	$\hbar\omega_{LT,C}$	Ω_C
Along the radius	2.7	133	12.8	290	0	0
Along the wire axis	0	0	0	0	16	327

Table 5.1: Summary of the longitudinal-transverse splitting $\hbar\omega_{LT,i}$ and associated Rabi splitting Ω_i resulting from the fit of the experimental polariton dispersion.

$$\hbar\omega_C = 3.343eV$$

Changing the microwire radius by ± 20 nm would change the mode quantum numbers leading to a new overall fit. From this consideration, the error on the fitted parameters has been estimated to be less than ± 10%. Consequently, the background dielectric function anisotropy, which is of the order few percents, cannot be resolved. $\gamma' = 0meV$ was sufficient to reproduce correctly the experimental data and therefore, has not been taken into account. This fact can be understood, a posteriori, owing to the two orders of magnitude separating the Rabi splitting and polariton linewidth in these structure.

Within the errorbars, a close to bulk Rabi splitting is recovered in these structures. Indeed, the Rabi splitting in the cross-section is given by $\Omega_{E\perp c}^{\mu\text{wire}} = \sqrt{\Omega_A^2 + \Omega_B^2} = 319meV \pm 30meV$ and is compatible with the bulk Rabi splitting $\Omega_{E\perp c}^{bulk} = 288meV$. For the Rabi splitting along the wire, we have: $\Omega_{E\parallel c}^{\mu\text{wire}} = \Omega_C = 327meV \pm 33meV$ which is compatible to the bulk Rabi splitting $\Omega_{E\parallel c} = 288meV$. Linewidth of polariton modes is around 4 meV on figure 5.5. Therefore, the figure of merit (Rabi splitting over linewidth) in this system is 75 at room temperature which is record value at room temperature.

5.2.3 Polariton dispersion perpendicularly to the wire axis: 1D character

Polariton dispersion perpendicularly to the wire axis

Thanks to the 1D Fourier spectroscopy, it is possible to demonstrate the 1D character of these polaritons by studying the polariton dispersion along the angle of emission ϕ around the wire cross-section. Figure 5.6 shows the measured polariton dispersion versus the angle ϕ for $\theta = 0°$ at room temperature on the same sample and at the same position than in figure 5.5. Polariton modes are found to be strictly dispersionless, i.e., strictly monomode in the plane perpendicular to the wire main axis. This is a direct evidence of the one-dimensional (1D) nature of the polaritons investigated in this thesis. Since a hexagon is invariant by rotation of $\Delta\phi = 60°$, the knowledge of $E(\phi)$ over 60° is sufficient to know it over 360°.

Intensity modulation as function of the angle ϕ in the figure 5.6 corresponds to the far-field emission of HWGMs in the strong coupling regime. Since the polariton wavefunction matches the one of the associated photonic modes, the far-field emission corresponds to the far-field emission of the HWGMs described in reference [64]. Because of symmetry considerations, each HWGM is twice degenerated in a traveling clockwise and a counter-clockwise modes. Their wavefunctions are simply connected by the transformation $\phi \to -\phi$. Therefore, their far-field emissions overlap on figure 5.6 creating a complex intensity modulation as a function of the angle ϕ without any clear behavior.

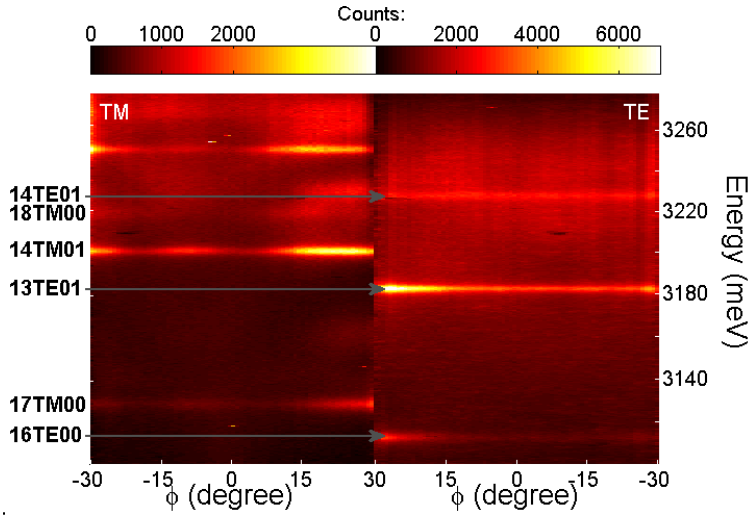

Figure 5.6: Dispersion measurement in ZnO microwires at room temperature as a function of the angle of emission perpendicularly to the wire. The figure is split into TE (left panel) and TM (right panel) polarizations. This measurement has been performed on the same microwire and at the same position than in figure 5.5.

1D density of polariton states

We will now study the density of states of such polaritons in order to emphasize its one-dimensional character. Since the polariton dispersions are flat along the angle ϕ for $\theta = 0°$ (ie. $k_z = 0$), it is reasonable to assume that it is flat along the angle ϕ whatever the value of θ is. Therefore, we will extract the density of states directly from the figure 5.5 assuming no dependency with the ϕ angle.

Experimentally, the density of states is extracted by summing up the modified intensity on figure 5.5 over all the angles of emission θ at a given energy E. It gives a parameter that we will call $\zeta(E)$. First, let us demonstrate that this process allows to obtain the density of states of these polariton states. We have:

$$\zeta(E) = \int_{\theta=-\pi/2}^{\theta=\pi/2} I(E,\theta)\frac{E}{\hbar c}cos(\theta)d\theta \tag{5.4}$$

where $I(E,\theta)$ is the intensity of the polariton state at a given energy E and angle of emission θ given by the figure 5.5. The angle of emission θ is connected to the momentum along the wire axis k by the relation:

$$k = \frac{E}{\hbar c}sin(\theta)$$

Let exchange the variable θ by k in equation 5.4:

$$\zeta(E) = \int_{k=-\infty}^{k=\infty} I(E,k)dk \tag{5.5}$$

$\frac{E}{\hbar c}$ has been approximated by $+\infty$ in equation 5.5 because we focus on the polariton emission close to $k = 0$, ie. in the range angle of emission [-30° ; 30°]. The polariton intensity $I(E, k)$ is given by the following convolution:

$$I(E,k) = \delta(E - E_p(k)) \otimes \mathcal{L}(E) = \mathcal{L}(E - E_p(k))$$

where $E_p(k)$ is the polariton dispersion and $\mathcal{L}(E)$ is the line shape of the polariton state (ie. Lorentzian for example). In equation 5.5, let us now exchange the variable k by E_p. It leads to:

$$\zeta(E) = \int_{E_p=-\infty}^{E_p=\infty} \mathcal{L}(E - E_p) \frac{\partial k}{\partial E_p} dE_p \tag{5.6}$$

The general formula to compute a one-dimensional density of state $\rho(E)$ with only one free degree of freedom k is given by:

$$\rho(E) = \frac{1}{\pi} \left(\frac{\partial E}{\partial k} \right)^{-1}$$

Therefore, we can write:

$$\zeta(E) = \pi \int_{E_p=-\infty}^{E_p=\infty} \mathcal{L}(E - E_p) \rho(E_p) dE_p \tag{5.7}$$

Assuming that the linewidth Γ of $\mathcal{L}(E - E_p)$ is small enough so that $\rho(E_p)$ is constant on Γ, we write:

$$\zeta(E) = \pi \rho(E) \int_{E_p=-\infty}^{E_p=\infty} \mathcal{L}(E - E_p) dE_p$$

Finally, the density of state at a given energy E is given by the relation:

$$\rho(E) = \frac{\zeta(E)}{\pi \mathcal{L}_0}$$

where: $\mathcal{L}_0 = \int_{E_p=-\infty}^{E_p=\infty} \mathcal{L}(E - E_p) dE_p$ is the integral of the polariton lineshape.

Figure 5.7 presents the density of states up to a multiplicative factor of the polariton labeled 13TE01 on figure 5.5 using this method. The blue curve is the usual density of states for a 1D massive particle with a parabolic dispersion and is proportional to $1/\sqrt{E - E_p^0}$. A good agreement is found in the range [3.185 eV - 3.215 eV] comparing to a 2D or 3D density of states (blue dashed lines on figure 5.7). The density of states presented on figure 5.7 clearly support the demonstration of the 1D nature of these polaritons.

5.2.4 Polarization dependency

The polarization dependency, in ZnO microwires in the strong coupling regime, is driven by the strong artificial anisotropy caused by the excitons resonance A and B ($E \perp c$) and C ($E \parallel c$). For the modes 13TE01 and 14TM01 on figure 5.5, these considerations result in a polarization switching as a function of the angle of emission θ.

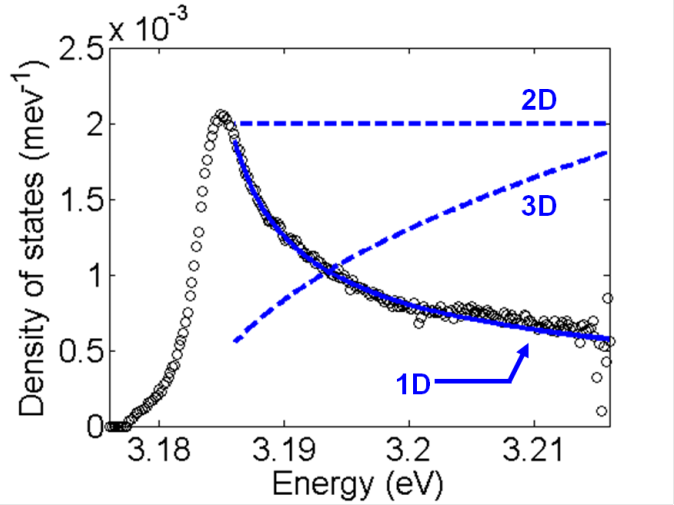

Figure 5.7: Density of states up to a multiplicative factor of the polariton labeled 13TE01 on figure 5.5. The blue line corresponds the the density of states for a 1D massive particle with a parabolic dispersion. Dashed blue lines corresponds to the 2D and 3D density of states

The absolute dielectric function is represented on figure 5.8 using the parameters extracted from the dispersion fits at room temperature (figure 5.5 a)). The dielectric function in the cross-section of the wire (along the wire) takes into account the A and B excitons (C exciton). Close to the A and B resonances, for example, an important difference between the dielectric functions ϵ_r and ϵ_z appears resulting in an important energy dependent birefringence. The differential dielectric function $\Delta\epsilon = \epsilon_r - \epsilon_z$ is represented on the panel b) of figure 5.8. A large mismatch between ϵ_r and ϵ_z is indeed evidenced on this figure. It results in a birefringence which modifies the polariton polarization dependency as a function of the energy (and therefore, as a function of the angle of emission) compared to the uncoupled WGM model developed in chapter II.

The angular dependence of the polarization degree in the strong coupling regime is highly non-trivial. Therefore, we have used the same model than in subsection 5.2.2 in order to compute the theoretical polarization degree. The HWGM has been approximated by WGM in a cylinder. Figure 5.9 displays the angular θ dependency of the polarization degree of two polariton modes (called 14TM01 and 13TE01 on figure 5.5). Polarization degree is defined by:

$$\rho = \frac{I_{TM} - I_{TE}}{I_{TM} + I_{TE}}$$

where I_{TM} (I_{TE}) is the polarization intensity in the TM (TE) polarization.

At angle $\theta = 0°$, both modes are pure either TM or TE. The most striking feature is the change in the polarization observed with increasing emission angle θ. The 13TE01 (14TM01) mode at $\theta = 0°$ completely switches to TM (TE) mode at θ 40 ($\theta = 30$). This polarization switching is mainly due to the strong coupling regime. Indeed, because of the strong energy dependent birefringence, the cavity mode is mixed with every exciton states simultaneously. It is satisfactorily reproduced by the model in the strong coupling (solid lines in figure 5.9) for the TE mode but not for the TM mode. In fact, a complete agreement on this point is more difficult to achieve for two reasons:

- The polarization mixing is sensitive to the geometry of the system (this model assumes a circular and not hexagonal cavity). Indeed, as we have seen in chapter II, the eigenstates

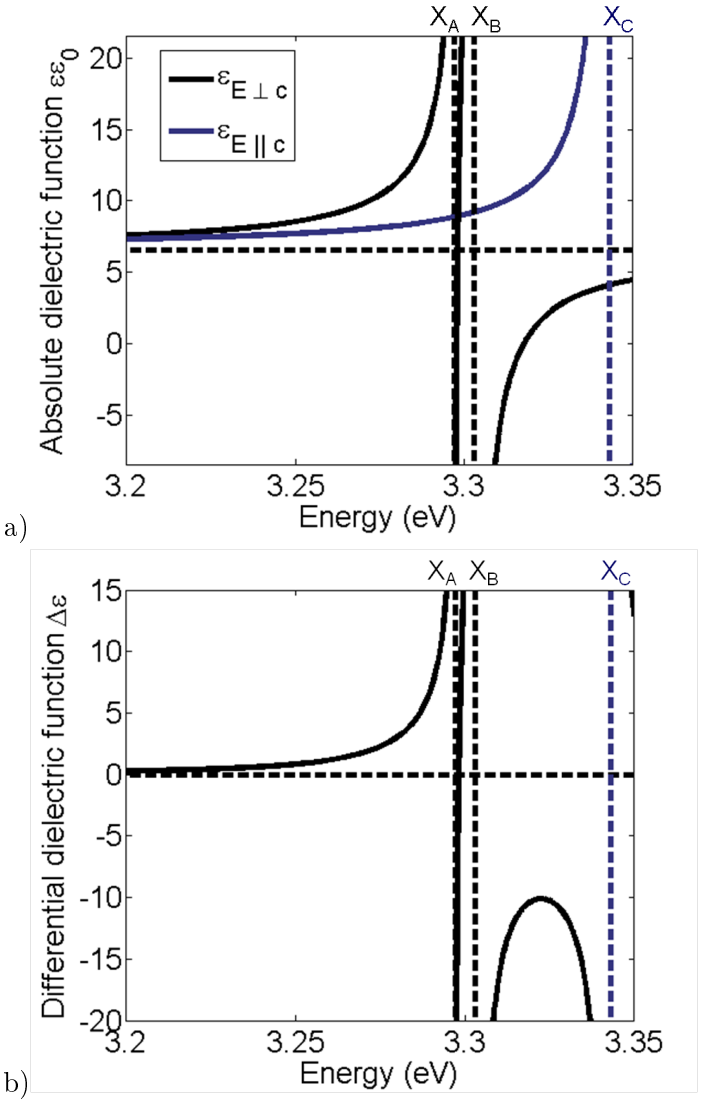

Figure 5.8: a) Absolute dielectric function in the cross-section of the wire (black line) and along the wire axis (blue line). Horizontal dashed line is the background dielectric function. b) Differential dielectric function $\Delta\epsilon = \epsilon_r - \epsilon_z$. Horizontal dashed line corresponds to a zero differential dielectric function. On panel a) and b), the vertical dashed lines correspond to the exciton energy A,B and C.

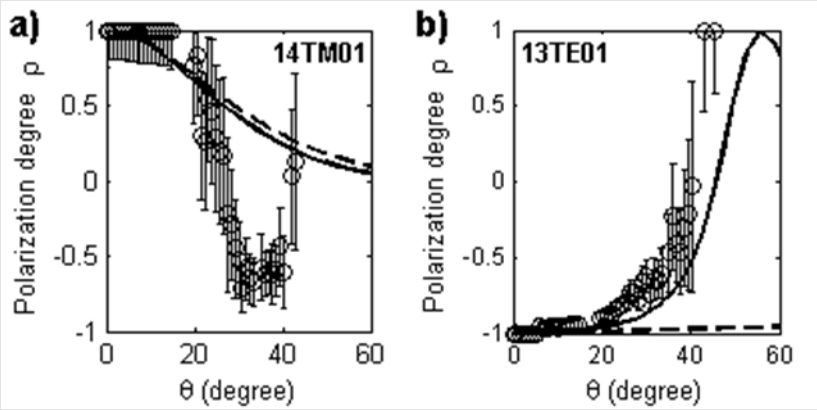

Figure 5.9: Angular θ dependence of the polarization degree of modes a) 14TM01 and b) 13TE01. Open symbols are the measurements, solid and dashed lines are the calculations for polariton modes and bare (uncoupled) optical WGMs, respectively.

in a wire with a hexagonal cross-section can be expressed as a linear combination of the eigenstates of a cylinder. As shown in reference [62], about 10 cylinder harmonics have to be taken into account to define a given HWGM. As a consequence, the modification caused by the strong coupling regime on the polarization can be important. This is relevant especially for TM modes because the electric field for TM mode has a large component parallel and perpendicular to the wire axis at non-zero angle θ.

- The weak TM (TE) components of B (C) excitons have been neglected. B (C) exciton has a small (below 1 meV) longitudinal-transverse splitting along the wire axis (in the cross-section of the wire)[91]. Therefore, they can induce an additional modification of the polariton polarization degree as a function of the angle θ.

5.3 Comparison with GaN microwires

With ZnO microwires, the hope for electrical injection of polaritons is very little since p-doping technology of ZnO is not mature and well-controlled yet. On the other hand, n/p-doping of nitrides is much more developed and polariton lasing [92] at room temperature have been realized with microcavities based on nitrides. However, electrical injection within microcavities is a challenging task: free carriers must reach the quantum wells placed at the heart of the structure, i.e. in the cavity layer. This requires the fabrication of p and n doped Bragg mirrors or advanced etching technique. In addition, large bandgap microcavities have intrinsic drawbacks for operation in the strong coupling regime at room temperature like e.g. a low Rabi splitting in spite of large exciton oscillator strength. This is due to the large fraction of the electromagnetic field contained in the Bragg mirrors, and to the presence of large polarization and piezo electric-fields at every heterointerfaces that reduces the exciton oscillator strength by quantum-confined Stark effect [93].

In order to overcome these problems, we will investigate a new strategy based on GaN microwires. Indeed, they constitute a very interesting alternative for electrical injection compared to microcavities or ZnO microwires. Unlike ZnO, Nitrides-based microwires can be nowadays designed into p-i-n diodes for electrical injection [94, 95]. Moreover, the growth and nanofabrication of this material is technologically more mature, thus more complex structures with

embedded quantum wells or quantum-dots in the strongly coupled microwire can be envisaged on a short-term. Therefore, reaching the strong coupling regime in GaN microwires is of high interest.

In this section, we will present a study performed on GaN microwires to demonstrate the strong coupling regime. First, we will discuss the growth of these structures. The result is a GaN microwire with a hexagonal cross-section (such as ZnO microwires) with a doped segment whereas the rest of the wire is undoped. Then, using 1D Fourier spectroscopy, the strong coupling regime will be characterized. Finally, an interesting transition from strong to weak coupling regime between the doped and undoped segment of the wire will be evidenced.

5.3.1 Growth of GaN microwires

GaN microwires have been grown by MOVPE on c-plane sapphire substrates by our collaborators in the CRHEA laboratory: Blandine Alloing and Jesus Zuniga Perez. In order to promote the vertical growth along <0001> , and after a nucleation step in which truncated GaN pyramids are formed, silane is injected into the reactor during the first 30 min of the growth together with NH3 and TMGa [96]. As a result, the first half of the microwire is highly n-doped. Then, silane injection is stopped so that the upper part of the wire is nominally undoped. During this step, the TMGa to NH3 ratio (i.e. the V/III ratio) is much larger than that conventionally used for two-dimensional growth. This growth procedure results in a transition layer, 1 to 2 micrometer thick, at the interface between the doped and undoped segments of the wire (see figure 5.10 a) and b) z=40µm to z=42µm). The microwires thus obtained feature 2 to 10 micrometers in diameter and 20 to 40 micrometers in length. As shown in figure 5.10, a low photonic disorder has been reached over 10 µm. In all cases, the wurtzite GaN c-axis coincides with the wire longitudinal axis (referred to in this thesis as z).

5.3.2 Spatially resolved photoluminescence on a single GaN microwire

Figure 5.10 b) presents a spatially resolved photoluminescence experiment at 10K. The most striking feature is the ensemble of spectrally narrow bent stripes separated by a few tens of meV from each other and visible over the whole length of the wire. In the upper part of the wire (22µm<z<41µm) which is nominally undoped, they correspond to HWGMs in the strong coupling regime with the free excitons (the peaks on figure 5.10 c), black line) as will be discussed below. A weak contribution of A and B exciton (3482.5meV and 3487.5meV) can also be seen in this region (figure 5.10 c) gray line). In the lower part of the wire (z>41µm), it is heavily n-doped with a rough estimate of the concentration of $n\ 1 - 2.10^{20} cm^{-3}$ based on the high energy edge (at 3555 meV) of the photoluminescence which exceeds by 45mev the exciton energy of undoped GaN [97]. In this region we show that the HWGMs are in the weak coupling regime.

5.3.3 Strong coupling characteristics of the undoped segment of GaN microwires

Firstly, in order to demonstrate the strong coupling regime like in the previous section for ZnO microwires, we measured the angular dispersion of the emission of several HWGMs in the undoped segment of a single microwire. We chose to work with large wire diameters (3-7 microns) for two reasons: first, the larger the diameter, the higher the quality factor of the HWGM at a given energy [64]; second, the low free spectral range $\Delta = E_{m+1} - E_m$ between two consecutive HWGM, of 23.5 meV, provides us with about 20 well separated HWGMs within a detection

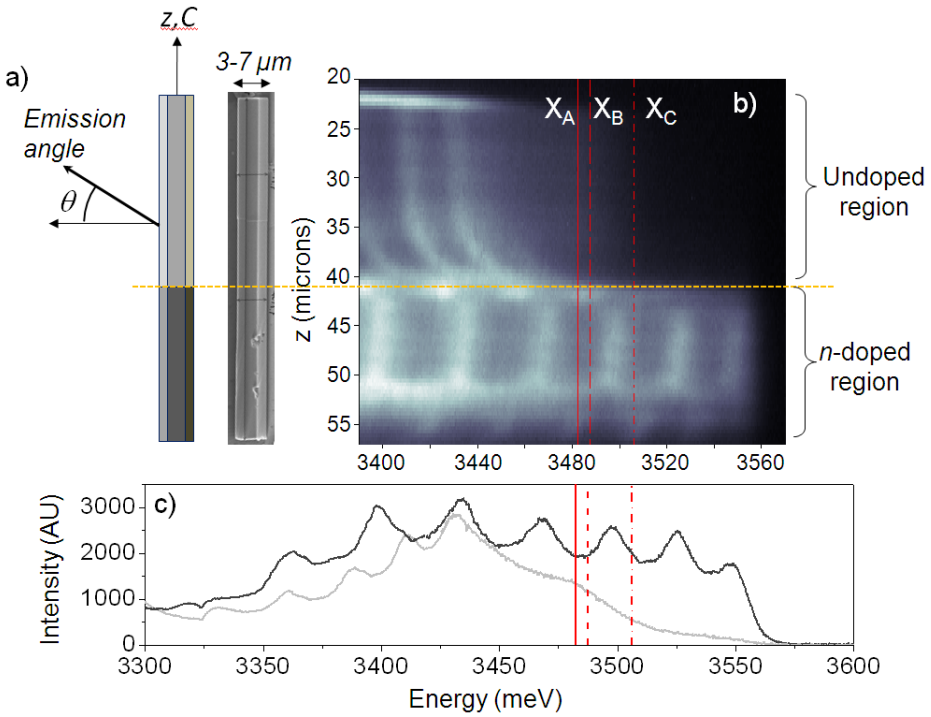

Figure 5.10: a) Schematic representation of a GaN microwire. The dark grey region represents the n-doped segment and the light gray one represents the undoped segment. Next to it is shown a typical SEM micrograph of a GaN microwire. b) micro-photoluminescence spectrum (photon energy on the horizontal axis, PL intensity is color scaled) versus position on the microwire (vertical axis z) in the near band edge region of GaN at T=10K. The bright bent lines are whispering gallery modes in the strong (undoped region, i.e. z=22µm to z=40µm) and weak coupling regime (doped region, i.e. z=42µm to z=51µm) depending on the position z. The exciton levels of undoped GaN at T=10K are indicated by the red vertical lines. c) Emission spectra obtained from slices of measurement b) taken at z=31µm (light gray solid line, undoped segment) and z=47µm (black solid line, doped segment).

spectral window of [3100,3500] meV. As in ZnO, there are three excitons involved in the light matter interaction called A,B and C in the range 3480 meV to 3500 meV at 4K.

The results are shown on the upper panels of figures 5.11 and 5.12 for temperatures of 10K and 300K respectively. In this measurement only TE-polarized emission is detected (ie. $E \perp c$). As in ZnO microwires, another family of polaritons is observed for TM-polarization, with a larger contribution of the C exciton to the oscillator strength, a lower one from A and B, and a similar overall Rabi splitting. But due to poor thermal population of the C exciton, we found that the TM-polariton luminescence was too dim to be exploited quantitatively.

TE-polarized luminescence shows several well-resolved dispersion branches with decreasing curvature from low (figure 5.11 c) bottom) to high (figure 5.11 a), top) emission energy. Such a curvature change versus energy is a characteristic feature of the strong coupling regime between exciton levels and HWGMs in the microwire, leading to 1-dimensional exciton-polaritons. To confirm this interpretation, in section 5.3.4, we check experimentally that upon switching off the excitonic oscillator strength using the doped region of the microwire, the strong coupling also switches off.

Another striking feature is the spectral sharpness of these modes: the uncoupled region of the spectra (lowest energy) reveals a quality factor of the HWGMs between 600 and 700. Note that this value is a lower bound only since the measured linewidth is not always homogeneous. Indeed, on top of (and sometime superimposed to) the brightest HWGMs, dimmer ones are visible (mostly figure 5.12) with different energy spacing, which result possibly from a non-perfectly hexagonal cross-section.

Method to determine the exciton-photon coupling regime in a single GaN microwire

The model used for GaN microwires is the same than the model used for ZnO microwires at low temperature. Actually, since the diameter is larger ($\sim 3\mu m$), HWGMs will have large azimuthal number m (above 100). Therefore, the HWGM energy equation in the ray-light representation 2.5 reproduces properly the HWGM energy and a wave model is not necessary from this point of view. Therefore, in the specific case of GaN microwires, it is possible to extract the Rabi splitting and to reproduce the spectral position of the polariton modes. Again, we will focus in the range [-30° ; 30°] for the angle of emission where we do not need to take into account the oscillator strenght mixing at high angle (ie. above 30°) caused by the artificial birefringence.

The exciton energies and oscillator strenght are well documented in the literature [98, 99, 100] and are summarize on table 5.2 for 5K and 300K.

Results and discussion on the exciton-photon coupling regime in a single microwire

We applied this method to the measurements shown in figures 5.11 and 5.12 (upper panels, for the undoped region). The extracted α, n_∞ and Rabi splitting are summarized in table 5.2: a large background index $n_\infty = 3.1$ is found, and an overlap integral α of which deviation from 1 is contained within the error bars. This background index is larger than 2.6 usually found in the literature in the near-UV [98, 99]. Likely contribution to this deviation could be residual electron doping (density not measured) as well as the significant overlap of the HWGM with a large density of deep electronic levels (contained within the bandgap) located at the surface of the wire [101]. Note that the determination of the background index is realized using the lowest energy HWGMs, which are negligibly affected by the excitons oscillator strength. Owing to the form of equation 5.1 a large uncertainty on the background index has no impact on the uncertainty of the Rabi splitting.

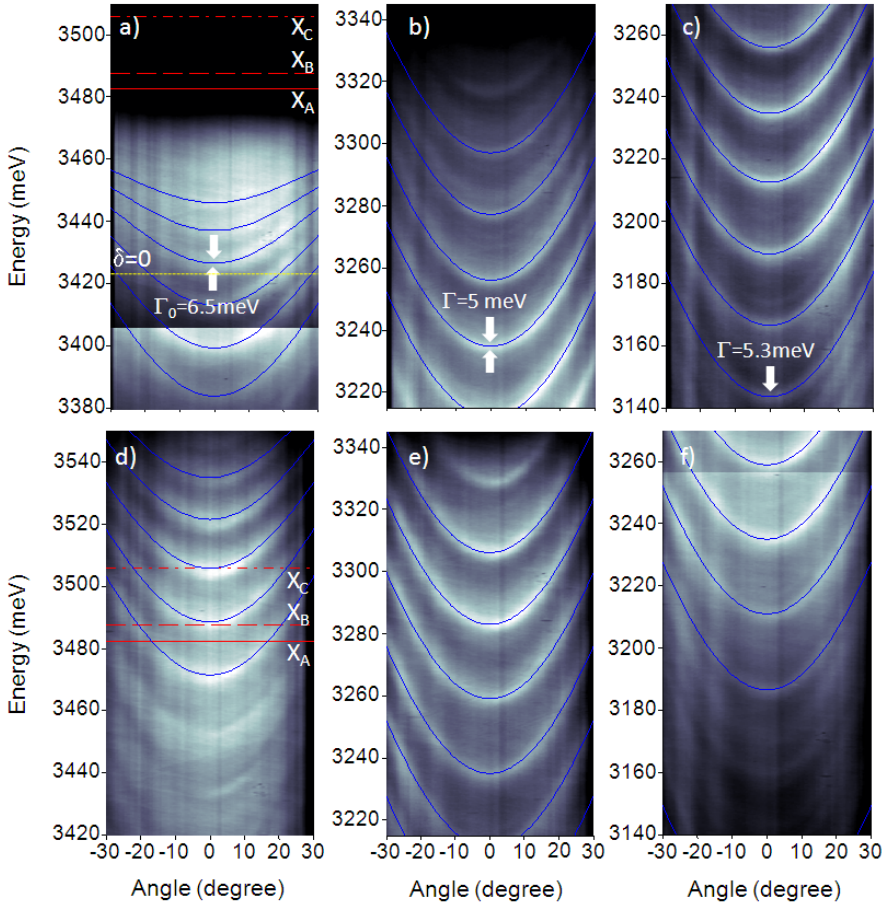

Figure 5.11: Measured TE-polarized photoluminescence intensity (color scale) of the undoped (upper panels a, b and c) and heavily n-doped (lower panels d, e and f) segment of the wire at T=10K with angular (x-axis) and spectral (y-axis) resolution.The free exciton energies labeled X_A, X_B and X_C are indicated as straight red lines (solid, dashed and dot-dashed respectively). The blue solid lines are the calculated dispersion branches. The contrast of the color scale has been sometime adjusted within the same image in order to maximize the visibility of the dispersion branches. In a) the energy corresponding to polaritons with zero detuning between excitons and uncoupled HWGM is indicated by the yellow dashed line. The linewidth Γ of selected modes is indicated in panel b) and c)

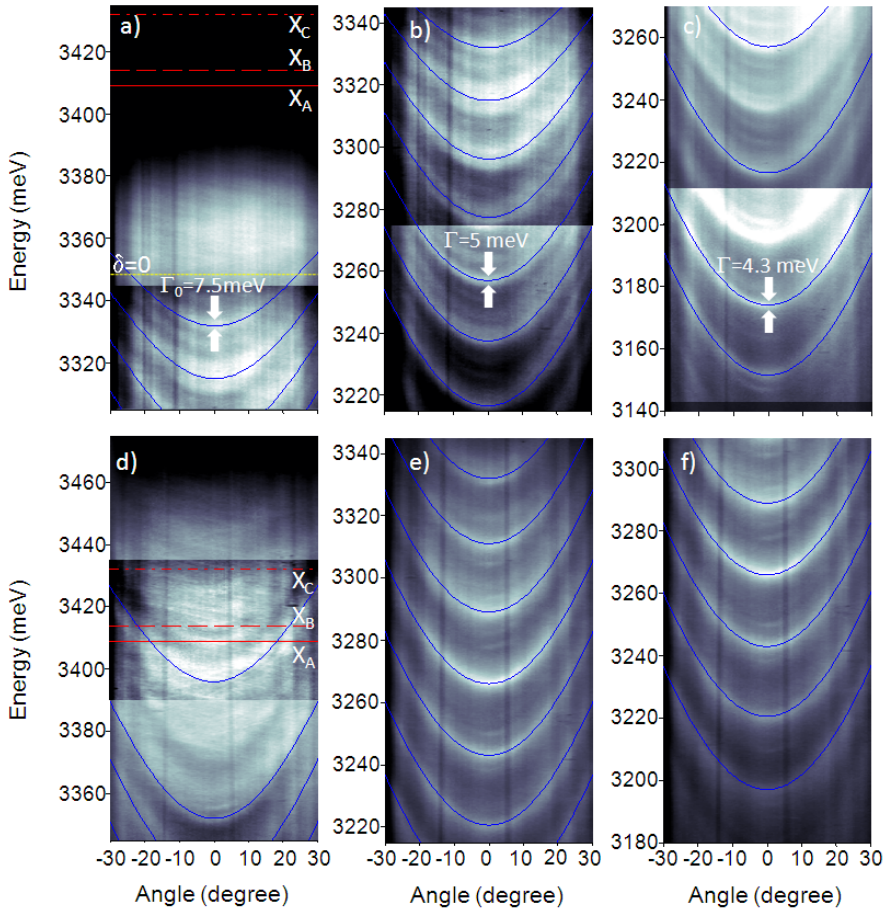

Figure 5.12: Like figure 5.11 but at room temperature. The measurements have been done on the same microwire as that of figure 5.11

T(K)	E_{XA} (meV)	Ω_A (meV)	E_{XB} (meV)	Ω_B (meV)	E_{XC} (meV)	Ω_C (meV)
5	3482.5	90	3487.5	78	3506	37
300	3409	90	3414	78	3432	37

T(K)	n_∞	α	Ω (meV)	Γ_0 (meV)
5	3.1±0.1	1±0.1	125±13	6.5±1
300	3.1±0.1	1±0.3	125±50	7.5±1

Table 5.2: Exciton energies (E_{Xi}) and Rabi splittings (Ω_i) used in this calculation are those found elsewhere for weakly strained bulk GaN [98, 99, 100] at T=10K and room temperature. α is the normalized spatial overlap integral and n_∞ is the background index. The resulting overall Rabi splitting Ω, and the measured linewidth Γ_0 of the polariton branch around zero detuning are given in bold characters.

The large value of α is the first main result since it demonstrates unambiguously the strong coupling regime at 10K and 300K. It leads to an overall Rabi splitting of $\Omega = 125meV \pm 13meV$ at 10K, and $\Omega = 125meV \pm 50meV$ at room temperature. The linewidth Γ_0 of the mode at $\theta = 0°$ (cf. figure 5.11 a) at T=10K and figure 5.12 a) at room temperature) is fitted with a Lorentz lineshape by carefully removing the background emission, for which we have taken advantage of the fact that this emission is not angle dependent. We find $\Gamma_0 = 6.5meV \pm 1meV$ at T=10K and $\Gamma_0 = 7.5meV \pm 1meV$ at room temperature. Finally, comparing Γ_0 and Ω at low and room temperatures shows unambiguously that the strong coupling regime is achieved in both cases with a conservative estimate of the figure of merit (defined as the ratio between Rabi splitting and polariton linewidth) of 20 at 10K and 15 at room temperature.

Like in ZnO microwires, the very fact that each polariton branch is well separated from the neighbouring ones in energy indicates that every branch is associated to a single transverse mode with k_z as only degree of freedom. As a result polaritons in these GaN microwires also have a one-dimensional character.

The thus obtained dielectric functions normalized by the background constant ϵ_∞ (to get rid of the large uncertainty on the background index measurement which contributes only as a scaling factor to the dielectric function), are plotted 5.13 c) and d), together with the experimental points obtained from the curvature of each polariton modes. The shape of this normalized dielectric function depends only on the regime of coupling with the excitons: in the strong coupling regime, we observe as expected a strong divergence of $\frac{\epsilon(E)}{\epsilon_\infty}$ upon approaching the exciton energy (figure 5.13 c) and d), undoped segment). While when the exciton levels are suppressed, the dielectric function is not perturbed at this energy (figure 5.13 c) and d), doped region).

Interestingly, with this method one can verify a posteriori that the uncoupled HWGMs are equally spaced in energy by $\Delta = 23.5 \pm 0.3meV$ (cf. figure 5.13 a) and b), hollow circles plots). In the limit of modes of large angular momentum m this equal spacing is in agreement with a wire of hexagonal cross-section given by equation 2.5. Δ is then simply connected with the radius of the microwire and the background index by the relation $\Delta = \frac{hc}{6n_\infty R}$, where R is the small radius of the hexagon. $R = 2.7$µm is found in agreement with the micro-PL pictures.

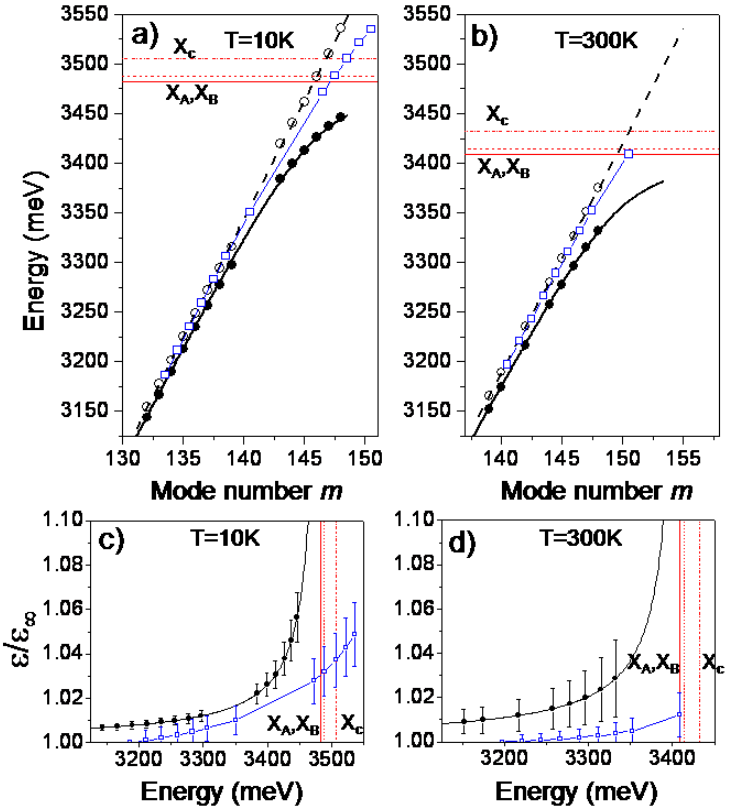

Figure 5.13: Measured polariton energy at $\theta = 0°$ (black filled circles) at T=10K (a) and room temperature (b) versus azimuthal number in the undoped segment. The black hollow circles are the calculated uncoupled HWGMs energy in the undoped segment. Blue hollow squares are the HWGMs energy at $\theta = 0°$ obtained in the doped segment. The black dashed line is a linear fit of the uncoupled HWGMs energy which provides a free spectral range of $\Delta = 23.5 \pm 0.3 meV$. The black solid line is the calculated polariton energy at $\theta = 0°$, assuming that the corresponding uncoupled HWGMs are equally spaced in energy by Δ. The exciton levels A, B and C are indicated with red lines. Lower panels show the measured and fitted (using equation 5.2 and the parameters listed table 5.2) values of the dielectric function in the undoped (black filled circles and black line respectively) at 10K (c) and room temperature (d). Hollow blue squares are values of the dielectric function obtained in the doped region (the first data points have been arbitrarily normalized to one).

5.3.4 Switching off of the strong coupling regime due to Moss-Burstein effect: spectroscopy of a heavily doped segment of a GaN microwire

We will know focus on the doped segment of the GaN microwires. Heavy n-doping is an interesting situation in the context of the strong coupling regime between exciton and photon because of its effect on the excitons: upon increasing the free charges density, exciton oscillator strength decreases and gets spectrally broader. At large doping level, like in the present case, bound electron-hole states do not exist anymore. Instead, correlated many-electrons plus one-hole states are present (sometime called "Mahan exciton" or "Fermi edge singularity") which exhibit a strongly reduced oscillator strength as compared to that of exciton in the undoped case, but slightly enhanced with respect to uncorrelated electron-hole recombination in the doped case [102, 103]. Far beyond the Mott transition, these states have a recombination energy largely blueshifted with respect to the undoped band to band transition. Indeed in this regime, the bandgap renormalization (redshift due to Coulomb interaction between free electrons) is dominated by Moss-Burstein effect (conduction band filling).

In the case of GaN microwires, in the n-doped region of the wire, we observe a high energy edge of photoluminescence 45meV above the free excitons energies of undoped GaN (see figure 5.10, right panel). This behavior is consistent with the aforementioned regime of very large doping density. Indeed the high energy photoluminescence (between 3480meV and 3560meV) results from the recombination between a photogenerated hole and any electron between the conduction band edge and the Fermi energy. This mechanism involves non k-conserving recombinations which are allowed in the degenerate regime due to break-up of the single electron excitations picture [104]. The important point in the context of this work is that in this regime, the excitonic levels with the energy and oscillator strength characteristic of undoped GaN are completely suppressed, i.e. the strong coupling regime between excitons and HWGMs is switched off.

We performed angle-resolved spectroscopy of the same microwire studied in the previous section, but this time on the heavily n-doped segment to measure how the strong coupling regime is affected by the suppression of the excitonic transitions. The results are shown on the lower panels of figures 5.11 and 5.12. Well-resolved dispersion branches of HWGMs are observed. Their linewidth is as narrow as that of the undoped segment, i.e. in the 5 meV range. This is true even for modes lying above the energy of the undoped GaN exciton. Indeed, no absorption induced broadening is expected [103] in heavily n-doped GaN.

Regarding the shape of the dispersion branches, their curvature in the vicinity of the band edge is much less flattened than in the undoped region. Using equation 5.1, we could fit each dispersion branch independently (blue solid lines in figures 5.11 and 5.12 lower panels) and thus determine the dielectric function in this region in order to compare it with the one obtained in the strong coupling regime (figure 5.13 c) and d) hollow blue squares). In this regime, the divergence at the exciton energy has disappeared and a slowly increasing behavior is observed instead, likely due to onset of absorption at the energy of the transition from the Valence band to the Fermi level in the renormalized conduction band [103].

Note that in n-doped (electron densities up to $10^{20} cm^{-3}$) bulk GaN a broad resonance with slightly enhanced oscillator strength (with respect to the band-to-band transition) has been already reported and attributed to Fermi edge singularity [103]. The latter could possibly participate in the gentle increase of the dielectric function that we observe at high energy.

Assuming that the diameter of the wire is the same in both doped and undoped regions of the wire (as is the case on the SEM micrograph of figure 5.10), we also plotted the modes energy versus mode number in order to directly visualize that the anti-crossing of HWGMs with exciton levels is lost, i.e. the HWGMs in this region are in the weak coupling regime with the microwires

electronic excitations. The direct comparison of both doped and undoped region of the same microwire is the second main result observed in these structures. Everything else being identical, one can observe directly how removing the excitonic transition results in switching off the (very) strong coupling regime with the HWGMs.

Chapter 6

Quenching of the polariton/LO phonon interaction at room temperature

Contents

In the previous chapter, we have seen that the strong coupling regime is achieved at room temperature with a high figure of merit (~75) in ZnO microwires. Linewidth of these polaritons are surprisingly low as compared to the bare exciton broadening in ZnO at room temperature (full width at half maximum $\sim 40meV$).

The goal of this chapter is to characterize and understand this small polariton linewidth at room temperature with respect to the exciton broadening. First, we will discuss in details the expected linewidth of these polaritons at room temperature using a simple two oscillators model. We will show that this model fails to predict properly the polariton linewidth in ZnO microwires. Then, we will extract the thermal contribution to this linewidth in studying the temperature dependency of the polariton modes. Finally, we will explain, with a simple physical picture and, then, with a modeling using the Fermi golden rule, the quenching of the polariton/LO phonon interaction in these structures. This effect has an important impact for the study of polaritons in the quantum degenerate regime at room temperature since it allows to obtain polariton linewidth at room temperature identical to the low temperature ones.

6.1 Failure of the damped coupled oscillators model

At first glance, the polariton mode linewidth (FWHM around 4 meV on figure 6.2 right panel) at room temperature seems to be relatively low compared to the bare exciton broadening (FWHM around ~40meV).

The temperature dependency of ZnO excitons has been extensively studied by Klingshirn [46]. Figure 6.1 presents the temperature dependency of the exciton broadening (taken from reference

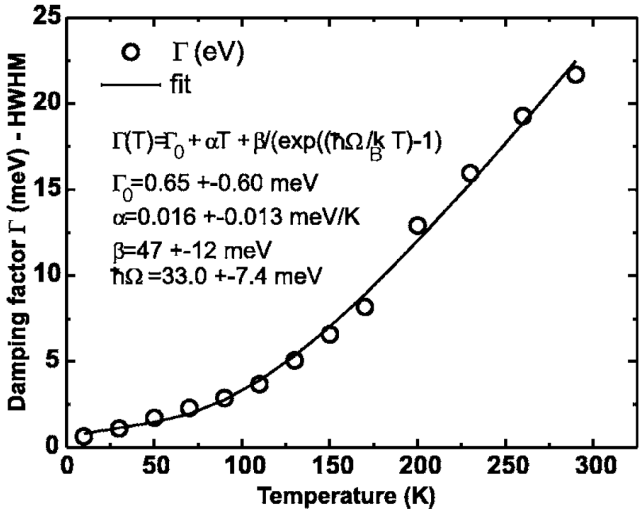

Figure 6.1: The temperature dependence of the broadening (half width at half maximum) of the A and B exciton resonance of ZnO. Taken from reference [46]

[46]). In this reference, it is well reproduced using a linewidth dependency versus temperature given by:

$$\Gamma(T) = \Gamma_0 + \alpha T + \frac{\beta}{exp(\frac{\hbar E_{LO}}{k_b T}) - 1}$$

where Γ_0 is the linewidth (half width at half maximum) at 0K, α is the contribution of the acoustic phonons and β is the average coupling strength with every optical phonon modes with an effective phonon energy $\hbar E_{LO}$ which is an average of all optical phonons from 12.5 meV to 73.3 meV. Numerical values of these parameters are given on figure 6.1. Close to 0K, the broadening $\Gamma_0 = 0.65meV$ [46] may have contribution from inhomogeneity in the structure studied. The exciton broadening (half width at half maximum) ranges from 0.65 meV to 20 meV between 0K and 300K.

A relevant quantity to predict the polariton mode linewidth is the excitonic fraction of the considered polariton mode at room temperature (ie. the Hopfield coefficient[28] defined in chapter 1). In the coupled oscillators model, it reads:

$$|X|^2 = \frac{\Omega^2}{\Omega^2 + (2\Delta)^2}$$

where Ω is the Rabi splitting and $\Delta = E_X - E_p$ is the energy difference between the exciton state and the polariton mode of interest. For example, we have $|X|^2 = 1/2$ for a polariton mode at an energy $E_p = E_X - \Omega/2$. Left panel of figure 6.2 is the calculated excitonic fraction for TE polariton modes with respect to the energy axis of the right panel using parameters extracted from the dispersion fitting (see chapter 4). In this expression, only one exciton resonance has been assumed (called $X_{A/B}$) which gathers all the oscillator strength ($\Omega = 300meV$) owing to the small splitting between A and B exciton compared to the Rabi splitting. As a result, the excitonic fraction of such polariton modes is quite high (above 35% in this energy range). The highest energy TE polariton mode has an excitonic fraction exceeding 80% at $\theta = 0°$.

Let us consider $I_X(E, \Gamma_X)$ and $I_\gamma(E, \Gamma_\gamma)$ respectively, the emission spectra of uncoupled exciton and photon, with homogeneous linewidths Γ_X and Γ_γ. In a naive coupled oscillators

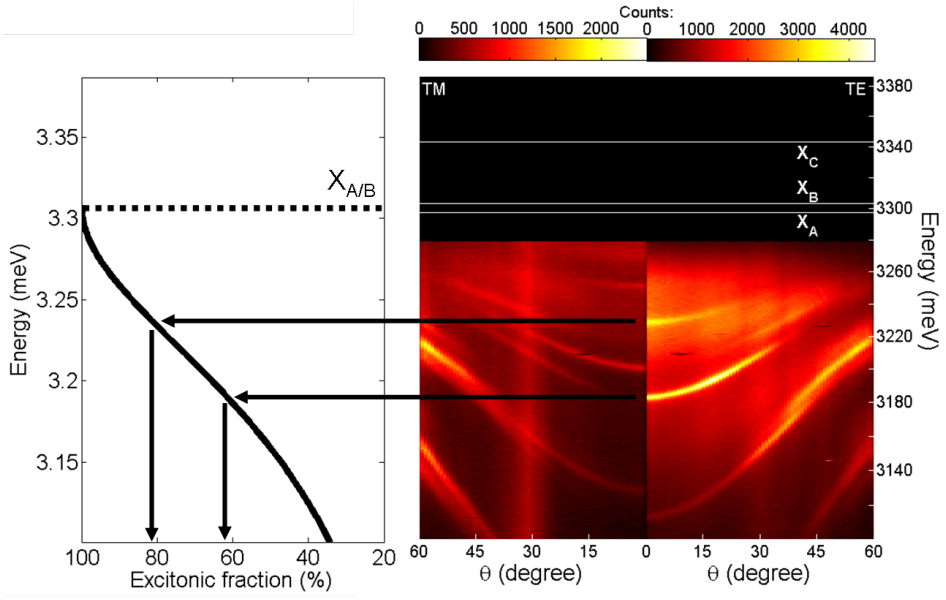

Figure 6.2: Right panel: Dispersion measurements in ZnO microwires at room temperature as a function of the angle of emission along the wire. Both figures are split into TE (left panel) and TM (right panel) polarizations. It is the same figure than figure 5.5 a). Left panel: Calculated fraction with the same energy axis using parameter extracted from dispersion fitting. $X_{A/B}$ stands for the A/B exciton resonances

model, the polariton spectrum $I_p(E,\Gamma_p)$ is given by the convolution of the lineshapes of the exciton and the photon [105]. The linewidth of each oscillator is weighted by its contribution to the polariton state (ie. $|X|^2$ for the exciton state and $|\gamma|^2$ for the photon state). It leads to:

$$I_p(E,\Gamma_p) = I_X(E,|X|^2\Gamma_X) \otimes I_\gamma(E,|\gamma|^2\Gamma_\gamma) \tag{6.1}$$

In the case of polaritons in ZnO microwires at room temperature, it is reasonable to consider a homogenous broadening for both the exciton (owing to exciton-phonon scattering) and the photon (owing to photon escape) resulting in Lorentzian lineshapes. Therefore, the polariton mode linewidth extracted from equation 6.1 is simply the average value of the bare exciton linewidth and the photon linewidth:

$$\Gamma_p = |X|^2\Gamma_X + |\gamma|^2\Gamma_\gamma \tag{6.2}$$

Let us overestimate the Quality factor of our structure in equation 6.2 and set $\Gamma_\gamma = 0meV$. In this ideal case, the polariton mode linewidth is limited only by the excitonic linewidth, ie. $\Gamma_p = 32meV$ (FWHM) for the highest energy polariton mode of figure 6.2 in TE polarization at 3.23eV. Even in overestimating the quality factor in these structures, it is not possible to reproduce properly the polariton mode linewidth of 4meV with such a high excitonic content using a standard coupled oscillators model. Now that the "smaller than normal" linewidth problem is set, we will explain how such a small linewidth is possible in these structures.

6.2 Temperature dependency of the angle resolved photoluminescence

It is interesting to decrease the exciton broadening (by decreasing the lattice temperature) in order to separate the thermal contribution to the polariton mode linewidth from the photonic contribution. Moreover, in TE polarization on figure 6.2, there is no polariton mode emission in the range $[E_X\ E_X - 70meV]$ while we have already seen bright emissions of polariton modes emission in this range at low temperature (see figure 5.3). In any case, if the excitonic broadening decreases, one should expect to see polariton modes appearing in this region close to the excitonic transition.

General features Angle resolved photoluminescence for various temperatures ranging from 10K to 218K is shown in figure 6.3. In the panels of figure 6.3, the energy axes are offset in order to always focus in the spectral range $[E_X, E_X - E_{LO}]$ whatever the temperature is. At low temperature, the photoluminescence is dominated by the bound exciton complexes emission which vanishes above 70K because of its low localization energy (~16meV).

Let us now focus on polariton modes versus temperature. First of all, the exciton photon detuning (ie. $\delta = E_\gamma - E_X$) increases for increasing temperatures resulting in a spectral shift of the polariton states towards the exciton energy. As a result, the excitonic fraction every polariton modes in figure 6.3 increases as well. It results in a decrease of the curvature of the polariton dispersions for increasing temperatures. This is clearly visible in figure 6.3 for the the lowest energy TE polarized polariton mode while the polariton modes at higher energy are affected in a lesser extent because of their higher excitonic content (above 88%).

Absence of TM polarized polariton branches at low temperature At low temperature (see figure 6.3 for T=10K and T=49K), we observe that TM polarized polariton branches are not populated whereas the excitation energy was tuned far above the band gap (ie. HeCd laser: 3.815eV/325nm). The reason is the following: since the spectral separation between the A/B excitons and the C exciton is $45meV$, the C exciton cannot be thermally populated at low temperature (ie. below $\sim 130K$ on figure 6.3). As we will see in details in chapter 8, polariton modes are mainly filled via the LO phonon replica of the excitons in the linear regime. Moreover, we have measured the polarization degree of the LO phonon replica of the A/B excitons to be superior to 90% in the TE polarization. As a consequence, TM polarized polariton modes cannot be filled efficiently at low temperature because the C exciton is not populated. On the other hand, TE polarized polariton branches are filled via the LO phonon replica of the A/B excitons even at low temperature. In figure 6.3, TM polarized polariton modes are clearly populated only above 131K which is consistent with a thermal population of the C exciton (ie. $kT \sim 11meV$ at 131K corresponding to a boltzmann factor of 1.7%) as well as an enhancement of the probability to thermally populate the C exciton caused by the increase of the exciton linewidth.

Well-resolved polariton modes with exceedingly high excitonic fraction up to 99.98% One of the main results of figure 6.3 is the presence of highly excitonic polariton modes at low temperature. Indeed, on figure 6.4, which is a zoom on the range [3.3eV ; 3.387eV] of the panel $T = 49K$ of figure 6.3, there is a polariton mode 10 meV below the excitonic resonance with a shallow, but unambiguous, curvature. It is even clearer on figure 6.3 for T=81K, where the bound excitons emission has vanished. In this figure, the emission of three well-defined polariton modes is observed (two TE polarized and one dim TM polarized) around 3351 meV (ie. 24 meV

below A exciton energy) with linewidths about 2 meV and excitonic fractions ranging from 96% to 98% for the TE polarized ones.

Polariton modes with high excitonic content are spectrally narrow enough thanks to the low excitonic linewidth and the large Rabi splitting. In our case, the low excitonic linewidth arises from the bulk character of the microwires. From the polariton mode linewidth on figure 6.3, we can infer that the pure excitonic linewidth, including its inhomogeneous and homogenous component, is smaller than $1meV$. This value is smaller than that reported in ZnO-based microcavities (from 5 to 15 meV, see chapter 3) where the ZnO layer is deteriorated because of its amorphous substrate. With such a low excitonic linewidth, it is possible to spectrally resolve polariton modes which are as close as $2meV$ below the exciton energy such as polariton mode 1 on figure 7.1 in chapter 7. This polariton mode has an excitonic fraction up to 99.98%. It is possible to set a criterion to observe polariton branches with an excitonic fraction up to 99%. It requires that the Rabi splitting over the excitonic linewidth ratio is larger than 40, ie.: $\Omega/\Gamma_X > 40$. This criterion is greatly satisfied for ZnO microwires at low temperature, ie. $\Omega/\Gamma_X \sim 300$. As this criterion does not take into account motional narrowing or effects such as the quenching of the polariton/LO phonon interaction which are lowering the polariton mode linewidth, this criterion is a sufficient condition to observe polariton branches with excitonic fraction up to 99%.

From the photonic point of view, it is possible to observe highly excitonic polariton modes even with a low quality factor in ZnO microwires. Indeed, for a polariton mode made up of 90% of excitons in a cavity with a quality factor of 50, the polariton mode linewidth is about $8meV$. Again, since effects such as motional narrowing or quenching of the polariton/LO phonon interaction has been neglected, this value is a maximum value of the polariton mode linewidth.

Thermal broadening: two sets of polariton modes in ZnO microwires Interestingly, the three polariton modes around 3351 meV on figure 6.3 vanish at T=220K whereas the linewidth of the lowest energy polariton mode on figure 6.3 is hardly affected by the increase of the temperature despite its high excitonic content (ie. $\sim 53\%$). We can conclude that there are two kinds of polariton modes in ZnO microwires: those which are affected by the phonon population (ie. which emission depends on the lattice temperature) and those which are isolated from this bath. In the following section, we will see that this effect is well understood in terms of quenching of the polariton/LO and acoustic phonon interaction for polaritons with energy below the first LO phonon replica.

6.3 Quenching of the LO phonon interaction

6.3.1 Simple physical picture

As explained in reference [106], when the phonon contribution to the polariton mode linewidth (thermal contribution) needs to be considered, this crude assumption is, in general, incorrect because the exciton-photon interaction dominates in general over the exciton phonon by one order of magnitude. In ZnO microwires, it is the case, even at room temperature because of the large Rabi splitting ($\sim 300meV$). Then, the correct physical picture to account for the thermal contribution to the polariton mode linewidth is scattering between polaritons and phonons: phonon interaction is then a perturbation to the polariton picture. At low temperature (ie. $kT \ll E_{LO}$ where E_{LO} is the LO phonon energy), the optical phonons are not populated and only the interaction of polaritons with acoustic phonons has to be taken into account. On the other hand, at room temperature, there is a non-negligible population of LO phonons ($kT \sim 26meV$ to be compared to $E_{LO} = 72meV$. Consequently, the interaction between polariton and the thermal

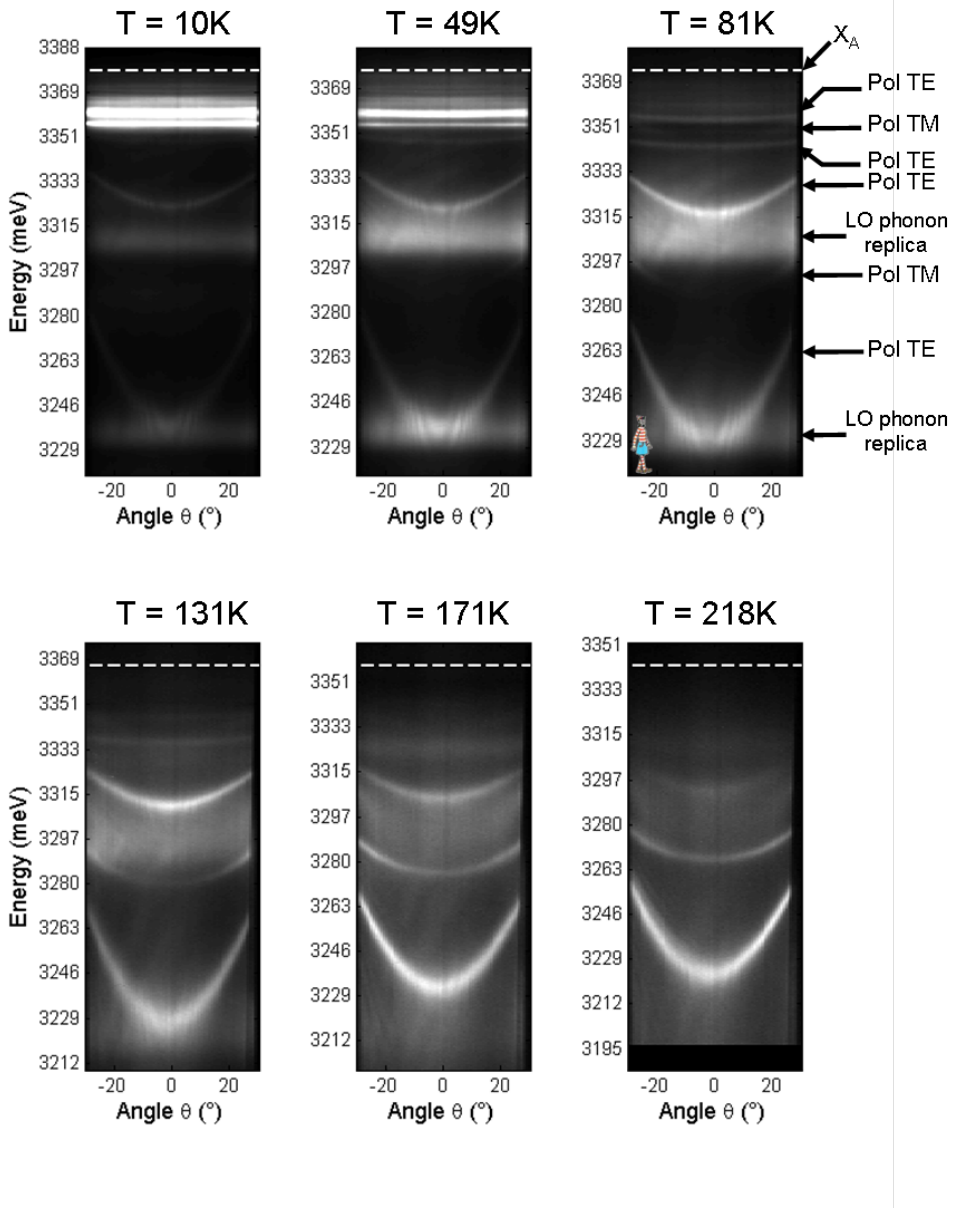

Figure 6.3: Temperature dependency of the angle resolved photoluminescence (grey scale) in the range [10K 218K]. The temperature is given at the top of each image. X_A stands for the A exciton energy (white dashed line). Pol TE (TM) corresponds to TE (TM) polarized polariton mode.

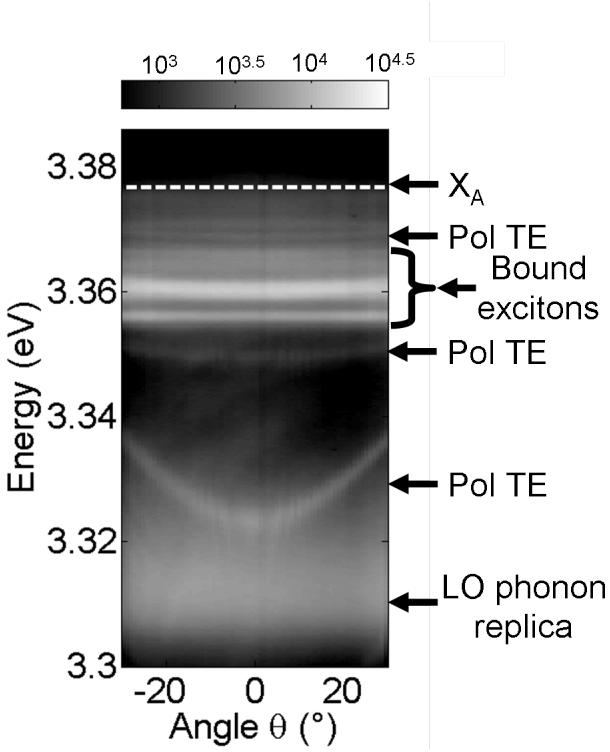

Figure 6.4: This figure is a zoom on the range [3.3eV ; 3.387eV] of the panel $T = 49K$ of figure 6.3 in a logaritmic grey scale.

bath of LO phonons cannot be neglected. Low-temperature experiments with microcavities have already shown that the polariton/phonon interaction was leading to a significant reduction of the polariton scattering with acoustic phonons [107] compared to a coupled oscillators model.

We will now qualitatively explain the contribution of the LO phonon-polariton interaction to the polariton mode linewidth. In ZnO, the LO phonon mode that has the strongest interaction with the excitons is that at 72.6 meV [29]. Let us consider two polariton branches as drawn on figure 6.5. In the top (bottom) panel, the polariton energy E_p at zero momentum is in the range $[E_X - E_{LO}, E_X]$ ($[0, E_X - E_{LO}]$). Two scattering mechanisms are considered:

For the top panel of figure 6.5:
$$Polariton(E_p, k) + LOphonon(72meV, q) \Downarrow Exciton(E_p + 72meV, k + q)$$

For the bottom panel of figure 6.5:
$$Polariton(E_p, k) + LOphonon(72meV, q) \Downarrow Polariton(E_p + 72meV, k + q)$$

Since the LO phonon dispersion is almost flat, the final state can have a large momentum and match with any polaritons or exciton states at the energy $E_p + E_{LO}$. As a consequence, polariton modes in the range $[E_X - E_{LO}, E_X]$ (top panel of figure 6.5) can scatter toward any exciton states in the reservoir whereas polariton modes in the range $[0, E_X - E_{LO}]$ can scatter only toward polariton states. According to the Fermi golden rule, the scattering probability directly depends on the finale density of states. Since the lower polariton branch density of states is four orders of magnitude lower than that of bare excitons, polariton modes in the

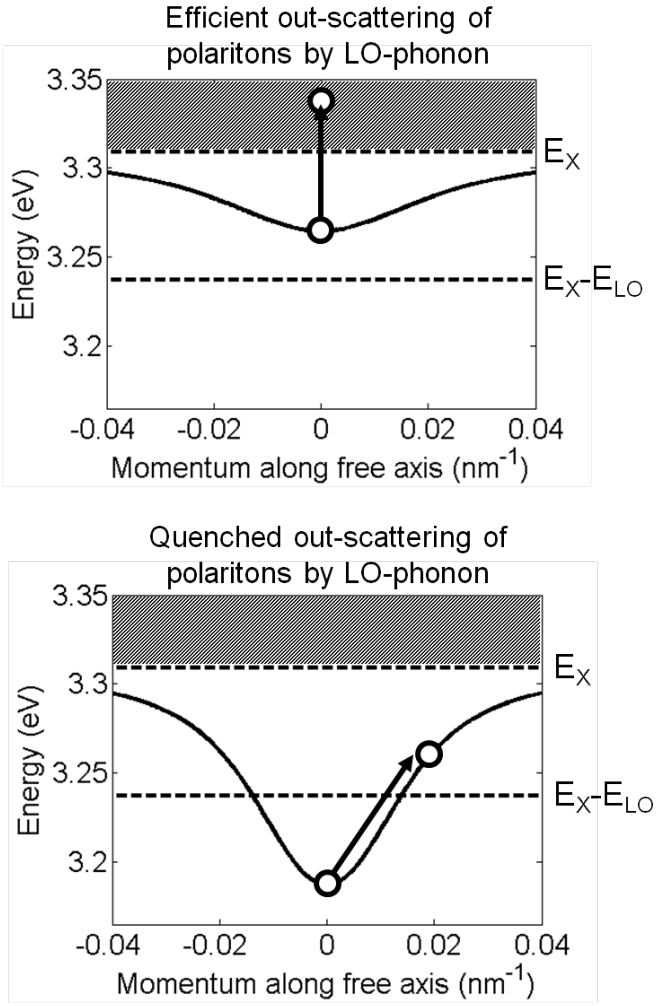

Figure 6.5: Simple physical representation of the LO phonon interaction quenching.

range $[0, E_X - E_{LO}]$ are much less affected by the phonon interaction compared to those in the range $[E_X - E_{LO}, E_X]$. Naturally, this effect is temperature dependent. At low temperature ($k_B T \sim 1meV$ for example), LO phonons with an energy of 72 meV are not populated and none of the polariton modes presented on figure 6.5 are affected by LO phonon interaction. On the contrary, at high temperature ($k_B T \sim 26meV$ for example), the LO phonons states are populated and polariton modes in the range $[E_X - E_{LO}, E_X]$ are affected by the LO phonon interaction because of the high exciton density of states. At room temperature, the LO phonon interaction is quenched below the energy $E_X - E_{LO}$ resulting in a much smaller thermal contribution to the linewidth compared to the range $[E_X - E_{LO}, E_X]$.

6.3.2 LO phonon interaction as a perturbation to the strong coupling: Fermi-golden rule

To get a better understanding of this effect, we use the Fermi "golden rule" to compute the 1D polariton scattering rate Γ with acoustic and optical phonons [108]. An important assumption can be made: because the polariton density of states is four orders of magnitude lower than that of bare excitons, the scattering rate from one polariton branch to another one can be neglected

as compared to the scattering of polaritons toward bare exciton reservoir. In this limit, the scattering rate of polariton modes of energy E_{LP} with thermal phonons reads:

$$\Gamma(E_{LP}) = \Gamma_{ac}(E_{LP}) + \Gamma_{LO}(E_{LP}) \tag{6.3}$$

where $\Gamma_{ac}(E_{LP})$ ($\Gamma_{LO}(E_{LP})$) is the scattering rate of polariton modes of energy E_{LP} with acoustic (LO) phonons. Using the Fermi "golden rule", it reads:

$$\Gamma_{ac}(E_{LP}) = \pi V |X(E_{LP})|^2 \int d^3\boldsymbol{q}(2\pi)^{-3} N(\boldsymbol{q}) |M_{ac}(\boldsymbol{q})|^2 \delta(E_{LP} - E_X(\boldsymbol{q}) + E_{ac}(\boldsymbol{q}))$$

$$\Gamma_{LO}(E_{LP}) = \pi V |X(E_{LP})|^2 \int d^3\boldsymbol{q}(2\pi)^{-3} N(\boldsymbol{q}) |M_{LO}(\boldsymbol{q})|^2 \delta(E_{LP} - E_X(\boldsymbol{q}) + E_{LO})$$

$|X(E_{LP})|^2$ is the excitonic fraction of the considered polariton state, V is a quantization volume, $\boldsymbol{q}$, $E_{ac}(\boldsymbol{q})$ and E_{LO} are the phonon momentum and energies, respectively, and $M_{ac(LO)}(\boldsymbol{q})$ are the matrix element for exciton and acoustic phonon (optical LO phonon) interaction. The polariton momentum is negligible as compared to $\boldsymbol{q}$. The phonons are assumed to be at thermal equilibrium, thus following a Bose distribution $N(\boldsymbol{q})$ at the lattice temperature. The results of this calculation are shown in figures 6.6 (a) and (b) as red solid lines for temperatures of 70 K (figure 6.6 (a)) and 300 K (figure 6.6 (b)), respectively.

At low temperature, only low-energy acoustic phonons are populated and the LO-phonon population is negligible. Since the strength of the exciton-acoustic phonon interaction is much smaller than the one of the exciton-LO phonon interaction, the polariton-phonon scattering induces a low thermal broadening over the range of polariton mode energy (the red plot in figure 6.6 (a)). At room temperature, thermal broadening increases dramatically, but only for polariton modes contained within the energy range $\Delta = [E_X, E_X - E_{LO}]$ ($E_{LO} = 72meV$), while those at lower energy remain virtually unaffected regardless of their excitonic fraction (the red plot in figure 6.6 (b)). The reason is as follows: At room temperature, polariton modes of which energy is contained within Δ can undergo scattering with a thermal LO phonon and end up in the pure excitonic states of the reservoir at large momenta. This is a very efficient process because of the large exciton–LO-phonon matrix elements and because of the very high density of states of pure exciton states. A second kink is visible on this plot (figure 6.6 (b), red plot at $\sim 3290meV$), which is owing to the contribution of acoustic phonons in this energy range. For polariton states of energy lower than $E_X - E_{LO}$, LO-phonon (and a fortiori acoustic-phonon) energy is too low to scatter a polariton to the pure exciton states of large momentum. Instead, the scattering can end up only in the polariton states, a process strongly weakened as compared to the previous one owing to the very low density of polariton states.

We have verified this effect experimentally. To do so, we have analyzed the temperature dependence of polariton emission in a tapered microwire. This tapered shape allows tuning of the polariton mode energies along the wire axis. The results are shown on figure 6.6. The black-and-white images in figures 6.6 (a) and (b) are the PL intensity plots (gray scale) obtained at 70 and 300 K, respectively, with spatial resolution (abscissa) and spectral resolution (ordinate), of a segment of microwire 30 µm long. At 70 K, sharp polariton modes are visible within the energy range Δ (modes S3, S4, and S5) as well as below Δ (modes S1 and S2). Their curved shape is owing to the tapered shape of the microwire: the diameter increases from left to right. At 300 K, however, polariton modes S3, S4, and S5 as well as the part of the S2 mode where energy falls within Δ (corresponding to positions L $<$ 34 µm along the wire axis) are completely

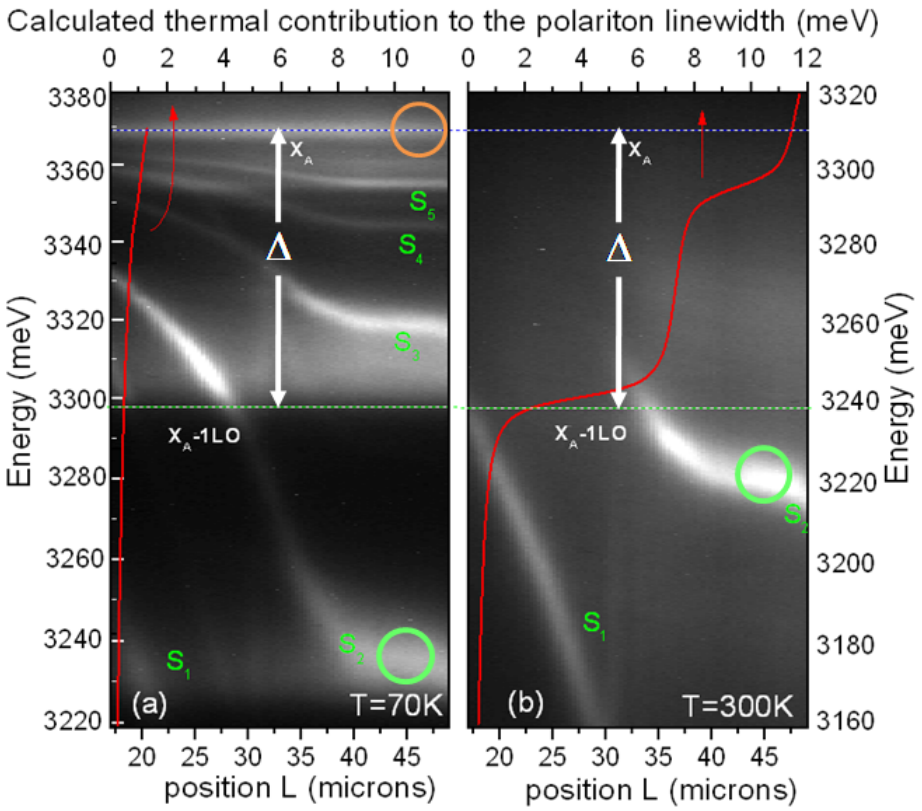

Figure 6.6: Spatially resolved TE-polarized emission spectrum along a 32 µm segment of a tapered microwire at temperature (a) T = 70 K and (b) T = 300 K. Along this portion of the microwire, the inhomogeneous diameter (presently increasing from left to right) provides a natural way to continuously vary the exciton-photon detuning. S1–S5 label the five visible polariton modes at 70 K. The $\Delta = (E_X, E_X - E_{LO})$ energy range is shown by the white arrows. Red solid lines show the calculation of the phonon contribution to the polariton linewidth vs energy.

washed out by phonon damping (figure 6.6 (b)). On the other hand, the part of the S2 mode where energy is lower than Δ (positions L $>$ 34 µm) remains unaffected, showing that phonon damping is strongly suppressed below Δ.

A more direct and quantitative demonstration of this effect is obtained by performing a measurement of the polariton linewidth versus temperature. To do so, a polariton mode of energy situated directly below Δ (mode S2 at L=40µm, green circle in figure 6.6 (a)) is chosen. It is angle resolved to look at the homogeneous linewidth at $k_z = 0$. For the sake of comparison, the linewidth of free exciton A is also measured (same position, L = 40 µm, white circle in figure 6.6 (a)). The results are shown on figures 6.7 (a) and (b). For temperatures increasing from 10 to 300 K, the linewidth of polariton mode S2 stays fixed at 8 meV. At 10 K, this value corresponds uniquely to the HWGM damping contribution Γ_p. Upon increasing temperature, this contribution decreases slightly owing to the change of excitonic fraction (from 30% to 47%), and can be calculated. It is shown by the blue dashed plot of figure 6.7 (b). Thus, the thermal contribution to the polariton mode linewidth is the difference between the dashed blue plot and the total linewidth (red plot): It does not exceed 3 meV at 300 K. This result is particularly striking when one considers the excitonic fraction of this mode, 47% at 300 K. For comparison, the thermal contribution to the bare exciton linewidth (6.7 (c)] amounts to 9meV, already at 120 K. It becomes too broad at larger temperatures to be measured properly.

This model fairly reproduces TE polarized polariton modes. Figure 6.8 presents the polarization degree (ie. $\rho = \frac{I_{TE}-I_{TM}}{I_{TE}+I_{TM}}$) at room temperature, spatially resolved on the same microwire than figure 6.6. As already shown, the energy cut-off to undergo the quenching of the LO phonon interaction corresponds to the energy $X_A - 1LO$ for TE emission. For TM emission, we should expect a cut-off 45 meV above the TE one since the C exciton is 45 meV above the A and B excitons. However, this cut-off is at an energy slightly lower than the energy $X_C - 1LO$. Actually, this difference is explained by the weak TM component of the A/B excitons. Indeed, at large wavevectors, A/B excitons turn to TM polarization and it is possible for TM polarized polariton mode to scatter towards these states by absorbing a LO phonon. Finally, TM polarized polariton modes can survive at slightly higher energy than TE ones with a cut-off in between $X_A - 1LO$ and $X_C - 1LO$.

Since we have understood the main contributions to the polariton linewidth, we can properly extract the quality factor of HWGMs from figure 6.2 at room temperature, using the following relation for the polariton linewidth Γ_p with a photonic fraction $|\gamma|^2$:

$$\Gamma_p = |\gamma|^2 \Gamma_\gamma + \Gamma_p^{ph}$$

where Γ_p^{ph} is the thermal broadening due to interaction between polaritons and the phonon bath (given by equation 6.3) and Γ_γ is the photonic linewidth. It gives $\Gamma_\gamma = 5meV$ and a quality factor of 600 for this microwire.

In principle, the quenching of the LO phonon interaction can be observed on any structures exhibiting strong coupling regime. However, in ZnO microwires, owing to the large Rabi splitting compared to the LO phonon energy, quenching of the LO phonon interaction appears for polaritons with a significant excitonic fraction up to 80%. From these considerations, a general criterion can be drawn: a polariton with 50% excitonic fraction is isolated from thermal phonon damping if falf of the normal mode splitting exceeds the LO phonon energy:

$$\frac{\hbar\Omega}{2} > E_{LO}$$

In practice, this criterion is difficult to meet, considering the large LO phonon energy in most

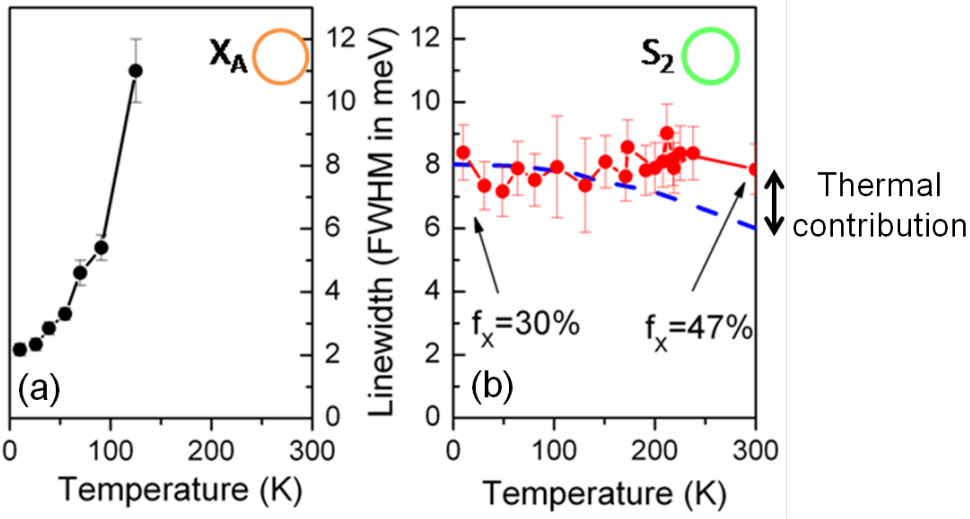

Figure 6.7: (a) Pure exciton linewidth vs temperature (energy and position shown by the orange circle in figure 6.6 (a)). (b) Measured homogeneous linewidth of polariton mode S2 vs temperature (red round symbols), when its energy lies below Δ. The dashed blue line plots the photon-escape contribution to the linewidth (100% contribution to the linewidth at 10 K). The homogeneous linewidths are obtained from angle-resolved measurement carried out in a region centered on L = 43 µm (green circles in figures 6.6 (a) and (b)).

semiconductors as compared to the Rabi splitting usually achieved in microcavities. In ZnO microwires, this criterion is met, thanks to the very large oscillator strength combined with the microwire geometry that provides a large Rabi splitting.

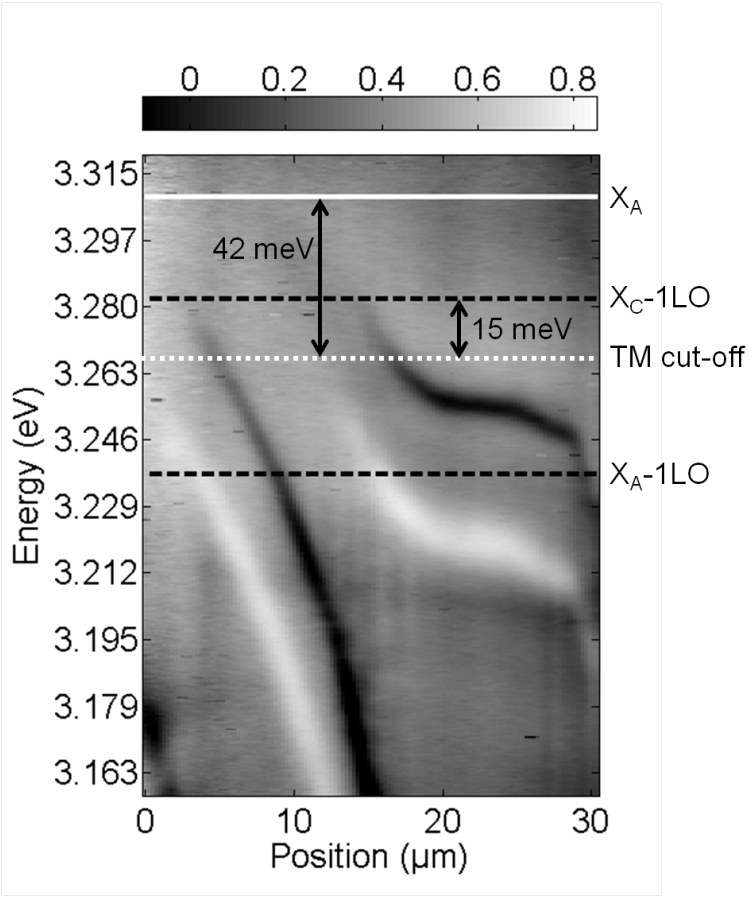

Figure 6.8: Spatially resolved polarization degree (grey scale) of the photoluminescence on the same tapered microwire than figure 6.6 at room temperature. White (black) corresponds to TE (TM) emission. $X_A - 1LO$ is the cut-off energy for TE polariton modes to undergo quenching of the LO phonon interaction. Using experimental criterion, the cut-off for TM polarized polariton modes is given by the white dashed line (called "TM cut-off")

Part III

Non-linear properties of 1D polaritons in ZnO microwires

Chapter 7

Stimulated relaxation of 1D polaritons at low temperature

Contents

In the part II, we have demonstrated that the polaritons in ZnO microwires exhibit a large Rabi splitting $\Omega = 300meV$ at room temperature. Moreover, the polaritons situated in the range $[0\ E_X - E_{LO}]$ are not affected by the interaction with the LO phonons and feature almost the same linewidth than at low temperature. Therefore, these polaritons are interesting candidates to obtain the quantum degeneracy regime at room temperature.

A non-linear emission in ZnO microwires has been observed at room temperature by the team of our collaborator professor Zhanghai Chen [109]. They have reported indications for polaritons lasing using a nanosecond pulsed laser with a very high peak power. However, this laser has a low repetition rate ($f = 10Hz$, ie. 10 pulses per second) and, therefore, generates an emission with a low signal to noise ratio. Moreover, it is difficult to couple with a time-resolved detector. Although this result is convincing, the conservation of the strong coupling regime remains ambiguous.

In order to observe polariton lasing regime unambiguously, we choose to study the stimulated relaxation of polaritons in ZnO microwires at low temperature because it has a much lower threshold. Indeed, at room temperature, because of the quenching of the LO phonon interaction, the excitons from the reservoir have to release at least 72 meV (ie. the LO phonon energy) to scatter from the exciton states towards the polariton states. On the other hand, at low

temperature, there are plenty of polariton modes closer to the excitonic reservoir (ie. even 2 meV below the exciton energy). In this regime, an original regime of polariton lasing with an exceedingly high excitonic fraction is observed.

In this chapter, we will present the experimental facts describing the polariton lasing we have observed in ZnO microwires at low temperature. Firstly, we will discuss the general behavior of the power dependency of the polaritons photoluminescence up to the quantum degeneracy regime as well as the consequences of the high excitonic character (up to 97%) of these states. Then, we will enter into the details of the polariton lasing regime in order to demonstrate that:

- there is a macroscopic occupancy of the polariton state by studying the power dependency of the intensity of the light emitted by the polariton state
- there is an increase of the coherence time in the system
- the strong coupling regime is preserved above the threshold

7.1 General features of the polariton lasing with a high excitonic content in ZnO microwires at low temperature

7.1.1 Introduction of the polariton lasing regime in ZnO microwires at low temperatures

Before presenting the detailed features of the polariton lasing in a single ZnO microwire at low temperature, we should briefly discuss the photoluminescence spectrum below and then above the lasing threshold. Figure 7.1 presents the spatially resolved photoluminescence of a single ZnO microwire at 40K. A logarithmic color scale has been used to compare simply the different components of this spectrum. Below the A and B excitons energies, we can observe the bound exciton complexes at 3.36 eV and 3.363 eV as well as the emission of the polariton modes, numbered from 1 to 5. As shown on the bottom panel of figure 7.1, the microwire diameter is increasing from the positions x=0 µm to x=7 µm, it is almost constant from the positions x=7 µm to x=10µm and decreases from x=10 µm to x=12 µm. Since the energy of the HWGMs is inversely proportional to the radius of the wire, the energy of the resulting polariton mode will increase for decreasing wire radius.

In order to reach the polariton lasing regime, we have measured the photoluminescence of the microwire already described on the figure 7.1 at various pulsed excitation power. The position and the spot size of the laser is tuned to shine a region of the microwire with a constant radius (see figure 7.1). We choose to study the spatially resolved photoluminescence instead of the angular resolved experiment. Indeed, the photonic disorder (ie. caused by the radius gradient) tends to localized the polaritons. Therefore, the photoluminescence in the momentum space is drastically sensitive to the position along the wire of the laser. To overcome this difficulty, we choose to collect the light intensity emitted by a polariton state at a given position rather than at a given momentum along the wire axis. This method has a drawback: we cannot access the polariton distribution in the momentum space to describe its thermalization for example.

Figure 7.2 represents the spatially resolved photoluminescence along the same microwire than figure 7.1 for three different excitation powers (from left to right on figure 7.2: $0.8\%P_{Th}$, $7\%P_{Th}$ and $160\%P_{Th}$) where P_{Th} is the threshold power of the polariton lasing regime. We observe that the intensity of the polariton 4 (numbered on figure 7.1) for increasing pumping power dominates all the other components of the spectrum above the threshold pumping power P_{Th} due to the lasing non-linearity. This polariton state is situated 16 meV below the A exciton

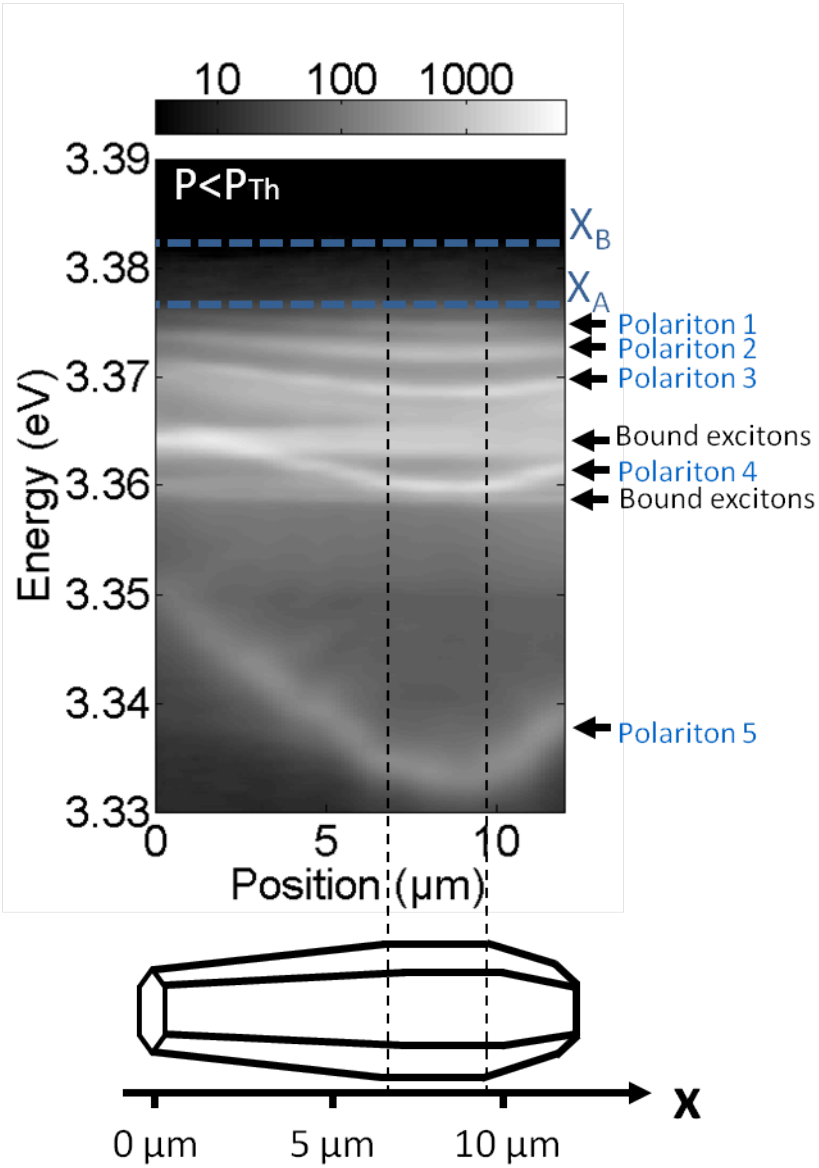

Figure 7.1: Top panel: Spatially resolved photoluminescence in a logarithmic color scale along a single ZnO microwire below polariton lasing threshold. Bottom panel: Schematic representation of the microwire studied in this experiment displaying the radius gradient corresponding to the photoluminescence.

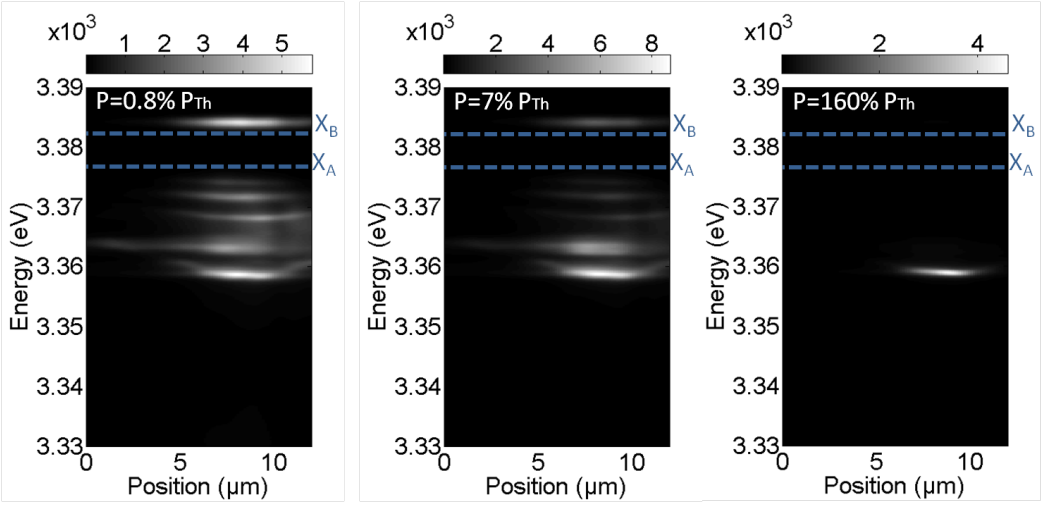

Figure 7.2: Spatially resolved photoluminescence (color scale) along the same microwire than figure 7.1 for three different pulsed excitation powers (from left to right: $0.8\%P_{Th}$, $7\%P_{Th}$ and $160\%P_{Th}$). P_{Th} is the threshold power of the polariton lasing regime.

energy (ie. in the range $[E_X - E_{LO}\ E_X]$) and, therefore, is broadened at room temperature because its interaction with the LO phonon is not quenched. Its energy difference with respect to the A exciton energy is 16 meV as compared to the Rabi splitting $\Omega = 300meV$. It results in an excitonic fraction as large as 97%.

7.1.2 Polariton lasing with high excitonic content

Figure 7.4 presents the excitonic fraction associated to the photoluminescence presented on figure 7.1 using a model with one exciton resonance. The polariton 4, which is lasing on figure 7.2, is situated 17 meV below the A exciton energy and has an excitonic fraction of the order of 97%. Polariton lasing with a 97% excitonic content is an unusual situation leading to the following questions:

What is the effective mass and the De Broglie wavelength of such polaritons? The polariton effective mass m_p^* is a way to characterize the extension of the polariton state in the momentum state (as well as in the real space). Moreover, at thermal equilibrium, this effective mass, and the associated De Broglie wavelength, are directly connected to the critical temperature and the critical density of the quantum degenerate transition . In the limit of two-coupled oscillators model, the polariton effective mass m_p^* can be expressed by:

$$\frac{1}{m_p^*} = \frac{1}{2}\left[\left(\frac{1}{m_\gamma} + \frac{1}{m_X}\right) - \left(\frac{1}{m_\gamma} - \frac{1}{m_X}\right) \times \left(2|X|^2 - 1\right)\right]$$

where $|X|^2$ is the excitonic fraction, m_γ is the photon effective mass and m_X is the exciton mass. The 1D De Broglie wavelength at a temperature T is given by:

$$\Delta = \frac{h}{2\pi m_p^* k_B T}$$

Left panel of figure 7.3 is the polariton effective mass as a function of the excitonic fraction in a semilogaritmic scale. In ZnO, it goes from $22eV$ for the pure photon to $1MeV$ for the pure

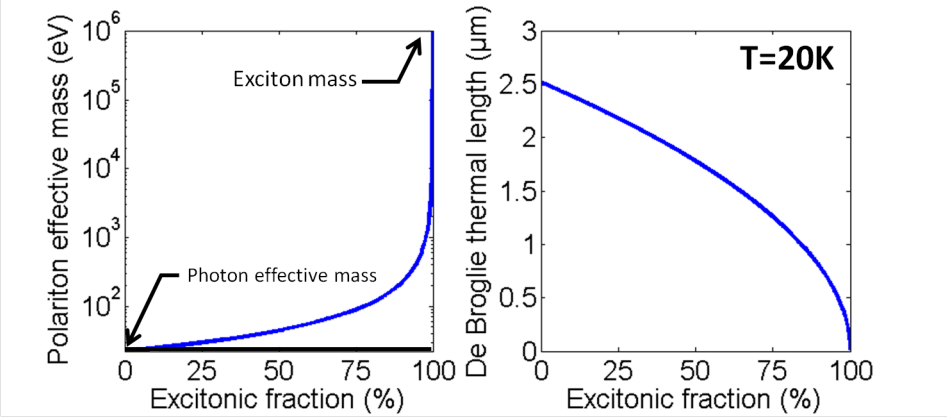

Figure 7.3: Left panel: Polariton effective mass as a function of its excitonic fraction on a semilogaritmic scale. Right panel: Corresponding De Broglie thermal length at a temperature of 20K for the polariton gas as a function of the excitonic fraction.

exciton but remains close to the pure photon effective mass on the range [0% 80%]. A strong divergence arises on the last percentages of excitonic content. With its excitonic content of 97%, the polariton 4 (defined on figure 7.1) has an effective mass around $720eV/c^2$. This value is one order of magnitude larger compared to polariton modes with an excitonic content around 50% but is still three orders of magnitude smaller than the exciton mass. Therefore, the spatial extension of its wavefunction is still much larger than the exciton Bohr radius and the quantum degenerate regime threshold will be much smaller than the threshold of the Mott transition.

Indeed, at thermal equilibrium, assuming a temperature of the polariton gas of 20K, it is possible to compute the De Broglie thermal wavelength (see right panel of figure 7.3). It goes from 2.5µm for pure photons down to $12nm$ for pure excitons. For the polariton 4, it leads to a De Broglie thermal wavelength around $450nm$, which is larger than the critical mean interparticle distance of $14nm$ to reach the electron-hole plasma regime (see section 3.1.1). Finally, even with this high excitonic content, the photon dressing of the exciton state is still efficient to protect the exciton to be ionized.

What about the polariton-polariton interaction? As discussed in chapter 3, polariton is an original boson that can be studied in the quantum degenerate regime. One of its peculiar property is the fact that it is an interacting particle. Importantly, these interactions can be large enough to reach the thermal equilibrium. This polariton-polariton interaction allows to reach the Tonk-Girardeau regime where the polaritons are expected to "fermionized" (ie. to behave like fermions). Therefore, it is interesting to be able to have large polariton-polariton interaction.

In our case, polariton lasing is achieved under non-resonant excitation on a polariton mode with a slightly smaller excitonic content (ie. 97%) because of the spectral selectivity of the gain mechanism (see chapter 8 for a discussion on the relaxation mechanisms). However, it is possible, for example, to manipulate the polariton 1 (defined on figure 7.1) resonantly to study polariton modes made up of 99.98% of excitons up to the quantum degenerate limit.

Interstingly, the polariton-polariton interaction strength depends on the square of the excitonic content, ie. $|X|^4$. Therefore, in the case of ZnO microwires, we can easily tune this interaction strength from its maximum value in ZnO (ie. corresponding to pure excitons) down to an order of magnitude below by comparing polariton modes with excitonic fractions of 30% and the polariton 4, for example, in which the excitonic fraction is 97%.

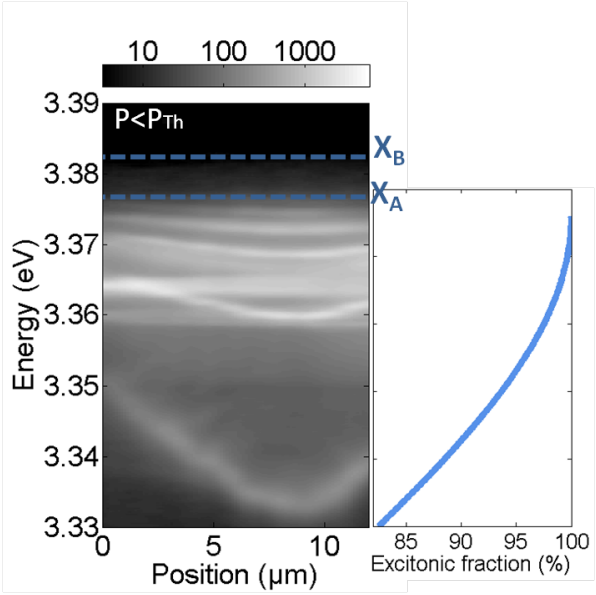

Figure 7.4: Figure 7.1 with the associated excitonic fraction as a function of the spectral position of polariton mode.

What is the coherence time of polaritons with a high excitonic content? The coherence time of polariton is a key parameter to reach the quantum degenerate limit and to establish coherence over all the polaritons. It is a function of the coherence time of the exciton τ_X and the radiative lifetime of the photon τ_γ^r given by the relation:

$$\frac{1}{\tau_p^r} = \frac{|X|^2}{\tau_X} + \frac{|\gamma|^2}{\tau_\gamma^r} \tag{7.1}$$

The quality factor of the pure photonic modes associated to the polariton modes on figure 7.1 is around $Q = 50$ and corresponds to a radiative lifetime of $60fs$. Generally, for polariton modes with $|X|^2$ and $|\gamma|^2$ of the order of 50%, the formula 7.1 is reduced to $\frac{1}{\tau_p^r} = \frac{|\gamma|^2}{\tau_\gamma^r}$ because the exciton coherence time is much larger than the photon lifetime. Therefore, the coherence time of the polariton mode is limited by the radiative decay of its photonic component. In the case of ZnO microwires, the low photonic radiative lifetime is counterbalanced by the high excitonic content of the polariton mode. The excitonic coherence time of the exciton in ZnO at 10K has been measured to be $1.6ps$ [47]. It leads, for polariton 4, to an overall coherence time of $0.9ps$. Contrary to the usual case, the photonic $\frac{\tau_\gamma^r}{|\gamma|^2} = 2ps$ and excitonic $\frac{\tau_X}{|X|^2} = 1.6ps$ components of the polariton coherence time are of the same order of magnitude. Finally, thanks to this enhancement of the coherence time, the high excitonic content of the polariton state leads to a smaller quantum degeneracy threshold compared to a polariton with an excitonic fraction $|X|^2$ of 50%.

7.1.3 Difficulties with continuous wave laser excitation

Continuous excitation creates polaritons in a steady state and is ideal to study its behavior as a function of the excitation power for example. Indeed, the collected photoluminescence is not time dependent contrary to a pulsed excitation. However, in our case, continuous excitation is not suitable to study ZnO microwires as they stand.

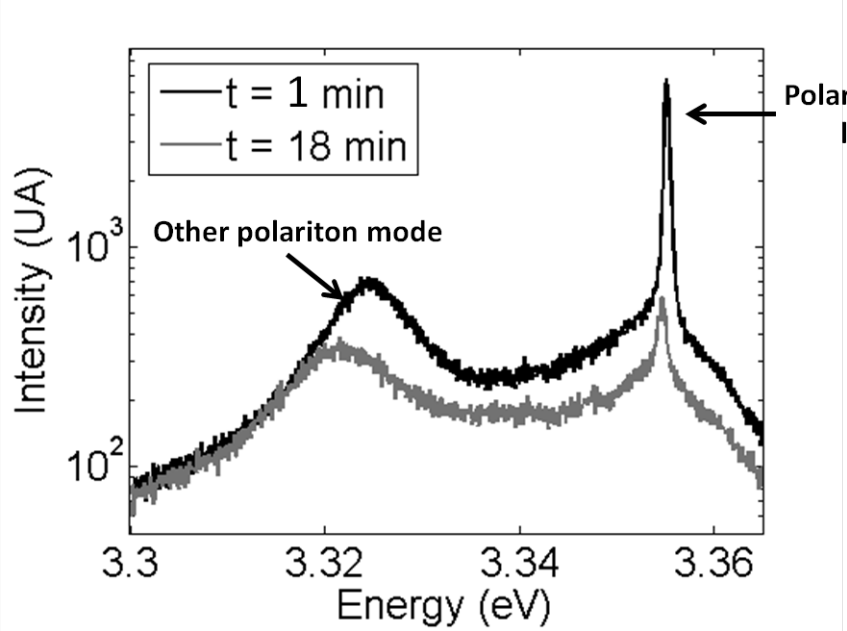

Figure 7.5: Photoluminescence spectrum using a continuous and non-resonant laser at 40K. Both spectrum are obtained under the same pumping power. Black line: Spectrum after 0 minute of continuous UV illumination. Grey line: Spectrum after 18 minutes of continuous UV illumination.

Figure 7.5 presents the photoluminescence of a ZnO microwire non-resonantly pumped above the polariton lasing threshold by a continuous wave laser. On the black line spectrum of figure 7.5, the polariton mode at 3.355eV is in the non-linear regime whereas the polariton mode at 3.324eV is still in the linear regime. The grey line spectrum is realized at the same position along the wire and at the same pumping power after 18 min of UV continuous laser illumination. An important decrease of the intensity for both polariton modes is visible on this grey line. Figure 7.6 presents the evolution of the maximum intensity of both polariton modes as a function of the UV illumination time. Both polariton modes features a decrease of the maximum intensity. Because of its non-linear character, the emission of the polariton branch at 3.355eV is much more affected than the one of the polariton branch at 3.324eV. In any case, this effect prevents from performing reproducible experiments on ZnO microwires under continuous wave excitation. Here is a list of the experimental observations done on this effect:

1. It is not directly reversible in vacuum, ie. if we stop the UV illumination after 20 minutes and wait for few hours, the polariton mode intensity will remain the same under UV illumination.

2. On the other hand, it is possible to recover the initial intensity value by heating the ZnO microwires up to room temperature and at room pressure and return to low temperature.

3. This effect is not observed under pulsed excitation.

4. The time constant associated to this effect is of the order of 10 to 20 minutes and depends on the pumping power.

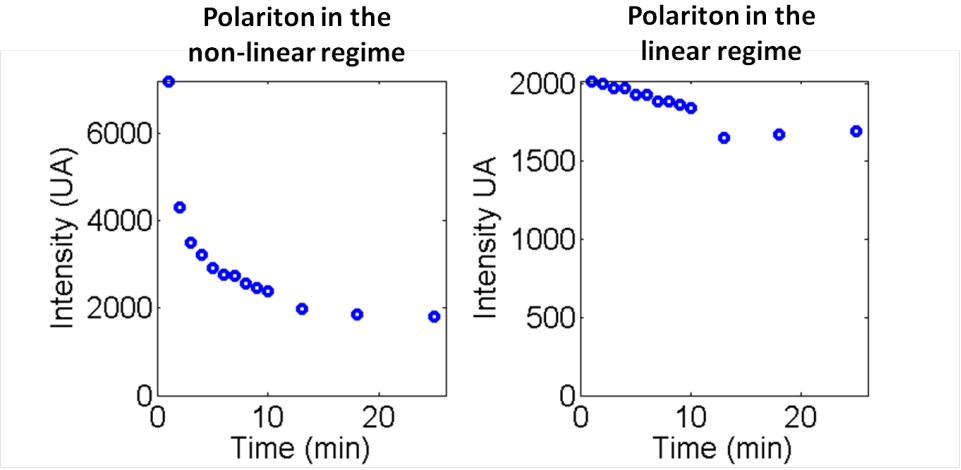

Figure 7.6: Maximum intensity of two polariton modes versus the continuous UV illumination. Left panel corresponds to the polariton mode in the non-linear regime on figure 7.5. Right panel corresponds to the polariton mode in the linear regime on figure 7.5.

In the case of ZnO microwires, the exact origin of this effect is not clear yet. However, it is possible to suspect the role of oxygen adsorption and desorption at the surface of ZnO [110, 111, 112]. This effect is pronounced for wire because of their large surface to volume ratio compared to thin film. Without any UV illumination, oxygen molecules are adsorbed at the surface of ZnO via the reaction:

$$O_2(gas) + e^- \rightarrow O_2^-(adsorbed)$$

where an electron, resulting from the extrinsic n-doping of ZnO, is captured by an oxygen molecule which is finally stuck at the surface. This effect reduces the extrinsic carrier density and increases the upward band bending close to the surface. In our case, the excitons photogenerated close to the suface by the UV illumination can be dissociated because of the surface electric field. The hole is attracted by the trapped oxygen molecule and, then, interacts with it via the reaction:

$$O_2^-(adsorbed) + h^+ \rightarrow O_2(gas)$$

It results that the upward band bending is decreased and the free electron, initially trapped at the surface, is released in the bulk of the wire.

This effect fits with the four experimental observations described at the beginning of this section:

1. If the UV illumination releases an oxygen molecule, re-adsorption of an oxygen molecule once the UV illumination is switched off is unlikely in vacuum (ie. in the cryostat).

2. At room temperature and condition, oxygen molecules is re-adsorbed at the microwire surface. The microwire recovers its original properties.

3. This effect is sensitive to the number of injected carriers. For a similar peak power, in our case, continuous excitation injects 10^4 more carriers than pulsed excitation for a given illumination time.

4. The time constant of this effect (10 to 20 minutes) is of the same order of magnitude than the time constants measured in reference [111] in vacuum and with similar excitation conditions.

However, the effect of oxygen adsorption and desorption on the polariton intensity is not clear. Indeed, if it reduced the upward band bending, this effect should enhance the strong coupling regime by increasing the active exciton and photon overlap. In any case, it should not reduce the intensity of the polariton mode. On the other hand, oxygen desorption tends to increase the number of free electrons in the bulk of the wire and could induce band filling in the conduction band. However, a large number of electrons should be released to band fill the conduction band and this hypothesis is unlikely. In any case, the exact mechanism reducing the intensity of the polariton mode is not clear yet.

Oxygen adsorption and desorption may be reduced by covering the microwires surfaces with a coating transparent in the UV range like SiN in order to passivate the surface and suppress oxygen desorption.

7.2 Characteristics of the non-linear emission: proofs for stimulated relaxation of 1D polariton modes

In this section, we turn back to pulsed excitation to demonstrate and study the polariton lasing regime in ZnO microwires. First, we will show that the emission features superlinearity and linewidth narrowing which are the main characteristics of a stimulated relaxation towards the polariton state (ie. called as well polariton lasing regime). We will show that the strong coupling regime is preserved well above the threshold of the polariton lasing regime.

7.2.1 Stimulated relaxation

Figure 7.7 presents the power dependency of the intensity as well as the spectral linewidth of the light emitted by the polariton state at 10K. The power axis is threshold normalized, ie. it corresponds to the ratio $^{P}/_{P_{Th}}$ where P_{Th} is the threshold power. The fine description of the power dependency of the polariton intensity in figure 7.7 is given in chapter 8 in terms of relaxation mechanisms from the excitonic reservoir. First, we observe an increase of the logaritmic-logaritmic slope of the intensity at $P/P_{Th} = 10^0$ (blue dots on figure 7.7). In order to be quantitative, if we assume that the power dependency of the intensity is a power law before and after threshold, the exponent would go from 1.8 to 3.3. As a consequence, there is a non-linear increase of the number of particles relaxing towards the polariton state because of the bosonic stimulation.

At the same threshold power $P/P_{Th} = 10^0$, there is a steep decrease of the linewidth of the emission of the polariton mode (black dots on figure 7.7) from 1.4 meV down to the spectral resolution of our monochromator ($\sim$ 250µeV). If homogeneous, the linewidth of the polariton mode Γ^p (HWHM) is connected to its coherence time by the relation:

$$t^p_{coh} = \frac{\hbar}{\Gamma^p} \tag{7.2}$$

If not, $\frac{\hbar}{\Gamma^p}$ is a lower bound of the coherence time. Below threshold, the coherence time obtained with the formula 7.2 is around $1.6ps$ which is of the same order of magnitude than the estimation obtained in section 7.1.2, ie. $\tau_c = 0.9ps$. Above threshold, the linewidth of the polariton mode on figure 7.7 goes down to the resolution of our experiment (ie. 250µeV). It

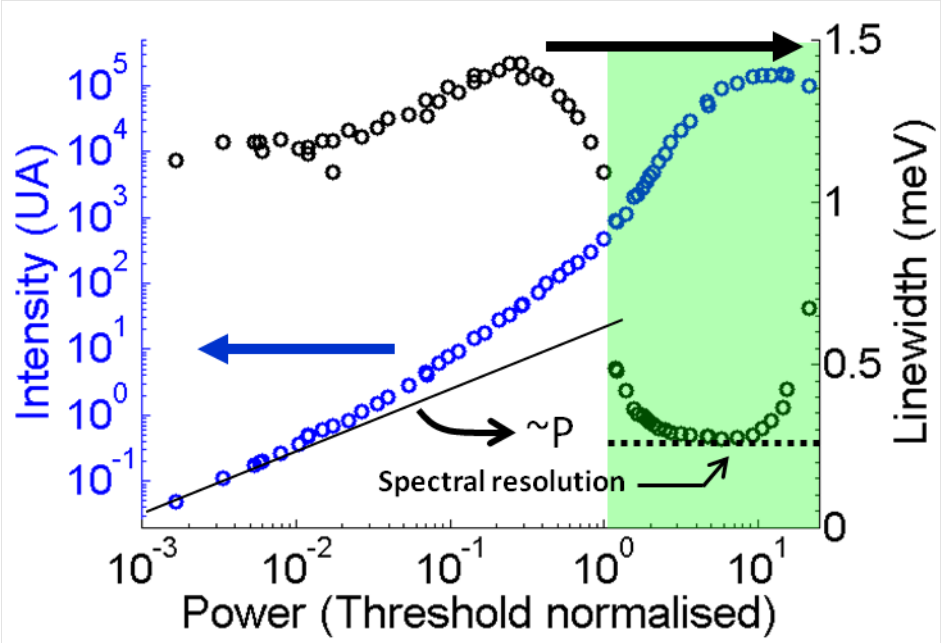

Figure 7.7: Blue dots: Power dependency of the intensity of the light emitted by the polariton state at 10K in logarithmic-logarithmic scale. Black line: Calculated linear behavior in a logaritmic logaritmic scale. Black dots: Power dependency of the spectral linewidth of the light emitted by the polariton state at 10K in a semi-logarithmic scale. The semi transparent green area defines the polariton lasing regime. The power axis is threshold normalised, ie. it corresponds to the ratio P/P_{Th} where P_{Th} is the threshold power.

means that, above threshold, the polariton coherence time is superior to $8ps$ which is larger than the estimated coherence time $\tau_c = 0.9ps$. In this regime, the temporal coherence of the polariton gas is not limited by the polariton coherence lifetime thanks to the bosonic stimulation. The coherence of the polariton gas is preserved over 4.8 times the coherence time of a single polariton. Between $P/P_{Th} = 3.10^{-2}$ and $P/P_{Th} = 4.10^{-1}$, the linewidth of the polariton mode is slightly increasing from 1.2meV to 1.4meV. This small increase can be assigned to polariton-polariton or polariton-exciton interactions which tends to decrease the coherence time of the polariton mode.

Above $P/P_{Th} = 10$, the linewidth increases from 250µeV to 700µeV. This increase is caused by the blueshift of the polariton state integrated in time which is properly described in the following section.

7.2.2 Strong coupling regime preserved above threshold

The previous arguments about the non-linear emission and the linewidth narrowing characterizes a bosonic stimulation. However, they are valid for polaritons as well as photons in the case of regular lasing, ie. stimulated emission. In this subsection, we will demonstrate that the strong coupling is preserved above the non-linear threshold.

Blueshift of the polariton mode

The key parameter to demonstrate that the strong coupling regime is preserved is the spectral blueshift of the polariton mode. It corresponds to the spectral shift δE^p of the polariton state

upon increasing pumping power compared to its initial energy at low pumping power, ie. $E^p(P = 0)$. It is given by the relation:

$$\delta E^p = E^p(P) - E^p(P = 0)$$

It originates from the repulsive character of the exciton-exciton interaction. The strong coupling regime is preserved if it is small compared to the other characteristic quantities of the system (such as the Rabi splitting, the spectral distance to the next exciton or photon state, etc...). In this case, the polariton state is lasing instead of a pure photonic mode. As shown on figure 7.8, from low power up to 10 times the threshold power, the blueshift of the polariton 4 (defined on figure 7.1) is of the order of 250µeV which is much smaller than:

- the Rabi splitting ($\sim 300meV$)
- the energy difference between the polariton state and the A exciton ($\sim 18meV$)
- the energy difference between the polariton state and the bound exciton complexes ($\sim 2meV$)

As a consequence, the strong coupling is preserved above threshold. To rule out any possible ambiguity, we time-resolved the emission the polariton mode. The luminescence decay is shown on figure 7.10 a) after a pulsed excitation with a peak power above the polariton lasing threshold. Notice that this experiment has been performed on a different polariton mode than the polariton 4 from figure 7.1. First, we can see that the energy of the polariton mode is shifting from 3.34625 eV to 3.345 eV because of the decrease of the exciton and polariton populations. The shift of the polariton mode extracted from this figure is presented on the figure 7.10 b). First, we can see that the blue shift decreases smoothly over time and goes back to its non-blueshifted value with a time constant of $25ps$. Therefore, the lasing mode is not jumping from mode to mode over time and is a single polariton state.

Finally, owing to the small blueshift compared to the characteristic quantities of the system and its smooth character as a function of time, we can state that the strong coupling regime is preserved above threshold.

Origin of the blue shift

The blueshift of the polariton mode originates from the repulsive exciton-exciton interaction (described in references [113, 114] for quantum wells based microcavities and reference [115] for bulk materials). Three different situations emerge resulting in a blueshift of the polariton mode:

- Exciton-exciton interaction induces a blue shift of the bare exciton energy. However, in a bulk material, this blueshift is in principle exactly counterbalanced by a decrease of the oscillator strength caused by a band filling effect and, as a consequence, a decrease of the binding energy [46]. Therefore, in ZnO microwires, the exciton energy would remain constant with increasing pumping power while only the Rabi splitting would be reduced.
- Polariton-polariton interaction induces a blue shift of the polariton energy given by the relation [116]:

  $$\delta E^p = g\,|\psi|^2$$

  where g is polariton-polariton interaction constant [117, 118] and ψ is the wavefunction of the polariton mode. δE^p is negligible below threshold because the polariton density is much

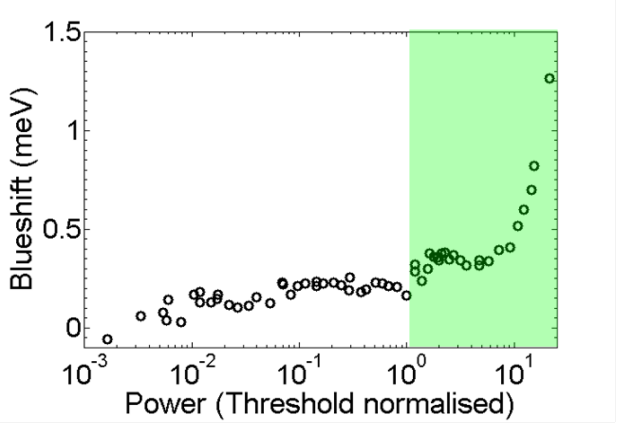

Figure 7.8: Power dependency of the blueshift of the light emitted by the polariton state in semi-logarithmic scale. The semi transparent green area defines the polariton lasing regime. The power axis is threshold normalised, ie. it corresponds to the ratio P/P_{Th} where P_{Th} is the threshold power.

smaller than the unity, ie. $|\psi|^2 \ll 1$. Above threshold on figure 7.8, the blueshift is constant from $P/P_{Th} = 1$ to $P/P_{Th} = 10$ while it is increasing above $P/P_{Th} = 10$. This behavior cannot originate from the polariton-polariton interaction. Indeed, the blueshift displays on figure 7.8 has to be compared to the power dependency of the polariton population given on figure 7.7. In the range $P/P_{Th} = 1$ to $P/P_{Th} = 10$, the blueshift is constant while the polariton population is increasing. On the other hand, above $P/P_{Th} = 10$, the blueshift is increasing while the intensity is saturating.

- Exciton-polariton interaction creates a mix behavior between the two previous interactions. In this case, the blueshift is sensible to the exciton and polariton populations.

Finally, we can conclude that the blueshift displays on figure 7.8 originates from either exciton-exciton interaction or exciton-polariton interaction. A measurement on other lower polariton or upper polariton states would dertermine if the blueshift originates from a decrease of the Rabi splitting or a blueshift of the lower polariton state. Because of the large Rabi splitting $\Omega = 300meV$, we cannot access upper polariton branch. The blueshift of polariton 1 to 4 (numbered on figure 7.1) are presented on figure 7.9. Because of the high intensity of the polariton 4 above threshold, it is not possible to access the blueshift of the polariton 1 to 3 above threshold. However, below threshold, the blueshifts of polariton 1 to 4 are almost constant emphasizing the fact that the strong coupling regime is preserved up to the threshold.

7.2.3 Emission pattern in the direction perpendicular to the wire in the non-linear regime

The emission pattern along the cross-section of the wire gives an insight into the confinement of the polariton state. Figure 7.11 presents the polariton emission pattern perpendicularly to the wire axis, ie. along the ϕ angle. Below polariton lasing threshold (left panel $P/P_{Th} = 0.6$), a non-dispersed and strong emission is observed at $3.359eV$ and $3.364eV$ corresponding to the bound exciton complexes. The weak and non-dispersed emission at $3.354eV$ corresponds to the polariton dispersion which is dispersed along the wire axis (not shown), ie. along the θ angle,

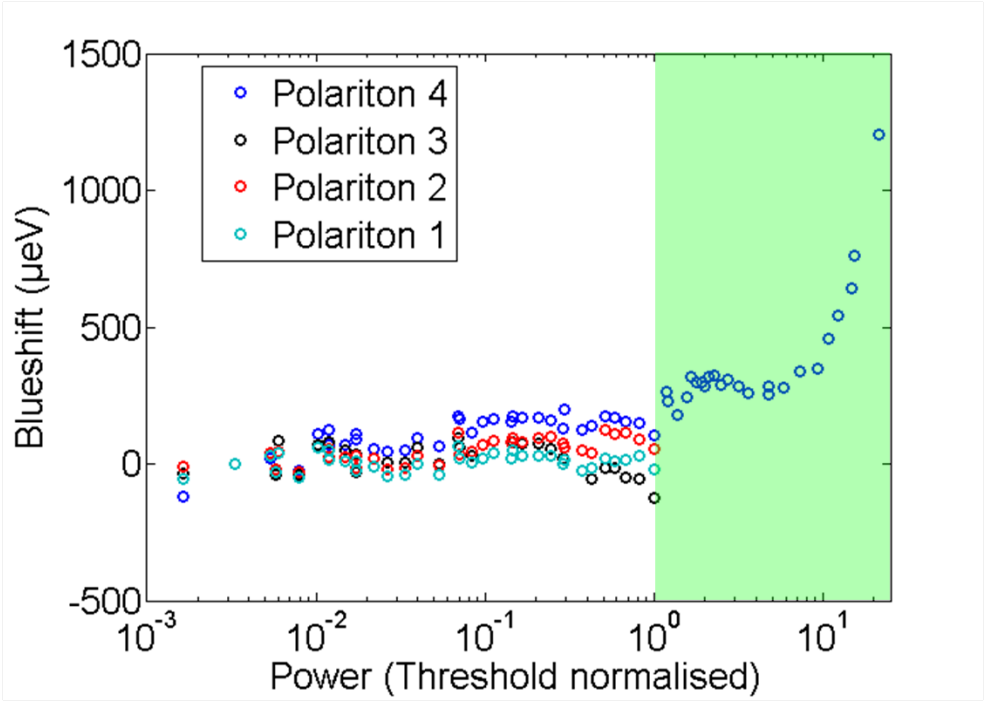

Figure 7.9: Blueshift of polaritons 1, 2 ,3 and 4 numbered on figure 7.1 on a semi-logarithmic scale. The power axis is threshold normalised, ie. it corresponds to the ratio $^{P}/_{P_{Th}}$ where P_{Th} is the threshold power.

and flat perpendicularly to the wire axis (see figure 7.11), ie. along the ϕ angle because of the confinement.

As already discussed in chapter 5, the flat dispersion does not feature any specific modulation. Indeed, as explained in reference [64], HWGMs, and then polariton modes, are twice degenerated. The far-field of the two degenerate modes overlap creating a non-modulated emission versus the angle of emission ϕ. However, above threshold on figure 7.11, a clear modulation appears as a function of the angle ϕ. This behavior is, in appearance, contradictory. Indeed, in the strong coupling regime, these modulations should not depend whether the polariton modes are lasing or not.

Actually, it is possible to explain this behavior by asuming that the two modes are not degenerate. Indeed, in a realistic strucure, ie. a non-perfect structure, the two modes are slightly coupled through back-scattering by imperfections. This coupling is lifting the degeneracy between the two modes. Below threshold, the splitting is smaller than the polariton linewidth and, therefore, modulation are invisible. On the other hand, above threshold, because of the linewidth narrowing induced by the polariton stimulation, the splitting is possibly larger than the polariton linewidth. In this case, mode selection between the two modes can favor one of them. The mechanism of this mode selection is not clear yet.

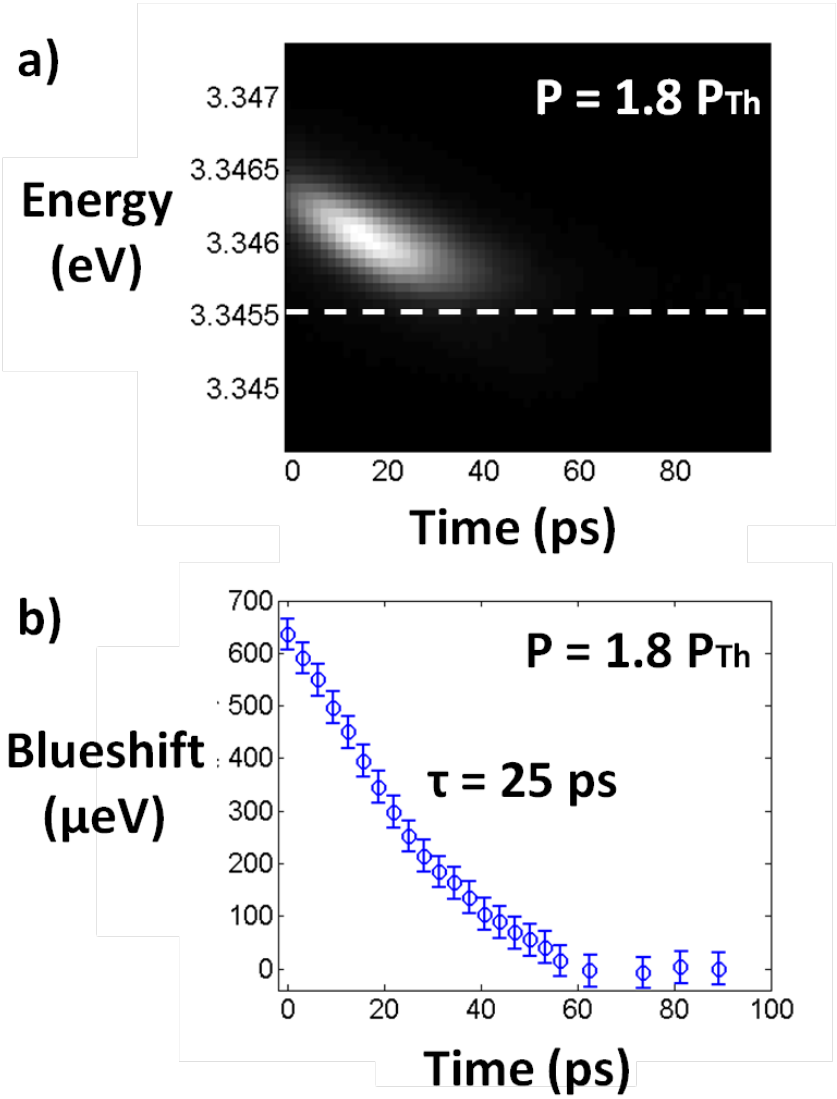

Figure 7.10: a) Time-resolved photoluminescence of a polariton state above the threshold of polariton lasing ($P = 1.8P_{Th}$). b) Time-resolved blue shift of the same polariton state than in panel a) for the same pumping power. The time constant associated to this decay of the blue shift is 25 ps.

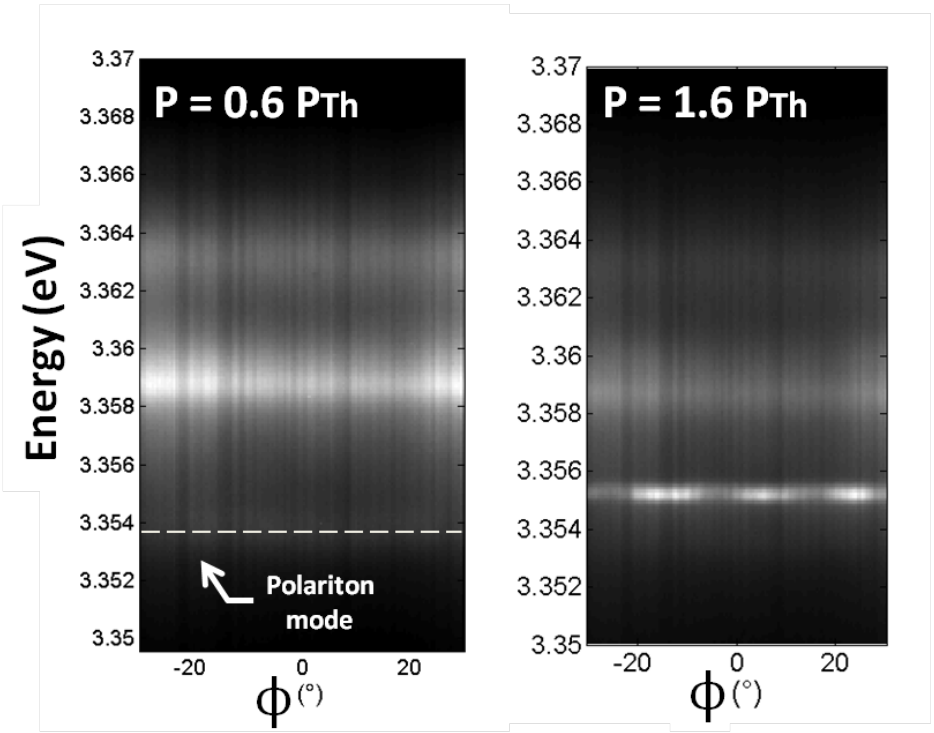

Figure 7.11: Angular-resolved photoluminescence perpendicularly to the axis wire, ie. along the ϕ angle, below (left panel $P/P_{Th} = 0.6$) and above (right panel $P/P_{Th} = 1.6$) threshold. The dashed white line in the left panel is a guideline for the emission pattern of the polariton mode

Chapter 8

Polariton lasing: Dynamics of the exciton reservoir and gain mechanism

Contents

Under non-resonant excitation, the dynamics of a polaritonic system implies rich physical concepts since it involves a gas of polaritons in interaction with a complex environment: excitons, phonons and other polaritons. A comprehension of the dynamics in such systems is necessary to understand the gain mechanism and develop strategies to decrease the polariton lasing threshold at room temperature. On a more fundamental aspect, a polariton gas is, by definition, an out-of-equilibrium system since the polariton lifetime is extremely short (ie. of the order of the picosecond). Therefore, some of its properties, such as thermal equilibrium and temperature, depend on its environment.

Up to now, there have already been many works dedicated to the dynamics of polaritons [119, 120, 121] discussing the role of reservoir relaxation via acoustic phonons-exciton or exciton-exciton scattering. However, these studies concern microcavities based on different materials, different excitonic confinement (quantum wells) and different excitation strategy than ZnO microwires. With ZnO microwires, we have an interesting advantage over microcavity due to the absence of mirror: we can study all the other components of the luminescence such as the LO phonon replica of the exciton or the bound exciton states. Furthermore, in ZnO microwires, it is possible to pump the excitons resonantly while it is impossible in a microcavity.

In this chapter, we will discuss different aspects of the dynamics in ZnO microwires from the experimental point of view. First, we will discuss two main characteristics of the excitonic

reservoir: its thermalization time and its lifetime. Then, we will discuss the relaxation mechanisms from the excitonic reservoir towards the polariton states in both, the linear regime and the non-linear regime.

8.1 Dynamics of the excitonic reservoir in ZnO microwires

With ZnO microwires, it is possible to directly inject excitons in the system. The reservoir of excitons is then the first step to study the dynamics of the complete system. Thanks to the LO phonon replica of the excitons, which can be considered as a photocopy of the exciton reservoir, it is possible to study the exciton state. First, we will discuss the thermodynamics of this reservoir and show that the thermalization of the exciton gas is fast, ie. of the order of few picoseconds, below the polariton lasing regime. Then, we will study the lifetime of the excitons and show that it depends on the excitation power. This effect will be explained by the saturation of non-radiative channels. Once the exciton decay time will be understood, we will be able to study the decay of polaritons in this system.

8.1.1 Thermodynamics of the reservoir

In order to measure the thermalization time of the exciton gas, we choose to study the impulse response of the exciton level at 10K below the polariton lasing threshold (ie. $P/P_{Th} = 47\%$). The energy of the laser was set 10 meV above the exciton energy and the photoluminescence of the 2^{nd} LO phonon replica was time-resolved (resolution $\sim 10ps$ in this experiment). As we have already seen, a LO phonon replica of the exciton gives a direct insight on the exciton kinetic energy distribution and, therefore, to its thermodynamics state. Notice that the emission of a LO phonon does not select any specific exciton momenta unlike direct recombination. The lineshape of the 2^{nd} LO phonon replica of the exciton is given by (see chapter 5):

$$I_{LO}(\tilde{E}) \propto \sqrt{\tilde{E}} \times e^{-\frac{\tilde{E}}{k_B T_X}} \otimes \mathcal{L}(\tilde{E}, \Gamma_X)$$

where $\tilde{E} = E - (E_X - m \times E_{LO})$, $k_B T_X$ is the thermal energy of the exciton gas and $\mathcal{L}(\tilde{E}, \Gamma_X)$ is a lorentzian with a linewidth Γ_X. $(E_X - m \times E_{LO})$ gives the low energy side of the LO phonon replica emission. Of course, $I_{LO}(\tilde{E})$ is zero for $\tilde{E} < 0$. The collected luminescence $I_{LO}(t, \Delta t)$ at a time t during an interval Δt can be expressed by:

$$I_{LO}(t, \Delta t) = \begin{array}{c}\text{Detection} \\ \text{efficiency}\end{array} \times \begin{array}{c}\text{Probability per time unit for} \\ \text{an exciton to emit} \\ \text{a photon and a LO phonon}\end{array} \times \begin{array}{c}\text{Exciton} \\ \text{population}\end{array} \times \Delta t \qquad (8.1)$$

The expression 8.1 can be rewritten in a formal way:

$$I_{LO}(t, \Delta t) = K \times \Gamma_{X \to \gamma + LO} \times n_X(t, \Delta t) \times \Delta t \qquad (8.2)$$

The direct consequence of formula 8.2 is that the time-resolved luminescence of the LO phonon replica is directly the time-resolved luminescence of the exciton reservoir up to a multiplicative factor.

The temperature of the exciton gas can be directly extracted from the LO phonon replica lineshape. Similar experiments has been done for example in reference [122] in ZnSe quantum wells. Figure 8.1 presents the time-resolved photoluminescence in the spectral range of the 2^{nd}

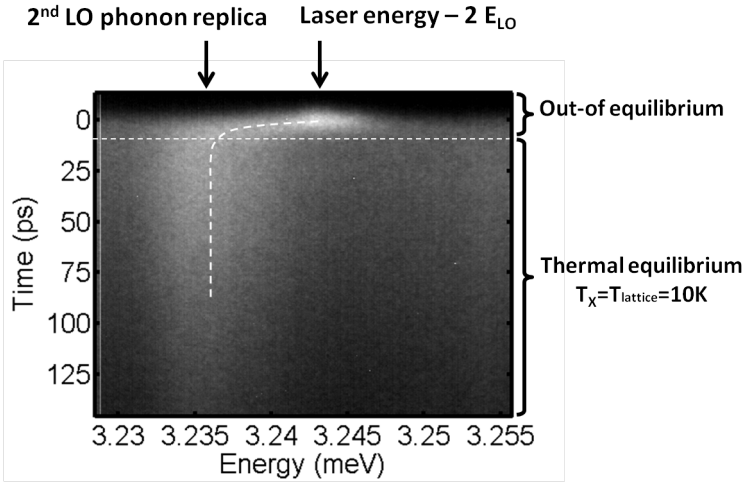

Figure 8.1: Time-resolved photoluminescence in the spectral range of the 2^{nd} LO phonon replica at 10K. The pumping power was $^{P}/_{P_{Th}} = 47\%$. The white dashed line is a guideline showing the thermalization of the exciton gas

LO phonon replica. At $t = 0ps$, we can clearly see the out-of-equilibrium hot excitons created by the excitation. The laser energy was $3.387eV$ and its replica is at $3.243eV$, which is $2 \times 72meV$ below. Thermal equilibrium is restored after $10ps$. Since, the resolution of this experiment was $10ps$, we can state that the thermalization time for figure 8.1 is below $10ps$. After $10ps$, the temperature of the exciton gas is measured to be 10K by fitting the LO phonon replica lineshape. Since the exciton temperature is the same than the lattice temperature, it means that the exciton gas thermalizes mainly with the phonon bath. Indeed, if the thermalization was exclusively caused by exciton-exciton interaction for example, the exciton mean kinetic energy would not change, leading at equilibrium to a temperature of $140K$ given by the laser mean energy (ie. $\sim 10meV$). As a consequence, the thermalization time scale with the phonon bath in the ZnO microwires is lower than $10ps$.

8.1.2 Excitons and polaritons decay time

Excitons decay time

Using the same experimental strategy, we can measure the overall decay time of the reservoir. In the previous section, we have determined that the thermalization time is below 10ps in these structures. We find that for any excitation power and temperature, the decay time is orders of magnitude larger than the thermalization time. As a consequence, the rise time of the replica luminescence is always connected to this quantity which is sub-resolution. Because of this fast thermalization, it is valid to sum the LO phonon replica luminescence over its spectral extension in order to recover the exciton decay time: the decay time is the same on the whole replica extension since the excitons thermalize rapidly. Finally, we obtain a decay spectrum as shown in figure 8.2 with a quasi mono-exponential behavior.

The extraction of the decay time has been realized for various pumping power. Figure 8.3 presents the result of this process as a function of the pumping power. The power axis is normalized to the polariton lasing threshold.

We find a 3-fold increase of the decay time for increasing excitation power. It tends to

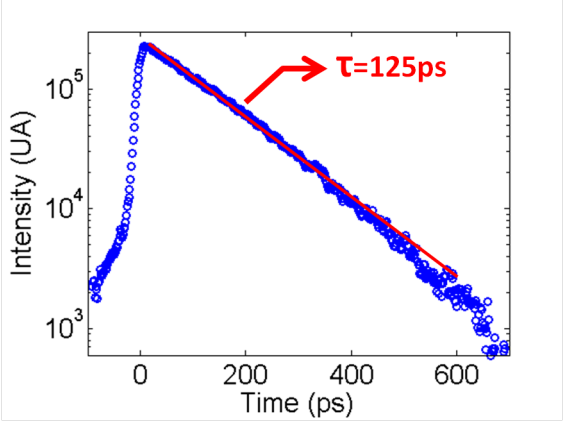

Figure 8.2: Photoluminescence decay of the LO phonon replica at 10K under pulsed excitation ($P/P_{Th} = 47\%$). The red line is a monoexponential fit with a time constant of 125ps.

saturate to $150ps$ above $P/P_{Th} = 0.5$. This striking behavior can only be explained assuming the presence of saturating non-radiative channels. In this model, the exciton has two decay channels:

- the exciton decays towards a state which does not saturate. It can be the LO phonon emission channel for example. The associated time constant is τ_X.
- the exciton decays towards localized trap states off finite number N like impurities or surface states [123]. The lifetime of these trap states is called τ_S. The relaxation time constant from the exciton reservoir towards N trap state is called $\tau_{X\to S}$. Once the N states are filled, this channel is blocked. In order to accumulate enough population to reach the saturation in the saturating state, we need to have: $\tau_S > \tau_{X\to S}$.

The rate equations describing this model are:

$$\text{Exciton states: } \frac{dn_X}{dt} = -\frac{n_X}{\tau_X} - \frac{n_X}{\tau_{X\to S}}(1 - \frac{n_S}{N}) + n_0\delta(t) \tag{8.3}$$

$$\text{Trap states: } \frac{dn_S}{dt} = \frac{n_X}{\tau_{X\to S}}(1 - \frac{n_S}{N}) - \frac{n_S}{\tau_S}$$

where the term $n_0\delta(t)$ stands for the creation of n_0 excitons at $t = 0ps$.

At low excitation power, the trap states are not saturated, ie. $n_S \sim 0$ and the effective exciton decay time is given by the relation: $\frac{1}{\tau'_X} = \frac{1}{\tau_X} + \frac{1}{\tau_{X\to S}}$. At high excitation power, the trap states are completely saturated, ie. $n_S \sim N$, and the effective exciton decay is simply τ_X.

Since the experiment is carried out with ps pulses, the impulse response of these equations is calculated numerically. Then, we performed a mono-exponential fit on the impulse response in order to extract the same quantity than the experimental quantities. A quantitative agreement has been found on this fitting process (red line on figure 8.3) with the following time constants :

$$\tau_X = 155ps \pm 15ps$$

$$\tau_{X\to S} = 120ps \pm 30ps$$

$$\tau_S > 120ps$$

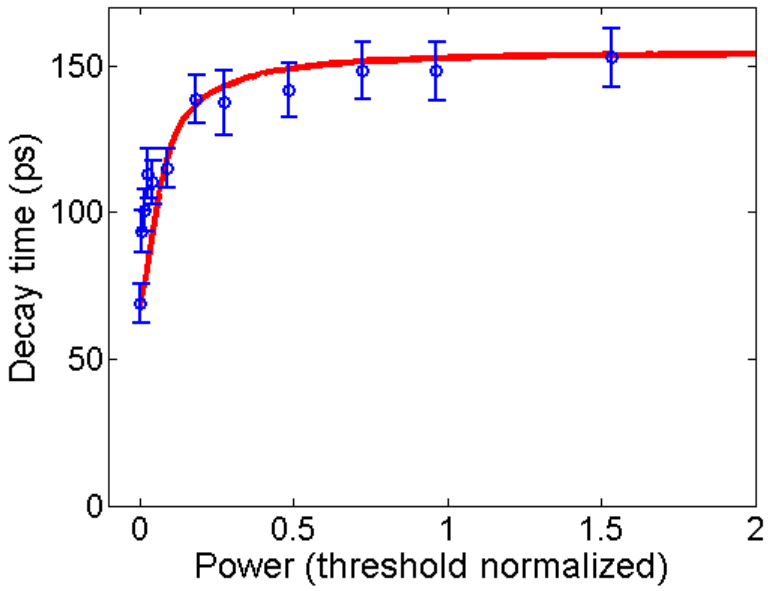

Figure 8.3: Blue dots: Decay time of the LO phonon replica as a function of the pumping power at 10K. The power axis is threshold normalized, ie. $P/P_{Th} = 1$ corresponds to the polariton lasing threshold. This experiment has been performed on the same polariton state than the experiments presented in chapter 7 (cf. figure 7.1 in chapter 7 for example). Red line: calculation including the effect of saturating non-radiative channels described in the text.

Notice that the exciton lifetime $\tau_X = 155ps$ is not the exciton radiative lifetime since, in the strong coupling regime, this quantity is not relevant anymore. The exciton lifetime $\tau_X = 155ps$ may be associated to the LO phonon replica channel or simply to non-radiative channels other than trap states.

As shown on figure 8.3, we have been able to measure the exciton decay time above the polariton lasing regime (up to $P/P_{Th} = 1.5$). If the main decay channel of the exciton state was the relaxation towards the polariton states, we should observe a decrease of its lifetime above threshold. The fact that the decay time of the exciton state is constant even above threshold is an indication that the relaxation towards the polariton states is dragging only a small fraction of the total exciton population, at least up to $P/P_{Th} = 1.5$. Indeed, it is very likely that the excitons situated at the middle of the microwire are not coupled to the polariton states since they have a negligible overlap with the HWGMs. As a consequence, the luminescence of the LO phonon replica is dominated by these excitons and two exciton reservoirs coexist in these structures.

Polariton decay time

We measured the time-resolved photoluminescence of the polaritons 1, 2, 3 and 4 of figure 7.1 in chapter 7 which are, respectively, 2meV, 3.5meV, 6 meV and 19 meV below the exciton energy. Notice that the polaritons 1, 2 and 3 do not lase in the investigated range of excitation power. The rise time was measured to be smaller than the resolution (ie. $5ps$ in this experiment) which is coherent with the low quality factor (~50) of this microwire. A polariton has a radiative lifetime of the order of the picosecond. Therefore, like the LO phonon replica, it is a photocopy of the time decay of its reservoir in the linear regime, ie below the polariton lasing threshold.

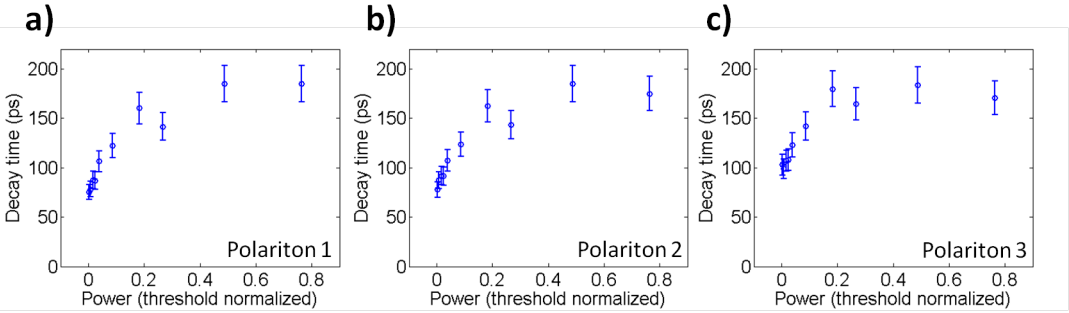

Figure 8.4: Decay time of the polariton modes 1, 2 and 3 (numbered on figure 7.1 in chapter 7) at 10K under pulsed excitation. The power axis is threshold normalized, ie. $P/P_{Th} = 1$ corresponds to the polariton lasing threshold. This experiment has been performed on the same microwire and detuning than the experiments presented in chapter 7 (cf. figure 7.1 in chapter 7 for example).

The decay time extracted from a mono-exponential fitting process for the polaritons 1, 2 and 3 is presented on figure 8.4. Comparing figures 8.3 and 8.4, which have different scales on the time axis, we can infer that these three polaritons are filled by the exciton reservoir since they have qualitatively the same decay time power dependency. However, a full modelization would be required to describe properly the polariton decay time. Indeed, as we will see in section 8.3, two-body scattering takes place in the system to fill some of the polariton states. It is not clear whether or not this mechanism should modify the decay time of the three polaritons displayed in figure 8.4.

The time-resolved photoluminescence of polariton 4 has been studied as well and is shown for two different excitation powers (Blue dots: $P/P_{Th} = 77\%$, black dots: $P/P_{Th} = 2\%$) on figure 8.5. We can separate these decays in two parts: a mono-exponential decay after $100ps$ and a non mono-exponential decay before $100ps$. Both of these components are modified for increasing excitation power. Moreover, the rise time of the luminescence of the polariton 4 is above the resolution of our experiment and evolves with the excitation power as well. As a consequence, its general behavior is not clear. However, this fact is the first indication that the polariton 4 is not filled in the same way than polaritons 1, 2 and 3 of figure 7.1 in chapter 7. Actually, we will see in section 8.3 that the filling of this polariton involves a two-body process which does not fill the polaritons at higher energy because of its spectral selectivity. This process is expected to change the time-resolved photoluminescence of this polariton compared to polariton 1, 2 and 3.

8.2 Relaxation from the excitonic reservoir towards the polariton states

In this section, we want to describe experimentally two relaxation mechanisms from the excitonic reservoir towards the polariton states. At low exciton density, the polaritons in ZnO microwires are mainly fed by the LO phonon replica of the exciton. At higher density and low temperature, another mechanism builds-up, which involves two body scattering within the reservoir, and fills the polariton states. We will show that this mechanism only fits with two possible scenarios: the scattering of excitons with bound excitons and the bi-exciton decay.

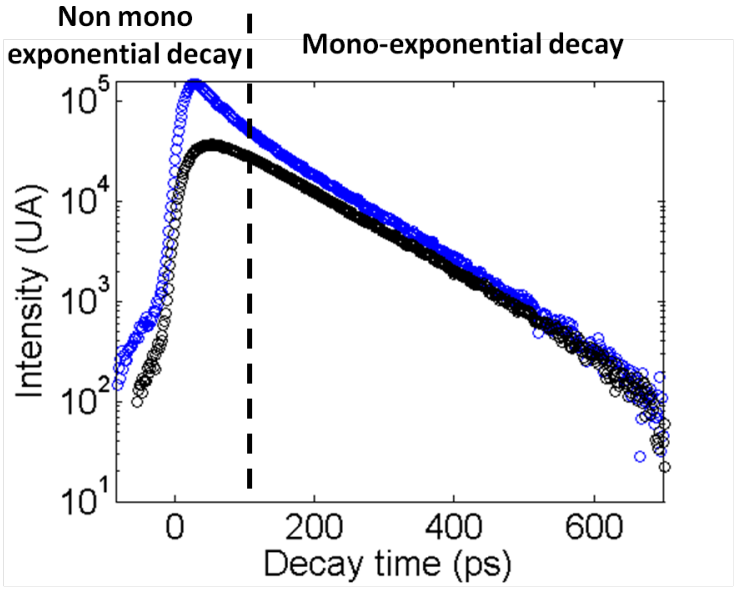

Figure 8.5: Photoluminescence decay of the polariton 4 (numbered on figure 7.1 in chapter 7) at 10K under pulsed excitation for two different excitation power (Blue dots: $^{P}/_{P_{Th}} = 77\%$, black dots: $^{P}/_{P_{Th}} = 2\%$).

8.2.1 LO phonon polariton feeding in the linear regime

The analysis done in this subsection is based on spatially resolved photoluminescence experiments (ie. similar to figures 8.6 in this chapter and 7.1 in chapter 7) carried out at different temperatures under continuous wave excitation and in the linear regime, ie. below the polariton lasing regime. In these experiments and for certain ranges of position along the wire, the polariton energy changes continuously along the wire axis. The goal of this section is to study the intensity of the polariton state as a function of its spectral position to observe an enhancement of the polariton intensity at the LO phonon energy.

8.2.2 Method

In order to extract the polariton intensity independently from the pumping power, we choose to normalize the spectrum shown on figure 8.6 by the exciton intensity. It results in an artificial spectrum where the number of excitons is constant as a function of the position along the wire.

The polariton energies in ZnO microwires are drastically modified by the gradient of radius. We take advantage of this gradient to continuously tune the polariton energy across the LO phonon replica. Experimentally, it is easier to address the polariton intensity at a given energy E rather than at a given position. Indeed, the emission background does not depend on the position along the wire because it is not coupled to HWGMs while it varies quickly along the energy axis. Therefore, we will focus on the quantity $\mathcal{M}(E)$ which is the polariton intensity integrated along the position axis after having carefully removed the constant background. Notice that this quantity $\mathcal{M}(E)$ is not directly the polariton intensity at an energy E. Indeed, polaritons with different energies contribute to this quantity. However, we will show now that it allows us to obtain the polariton intensity at a given energy after correction. The following calculus is similar to the one presented in section 5.2.3. $\mathcal{M}(E)$ is given by:

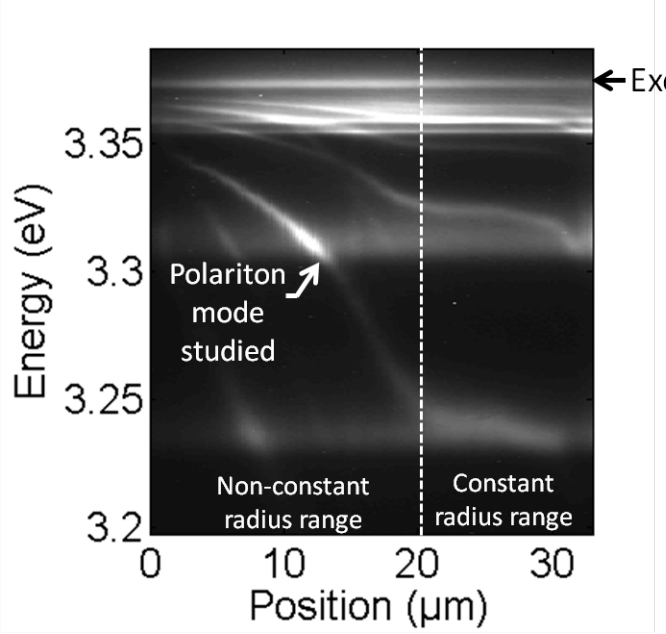

Figure 8.6: Spatially-resolved photoluminescence along a ZnO microwire in the linear regime at 55K using a continuous excitation. This section focus in the non-constant radius range, from 0 µm to 20 µm, where the energy of the polariton modes is continuously changing. The exciton photoluminescence is situated at 3.373 eV.

$$\mathcal{M}(E) = \int_{-\infty}^{+\infty} I_p(E - E_p(z))dz$$

where $I_p(E - E_p(z))$ is the polariton intensity at an energy E and a position z along the wire axis. $E_p(z)$ is the relation between the polariton energy and the position along the wire axis. Let us exchange the variable z and $E_p(z)$:

$$\mathcal{M}(E) = \int_{-\infty}^{E_X} I_p(E - E_p)\frac{\partial z}{\partial E_p}dE_p$$

Let us now linearize $E_p(z)$ around the position z_0 which satisfies $E_p(z_0) = E$. In our case, this assumption is valid since $E_p(z)$ is linear on the linewidth Γ of the polariton lineshape $I_p(E-E_p)$ (see figure 8.6). We have: $E_p(z) = K(z_0)\times(z-z_0)+E_p(z_0)$ and then $\frac{\partial E_P}{\partial z}|_{z_0} = K(z_0)$. Therefore, we can write:

$$\mathcal{L}_0(E) = \frac{\mathcal{M}(E)}{K(z_0)}$$

where $\mathcal{L}_0(E) = \int_{-\infty}^{E_X} I_p(E - E_p)dE_p$ is the polariton intensity at an energy E. Therefore, by dividing the quantity $\mathcal{M}(E)$ by the slope of the curve $E_p(z)$ at a position z_0 satisfying $E_p(z_0) = E$, we can recover the polariton intensity at an energy E.

8.2.3 Results and discussion

This treatment has been applied to the figure 8.6 as well as the same experiments for various temperatures. The extracted polariton intensity $\mathcal{L}_0(E)$ is represented as a function of the polari-

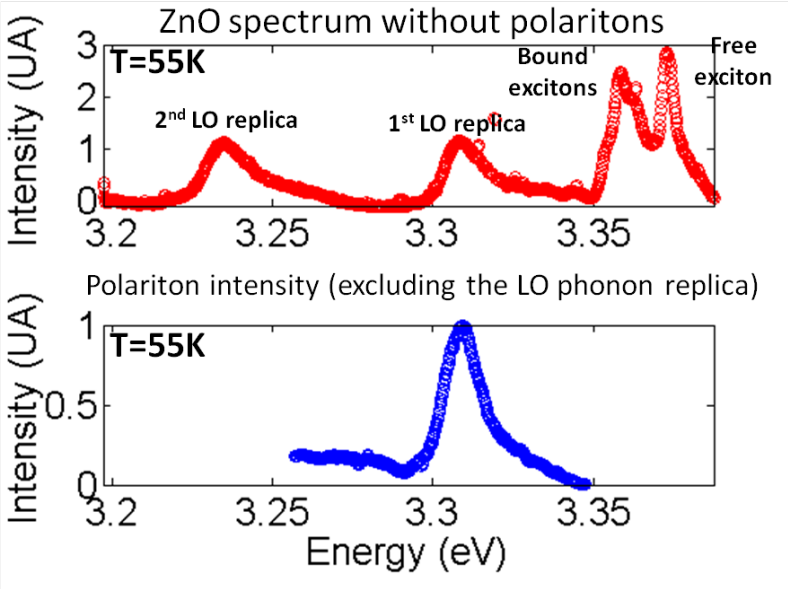

Figure 8.7: Top panel: photoluminescence spectra on a ZnO microwire at 55K under continuous excitation on a wire length without any polariton. From low to high energy, we observe four peaks corresponding to the 2^{nd} and 1^{st} LO phonon replica of the exciton, the bound excitons and the free exciton. Bottom panel: Polariton intensity extracted from the method described in the text as a function of its energy. Notice that the emission background (including the LO phonon replica) has been removed. Both panels have the same energy axis but different intensity axis.

ton energy E in the bottom panel of figure 8.7. The top panel is simply the photoluminescence of the same ZnO microwire in position range where there is no polariton state. Comparing both panels of figure 8.7, the enhancement of the polariton intensity is clearly correlated with the LO phonon replica lineshape. Therefore, it is reasonable to state that the mechanism filling the polariton state in the linear regime involves LO phonons or the LO phonon replica. The simplest mechanism is the emission of one LO phonon and a polariton by an exciton. If we compared the polariton intensity out of LO phonon replica, at 3.387, and on the LO phonon replica, at 3.309, the polariton luminescence is multiplied by a factor 10. We can conclude that, at 55K, the main mechanism filling the polariton state includes a LO phonon replica of the excitons.

Figure 8.8 a) represents the polariton intensity taken on the same polariton state for five different temperatures ranging from 10K to 125K. In the figure b), it is simply the photluminescence of the same microwire in a region without any polariton state. First, we can see that, at 10K and 26K, there are two additional contributions from $3.26eV$ to $3.295eV$. The exact origin of these extra-contributions is not clear and could be attributed to shallow donors, surface states or LO-phonon replicas of the ZnO bound excitons resonantly exciting the polariton modes. These two peaks corresponds to two emissions in the photoluminescence spectra (see figure 8.8 b)). There is as well a broad contribution above $3.32eV$ for these two temperatures 10K and 26K. These contributions do not correspond to any peak in the photoluminescence experiment. By elimination, this broad contribution above $3.32eV$ is likely due to the acoustic phonons mediated relaxation. For increasing temperatures, it is clear that the LO phonon contribution dominates over all the other contributions.

The exciton relaxation assisted by the emission of LO phonons has the important advantage

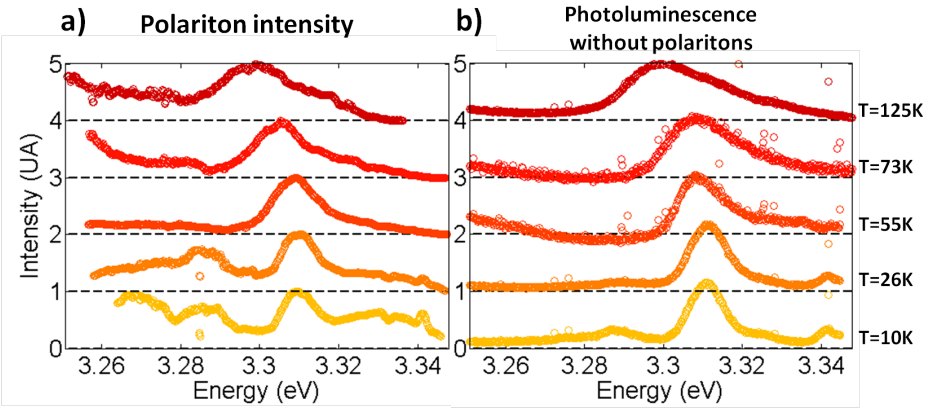

Figure 8.8: a) Polariton intensity extracted as a function of its energy for 10K, 26K, 55K, 73K and 125K. b) Photoluminescence of a ZnO microwire without any polariton state for 10K, 26K, 55K, 73K and 125K. Each spectrum is offset compared to the previous temperature by a factor 1. The background of each spectrum is represented with dashed lines.

to allow the excitons to release a large amount of energy (given by $m \times 72meV$ where m is the phonon replica number) and to relax directly close to the $k = 0$ polariton state. Therefore, it is an efficient process compared to acoustic phonons mediated relaxation.

8.3 Gain mechanism of the polariton lasing at low temperature

In this section, we are going to discuss the possible gain mechanisms to reach the polariton lasing regime in ZnO microwires at low temperatures. First, we will describe the experimental facts allowing to conclude that the lasing polaritons are filled via a two body process involving excitons and that this mechanism is spectrally selective. Then, we will show that among several possible mechanisms only two are not ruled out by the experimental facts: the bound exciton/free exciton scattering and the biexciton decay.

8.3.1 Gain mechanisms of the polariton lasing: Experimental facts

Gain mechanism: Two body scattering involving excitons

In the experiments presented in this chapter (like in the chapter 7), the pulsed laser energy was set to the A/B exciton energy. As a consequence, we are directly injecting excitons in the structure. Figure 8.9 corresponds to the same experiment than the power dependency of the lasing polariton shown on figure 7.7 except that the different regimes are separated. The abscissa of figure 8.9 is the threshold normalized excitation power P/P_{Th} and is proportional to the number of excitons in the system while the intensity axis is proportional to the number of polaritons. We can separate this power dependency on three regimes numbered on figure 8.9:

1. In the first regime, at the lowest exciton density, the polariton population is almost linear with the exciton population with a power law exponent of 1.1: if the number of excitons in the system is doubled, the number of polaritons will be doubled as well. Therefore, in this regime, the relaxation from the reservoir towards the polariton states is assisted by exciton-phonon scattering or exciton-intrinsic carriers scattering.

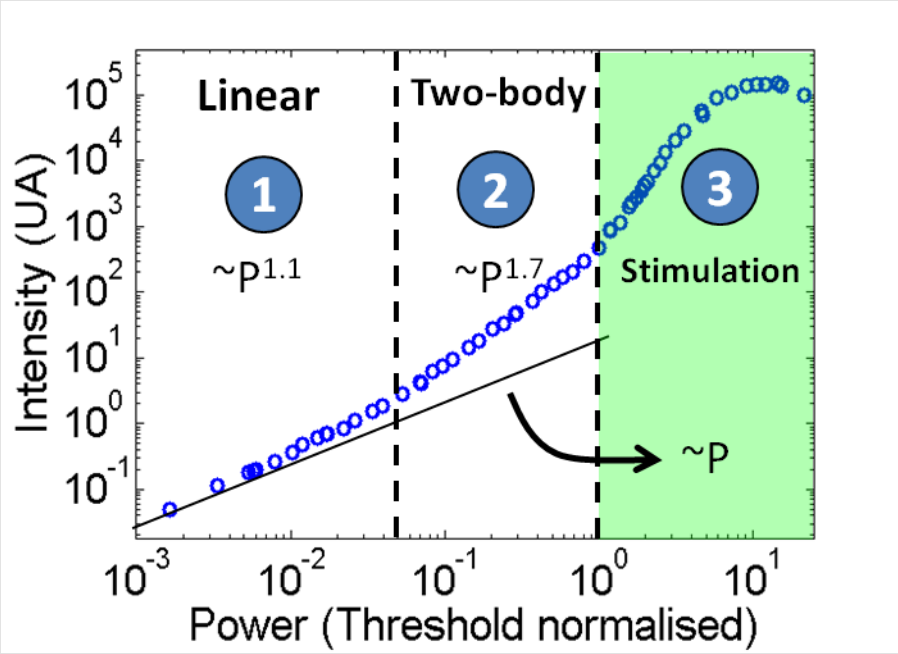

Figure 8.9: Same figure than figure 7.7. Blue dots: Power dependency of the intensity of the light emitted by the polariton state in logarithmic-logarithmic scale at 10K under pulsed excitation. Black line: Calculated linear behavior in a logaritmic logaritmic scale. The dashed lines separate the different regimes: 1 is the linear regime, 2 is the regime involving a two-body process and 3 is the polariton lasing regime (ie. the semi transparent green area). The power axis is threshold normalised, ie. it corresponds to the ratio P/P_{Th} where P_{Th} is the threshold power.

2. In the second regime, the polariton population increases almost quadratically with the number of excitons with a power law exponent of 1.7. Since this exponent is almost twice the exponent in the linear regime, the main relaxation mechanism in this second regime requires two excitons.

3. The third regime is the polariton lasing regime characterized by a highly non-linear behavior above threshold (semi-transparent green area of the figure 8.9) followed by a saturation of the polariton intensity which can be assigned to gain saturation.

Fine description of the power dependency Before entering into a detailed modelization of this behavior, it is preferable to study the power dependency of the exciton state through its LO phonon replica which is displayed on figure 8.10. Intriguingly, below the polariton lasing threshold, the power law exponent is 1.24. Since the laser injection takes place in the exciton state, its power dependency is almost linear, ie. the initial number of excitons is fixed by the pump power. However, in our case, we have seen that the decay time of the exciton states increases with increasing pumping power because of the saturating trap states. The intensity presented on figure 8.10 are time-integrated on each pulse. Therefore, we expect its power dependency to be slightly super-linear, because of the increase of the decay time as a function of the excitation power, which is explaining this power law exponent of 1.24. Above $P/P_{Th} = 1.5$, the intensity of the LO phonon replica is slightly saturating. This fact can be explained assuming that the the LO phonon decay time is decreasing because of stimulated relaxation which is taking place

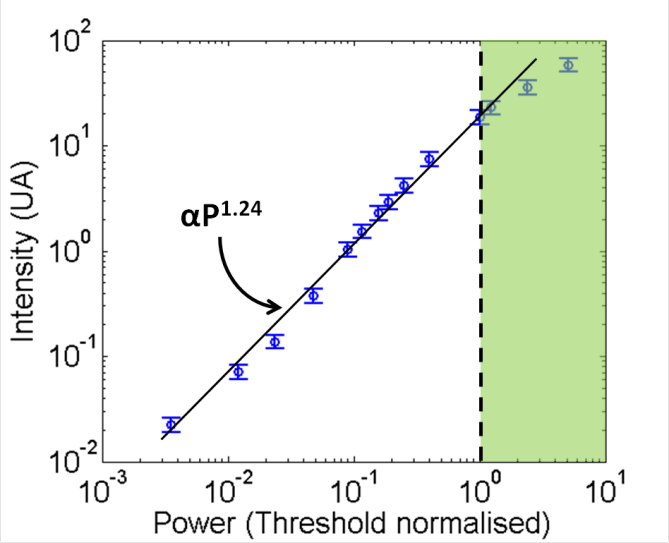

Figure 8.10: Power dependency of the intensity of the LO phonon replica luminescence in logarithmic-logarithmic scale. Black line: Fitted power law with a power law exponent of 1.27. The polariton lasing regime corresponds to the semi transparent green area. The power axis is threshold normalised, ie. it corresponds to the ratio $^{P}/_{P_{Th}}$ where P_{Th} is the threshold power.

in the system. In any case, the intensity of the LO phonon replica is not saturating just above threshold which means that the excitonic reservoir is weakly affected by the polariton lasing regime. Indeed, as explained in section 8.1.2, a large part of the exciton reservoir is spatially separated from the polariton modes. Therefore, the depletion of the reservoir by the two body scattering is neglected in the following modelization.

We can now write the rate equations that agree with our observations below the polariton lasing threshold. Since we just want to qualitatively reproduce the power dependency of figure 8.9, we have neglected the saturating trap states which leads to a linear behavior of the exciton reservoir. The rate equations are:

$$\text{Exciton state: } \frac{dn_X}{dt} = -\Gamma_X n_X + n_0\delta(t) \tag{8.4}$$

$$\text{Polariton state: } \frac{dn_p}{dt} = \Gamma'_X n_X + \Gamma'_{XX} n_X^2 - \Gamma_p n_p \tag{8.5}$$

where Γ_X is the probability per time units for an exciton to leave the exciton state, Γ'_X is the probability per time units that an exciton decay toward the polariton state (via scattering with LO and acoustic phonons for example), Γ_p is the probability per time units for a polariton to emit a photon, $n_0\delta(t)$ is the pulsed pumping term which creates n_0 excitons and Γ'_{XX} is the probability per time units that one exciton-exciton scattering creates one polariton. The exact nature of this last mechanism will be discussed in the section 8.3.1.

We have simulated numerically the behavior of the equations 8.4 and 8.5 in the pulsed regime. In a second step, the intensity decay obtained for both the polariton and exciton states are time-integrated. Figure 8.11 presents the calculated power dependency (black dots) resulting from this treatment with the following parameters: $\Gamma'_X = 10^{-3}ps^{-1}$, $\Gamma_p = 1ps^{-1}$ and $\Gamma'_{XX} = 10^{-6}ps^{-1}$. The values of Γ'_X, Γ_p and Γ'_{XX} used for this numerical simulation have been chosen arbitrarily. However, they allow to describe qualitatively the power dependency observed in figure

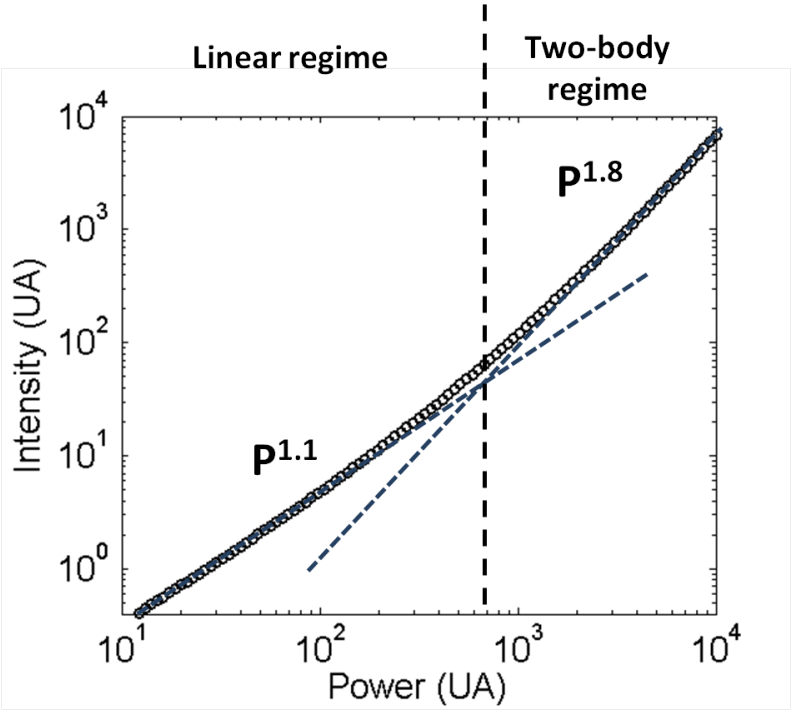

Figure 8.11: Calculated power dependency given by the equation 8.5. Two distinct regimes are visible with non-integer power law exponent. Parameters used to simulate this power dependency are given in the text.

8.9. Indeed, two non-integer power law exponents can be extracted from figure 8.11 because of the pulsed character of our experiment: 1.1 in the linear regime and 1.8 in the two-body regime. During the population decay, the system undergoes the two-body regime at the beginning of the decay and the linear regime after. The power law exponent is, therefore, not an integer number, since the power dependency is smoothed. Finally, the modification of the power law exponent is consistent with a transition between the linear regime and the two body scattering regime in a pulsed experiment. A reservoir dynamics like that of equation 8.3 should be coupled to the equations 8.4 and 8.5 as well as the stimulated relaxation towards the polariton state to reproduce properly the whole power dependency shown on figure 8.9.

Comparison with non-lasing polariton modes From figure 7.2, it is possible to extract the intensity of the two non-lasing polaritons numbered polaritons 2 and 3. The power dependency of the intensities of polariton 2 and 3 has been appended to figure 8.9 and are presented on figure 8.12. In the linear regime, the three polaritons are linear. However, contrary to the lasing polariton (blue dots), the two non-lasing polaritons (red and black dots) saturate in the second regime. Firstly, this measurement supports the fact that the lasing polariton is filled via a two-body process while the non-lasing polaritons are not. Secondly, we can infer from figure 8.12 that the two-body process filling the lasing polariton is spectrally selective. Indeed, polariton 2 (black dots) and 3 (red dots) have, respectively, an energy 3.5meV and 6meV below the exciton energy while polariton 4 (blue dots) have an energy 18meV below the exciton energy. As we have seen in section 8.1.2, two exciton reservoirs coexist in these structures. The fact that the polaritons 2 and 3 (red and black dots) saturate above $^{P}/_{P_{Th}} = 5.10^{-2}$ is an indication that the exciton reservoir filling the polariton states is depleted by the two body mechanism, contrary to

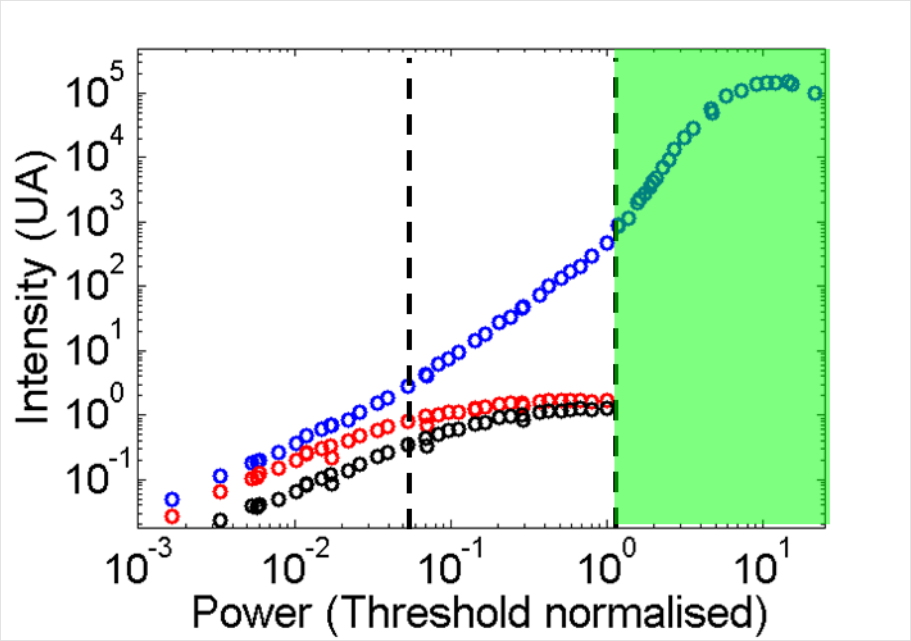

Figure 8.12: Power dependency of the intensity of the light emitted by the polariton state in logarithmic-logarithmic scale. Blue dot corresponds to the polariton 4 situated 18 meV below the A exciton energy on figure 7.1 in chapter 7. Red dot corresponds to the polariton 3 situated 6 meV below the A exciton energy on figure 7.1 in chapter 7. Black dot corresponds to the polariton 2 situated 3.5 meV below the A exciton energy on figure 7.1 in chapter 7.

the second reservoir, which is spatially uncoupled and exhibits a linear behavior.

Spectral selectivity of the gain mechanism

From the above results, it seems clear that two-body scattering is the main contribution to the gain mechanism in the polariton lasing regime. In order to characterize the spectral selectivity of this gain mechanism, we choose to measure the polariton lasing threshold as a function of the polariton energy. Indeed, as shown on figure 8.12, polaritons which are not selected by the two-body gain mechanism are not lasing. Thanks to the radius gradient, already discussed in chapter 5, the energy of a given polariton state (ie. associated to a given HWGM state), can be changed easily. Figure 8.13 presents the lasing threshold of a polariton mode at 4K using a pulsed picosecond laser as a function of $\Delta = E_{XA} - E_{pol}$ the energy difference between the A exciton and the polariton state.

In this out-of-equilibrium phase diagram, we can observe that the lasing threshold is increasing for increasing energy difference Δ. At first glance, this behavior can be understood simply because of the difficulty for the excitons to relax more and more energy to reach the polariton state. The threshold increases by a factor of 60 between $\Delta = 16.7meV$ and $\Delta = 40meV$. In this spectral range of energy, the photonic fraction changes rapidly. It goes from 1.3% at $\Delta = 16meV$ to 5.7% at $\Delta = 40meV$ and so does the polariton coherence time. The modification of the polariton coherence time τ_p in this spectral range has a non-negligible influence on the polariton lasing threshold that can be estimated using the formula:

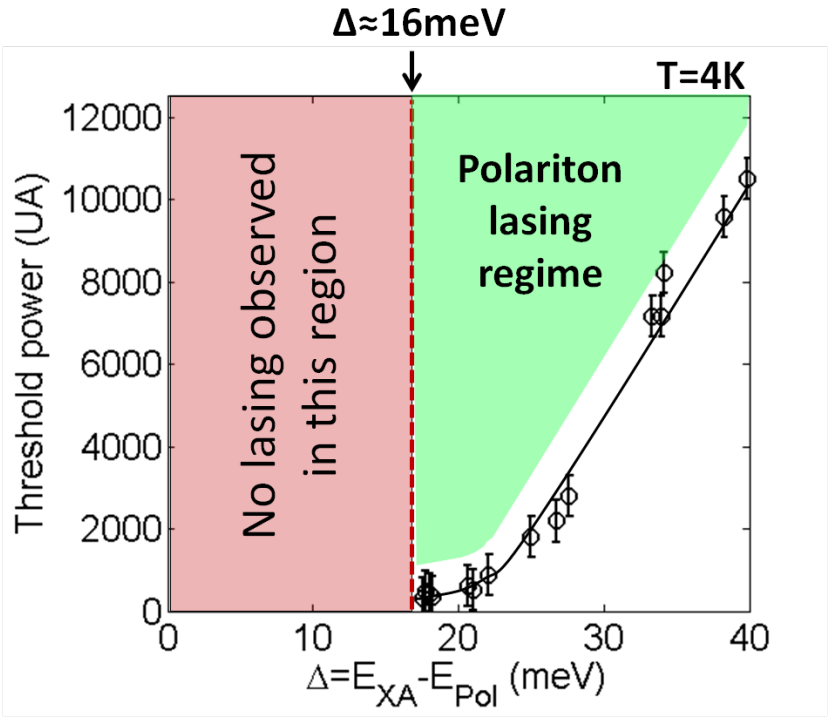

Figure 8.13: Threshold power as a function of the energy difference Δ between the A exciton and the polariton energies at 4K using a pulsed picosecond laser. Polariton lasing regime is not observed for the set of parameters in the semi-transparent red area. The green semi-transparent area corresponds the parameters where polariton lasing regime is observed. The black line is a guide for the eye.

$$\frac{1}{\tau_p} = \frac{|\gamma|^2}{\tau_\gamma} + \frac{|X|^2}{\tau_X}$$

where the exciton coherence time has been taken from reference [47], ie. $\tau_X = 10ps$, and the photon lifetime has been taken from section 7.1.2, ie. $\tau_\gamma = 60fs$. We found that the polariton lifetime goes from $3ps$ at $\Delta = 16.7meV$ to $0.9ps$ at $\Delta = 40meV$. The ratio between this two values is 3.3 and is not sufficient to reproduce the great increase in the polariton lasing threshold observed on figure 8.13 (a factor of 60 between $\Delta = 16.7meV$ and $\Delta = 40meV$).

The most striking feature of figure 8.13 is the range of energy difference Δ between 0meV to 16meV where polariton regime is never reached whatever the power excitation. In this range, the polariton emission saturates when polariton mode 4 is lasing. This spectral range where polaritons are not lasing is clearly due to a spectral selectivity of the two-body process.

The same measurement has been realized at various temperature (see figure 8.14) ranging from 4K to 52K. All of these plots have the same threshold power axis and can be compared. The main result of this figure is that, for increasing temperature, the lowest threshold shifts to higher energy and the threshold at a given energy difference Δ increases. Above 60K, the polariton lasing regime threshold becomes too high for our experiment and the gain mechanism is clearly not efficient anymore. Above 70K, the polaritons in the range $[E_X; E_X - E_{LO}]$, ie. close to the excitonic reservoir, become too broad: excitons has to release almost $72meV$ to reach the first narrow enough polariton state leading to a very high polariton lasing threshold.

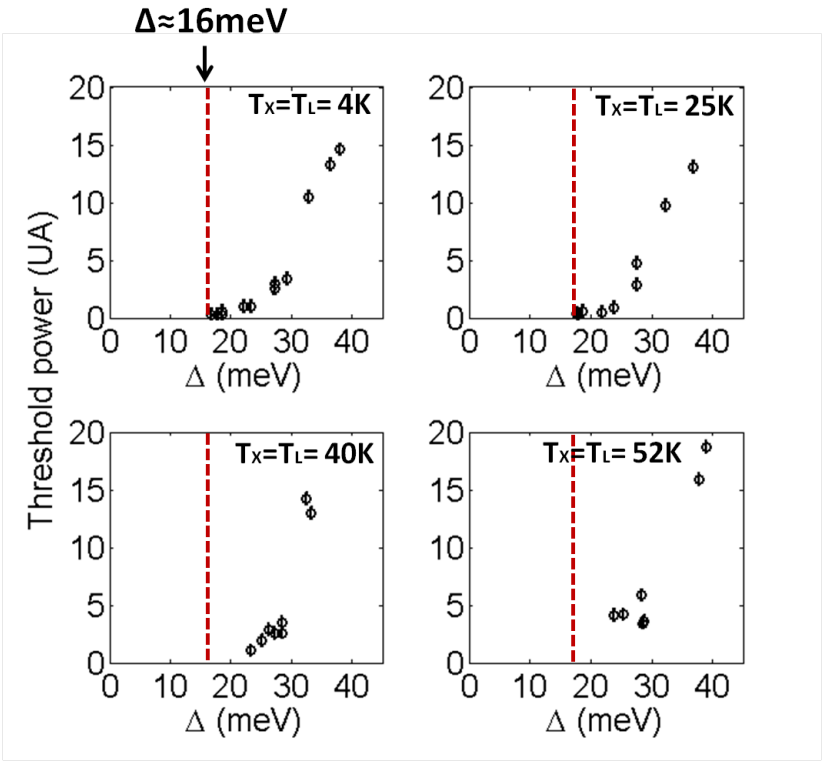

Figure 8.14: Threshold power as a function of the energy difference Δ for T=4K, T=25K, T=40K and T=52K. The red dashed lines correspond to the limit of the non-lasing region at 4K.

Gain mechanisms for the lasing polaritons: Which mechanisms are allowed?

These measurements provide conclusive information on the nature of the two-body scattering at play in the gain mechanism. Six different mechanisms can be envisaged [124] to describe our experimental observations which are schematically represented in figure 8.15.

Ruled out mechanisms

1. Exciton-acoustic phonons scattering Excitons from the reservoir can relax towards the polariton state via the emission of phonons (see panel 1 of figure 8.15). LO phonons are ruled out here since their energy ($72meV$) largely exceeds the energy difference Δ between the exciton and the polariton states. The emission of acoustic phonons is a linear process and does not reproduce the power dependency presented on figure 8.9.

2. Exciton-free charges scattering In this process, excitons scatter with free charges (see panel 2 of 8.15) because, in general, ZnO is slightly n-doped. The free charges goes to a higher energy state while the exciton can relax towards the polariton state. We can separate this mechanism in two cases:

- In the first case, the free charges are present because of the intrinsic doping. This process is a linear process since it requires only one exciton.
- In the second case, the free charges are photo-generated. This process is negligible in our experiments at low temperature because the excitation energy is set to the exciton energy.

3. Exciton-exciton scattering (see panel 3 of figure 8.15) This mechanism has been thoroughly studied in the literature[120, 119, 121] for quantum well excitons in microcavities in order to explain the exciton relaxation towards the polariton states avoiding the bootleneck effect. For simplification, let us consider first the simple case in which scattered excitons have the same initial energies and momenta.

Let us consider two excitons in the reservoir at an energy $\Delta/2$ (right part of figure 8.16). The scattering process is:

$$X_1(\Delta/2, k_0) + X_2(\Delta/2, k_0) \Longrightarrow P(E_p, 0) + X_3(E_3, 2k_0)$$

where X_i stands for the i^{th} exciton state and P for the polariton state. Because of energy and momentum conservation, we obtain the relations:

$$E_p = -\Delta \text{ and } E_3 = {}^{3\Delta}/_{2}$$

As a direct consequence, excitons has to have an energy of $\Delta/2$ in order to relax an energy Δ and reach the polariton state. The population of excitons, at the thermal equilibrium, is described by a Maxwell-boltzmann depicted on the left part of figure 8.16 with a mean energy of k_BT ($1meV$ at $10K$ from section 8.1.1). Therefore, this mechanism is less and less efficient for increasing Δ with a cut-off energy around $1meV$. This behavior is inconsistent with the threshold measurement presented on figure 8.13. It is still possible that the exciton-exciton scattering occurs at the laser energy Δ_{laser}, ie. before thermalization of the exciton gas. However, in this case, the threshold measurement should be peaked at value $-2\Delta_{laser}$ which is not what we observed on figure 8.13.

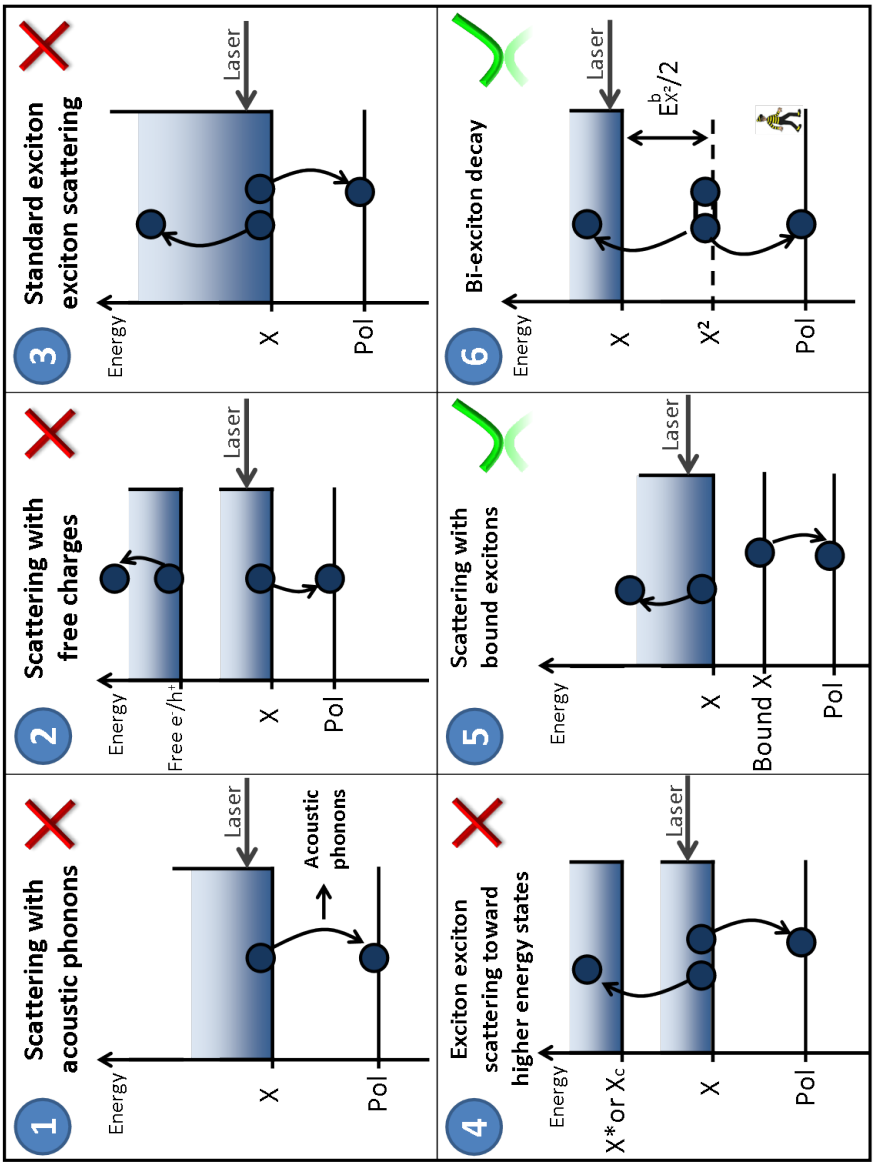

Figure 8.15: Overview of the six mechanisms described in the text. X stands for exciton state, X^2 for the bi-exciton state, Pol for the polariton state, bound X for the bound exciton state, $X*$ for the excited state of the exciton and X_C for the C-exciton.

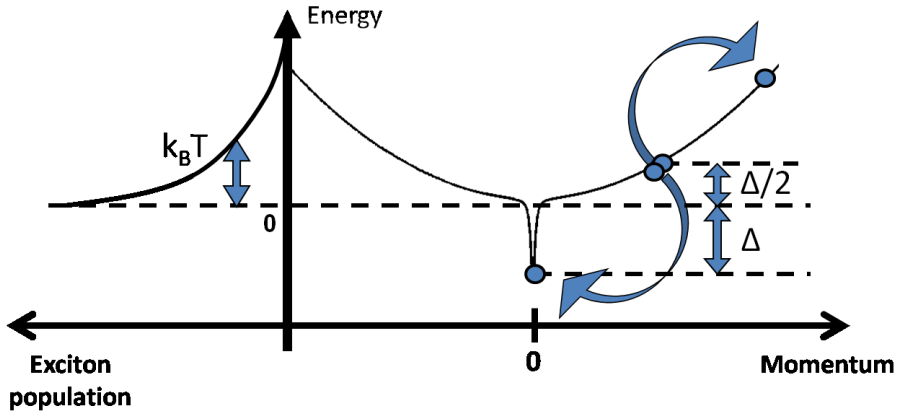

Figure 8.16: Right part: schematic representation of the exciton dispersion. In this scheme, the two scattered excitons have similar energies. Left part: schematic representation of the exciton population at a temperature T.

A more complete simulation is obtained in taking into account scattering of excitons with different initial energies and momentum [120, 119, 121]. However, this calculation results in a large gain in the same energy range than the simple model described above, ie. on a range given by the exciton gas temperature. This is not compatible with our measurements shown in figure 8.13 where the lowest threshold is at $\Delta = 16meV$. Moreover, such a process should be greatly enhanced by the increase of the exciton gas temperature as it results in a redshift of the peak gain which is inconsistent with figure 8.14.

4. Exciton-exciton scattering towards higher energy exciton states (see panel 4 of figure 8.15) This model has been suggested in order to explain the photonic lasing regime observed in bulk ZnO, CdS and CdSe structures at room temperature which was associated to a non-linear emission peak called P-band [125, 126]. The principle is given on figure 8.17. Two excitons from the A/B exciton reservoir scattered together, one is relaxing towards the polariton states while the other one scatters to a higher energy state. The process can be described by the following formula:

$$X_{1s}(E_1 \approx 0) + X_{1s}(E_2 \approx 0) \Longrightarrow X_{2s/c}(E_3 = \Delta, k_3 \approx 0) + P(E_4 = -\Delta, k_4 \approx 0)$$

In the case of ZnO, the higher energy states can be:

- The C exciton which is $45meV$ above the A/B excitons
- The A/B exciton excited states. The binding energy of this state is 3/4 the binding energy of the A/B exciton non-excited state. Therefore, the X_{2s} energy is $45meV$ above the exciton energy.

In both cases, the minimum energy the A/B excitons can relax are $\Delta = 45meV$ which is much larger than the measured lowest threshold energy of $16meV$ observed on figure 8.13.

Compatible mechanisms So far, we ruled out four mechanisms, the two following ones, on the contrary, are compatible with our measurements.

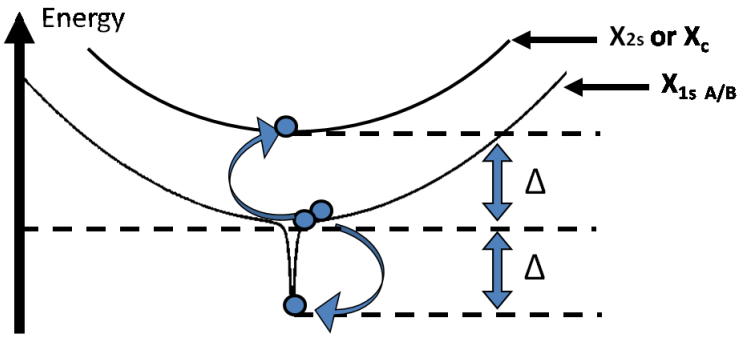

Figure 8.17: Schematic representation of the exciton dispersion. In this scheme, two excitons are scattering: one is relaxing towards the polariton state while the other one scatters towards a higher energy excitonic state. $X*$ stands for the exciton excited states.

5. Bound exciton-exciton scattering (see panel 5 of figure 8.15) In this process, excitons are scattering with bound exciton states. This process verifies the following criteria [127]:

- It is a two-body process which involves two photo-generated excitons, one in the exciton reservoir, one bound on an impurity.
- As shown on panel 5 of figure 8.15, this mechanism allows to excite polaritons with an energy right below the bound excitons (situated $16meV$ below the exciton energy). To explain this fact, we have displayed the two possible situations on figure 8.18. In the first one (panel a)), the exciton increases its kinetic energy while the bound exciton relax to the polariton state. The second one (panel b)) is drastically different since, because of the energy conservation, the exciton from the reservoir has to relax in the non lasing range where there is no obvious state available. Therefore, in this process, there is no gain in the non-lasing range, from $\Delta = 0meV$ to $\Delta = 16meV$, which is consistent with the figure 8.13.
- It has a weak temperature dependency since it depends only in the temperature of the exciton gas. Moreover, an increase of the temperature does not change the energy difference cut-off $\Delta = 16meV$.
- Above 60K, the thermal fluctuations tends to release the bound states. Therefore, this scattering process is suppressed because of the absence of bound states.

This mechanism is in qualitative agreement with our experimental observations. It is possible to argue that this process is very unlikely because of the low density of states of bound excitons compared to the free exciton one. However, this argument is counterbalanced by the large thermal population of this state compared to the free exciton state. Indeed, the thermal energy at 60K is $5meV$ while the binding energy of the bound states is $16meV$.

6. XX_A Biexciton decay [128, 124] At large excitonic density, a significant fraction of the population is bound into biexcitons (mainly the XX_A biexciton for ZnO). The biexciton can decay into an exciton and a polariton. The biexciton has already been observed in ZnO with a binding energy of $14meV \pm 1meV$ [129, 130]. Notice that this value is the binding energy with respect to the exciton states, ie. the binding energy of the biexciton reads:

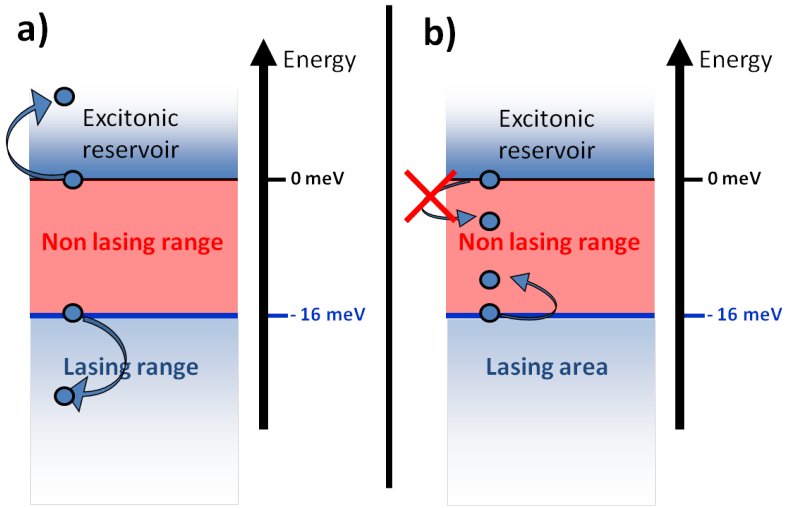

Figure 8.18: Schematic representation of the exciton-bound exciton scattering. a) Scattering towards a polariton state with an energy verifying $\Delta > 16meV$ b) Scattering towards a polariton state with an energy verifying $0 < \Delta < 16meV$

$$E^b_{X^2} = 2E_X - E_{X^2}$$

The decay of a biexciton is given by:

$$X^2(E_{X^2}, k) \Rightarrow X(E_X, k) + P(E_p, 0)$$

where the energy conservation leads to the relation:

$$E_p < E_X - E^b_{X^2} \tag{8.6}$$

The equation 8.6 means that the polariton emitted by the biexciton decay has an energy difference Δ larger than $14meV$.

Finally, this process fits with all of our experimental observations:

- It is a two body process since the biexciton is made up of two excitons
- It provides gain only below $\Delta = 14meV$. For larger energy differences Δ, this gain process involves biexciton at higher energy which is less and less likely because of its thermal population. Therefore, this mechanism is consistent with the figure 8.13.
- It depends only on the temperature of the biexciton gas.
- At high temperature (above $\sim 60K$), the biexciton is not stable anymore because of its binding energy of 14meV and does not provide gain anymore.

Conclusion

The work presented in this thesis provides a detailed description of the physics of one-dimensional strong coupling regime in ZnO microwires. In these structures, the three main excitons X_A, X_B, X_C are coupled with the one-dimensional (1D) Hexagonal Whispering Gallery Modes (HWGM) which are confined in the cross-section of the wire and free to propagate along the wire axis. we have shown that the strong coupling regime between this two fields is sustained from cryogenic temperature (10K) up to room temperature (300K) with a large Rabi splitting, ie. $\Omega = 300meV$ and a high figure of merit ~ 75. Notice that this value is the maximal splitting one can obtain using ZnO bulk material since it corresponds to the Rabi splitting of bulk polaritons. Interestingly, we have shown that these polariton modes are isolated from the phonon bath at room temperature thanks to the quenching of the polariton-phonon interaction. This effect results from large value of the Rabi splitting with respect to the LO phonon energy $\sim 72meV$. As a consequence, the polariton modes decoherence is almost suppressed at room temperature, ie. these modes features homogeneous linewidths at room temperature similar to the low temperature ones. We also strove to demonstrate the 1D character of these particles resulting from the fact that the polariton wavefunction matches the one of the pure HWGMs. Like in the ZnO case, the Rabi splitting measured in GaN microwires match the one of the GaN bulk polaritons, ie. $125meV$ from 10K to 300K. An original situation is observed in GaN microwires because of the highly-doped part of the GaN microwires necessary for the growth of this structure. Indeed, we have demonstrated that weak and strong coupling regimes are observed on a single microwire. Our study on GaN microwires emphasized our understanding on semiconductor-based microwires in the linear regime.

Our study on ZnO microwires in the non-linear regime has been focused on the low temperature regime. The polariton lasing regime has shown an original situation since it involves polaritons with an exceedingly high excitonic fraction $\sim 97\%$. We have shown that this 1D quasi-excitonic polariton field undergoes the quantum degenerate regime and that the strong coupling regime is preserved unambiguously even above threshold. The polariton mode exhibits a macroscopic occupation of the ground state and a linewidth narrowing which are two key signatures of the polariton lasing regime. Thanks to the bulk character of the microwire, we have been able to study the dynamics of this system. We found that the exciton reservoir, which is filling the polariton states, reaches quickly the thermal equilibrium with the lattice (below $10ps$). Apparently, a large part of the exciton reservoir is not coupled to the polariton mode, ie. these excitons do not fill the polariton states. We also shown that the lasing polariton mode is filled via a two-body process presenting peculiar spectral selectivity. This mechanism is attributed either to exciton-bound exciton scattering or biexciton decay.

Outlooks First of all, the polariton lasing threshold at room temperature is extremely high (see the introduction of 7) and prevents to obtain clear indications that the strong coupling regime is preserved. In the ZnO microwires, the laser absorption at the exciton energy is $2.10^5 cm^{-}1$ at room temperature [83] which corresponds to an absorption length of 50 nm. As a consequence,

most of injected excitons rely on the surface of the microwire and are poorly coupled to the polariton modes. It is then interesting to change our excitation strategy. From this point of view, the two-photon excitation with a laser energy at half the energy of the exciton is a much better way to inject excitons. Indeed, the spatial decay of the pumping laser is not exponential anymore for a two-photon absorption. Moreover, it has been shown experimentally that, in ZnO, the doubling efficiency is sufficient to reach non-linear regime at low temperature [128]. Therefore, this method should allow us a better pumping of the excitons in the microwire volume with a much better coupling to the polariton states at room temperature.

The second perspective relies on the overcoming of two technological locks. First, the next generations of both ZnO and GaN wires will be grown by MOCVD allowing an excellent diameter regularity as shown in the case of GaN (see section 5.3) and a larger wire length. Secondly, they will be covered by a transparent coating (SiN for example). This coating should passivate the surface of the wire (see section 7.1.3) accordingly to the reference [131] where they embedded ZnO nanowires in a polymethyl methacrylate (PMMA) layer. Once these two technological locks are removed, we will be able to study the phase diagram of 1D quantum degenerate polaritons at low temperature. Owing to the larger wire length, spatial correlation on hundreds of micrometers will allow to study the effect of the interactions between polaritons in this 1D system under non-resonant continuous wave excitation. ZnO microwires have a significant advantage from this point of view. Indeed, at low temperature, they provide well-defined polaritons close to the energy of the biexciton resonance ($7meV$ below the exciton resonance). Thanks to the polariton-biexciton interaction [132], it should be possible to tune the interactions between the polaritons by order of magnitudes as it has already been done in atomic physics [133]. In principle, with this effect, we should be able to study all the different regimes offered by the 1D confinement, ie. from quasi-condensation to Tonks-Girardeau regime and maybe the Super Tonks-Girardeau regime.

The result on GaN microwires offers as well a complete set of outlooks. The short term perspectives deals with the comparison of photon and polariton lasing on a single microwire thanks to the switching off of the strong coupling regime in the doped part. From a practical point of view, it is possible for the first time to compare the absolute value of the lasing threshold on a unique structure in either weak and strong coupling regime. Of course, this study should be done in taking into account the gain mechanisms in each part of the wire in order to have a better understanding of each threshold.

The long term perspectives on GaN rely on the electrical pumping of the polariton condensate. This step is based on a development of n and p doped part in a GaN microwire which is already under its way. The electrical contact is as well possible since these skills have been developed in the NPSC team of the Néel Institute by J. S. Hwang and F. Donatini for ZnO nanowires [134]. As a consequence, such a structure would be much less demanding compared to an electrically pumped microcavity from the growth point of view.

To go one step further, these microwires offer the unique possibility to couple the quantum degenerate polariton gas with an electron gas in a simple structure. This perspective takes advantages of the simple microwire structure and its wire shape. Indeed, it has been shown that radial growth of GaN around a GaN microwire [135, 136] is realizable in a single growth run. In our case, we are interested in recovering the GaN microwire with a thin layer $\sim 10nm$ of highly doped GaN. Since the growth is lattice matched, the HWGMs should not be affected by this thin layer. Such a system, ie. a degenerate gas of polaritons coupled to a sea of electrons, has been predicted, after electrical contacting, to engender a rich physics resulting from the coupling between a quantum degenerate Bose gas and a Fermi gas [137] with the potentiality to observe polariton-condensate mediated superconductivity.

Bibliography

[1] A. Amo, D. Sanvitto, F. P. Laussy, D. Ballarini, E. del Valle, M. D. Martin, A. Lemaitre, J. Bloch, D. N. Krizhanovskii, M. S. Skolnick, C. Tejedor, et L. Vina, "*Collective fluid dynamics of a polariton condensate in a semiconductor microcavity*", *Nature* (2009), vol. 457, pp. 291–295.

[2] A. Amo, J. Lefrere, S. Pigeon, C. Adrados, C. Ciuti, I. Carusotto, R. Houdre, E. Giacobino, et A. Bramati, "*Superfluidity of polaritons in semiconductor microcavities*", *Nature Physics* (2009), vol. 5, pp. 805–810.

[3] K. G. Lagoudakis, T. Ostatnický, A. V. Kavokin, Y. G. Rubo, R. André, et B. Deveaud-Plédran, "*Observation of Half-Quantum Vortices in an Exciton-Polariton Condensate*", *Science* (2009), vol. 326, no. 5955, pp. 974–976.

[4] K. G. Lagoudakis, M. Wouters, M. Richard, A. Baas, I. Carusotto, R. Andre, Le Si Dang, et B. Deveaud-Pledran, "*Quantized vortices in an exciton-polariton condensate*", *Nature Physics* (2008), vol. 4, pp. 706–710.

[5] D. Sanvitto, F. M. Marchetti, M. H. Szymanska, G. Tosi, M. Baudisch, F. P. Laussy, D. N. Krizhanovskii, M. S. Skolnick, L. Marrucci, A. Lemaitre, J. Bloch, C. Tejedor, et L. Vina, "*Persistent currents and quantized vortices in a polariton superfluid*", *Nature Physics* (2010), vol. 6, pp. 527–533.

[6] V. Kohnle, Y. Léger, M. Wouters, M. Richard, M. T. Portella-Oberli, et B. Deveaud-Plédran, "*From Single Particle to Superfluid Excitations in a Dissipative Polariton Gas*", *Phys. Rev. Lett.* (2011), vol. 106, p. 255302.

[7] K. G. Lagoudakis, B. Pietka, M. Wouters, R. André, et B. Deveaud-Plédran, "*Coherent Oscillations in an Exciton-Polariton Josephson Junction*", *Phys. Rev. Lett.* (2010), vol. 105, p. 120403.

[8] E. Wertz, L. Ferrier, D. D. Solnyshkov, R. Johne, D. Sanvitto, A. Lemaitre, I. Sagnes, R. Grousson, A. V. Kavokin, P. Senellart, G. Malpuech, et J. Bloch, "*Spontaneous formation and optical manipulation of extended polariton condensates*", *Nature Physics* (2011), vol. 6, pp. 860–864.

[9] F. Manni, K. G. Lagoudakis, B. Pietka, L. Fontanesi, M. Wouters, V. Savona, R. André, et B. Deveaud-Plédran, "*Polariton Condensation in a One-Dimensional Disordered Potential*", *Phys. Rev. Lett.* (2011), vol. 106, p. 176401.

[10] Lambert K. van Vugt, Sven Rühle, Prasanth Ravindran, Hans C. Gerritsen, Laurens Kuipers, et Daniël Vanmaekelbergh, "*Exciton Polaritons Confined in a ZnO Nanowire Cavity*", *Phys. Rev. Lett.* (2006), vol. 97, p. 147401.

[11] Bose, "*Plancks Gesetz und Lichtquantenhypothese*", *Zeitschrift fur Physik A Hadrons and Nuclei* (1924), vol. 26, pp. 178–181. 10.1007/BF01327326.

[12] A. Einstein, "*Quantentheorie des einatomigen idealen Gases*", *Sitzungsber. Kgl. Preuss. Akad. Wiss.* (1924), vol. 261.

[13] A. Einstein, "*Quantentheorie des einatomigen idealen Gases*", *Sitzungsber. Kgl. Preuss. Akad. Wiss.* (1925), vol. 3.

[14] J. F. Allen et A. D. Misener, "*Flow of Liquid Helium II*", *Nature* (1938), vol. 141, p. 75.

[15] P. Kapitza, "*Viscosity of Liquid Helium below the λ-Point*", *Nature* (1938), vol. 141, p. 74.

[16] M. H. Anderson, J. R. Ensher, M. R. Matthews, C. E. Wieman, et E. A. Cornell, "*Observation of Bose-Einstein Condensation in a Dilute Atomic Vapor*", *Science* (1995), vol. 269, no. 5221, pp. 198–201.

[17] S. O. Demokritov, V. E. Demidov, O. Dzyapko, G. A. Melkov, A. A. Serga, B. Hillebrands, et A. N. and Slavin, "*Bose-Einstein condensation of quasi-equilibrium magnons at room temperature under pumping*", *Nature* (2006), vol. 443, pp. 430–433.

[18] Jan Klaers, Julian Schmitt, Frank Vewinger, et Martin Weitz, "*Bose-Einstein condensation of photons in an optical microcavity*", *Nature* (2010), vol. 468, pp. 545–548.

[19] J. Kasprzak, M. Richard, S. Kundermann, A. Baas, P. Jeambrun, J. M. J. Keeling, F. M. Marchetti, M. H. Szymanska, R. Andre, J. L. Staehli, V. Savona, P. B. Littlewood, B. Deveaud, et Le Si Dang, "*Bose-Einstein condensation of exciton polaritons*", *Nature* (2006), vol. 443, pp. 409–414.

[20] Jacques Levrat, Raphaël Butté, Eric Feltin, Jean-Fran çois Carlin, Nicolas Grandjean, Dmitry Solnyshkov, et Guillaume Malpuech, "*Condensation phase diagram of cavity polaritons in GaN-based microcavities: Experiment and theory*", *Phys. Rev. B* (2010), vol. 81, p. 125305.

[21] Michiel Wouters et Iacopo Carusotto, "*Superfluidity and Critical Velocities in Nonequilibrium Bose-Einstein Condensates*", *Phys. Rev. Lett.* (2010), vol. 105, p. 020602.

[22] S. I. Tsintzos, N. T. Pelekanos, G. Konstantinidis, Z. Hatzopoulos, et P. G. Savvidis, "*A GaAs polariton light-emitting diode operating near room temperature*", *Nature* (2008), vol. 453, pp. 372–375.

[23] Daniele Bajoni, Pascale Senellart, Esther Wertz, Isabelle Sagnes, Audrey Miard, Aristide Lemaître, et Jacqueline Bloch, "*Polariton Laser Using Single Micropillar* GaAs-GaAlAs *Semiconductor Cavities*", *Phys. Rev. Lett.* (2008), vol. 100, p. 047401.

[24] O. El Daif, A. Baas, T. Guillet, J.-P. Brantut, R. Idrissi Kaitouni, J. L. Staehli, F. Morier-Genoud, et B. Deveaud, "*Polariton quantum boxes in semiconductor microcavities*", *Applied Physics Letters* (2006), vol. 88, no. 6, p. 061105.

[25] D. S. Petrov, G. V. Shlyapnikov, et J. T. M. Walraven, "*Regimes of Quantum Degeneracy in Trapped 1D Gases*", *Phys. Rev. Lett.* (2000), vol. 85, pp. 3745–3749.

[26] J.J. Hopfield et D.G. Thomas, "*On some observable properties of longitudinal excitons*", *Journal of Physics and Chemistry of Solids* (1960), vol. 12, no. 3-4, pp. 276 – 284.

[27] C. H. Henry et J. J. Hopfield, "*Raman Scattering by Polaritons*", *Phys. Rev. Lett.* (1965), vol. 15, pp. 964–966.

[28] J. J. Hopfield, "*Theory of the Contribution of Excitons to the Complex Dielectric Constant of Crystals*", *Phys. Rev.* (1958), vol. 112, pp. 1555–1567.

[29] C.F. Klingshirn, B.K. Meyer, A. Waag, A. Hoffmann, et J.M.M. Geurts, *Zinc Oxide: From Fundamental Properties Towards Novel Applications.* Materials Science, Springer, 2010.

[30] Markus R. Wagner, Jan-Hindrik Schulze, Ronny Kirste, Munise Cobet, Axel Hoffmann, Christian Rauch, Anna V. Rodina, Bruno K. Meyer, Uwe Röder, et Klaus Thonke, "Γ_7 *valence band symmetry related hole fine splitting of bound excitons in ZnO observed in magneto-optical studies*", *Phys. Rev. B* (2009), vol. 80, p. 205203.

[31] V., C. Savona, A. Piermarocchi, P. Quattropani, F. Schwendimann, et Tassone, "*Optical properties of microcavity polaritons*", *Phase Transitions: New aspects in optical properties of nanostructures* (1998), vol. **68**, pp. 169–279.

[32] C.F. Klingshirn, *Semiconductor optics.* Advanced texts in physics, Springer, 2007.

[33] W. Y. Liang et A. D. Yoffe, "*Transmission Spectra of ZnO Single Crystals*", *Phys. Rev. Lett.* (1968), vol. 20, pp. 59–62.

[34] P.Y. Yu et M. Cardona, *Fundamentals of Semiconductors: Physics and Materials Properties.* Graduate Texts in Physics, Springer, 2010.

[35] C.F. Klingshirn, *Semiconductor optics.* Advanced texts in physics, Springer, 2007.

[36] J. Grabowska, A. Meaney, K. K. Nanda, J.-P. Mosnier, M. O. Henry, J.-R. Duclère, et E. McGlynn, "*Surface excitonic emission and quenching effects in ZnO nanowire/nanowall systems: Limiting effects on device potential*", *Phys. Rev. B* (2005), vol. 71, p. 115439.

[37] Yang Zhang, Dai-Jang Chen, et Ching-Ting Lee, "*Free exciton emission and dephasing in individual ZnO nanowires*", *Applied Physics Letters* (2007), vol. 91, no. 16, p. 161911.

[38] Claus Klingshirn, J. Fallert, H. Zhou, J. Sartor, C. Thiele, F. Maier-Flaig, D. Schneider, et H. Kalt, "*65 years of ZnO research - old and very recent results*", *physica status solidi (b)* (2010), vol. 247, no. 6, pp. 1424–1447.

[39] S. F. Chichibu, T. Sota, G. Cantwell, D. B. Eason, et C. W. Litton, "*Polarized photoreflectance spectra of excitonic polaritons in a ZnO single crystal*", *Journal of Applied Physics* (2003), vol. 93, no. 1, pp. 756–758.

[40] Munise Cobet, Christoph Cobet, Markus R. Wagner, Norbert Esser, Christian Thomsen, et Axel Hoffmann, "*Polariton effects in the dielectric function of ZnO excitons obtained by ellipsometry*", *Applied Physics Letters* (2010), vol. 96, no. 3, p. 031904.

[41] J. Wrzesinski et D. Fröhlich, "*Two-photon and three-photon spectroscopy of ZnO under uniaxial stress*", *Phys. Rev. B* (1997), vol. 56, pp. 13087–13093.

[42] C. Cohen-Tannoudji, J. Dupont-Roc, et G. Grynberg, *Processus d'interaction entre photons et atomes.* Savoirs actuels. Série Physique, EDP Sciences, 1996.

[43] B. Deveaud, B. Deveaud, A. Quattrucci, P. Schwendimann, et Società italiana di fisica, *Confinamento di elettroni e fotoni in nanostrutture a semiconduttori.* Proceedings of the International School of Physics "Enrico Fermi", IOS Press, 2003.

[44] M. Matsushita, J. Wicksted, et H. Z. Cummins, "*Resonant Brillouin scattering in CdS. II. Theory*", *Phys. Rev. B* (1984), vol. 29, pp. 3362–3381.

[45] W. C. Tait, "*Quantum Theory of a Basic Light-Matter Interaction*", *Phys. Rev. B* (1972), vol. 5, pp. 648–661.

[46] Claus Klingshirn, Robert Hauschild, Johannes Fallert, et Heinz Kalt, "*Room-temperature stimulated emission of ZnO: Alternatives to excitonic lasing*", *Phys. Rev. B* (2007), vol. 75, p. 115203.

[47] K. Hazu, T. Sota, S. Adachi, Sf. Chichibu, G. Cantwell, D. C. Reynolds, et C. W. Litton, "*Phonon scattering of excitons and biexcitons in ZnO*", *Journal of Applied Physics* (2004), vol. 96, no. 2, pp. 1270–1272.

[48] Jun-Rong Chen, Tien-Chang Lu, Yung-Chi Wu, Shiang-Chi Lin, Wei-Rein Liu, Wen-Feng Hsieh, Chien-Cheng Kuo, et Cheng-Chung Lee, "*Large vacuum Rabi splitting in ZnO-based hybrid microcavities observed at room temperature*", *Applied Physics Letters* (2009), vol. 94, no. 6, p. 061103.

[49] F. Medard, D. Lagarde, J. Zuniga-Perez, P. Disseix, M. Mihailovic, J. Leymarie, E. Frayssinet, J. C. Moreno, F. Semond, M. Leroux, et S. Bouchoule, "*Influence of the excitonic broadening on the strong light-matter coupling in bulk zinc oxide microcavities*", *Journal of Applied Physics* (2010), vol. 108, no. 4, p. 043508.

[50] R. Schmidt-Grund, B. Rheinländer, C. Czekalla, G. Benndorf, H. Hochmuth, M. Lorenz, et M. Grundmann, "*Exciton-polariton formation at room temperature in a planar ZnO resonator structure*", *Applied Physics B: Lasers and Optics* (2008), vol. 93, pp. 331–337. 10.1007/s00340-008-3160-x.

[51] R. Shimada, J. Xie, V. Avrutin, U. Ozgur, et H. MorkoC, "*Cavity polaritons in ZnO-based hybrid microcavities*", *Applied Physics Letters* (2008), vol. 92, no. 1, p. 011127.

[52] Liaoxin Sun, Zhanghai Chen, Qijun Ren, Ke Yu, Lihui Bai, Weihang Zhou, Hui Xiong, Z. Q. Zhu, et Xuechu Shen, "*Direct Observation of Whispering Gallery Mode Polaritons and their Dispersion in a ZnO Tapered Microcavity*", *Phys. Rev. Lett.* (2008), vol. 100, p. 156403.

[53] Vincenzo Savona, "*Effect of interface disorder on quantum well excitons and microcavity polaritons*", *Journal of Physics: Condensed Matter* (2007), vol. 19, no. 29, p. 295208.

[54] P. Michetti et G. C. La Rocca, "*Polariton states in disordered organic microcavities*", *Phys. Rev. B* (2005), vol. 71, p. 115320.

[55] Ke Yu, Yongsheng Zhang, Rongli Xu, Shixi Ouyang, Dongmei Li, Laiqiang Luo, Ziqiang Zhu, Jin Ma, Shijie Xie, Shenghao Han, et Haoran Geng, "*Efficient field emission from tetrapod-like zinc oxide nanoneedles*", *Materials Letters* (2005), vol. 59, no. 14-15, pp. 1866 – 1870.

[56] J.D. Jackson, *Classical electrodynamics.* Wiley, 1975.

[57] M. A. Kaliteevski, S. Brand, R. A. Abram, A. Kavokin, et Le Si Dang, "*Whispering gallery polaritons in cylindrical cavities*", *Phys. Rev. B* (2007), vol. 75, p. 233309.

[58] Ming Cai, Oskar Painter, et Kerry J. Vahala, "*Observation of Critical Coupling in a Fiber Taper to a Silica-Microsphere Whispering-Gallery Mode System*", *Phys. Rev. Lett.* (2000), vol. 85, pp. 74–77.

[59] D. W. Vernooy, V. S. Ilchenko, H. Mabuchi, E. W. Streed, et H. J. Kimble, "*High-Q measurements of fused-silica microspheres in the near infrared*", *Opt. Lett.* (1998), vol. 23, pp. 247–249.

[60] B. Gayral, J. M. Gerard, A. Lemaitre, C. Dupuis, L. Manin, et J. L. Pelouard, "*High-Q wet-etched GaAs microdisks containing InAs quantum boxes*", *Applied Physics Letters* (1999), vol. 75, no. 13, pp. 1908–1910.

[61] E. Peter, P. Senellart, D. Martrou, A. Lemaître, J. Hours, J. M. Gérard, et J. Bloch, "*Exciton-Photon Strong-Coupling Regime for a Single Quantum Dot Embedded in a Microcavity*", *Phys. Rev. Lett.* (2005), vol. 95, p. 067401.

[62] G. Pavlovic, G. Malpuech, et N. A. Gippius, "*Dispersion and polarization conversion of whispering gallery modes in nanowires*", *Phys. Rev. B* (2010), vol. 82, p. 195328.

[63] Thomas Nobis, Evgeni M. Kaidashev, Andreas Rahm, Michael Lorenz, et Marius Grundmann, "*Whispering Gallery Modes in Nanosized Dielectric Resonators with Hexagonal Cross Section*", *Phys. Rev. Lett.* (2004), vol. 93, p. 103903.

[64] Jan Wiersig, "*Hexagonal dielectric resonators and microcrystal lasers*", *Phys. Rev. A* (2003), vol. 67, p. 023807.

[65] A. Trichet, L. Sun, G. Pavlovic, N.A. Gippius, G. Malpuech, W. Xie, Z. Chen, M. Richard, et Le Si Dang, "*One-dimensional ZnO exciton polaritons with negligible thermal broadening at room temperature*", *Phys. Rev. B* (2011), vol. 83, p. 041302.

[66] P., J. van den Berg, et Fokkema, "*The Rayleigh hypothesis in the theory of diffraction by a cylindrical obstacle*", *Antennas and Propagation, IEEE Transactions on* (1979), vol. 27, pp. 577–583.

[67] P. Vashishta et R. K. Kalia, "*Universal behavior of exchange-correlation energy in electron-hole liquid*", *Phys. Rev. B* (1982), vol. 25, pp. 6492–6495.

[68] Lev. P., Sandro Pitaevskii, et Stringari, *Bose-Einstein Condensation*. International Series of Monographs on Physics 116, Oxford University Press, 2003.

[69] A. Imamog¯lu, R. J. Ram, S. Pau, et Y. Yamamoto, "*Nonequilibrium condensates and lasers without inversion: Exciton-polariton lasers*", *Phys. Rev. A* (1996), vol. 53, pp. 4250–4253.

[70] R. P. Leavitt et J. W. Little, "*Simple method for calculating exciton binding energies in quantum-confined semiconductor structures*", *Phys. Rev. B* (1990), vol. 42, pp. 11774–11783.

[71] F. Boeuf, R. André, R. Romestain, Le Si Dang, E. Péronne, J. F. Lampin, D. Hulin, et A. Alexandrou, "*Evidence of polariton stimulation in semiconductor microcavities*", *Phys. Rev. B* (2000), vol. 62, pp. R2279–R2282.

[72] G. Nardin, G. Grosso, Y. Léger, B. Pietka, F. Morier-Genoud, et B. Deveaud-Pledran, "*Hydrodynamic nucleation of quantized vortex pairs in a polariton quantum fluid*", *Nature Physics* (2011), vol. 7, pp. 635–641.

[73] G. Roumpos, M. D. Fraser, A. Loffler, S. Hofling, A. Forchel, et Y. Yamamoto, "*Single vortex-antivortex pair in an exciton-polariton condensate*", *Nature Physics* (2011), vol. 7, pp. 129–133.

[74] D.G. et Thomas, "*The exciton spectrum of zinc oxide*", *Journal of Physics and Chemistry of Solids* (1960), vol. 15, no. 1-2, pp. 86 – 96.

[75] Marian Zamfirescu, Alexey Kavokin, Bernard Gil, Guillaume Malpuech, et Mikhail Kaliteevski, "*ZnO as a material mostly adapted for the realization of room-temperature polariton lasers*", *Phys. Rev. B* (2002), vol. 65, p. 161205.

[76] R. Johne, D. D. Solnyshkov, et G. Malpuech, "*Theory of exciton-polariton lasing at room temperature in ZnO microcavities*", *Applied Physics Letters* (2008), vol. 93, no. 21, p. 211105.

[77] Chris Sturm, Helena Hilmer, RÃ¼diger Schmidt-Grund, et Marius Grundmann, "*Observation of strong exciton-photon coupling at temperatures up to 410 K*", *New Journal of Physics* (2009), vol. 11, no. 7, p. 073044.

[78] T. Guillet, M. Mexis, J. Levrat, G. Rossbach, C. Brimont, T. Bretagnon, B. Gil, R. Butte, N. Grandjean, L. Orosz, F. Reveret, J. Leymarie, J. Zuniga-Perez, M. Leroux, F. Semond, et S. Bouchoule, "*Polariton lasing in a hybrid bulk ZnO microcavity*", *Applied Physics Letters* (2011), vol. 99, no. 16, p. 161104.

[79] S. Christopoulos, G. Baldassarri Höger von Högersthal, A. J. D. Grundy, P. G. Lagoudakis, A. V. Kavokin, J. J. Baumberg, G. Christmann, R. Butté, E. Feltin, J.-F. Carlin, et N. Grandjean, "*Room-Temperature Polariton Lasing in Semiconductor Microcavities*", *Phys. Rev. Lett.* (2007), vol. 98, p. 126405.

[80] Tien-Chang Lu, Jun-Rong Chen, Shiang-Chi Lin, Si-Wei Huang, Shing-Chung Wang, et Yoshihisa Yamamoto, "*Room Temperature Current Injection Polariton Light Emitting Diode with a Hybrid Microcavity*", *Nano Letters* (2011), vol. 11, no. 7, pp. 2791–2795.

[81] Lambert K. van Vugt, Brian Piccione, Chang-Hee Cho, Pavan Nukala, et Ritesh Agarwal, "*One-dimensional polaritons with size-tunable and enhanced coupling strengths in semiconductor nanowires*", *Proceedings of the National Academy of Sciences* (2011), vol. 108, no. 25, pp. 10050–10055.

[82] Chu Sheng, Wang Guoping, Zhou Weihang, Lin Yuqing, Chernyak Leonid, Zhao Jianze, Kong Jieying, Li Lin, Ren Jingjian, et Liu Jianlin, "*Electrically pumped waveguide lasing from ZnO nanowires*", *Nature Nanotechnology* (2011), vol. 6, pp. 506–510.

[83] W. Y. Liang et A. D. Yoffe, "*Transmission Spectra of ZnO Single Crystals*", *Phys. Rev. Lett.* (1968), vol. 20, pp. 59–62.

[84] Aishi Yamamoto, Takeo Kido, Takenari Goto, Yefan Chen, Takafumi Yao, et Atsuo Kasuya, "*Dynamics of photoexcited carriers in ZnO epitaxial thin films*", *Applied Physics Letters* (1999), vol. 75, no. 4, pp. 469–471.

[85] Markus Müller, Joël Bleuse, et Régis André, "*Dynamics of the cavity polariton in CdTe-based semiconductor microcavities: Evidence for a relaxation edge*", *Phys. Rev. B* (2000), vol. 62, pp. 16886–16892.

[86] U. Ozgur, Ya. I. Alivov, C. Liu, A. Teke, M. A. Reshchikov, S. Dogan, V. Avrutin, S.-J. Cho, et H. Morkoc, "*A comprehensive review of ZnO materials and devices*", *Journal of Applied Physics* (2005), vol. 98, no. 4, p. 041301.

[87] D. C. Reynolds, C. W. Litton, et T. C. Collins, "*Zeeman Effects in the Edge Emission and Absorption of ZnO*", *Phys. Rev.* (1965), vol. 140, pp. A1726–A1734.

[88] B. Segall et G. D. Mahan, "*Phonon-Assisted Recombination of Free Excitons in Compound Semiconductors*", *Phys. Rev.* (1968), vol. 171, pp. 935–948.

[89] X. W. Sun et H. S. Kwok, "*Optical properties of epitaxially grown zinc oxide films on sapphire by pulsed laser deposition*", *Journal of Applied Physics* (1999), vol. 86, no. 1, pp. 408–411.

[90] W. Shan, W. Walukiewicz, J. W. Ager, K. M. Yu, H. B. Yuan, H. P. Xin, Cantwell, G., et J. J. Song, "*Nature of room-temperature photoluminescence in ZnO*", *Applied Physics Letters* (2005), vol. 86, no. 19, p. 191911.

[91] Marian Zamfirescu, Alexey Kavokin, Bernard Gil, Guillaume Malpuech, et Mikhail Kaliteevski, "*ZnO as a material mostly adapted for the realization of room-temperature polariton lasers*", *Phys. Rev. B* (2002), vol. 65, p. 161205.

[92] Gabriel Christmann, Raphael Butte, Eric Feltin, Jean-Francois Carlin, et Nicolas Grandjean, "*Room temperature polariton lasing in a GaN/AlGaN multiple quantum well microcavity*", *Applied Physics Letters* (2008), vol. 93, no. 5, p. 051102.

[93] J.F. Nye, *Physical properties of crystals: their representation by tensors and matrices.* Oxford science publications, Clarendon Press, 1985.

[94] Andres de Luna Bugallo, Maria Tchernycheva, Gwenole Jacopin, Lorenzo Rigutti, FranÃ§ois Henri Julien, Shu-Ting Chou, Yuan-Ting Lin, Po-Han Tseng, et Li-Wei Tu, "*Visible-blind photodetector based on pin junction GaN nanowire ensembles*", *Nanotechnology* (2010), vol. 21, no. 31, p. 315201.

[95] Wei Guo, Meng Zhang, Animesh Banerjee, et Pallab Bhattacharya, "*Catalyst-Free InGaN/GaN Nanowire Light Emitting Diodes Grown on (001) Silicon by Molecular Beam Epitaxy*", *Nano Letters* (2010), vol. 10, no. 9, pp. 3355–3359.

[96] B. Alloing et al., *To be published in Int. J. of Nanotechnology.*

[97] M Leroux, B Beaumont, N Grandjean, P Lorenzini, S Haffouz, P Vennéguès, J Massies, et P Gibart, "*Luminescence and reflectivity studies of undoped, n- and p-doped GaN on (0001) sapphire*", *Materials Science and Engineering: B* (1997), vol. 50, no. 1-3, pp. 97 – 104.

[98] O. Aoudé, P. Disseix, J. Leymarie, A. Vasson, E. Aujol, et B. Beaumont, "*Femtosecond time-resolved interferences of resonantly excited excitons in bulk GaN*", *Superlattices and Microstructures* (2004), vol. 36, no. 4-6, pp. 607 – 614. European Materials Research

Society 2004, Symposium L. InN, GaN, AlN and Related Materials, their Heterostructures and Devices.

[99] R. Stępniewski, K. P. Korona, A. Wysmołek, J. M. Baranowski, K. Pakuła, M. Potemski, G. Martinez, I. Grzegory, et S. Porowski, "*Polariton effects in reflectance and emission spectra of homoepitaxial GaN*", *Phys. Rev. B* (1997), vol. 56, pp. 15151–15156.

[100] O. Aoudé, P. Disseix, J. Leymarie, A. Vasson, M. Leroux, E. Aujol, B. Beaumont, A. Trassoudaine, et Y. André, "*Continuous-wave and ultrafast coherent reflectivity studies of excitons in bulk GaN*", *Phys. Rev. B* (2008), vol. 77, p. 045206.

[101] Chris G. Van de Walle et David Segev, "*Microscopic origins of surface states on nitride surfaces*", *Journal of Applied Physics* (2007), vol. 101, no. 8, p. 081704.

[102] G. D. Mahan, "*Excitons in Metals: Infinite Hole Mass*", *Phys. Rev.* (1967), vol. 163, pp. 612–617.

[103] S. Shokhovets, K. Köhler, O. Ambacher, et G. Gobsch, "*Observation of Fermi-edge excitons and exciton-phonon complexes in the optical response of heavily doped n-type wurtzite GaN*", *Phys. Rev. B* (2009), vol. 79, p. 045201.

[104] F. Fuchs, K. Kheng, P. Koidl, et K. Schwarz, "*Fermi-edge singularity in degenerate n -type bulk InAs*", *Phys. Rev. B* (1993), vol. 48, pp. 7884–7888.

[105] P. Kinsler et D. M. Whittaker, "*Linewidth narrowing of polaritons*", *Phys. Rev. B* (1996), vol. 54, pp. 4988–4995.

[106] V. Savona et C. Piermarocchi, "*Microcavity Polaritons: Homogeneous and Inhomogeneous Broadening in the Strong Coupling Regime*", *physica status solidi (a)* (1997), vol. 164, no. 1, pp. 45–51.

[107] P. Borri, J. R. Jensen, W. Langbein, et J. M. Hvam, "*Direct evidence of reduced dynamic scattering in the lower polariton of a semiconductor microcavity*", *Phys. Rev. B* (2000), vol. 61, pp. R13377–R13380.

[108] S. Rudin, T. L. Reinecke, et B. Segall, "*Temperature-dependent exciton linewidths in semiconductors*", *Phys. Rev. B* (1990), vol. 42, pp. 11218–11231.

[109] L. Sun, S. Sun, H. Dong, W. Xie, M. Richard, L. Zhou, L. S. Dang, X. Shen, et Z. Chen, "*Room temperature one-dimensional polariton condensate in a ZnO microwire*", *ArXiv e-prints* (2010).

[110] T T Chen, C L Cheng, S-P Fu, et Y F Chen, "*Photoelastic effect in ZnO nanorods*", *Nanotechnology* (2007), vol. 18, no. 22, p. 225705.

[111] Q. H. Li, T. Gao, Y. G. Wang, et T. H. Wang, "*Adsorption and desorption of oxygen probed from ZnO nanowire films by photocurrent measurements*", *Applied Physics Letters* (2005), vol. 86, no. 12, p. 123117.

[112] Yanbo Li, Florent Della Valle, Mathieu Simonnet, Ichiro Yamada, et Jean-Jacques Delaunay, "*Competitive surface effects of oxygen and water on UV photoresponse of ZnO nanowires*", *Applied Physics Letters* (2009), vol. 94, no. 2, p. 023110.

[113] F. Tassone et Y. Yamamoto, "*Exciton-exciton scattering dynamics in a semiconductor microcavity and stimulated scattering into polaritons*", *Phys. Rev. B* (1999), vol. 59, pp. 10830–10842.

[114] C. Ciuti, P. Schwendimann, B. Deveaud, et A. Quattropani, "*Theory of the angle-resonant polariton amplifier*", *Phys. Rev. B* (2000), vol. 62, pp. R4825–R4828.

[115] E. Hanamura et H. Haug, "*Condensation effects of excitons*", *Physics Reports* (1977), vol. 33, no. 4, pp. 209 – 284.

[116] Lydie Ferrier, Esther Wertz, Robert Johne, Dmitry D. Solnyshkov, Pascale Senellart, Isabelle Sagnes, Aristide Lemaître, Guillaume Malpuech, et Jacqueline Bloch, "*Interactions in Confined Polariton Condensates*", *Phys. Rev. Lett.* (2011), vol. 106, p. 126401.

[117] M. M. Glazov, H. Ouerdane, L. Pilozzi, G. Malpuech, A. V. Kavokin, et A. D'Andrea, "*Polariton-polariton scattering in microcavities: A microscopic theory*", *Phys. Rev. B* (2009), vol. 80, p. 155306.

[118] C. Ciuti, V. Savona, C. Piermarocchi, A. Quattropani, et P. Schwendimann, "*Role of the exchange of carriers in elastic exciton-exciton scattering in quantum wells*", *Phys. Rev. B* (1998), vol. 58, pp. 7926–7933.

[119] M. M. Glazov, H. Ouerdane, L. Pilozzi, G. Malpuech, A. V. Kavokin, et A. D'Andrea, "*Polariton-polariton scattering in microcavities: A microscopic theory*", *Phys. Rev. B* (2009), vol. 80, p. 155306.

[120] D. Porras, J. Fernandez-Rossier, et C. Tejedor, "*Exciton and Polariton Condensation*". in *Quantum Coherence* (Walter Potz, Ulrich Hohenester, et Jaroslav Fabian, eds.), vol. 689 of *Lecture Notes in Physics*, pp. 153–189, Springer Berlin / Heidelberg, 2006.

[121] F. Tassone, C. Piermarocchi, V. Savona, A. Quattropani, et P. Schwendimann, "*Bottleneck effects in the relaxation and photoluminescence of microcavity polaritons*", *Phys. Rev. B* (1997), vol. 56, pp. 7554–7563.

[122] M. Umlauff, J. Hoffmann, H. Kalt, W. Langbein, J. M. Hvam, M. Scholl, J. Sollner, M. Heuken, B. Jobst, et D. Hommel, "*Direct observation of free-exciton thermalization in quantum-well structures*", *Phys. Rev. B* (1998), vol. 57, pp. 1390–1393.

[123] T. Schmidt, K. Lischka, et W. Zulehner, "*Excitation-power dependence of the near-band-edge photoluminescence of semiconductors*", *Phys. Rev. B* (1992), vol. 45, pp. 8989–8994.

[124] C. Klingshirn et H. Haug, "*Optical properties of highly excited direct gap semiconductors*", *Physics Reports* (1981), vol. 70, no. 5, pp. 315 – 398.

[125] Claude Benoit a la Guillaume, Jean-Marie Debever, et Frank Salvan, "*Radiative Recombination in Highly Excited CdS*", *Phys. Rev.* (1969), vol. 177, pp. 567–580.

[126] Douglas Magde et Herbert Mahr, "*Exciton-Exciton Interaction in CdS, CdSe, and ZnO*", *Phys. Rev. Lett.* (1970), vol. 24, pp. 890–893.

[127] B. Hönerlage et U. Rössler, "*Inelastic scattering of electrons with bound excitons*", *Journal of Luminescence* (1976), vol. 12-13, no. 0, pp. 593 – 597.

[128] J. Collet et T. Amand, "*Picosecond spectroscopy of excitons and biexcitons in ZnO at high density*", *Phys. Rev. B* (1986), vol. 33, pp. 4129–4135.

[129] J. M. Hvam, G. Blattner, M. Reuscher, et C. Klingshirn, "*The Biexciton Levels and Nonlinear Optical Transitions in ZnO*", *physica status solidi (b)* (1983), vol. 118, no. 1, pp. 179–189.

[130] H. Schrey, V.G. Lyssenko, et C. Klingshirn, "*Luminescence-assisted two-photon spectroscopy (LATS) - a new spectroscopic method applied to biexciton levels in highly excited CdS and ZnO*", *Solid State Communications* (1979), vol. 32, no. 10, pp. 897 – 899.

[131] Sunghoon Song, Woong-Ki Hong, Soon-Shin Kwon, et Takhee Lee, "*Passivation effects on ZnO nanowire field effect transistors under oxygen, ambient, and vacuum environments*", *Applied Physics Letters* (2008), vol. 92, no. 26, p. 263109.

[132] I. Carusotto, T. Volz, et A. Imamoglu, "*Feshbach blockade: Single-photon nonlinear optics using resonantly enhanced cavity polariton scattering from biexciton states*", *EPL (Europhysics Letters)* (2010), vol. 90, no. 3, p. 37001.

[133] S. Inouye, M. R. Andrews, J. Stenger, H.-J. Miesner, D. M. Stamper-Kurn, et W. Ketterle, "*Observation of Feshbach resonances in a Bose-Einstein condensate*", *Nature* (1998), vol. 392, pp. 151–154.

[134] Jun-Seok Hwang, Fabrice Donatini, Julien Pernot, Robin Thierry, Pierre Ferret, et Le Si Dang, "*Carrier depletion and exciton diffusion in a single ZnO nanowire*", *Nanotechnology* (2011), vol. 22, no. 47, p. 475704.

[135] L. Geelhaar, C. Cheze, W. M. Weber, R. Averbeck, H. Riechert, Th. Kehagias, Ph. Komninou, G. P. Dimitrakopulos, et Th. Karakostas, "*Axial and radial growth of Ni-induced GaN nanowires*", *Applied Physics Letters* (2007), vol. 91, no. 9, p. 093113.

[136] A. De Luna Bugallo, L. Rigutti, G. Jacopin, F. H. Julien, C. Durand, X. J. Chen, D. Salomon, J. Eymery, et M. Tchernycheva, "*Single-wire photodetectors based on InGaN/GaN radial quantum wells in GaN wires grown by catalyst-free metal-organic vapor phase epitaxy*", *Applied Physics Letters* (2011), vol. 98, no. 23, p. 233107.

[137] Fabrice P. Laussy, Alexey V. Kavokin, et Ivan A. Shelykh, "*Exciton-Polariton Mediated Superconductivity*", *Phys. Rev. Lett.* (2010), vol. 104, p. 106402.

Résumé

Dans cette thèse, nous avons étudié les propriétés expérimentales des polaritons unidimensionnels dans les microfils de ZnO dans le but d'étudier le régime de dégénérescence quantique des polaritons à haute température et en régime de confinement de basse dimensionnalité. ZnO est en effet un matériau semiconducteur à grand gap dans lequel l'exciton bénéficie d'une très forte énergie de liaison qui garantit leur stabilité à température ambiante. D'autre part, la géométrie en "fil" de section hexagonale et de diamètre micrométrique confine les modes photoniques et les rend unidimensionnels. On montre que l'interaction entre l'exciton et ces modes photoniques est en régime de couplage fort, et que les polariton-excitoniques qui en résultent sont eux aussi en régime de confinement unidimensionnel.

Cette thèse propose une étude détaillée de la physique de ces polaritons 1D. Dans un premier temps, on démontre que le régime de couplage fort unidimensionnel est conservé jusqu'à température ambiante avec une très grande énergie de Rabi de 300 meV pour une largeur de raie typique 75 fois plus faible. Cette faible largeur de raie, même à température ambiante, est une conséquence inattendue de la grande énergie de Rabi en comparaison de l'énergie maximum des phonons dans ZnO. Cet effet isole très efficacement les polaritons des vibrations thermiques du réseau.

Nous nous sommes intéressés aussi à une structure similaire: les microfils de GaN. Dans ces fils, on profite d'une zone fortement dopée pour comparer expérimentalement le spectre en régime de couplage faible et en régime de couplage fort dans le même fil.

Nous avons ensuite étudié les propriétés des gaz de polaritons dans les microfils de ZnO sous forte excitation dans le but d'atteindre le régime de dégénérescence quantique 1D. Nous démontrons qu'un régime de laser à polaritons est atteint à basse température en régime de couplage fort dans une situation inédite où les polaritons sont à 97% excitoniques. Cette propriété est comprise grâce à une étude détaillée des propriétés de relaxation des excitons vers les états de polaritons en régime de faible et forte excitations.

Cette thèse donne les bases de la compréhension des polaritons unidimensionnels dans les microfils de ZnO. Les propriétés observées montrent que les microfils de ZnO sont particulièrement adaptés à l'étude des gaz de polaritons dégénérés 1D à haute température.

Mots-clés: Polariton, couplage fort, unidimensionnel, ZnO, microfil, mode de gallerie hexagonal, boson, condensation, dégénerescence quantique

Abstract

In this thesis, we have studied the experimental properties of one-dimensional polaritons in the ZnO microwires in order to study the quantum degenerate regime in a one-dimensional polariton gas at high temperature. ZnO is a wide gap semiconductor material in which the exciton is stable at room temperature thanks to its high binding energy. The "wire" geometry with a micrometric scale hexagonal cross-section results in a one-dimensional confinement of the light. The ZnO excitons and these photonic modes are in the strong coupling regime resulting in new light-matter eigenstates called exciton-polaritons which are, as well, in the one-dimensional confinement regime.

This thesis provides a detailed study of the Physics of these 1D polaritons. As a first step, we demonstrate that the one-dimensional strong coupling regime is preserved up to room temperature with a very high Rabi splitting of 300 meV for a typical linewidth 75 times smaller. This small linewidth, even at room temperature, is an unexpected consequence of the high Rabi energy compared to the maximum phonon energy in ZnO. This effect efficiently isolates the polaritons from the thermal fluctuations of the lattice.

We have studied as well a similar structure: the GaN microwires. Because of a highly doped part in these wires, it is possible to compare experimentally the spectrum in weak and strong coupling regime in a single wire.

We have studied the properties of such polariton gas in ZnO microwires in the high excitation regime in order to reach the 1D quantum degeneracy limit. We have demonstrated that the polariton lasing regime is obtained at low temperature in the strong coupling regime and that it exhibits an unusual situation: the lasing polariton mode is made up of 97% of exciton. This property is understood thanks to a detailed study of the relaxation properties of the excitons towards the polariton states below and above the polariton lasing threshold.

This thesis provides the basics to understand the one-dimensional polaritons in ZnO microwires. The properties described in this thesis demonstrate that the ZnO microwires are particularly suitable for the study of 1D degenerate polariton gas at room temperature.

Keywords: Polariton, strong coupling, unidimensional, ZnO, microwire, hexagonal whispering gallery mode, boson, condensation, quantum degeneracy